

ALMA MATER STUDIORUM - UNIVERSITÀ DI BOLOGNA

FACOLTÀ DI INGEGNERIA
DOTTORATO DI RICERCA IN INGEGNERIA ELETTRTECNICA
XXI CICLO

Tesi di Dottorato

Diagnostic techniques for EHD and MHD interaction

Dott. **Gabriele Neretti**

Relatore:

Chiar.mo Prof.

CARLO ANGELO BORGHI

Coordinatore Dottorato:

Chiar.mo Prof.

Correlatore:

FRANCESCO NEGRINI

Prof.

ANDREA CRISTOFOLINI

Bologna, Italia, Marzo 2009

ALMA MATER STUDIORUM - UNIVERSITÀ DI BOLOGNA

FACOLTÀ DI INGEGNERIA
DOTTORATO DI RICERCA IN INGEGNERIA ELETTROTECNICA
XXI CICLO

Tesi di Dottorato

Diagnostic techniques for EHD and MHD interaction

Dott. Gabriele Neretti

Relatore:

Chiar.mo Prof.

CARLO ANGELO BORGHI

Coordinatore Dottorato:

Chiar.mo Prof.

Correlatore:

FRANCESCO NEGRINI

Prof.

ANDREA CRISTOFOLINI

Settore scientifico disciplinare di afferenza: ING-IND/31

Bologna, Italia, Marzo 2009

Many people helped and supported me during the realization of this Thesis. I want to express gratitude to all of them.

The first thought goes to my supervisors Carlo Angelo Borghi and Andrea Cristofolini. They showed me not only the beauty of plasmas but, more important, the great joy that the research can give to anyone who is able to give back devotion to it.

A special thanks goes to Mario Roberto Carraro. How “young Padawan” as I was, I will never forget his “Jedi” teachings.

To my PhD colleagues Maria, Chiara and Fabio. A big big thanks to their help during these years.

I’m particularly grateful to professor Richard B. Miles. He allowed me to spend six months as visiting PhD Student at the Mechanical and Aerospace Department of the Princeton University. This work has been made also possible due to his kindness.

To my family, to which I will never be sufficiently grateful enough. They always supported me in all my decisions. Thank you.

To Elena. She gave me peace and happiness in these last hard months. I love you.

Contents

Introduction	xix
I Diagnostic techniques theory	1
1 Microwave diagnostic	3
1.1 Introduction	3
1.2 Electromagnetic waves in collisionless plasmas	4
1.3 Electromagnetic waves in collisional plasmas	8
1.4 Microwave propagation theory	14
2 Schlieren diagnostic	25
2.1 Introduction	25
2.2 Light propagation in an inhomogeneous medium	25
2.3 Schlieren technique	27
2.4 Sensitivity of the Schlieren diagnostic	31
3 Spectroscopic diagnostic	35
3.1 Plasma thermodynamic equilibrium	35
3.2 Atomic and molecular emission spectroscopy	37
3.3 Plasma parameters spectroscopic evaluation	47
4 Pitot tube diagnostic	57
5 Electrostatic probes	61

II	EHD interaction experiments	63
6	Introduction to EHD applications	65
7	EHD interaction theory	67
7.1	The Dielectric Barrier Discharge	67
7.2	The EHD actuator based on the DBD	72
7.3	EHD air flow control	81
8	The EHD 3-phase actuator	85
8.1	The EHD 3-phase actuator setup	85
8.2	Diagnostic setup	92
8.3	Interpretation of the results	95
9	Nanopulses driving system for a DBD actuator	111
9.1	Nanopulses DBD actuator setup	111
9.2	Diagnostic setup	122
9.3	Interpretation of the results	127
10	EHD experiments conclusions	169
III	MHD interaction experiments	171
11	Introduction to MHD applications in the hypersonic flight	173
12	Non-intrusive nozzle characterization	177
12.1	Hypersonic wind-tunnel facility	177
12.2	Diagnostic setup	183
12.3	Interpretation of the results	186
13	MHD conical test body experiment	201
13.1	Test body magnetic configuration	201
13.2	Diagnostic setup	217
13.3	Interpretation of the results	218

14 MHD experiments conclusions	247
Appendix	251
A Plasma frequency	251
B Electromagnetic wave propagation theory	253
C Schlieren refraction in geometric optic	259
Bibliography	263

List of Figures

1.2.1	Electromagnetic wave frequency vs plasma frequency.	6
1.3.1	Refractive index at various electron heavy collision frequency.	11
1.3.2	Attenuation index at various electron heavy collision frequency.	11
1.3.3	Transmission factor with different electron collisional frequencies and electron-heavy collision frequencies	13
1.4.1	Hollow rectangular waveguide	17
1.4.2	Electric and magnetic field lines for a TE_{10} mode.	21
1.4.3	E-plane electric and magnetic field lines for the TE_{10} mode (side view).	21
1.4.4	H-plane electric and magnetic field lines for the TE_{10} mode (top view).	22
2.3.1	Schlieren setup with a point source [1].	27
2.3.2	Schlieren setup with a real extended light source [1].	28
2.3.3	Diagram of the knife edge plane. Undisturbed and displaced light source [1]	29
2.3.4	Schlieren image of a hand with knife edge gradually closed from a to d . It is possible to note the heat volutes. [1]	30
2.4.1	Z-configuration Schlieren setup scheme [1].	31
3.2.1	Scheme of the vibration-rotation energy levels for vibrational quantum number $v = 0 \div 1$ and rotational quantum number $J = 0 \div 5$	42

3.2.2	Scheme of the spectra of R , Q and P molecular branches. . .	43
3.2.3	Scheme of the energy transitions of the P (left-hand side) and R (right-hand side) branches.	45
3.2.4	R-branch of the rovibronical spectra of the Second Positive System of the N_2 molecule. The band head peak is easily visible.	46
3.3.1	Normalized Gauss (Doppler) and Lorentz (Stark) profiles of equal FWHM. In continuous line there is the Voigt profile, convolution of these two profiles [2].	55
4.0.1	Pitot tube scheme	58
4.0.2	Zoom of the pitot nose	58
7.1.1	Example scheme of DBD setup configuration.	68
7.1.2	Plasma formed by a DBD in air at atmospheric pressure. . .	69
7.1.3	Voltage and current vs. time characteristic of a DBD. Supply voltage $2[kV]$ peak, $5[kHz]$	71
7.2.1	DC surface corona fluid-dynamic actuator design from [3]. .	73
7.2.2	Velocity profile in still air for a DC Corona fluid-dynamic actuator with increasing current [4].	73
7.2.3	Typical EHD fluid-dynamic actuator arrangement.	74
7.2.4	Pitot scan of the boundary layer induced velocity by a DBD fluid-dynamic actuator supplied by an AC voltage of $5[kVp]$ at different frequencies.	76
7.2.5	Voltage and current vs. time characteristic of an asymmetric DBD actuator. It is possible to note the asymmetric behaviour of the current.	77
7.2.6	Photo Multiplier signal of ionized air measured over the bare electrode of a DBD actuator (top), and corresponding AC supply signal (bottom) [5].	79

7.3.1	Smoke visualization photographs of a flat panel positioned with an angle of attack of 26° ($Re = 3000$): baseline (left-hand side) and “steady plasma” control (right-hand) [6]. . .	82
7.3.2	Smoke visualization photographs of an airfoil positioned with an angle of attack of 25° ($Re = 20500$): baseline (left-hand side) and steady plasma control (right-hand) [6].	82
7.3.3	Effect of control on the flat panel performance at $Re = 9000$ and 20000 [6].	83
7.3.4	Pak-B blade with single DBD actuator photography on the left side and velocity measurements obtained using LDV on right one [7].	84
8.1.1	Top view of the 3-phase multielectrode flat panel. In continuous lines there are the top HV electrodes. In dashed the lower embedded grounded electrodes.	86
8.1.2	Transversal section of a couple of electrode of the 3-phase multielectrode configuration.	87
8.1.3	Scheme of the 3-phase EHD panel supply system. For phases S and T the scheme is the same that for phase R	88
8.1.4	Three-phase signal generator layout	89
8.1.5	Single Monophase Power amplifier branch. The actual design uses three of this branches, with a “dye” configuration on high voltage transformers.	90
8.1.6	Scheme and quotation of the wind tunnel used for the 3-phase EHD experiments.	91
8.2.1	Pitot tube position in the three phase EHD setup.	93
8.2.2	Position of the lens over the plasm.	94
8.2.3	Plasma Panel Experimental set-up. For phases S and T there is the same probe set-up as for phase R	96
8.3.1	Induced flow velocities at different frequencies and for the four wind tunnel conditions: $1[m/s]$ (a), $4[m/s]$ (b), $11[m/s]$ (c), $20[m/s]$ (d).	97

8.3.2	Schlieren image close to the actuator surface with a supply voltage equal to $5[kVp]$ and frequency of $9[kHz]$: left-hand side the external flow velocity is of $0[m/s]$, in the right-hand one is $16[m/s]$	99
8.3.3	Voltage and current vs. time characteristic of one phase of the asymmetric 3-phase DBD actuator.	100
8.3.4	Active power at different supply frequencies and for the four wind tunnel conditions: $1[m/s]$ (a), $4[m/s]$ (b), $11[m/s]$ (c), $20[m/s]$ (d).	101
8.3.5	Three phases supply voltage. Periods in which the plasma is formed for the phase S are emphasized.	102
8.3.6	FEM simulation of two different supply conditions for the RST phases. In the left-hand side $R = -[6kV]$, $S = [3kV]$ and $T = 3[kV]$, in the right one $R = 3[kV]$, $S = 3[kV]$ and $T = -6[kV]$. E-field and iso-potential line are showed.	103
8.3.7	Low resolution spectra of the Second Positive System of the N_2 molecule ($C^3\Pi_u \rightarrow B^3\Pi_g$).	104
8.3.8	Spectra of the $\Delta\nu-2$ sequence of the Second Positive System of N_2 molecule ($C^3\Pi_u \rightarrow B^3\Pi_g$).	105
8.3.9	Example of Boltzmann plot of $\Delta\nu-2$ sequence of the Second Positive Band of N_2 ($N_2 C^3\Pi_u \rightarrow B^3\Pi_g$).	106
8.3.10	Vibrational temperature as a function of power supplying frequency and voltage with $1[m/s]$ and $11[m/s]$ free stream velocities.	106
8.3.11	Partially resolved First Negative System of N_2^+ ($B^2\Sigma_u^+ - X^2\Sigma_g^+$).	108
8.3.12	Rotational temperature as a function of the airflow velocity at different supplying frequencies with the two different electrodes configuration.	109
9.1.1	Scheme of the single dielectric barrier discharge actuator.	113
9.1.2	Photo of the DBD actuator on.	114

9.1.3	Electrical scheme of the nanopulses driven DBD actuator.	115
9.1.4	Terminology used in the paper for the pulse and bias voltage polarities.	118
9.1.5	An equivalent scheme of the transformer made of sections of transmission lines connected to the <i>RLC</i> load.	118
9.1.6	Numerical calculation of the nanosecond pulses.	121
9.1.7	The measured pulse profile before and after optimization.	122
9.2.1	Schlieren setup.	125
9.2.2	Balance in a Faraday cage and actuator position.	126
9.2.3	Electrostatic probe spatial resolution. 1[kV] step-like potential.	127
9.3.1	Schlieren photograph of the induced wall-jet of the DBD actuator run in pulse-burst mode and position of the actuator respect the photograph itself.	128
9.3.2	Numerical results of the air density and velocity distribution 14 ms after the burst.	130
9.3.3	An example of experimental (left) and simulated (right) Schlieren images of the DBD plasma jets. The images are $20 \times 10[mm^2]$ each and correspond to 7, 14, and 21[ms] after the burst start.	131
9.3.4	Vortex propagation velocity as a function of the horizontal distance from the exposed electrode at different forces in the interaction region.	133
9.3.5	Variation of the DC bias maintaining constant pulses amplitude.	134
9.3.6	Induced tangential flow speed vs distance at different constant bias voltages. The error bar is $\sim 0.04[m/s]$	135
9.3.7	DC bias voltage switch experiments. Schlieren visualization.	136
9.3.8	Surface wipe experiments.	138
9.3.9	Nanosecond pulses combined with sinusoidal bias voltage.	140

9.3.10	Vortex speed vs distance for different PRRs with positive polarity of the pulses. Schlieren photograph.	142
9.3.11	Vortex speed vs distance for different PRRs with negative polarity of the pulses. Schlieren photograph.	144
9.3.12	Vortex speed vs distance for different pulse voltages with positive polarity of the pulses. Schlieren photograph.	145
9.3.13	Vortex speed vs distance for different pulse voltages with negative polarity of the pulses. Schlieren photograph	146
9.3.14	Vortex speed vs distance for different peak-to-peak sinusoidal bias voltages with positive polarity of the pulses. Schlieren photograph.	147
9.3.15	Vortex speed vs distance for different peak-to-peak sinusoidal bias voltages with negative polarity of the pulses. Schlieren photograph.	149
9.3.16	Voltage profiles with pulses near the bias voltage peaks of one polarity only.	150
9.3.17	Vortex speed vs distance for different voltage waveforms. The Schlieren images were taken at the same moment of time for pulses during negative half-cycle only, both half-cycles, and positive half-cycle only. The field of view of each Schlieren image is $20 \times 10[mm^2]$	150
9.3.18	Thrust measurements for different bias profiles. Bias $10[kV]$ peak-to-peak, $100[Hz]$; Pulses $3[kV]$, $25[kHz]$ 100% duty cycle.	151
9.3.19	Thrust measurements for different bias duty cycles. Bias: rectangular, $10[kV]$ peak-to-peak, $100[Hz]$; Pulses $3[kV]$, $25[kHz]$ 100% duty cycle.	152
9.3.20	Thrust measurements for different pulses duty cycles. Bias: rectangular, $10[kV]$ peak-to-peak, $100[Hz]$; Pulses $3[kV]$, $25[kHz]$ 100% duty cycle.	153

9.3.21	Thrust dependence on applied voltage parameters. Negative pulses. Bias: rectangular, 10[kV] peak-to-peak, 100[Hz]; Pulses 3[kV], 25[kHz] 100% duty cycle.	154
9.3.22	Thrust dependence on applied voltage parameters. Negative pulses. Bias: rectangular, 10[kV] peak-to-peak, 100[Hz]; Pulses 3[kV], 25[kHz] 100% duty cycle.	155
9.3.23	“Pulses plus AC bias” versus sinusoidal voltage: comparison of tangential body forces. Comparison data were taken from [8, 9].	156
9.3.24	Pulses plus AC bias versus sinusoidal voltage: comparison of tangential body forces (zoomed in). Comparison data were taken from [8, 9].	157
9.3.25	Surface potential distribution. Applied voltage profile: sinusoidal, 3[kHz], 10[kV] peak-to-peak. Electrodes edge at 0.	158
9.3.26	Surface potential distribution. Applied voltage profile: sinusoidal, 3[kHz], 10[kV] peak-to-peak. $C = 167[pF]$ in series with the plasma actuator. Electrodes edge at 0.	160
9.3.27	Suspended plate in the induced flow potential. A metallic plate with a surface of $S = 35[cm^2]$, put in the induced flow 3[cm] downstream gets positive charge. Applied voltage profile: sinusoidal, 3[kHz], 10[kV] peak-to-peak.	161
9.3.28	Surface potential distribution. Applied voltage profile: pulses + DC bias, 2[kV] DC bias, 3[kV] pulses at 10[kHz] PRR.	162
9.3.29	Surface potential for a fixed number of pulses. Applied voltage profile: pulses + DC bias, 2[kV] DC bias, 3[kV] pulses at 10[kHz] PRR.	163
9.3.30	Surface potential versus time for positive (left side) and negative (right side) surface charges.	164
9.3.31	Modified DBD plasma actuator scheme.	165

9.3.32	Modified DBD plasma actuator. Thrust versus PRR at 4[kV] positive DC bias voltage, 3[kV] negative pulses (left). Thrust versus bias voltage at 10[kHz] PRR, 3[kV] negative pulses (right).	166
9.3.33	Pulses plus AC bias versus sinusoidal voltage: comparison of tangential body forces (zoomed in). Comparison between the modified actuator and the “classical” one. Comparison data were taken from [8, 9].	166
12.1.1	Arc-heater scheme.	178
12.1.2	Nozzle mounted at the exit of the heating chamber (left-hand side) and Vacuum chamber of HEAT.	179
12.1.3	Mach number radial profile at the nozzle exit for condition A: (blue dots) measured values and (red line) mean profile.	181
12.1.4	Experimental Mach number mapping in the test section after the nozzle exit at condition A.	182
12.2.1	Position of the lenses for the spectroscopic measurements.	184
12.2.2	Horn antenna position for microwave absorption measurements.	185
12.3.1	Argon spectra of the plenum chamber.	187
12.3.2	Boltzmann Plot for Ar II, at the plenum pressure condition A.	188
12.3.3	Spectra captured in the plenum chamber in the condition A. The H_{β} line at 486.1[nm] is easily visible.	189
12.3.4	Microwave transmission signal for conditions A, B, C. At time equal to zero the plasma is ignited.	191
12.3.5	Time resolved electron number density in the plasma plume measured by means of different microwave frequencies. The electron-heavy collision frequency is in the range 2.9÷3.2[GHz].	194
12.3.6	Dissipated arc power and microwave frequency used for the electron density estimation.	195

12.3.7	Electron energy distribution functions along the nozzle for cases <i>A</i> and <i>D</i> (input data from table 12.3.5). $X = 0$ is the throat position, $x = -0.042$ is the nozzle inlet, $x = 0.28$ is the nozzle exit.	198
12.3.8	Molar fractions profiles of Ar metastable and electron (input data from table 12.3.5)	199
13.1.1	Wedge test body scheme [10].	202
13.1.2	Electrical insulation shield for the large body. A hole used for pressure measurements is visible.	204
13.1.3	Large test body assembly. Magnetic and iron sections are visible.	205
13.1.4	Large body scheme and B field distribution.	206
13.1.5	Magnetic flux density modulus on the shield wall (red line), at the end of the boundary layer (green line) and at the shock front surface (blue line).	207
13.1.6	Comparison between design and measured values of the normal component of the B field along the cone surface.	208
13.1.7	Magnetic (left-hand side) and non-magnetic (right-hand side) small test body. In the magnetic cone, magnetic and iron sections are visible.	209
13.1.8	Small body scheme and B field distribution.	210
13.1.9	MHD interaction regions (left-hand side) and Hall currents (right-hand side).	211
13.1.10	Annular channel in an axial symmetric geometry.	214
13.2.1	Electrical probes positioned on the conical insulating shield of the large test body.	219
13.3.1	Pressure behaviours with magnetic and non-magnetic test bodies in cold conditions (the blue line refers to the non-magnetic case, and the red line refers to the magnetic case).	220
13.3.2	Pressure behaviours with magnetic and non-magnetic test bodies without insulating walls of the vacuum chamber	221

13.3.3	Pressure measurements as functions of time with and without MHD interaction at flow conditions A (a), B (b) and C (c) with the large test body.	223
13.3.4	Flow pattern without MHD interaction (left-hand side) and with MHD interaction (right-hand side). Exposure time 1[ms].	224
13.3.5	MHD interaction around the magnetic cone (exposure time 0.5 [ms]). The optical axis is oblique with respect to the flow direction.	225
13.3.6	Hall voltage distribution along the conical surface of the test body at flow condition A	226
13.3.7	Hall voltage distribution along the conical surface of the test body at flow condition C	227
13.3.8	Geometry scheme of the small test body. The position of the two pressure sensors are visible.	228
13.3.9	Pressure measurements as functions of time with and without MHD interaction at flow conditions A (a), B (b) and C (c) with the small test body.	231
13.3.10	MHD interaction around the small magnetic test body.	233
13.3.11	Hall voltages along the conical surface of the small test body at the tree flow conditions and and in runs with a lower stagnation pressure.	234
13.3.12	$n_{Ar} \times \mu_e$ as a function of electron temperature and ionization degree α	236
13.3.13	Computed pressure field without and with MHD interaction.	238
13.3.14	Comparison of flow structure details between simulation and fast imaging.	238
13.3.15	Simulated azimuthal current densities.	239
13.3.16	Simulated Hall current streamlines.	239
13.3.17	Pressure along the body surface for numerical and experimental results in MHD and non-MHD runs.	240

13.3.18 Voltage along the body surface for numerical and experimental results in MHD runs.	240
13.3.19 Hall current streamlines for the extended domain.	241
13.3.20 Voltage along the body surface for numerical and experimental results in MHD runs for the extended domain.	242
13.3.21 Simulated azimuthal current densities in the extended domain.	242
13.3.22 Pressure along the body surface for numerical and experimental results in MHD and non-MHD runs. The extended domain is now used for simulations.	243
13.3.23 Computed pressure field with MHD interaction with the extended domain.	244
13.3.24 Computed temperature field with MHD interaction with the extended domain.	244
C.0.1 Diagram of elemental light refraction by a refractive index gradient dn/dy	259

List of Tables

1.4.1	Cutoff wavelengths for cavity modes.	20
8.1.1	Wind tunnel working conditions	92
8.3.1	EHD 3-phase experiment: power supply conditions.	96
12.1.1	Flow characteristic for the test conditions.	179
12.3.1	Electron temperature in the plenum chamber for the conditions A , B and C . Delay time 100[ms].	187
12.3.2	Electron number density [$part/m^3$] in the plenum chamber for the conditions A , B and C . Delay time 100[ms].	190
12.3.3	Electron excitation temperature in the plenum chamber for the D condition esteemed by continuum emission.	192
12.3.4	Electron number density measured in plenum chamber and the nozzle exit for condition D	194
12.3.5	Initial simulation conditions in the test cases listed in table 12.1.1	197
12.3.6	Inlet and exit electron (T_e) and excitation (T_i) temperatures and electron concentration at the nozzle exit in the test cases listed in table 12.1.1.	199
13.3.1	Time averaged of the pressure measurements for the large test body.	222
13.3.2	Time averaged of the pressure measurements on the cone pressure sensor for the small test body.	229

13.3.3	Time averaged of the pressure measurements on the cylinder pressure sensor for the small test body.	230
13.3.4	Accuracy analysis results for the NON-magnetic test body.	232
13.3.5	Accuracy analysis results for the magnetic test body.	232
13.3.6	Free stream values of the considered problem.	235
13.3.7	Free stream electric transport properties	237
13.3.8	Pressure comparison between measured and numerical runs for the condition C	241
13.3.9	Pressure comparison between measured and numerical runs for the condition C (extended computational domain).	244

Introduction

The impact of plasma technologies is growing both in the academic and in the industrial field. Nowadays, a great interest is focused in plasma applications in aeronautics and astronautics domains.

Plasma actuators based on the Magneto-Hydro-Dynamic (MHD) and Electro-Hydro-Dynamic (EHD) interactions are potentially able to suitably modify the fluid-dynamics characteristics around a flying body without the mean of moving parts. This could lead to the control of an aircraft with negligible response time, more reliability and big improvements in performances.

In order to evaluate the entity of the aforementioned interactions, a series of experiments and a wide number of diagnostic techniques have been realized. This thesis has been split in three main Parts.

In Part I the diagnostic techniques used further in the MHD and EHD experiments are described.

In Chapter 1 a fully description of microwave used as tool for electron number density evaluation is reported. The basic theory of Schlieren photograph technique is described in Chapter 2 and the radiation theory of atoms and molecules, and emission spectroscopy used for temperature and electron number density estimation are instead presented in Chapter 3.

Finally in Chapters 4 and 5 Pitot tube used for the evaluation of the velocity of a fluid and electrostatic probes employed for Hall potentials determination are shown respectively.

In Part II EHD interaction experiments are presented.

In Chapter 6 an introduction to the active flow control realized by means

of the EHD interaction based on the Dielectric Barrier Discharge (DBD) actuator is reported. After a discussion of the EHD theory and the possible fluid-dynamic applications explained in Chapter 7, two EHD experiments are illustrated.

In Chapter 8, a 3-phase multielectrode flat panel used as fluid-dynamic actuator is presented and fully described. Measurements and associated results are showed and discussed.

In Chapter 9 a single electrode pair DBD actuator driven by the combination of nanopulses and DC or AC bias is presented. The features and the performances of this new kind of supply system are described. In the last part of the chapter, a “modified” DBD actuator is introduced and first performance improvements are provided.

The Chapter 10 is dedicated to the conclusion remarks about the 3-phase and nanopuls EHD experiments.

In Part III MHD experiments are treated. Initially a brief introduction on the MHD applications in the hypersonic flight domain is showed in Chapter 11. In Chapter 12 an experimental characterization and an associated numerical validation of a Mach 6 argon plasma jet are realized. This characterization has been necessary for a fully description of the hypersonic plasma used for the MHD experiments described in Chapter 13. This Chapter includes the results of the MHD interaction over two axial symmetric bodies and a comparison between measurements and numerical simulations.

Finally The conclusion remarks about nozzle characterization and MHD experiments are presented in Chapter 14.

Part I

Diagnostic techniques theory

Chapter 1

Microwave diagnostic

1.1 Introduction

The plasma behaviour is complicated when it is considered as a medium for the propagation of electromagnetic waves. In the more generally assumption a plasma can be considered refractive, lossy, dispersive, resonant, anisotropic, nonreciprocal, nonlinear and inhomogeneous.

The first important simplification is to consider the plasma as *lorentzian*. A Lorentz plasma denotes to be described by a model in which the electrons interact each others only through collective spacecharge forces, and the heavy ions and neutral particles are at rest [11]. Hence it is possible to consider the ions and neutrals as a continuous stationary fluid through which the electrons move with viscous friction. These assumptions are in good agreement with reference to the cold plasmas analyzed in this work and allow to consider the interaction between plasma and electromagnetic waves depending only on a reduced number of parameters [11].

The most two important parameters are the *plasma frequency* ω_p and the *electron-heavy collision frequency* ν_{eH} .

The plasma frequency ω_p is the characteristic frequency with which the free electrons oscillate around the charge neutrality position (Appendix A). The electron-heavy collision frequency ν_{eH} is the frequency with which the elec-

trons collide with the heavy particles (ions or neutrals) and it assumes importance only in collisional plasmas.

The real meaning and purpose of these parameters will be explained in next sections.

The microwave diagnostic is a volume diagnostic able to determine both these parameters with good approximation and in a non-intrusive way.

1.2 Electromagnetic waves in collisionless plasmas

The plasma frequency is of fundamental importance with regard to the behaviour of the plasma as a medium for the propagation of an electromagnetic wave. It is in fact possible to determine two different conditions.

Still considering a collisionless plasma, if the electromagnetic wave frequency ω is lower than the plasma frequency ($\omega < \omega_p$) then the free electrons interact with the electric field of the incident wave and they are thus able to rearrange them selves. The electromagnetic wave (i.e. the disturbance) is not propagated beyond the point in which it exists.

If $\omega_p < \omega$, there is no interaction between electrons and wave, and a lossless propagation occurs.

If we consider now a “more real” bounded plasma, and an incident electromagnetic wave coming from the external space, the behaviour of the plasma considered as a medium still be can studied with reference to the plasma frequency.

If $\omega < \omega_p$ the electrons react to the electric field and they can be considered as little dipoles able to re-irradiate the incident wave and to totally reflect it without losses. The inner plasma electrons don't experience the presence of the electromagnetic wave because of the shielding behaviour of the outer electrons.

On the contrary, if $\omega_p < \omega$, the incident wave can pass through the plasma without any kind of losses (here reflections due to eventually abrupt change

in the interface gas and plasma are not considered).

The plasma behaviour depicted above, can also be described in terms of electron density because of the direct relation between plasma frequency and electron density. Indeed if in the equation (A.0.7) at page 252 we consider the situation $\omega_p = \omega$, which is the condition that separate the propagation and non-propagation regime, it is possible to calculate the so called *critical electron density* n_{ec} .

$$n_{ec} = \frac{\omega^2 m_e \epsilon_0}{e^2} = \frac{4\pi^2 m_e \epsilon_0}{e^2} \nu^2 \quad (1.2.1)$$

where ν is the frequency of the incident electromagnetic wave, ϵ_0 is the vacuum dielectric constant and e and m_e are respectively the charge and the electron mass.

The condition $n = n_{ec}$ (or the equivalent $\omega = \omega_p$) divides thus two different regimes. If $n < n_{ec}$ ($\omega > \omega_p$) the so called *collective interaction regime* exists and the plasma acts as a dielectric that leaves pass the electromagnetic wave without losses.

If $n > n_{ec}$ ($\omega < \omega_p$), the *particle interaction regime* holds and the plasma totally reflects the incident wave.

From figure 1.2.1 it is possible to state that the plasmas examined in this work are characterized by electron density in the order of $10^{16} \div 10^{19} [part/m^3]$ and the condition $\omega > \omega_p$ is reached for frequency in the microwave regime ($1 \div 100$ [GHz]).

Let now start to directly express the relations between electromagnetic wave inside a plasma and plasma frequency.

If we consider a collisionless plasma and a time-harmonic electric field $E(t) = E_0 e^{j\omega t}$ due to both the contribution of the external electric field, imposed by a source outside the plasma, and the internal electric field associated to the electron spacecharge displacement, it is possible to state that the motion equation results in

$$m_e \ddot{\xi} = -eE, \quad (1.2.2)$$

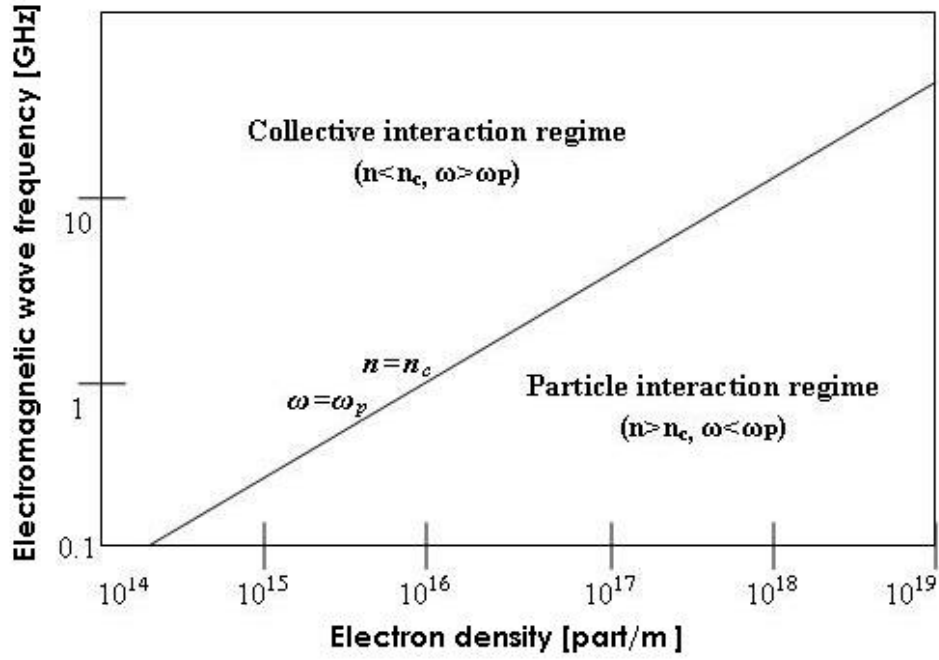


Figure 1.2.1: Electromagnetic wave frequency vs plasma frequency.

having solution

$$\dot{\xi} = \frac{e}{m_e \omega^2} E. \quad (1.2.3)$$

The resulting current density becomes

$$J = -n_e e \xi = -j \frac{n_e e^2}{m_e \omega} E. \quad (1.2.4)$$

As a consequence Ohm's law is derived with an imaginary electrical conductivity given by

$$\sigma = -j \frac{n_e e^2}{m_e \omega}. \quad (1.2.5)$$

In a linear medium, a complex conductivity can be expressed as a *complex dielectric constant* $\check{\epsilon}$ (see Appendix B for more explanations) also called *complex permittivity* (the symbol \sim denote a complex quantity).

$$\check{\epsilon} = \epsilon_0 \left(1 - j \frac{\sigma}{\epsilon_0 \omega} \right) = \epsilon_0 \left(1 - \frac{n_e e^2}{m_e \epsilon_0 \omega^2} \right) = \epsilon_0 \left(1 - \frac{\omega_p^2}{\omega^2} \right). \quad (1.2.6)$$

we can also define a complex relative permittivity

$$\check{\epsilon}_r = \frac{\check{\epsilon}}{\epsilon_0} = 1 - \frac{\omega_p^2}{\omega^2}. \quad (1.2.7)$$

This analysis can be applied to a plane wave traveling in the z direction varying as $e^{j\omega t - \check{\gamma}z}$, where $\check{\gamma} = \alpha + j\beta$ is the *complex propagation coefficient* and α and β are respectively the *attenuation* and *phase coefficients*. The above mentioned equation form of a plane traveling wave is treated in next section for microwave propagation with the addition of the dumping term α due to the presence of the conductivity σ .

Solving the wave equation in these condition, and assuming a medium with permeability $\mu_r=1$, it is possible to find the following relation

$$\check{\gamma}^2 = -\check{\epsilon}_r \frac{\omega}{c} \quad (1.2.8)$$

that leads to the dispersion relation

$$\check{\gamma} = j\check{\epsilon}_r^{1/2} \frac{\omega}{c} \quad (1.2.9)$$

where c is the light velocity.

In the case of $\omega < \omega_p$, from equation (1.2.7) the effective dielectric constant ϵ_r is negative and thus from the relation (1.2.9) the complex propagation coefficient is real, so the wave is attenuated without phaseshift:

$$\alpha = \left(\frac{\omega_p^2}{\omega^2} - 1 \right)^{1/2} \frac{\omega}{c} \xrightarrow{\omega^2 \ll \omega_p^2} \frac{\omega_p}{c}$$

$$\beta = 0. \quad (1.2.10)$$

From the point of view of an electromagnetic wave that impinges a plasma, the equation (1.2.10) shows how the incident wave is totally reflected at the boundary.

For $\omega > \omega_p$, $\tilde{\gamma}$ is complex and the wave propagates without attenuation but with a phaseshift:

$$\alpha = 0$$

$$\beta = \left(1 - \frac{\omega_p^2}{\omega^2}\right)^{1/2} \frac{\omega}{c} \xrightarrow{\omega^2 \gg \omega_p^2} \frac{\omega}{c}. \quad (1.2.11)$$

It is now useful to introduce the the *refractive index* μ defined as the ratio of the vacuum velocity of light c and the phase velocity v_Φ in the medium. The phase velocity is related to the phase coefficient β with the relation

$$\beta = \frac{2\pi}{\lambda} = \frac{\omega}{v_\Phi}. \quad (1.2.12)$$

The refractive index can so be determined from equation (1.2.12) as

$$\mu = \frac{\beta c}{\omega} = \left(1 - \frac{\omega_p^2}{\omega^2}\right)^{1/2}. \quad (1.2.13)$$

In this case in which $\omega > \omega_p$, the refractive index is less than unit, in contrast with the ordinary dielectrics.

1.3 Electromagnetic waves in collisional plasmas

The warm plasmas studied in this work, can be well approximated with a Lorentzian plasma model that includes a viscous damping term in the motion equation. With this new term the equation (1.2.2) becomes

$$m_e \ddot{\xi} = -eE - m_e \nu_{eH} \dot{\xi}. \quad (1.3.1)$$

The new dumping term $m_e \nu_{eH} \dot{\xi}$ is related to the Coulombian interaction between electrons and heavy particles; it takes in to account that, on the average, an electron loses direct momentum $m_e \dot{\xi}$ due to the collisions with heavy particles. The entity of this loss is measurable by means of the *electron-heavy collision frequency* (also called *collision frequency for momentum transfer*). If $E(t) = E_0 e^{j\omega t}$ the solution for the (1.3.1) becomes

$$\xi = \frac{eE}{m_e \omega (\omega - j\nu_{eH})}. \quad (1.3.2)$$

Following the proceeding used for the collisionless case, this time it is possible to define a complex conductivity $\check{\sigma}$ known as *Lorentzian conductivity* defined as

$$\check{\sigma} \equiv \sigma_{\Re} + j\sigma_{\Im} = \frac{n_e e^2}{m_e (\nu_{eH} + j\omega)} = \frac{n_e e^2 \nu_{eH} - j\omega}{m_e \nu_{eH}^2 + \omega^2}. \quad (1.3.3)$$

Recalling now the relations (1.2.6) and (1.2.7) it is now possible to define a new expression for the complex relative permittivity

$$\begin{aligned} \check{\epsilon}_r \equiv \Re\{\epsilon_r\} - j\Im\{\epsilon_r\} &= 1 - j \frac{\check{\sigma}}{\epsilon_0 \omega} = 1 - \frac{\omega_p^2}{\omega(\omega - j\nu_{eH})} \\ &= \left(1 - \frac{\omega_p^2}{\omega^2 + \nu_{eH}^2}\right) - j \left(\frac{\omega_p^2 \nu_{eH}/\omega}{\omega^2 + \nu_{eH}^2}\right). \end{aligned} \quad (1.3.4)$$

On regard the electromagnetic wave propagation, expression (1.2.9) showed us that the complex propagation coefficient $\check{\gamma}$ can be expressed in term of the complex relative permittivity $\check{\epsilon}_r$. It is now useful to introduce a *complex refractive index*

$$\check{\mu} \equiv \mu + j\chi = -j\check{\gamma} \frac{c}{\omega} = \check{\epsilon}_r^{1/2} \quad (1.3.5)$$

where μ and χ are respectively the (*real*) *refractive index* and the *attenuation index*. These coefficients are related with the $\check{\gamma}$ components as follow

$$\alpha = \chi \frac{\omega}{c} \quad (1.3.6)$$

$$\beta = \mu \frac{\omega}{c}. \quad (1.3.7)$$

Recalling now the equation (1.2.7) of the complex relative permittivity, it is possible to determine the refractive and attenuation index as function of the plasma and the electromagnetic incident wave frequencies and the electron-heavy collision frequency.

$$\begin{aligned} \mu &= \Re(\epsilon_r^{1/2}) = \\ &= \left\{ \frac{1}{2} \left(1 - \frac{\omega_p^2}{\omega^2 + \nu_{eH}^2} \right) + \frac{1}{2} \left[\left(1 - \frac{\omega_p^2}{\omega^2 + \nu_{eH}^2} \right)^2 + \left(\frac{\omega_p^2}{\omega^2 + \nu_{eH}^2} \frac{\nu_{eH}}{\omega} \right)^2 \right]^{1/2} \right\}^{1/2}, \end{aligned} \quad (1.3.8)$$

$$\begin{aligned} \chi &= -\Im(\epsilon_r^{1/2}) = \\ &= \left\{ -\frac{1}{2} \left(1 - \frac{\omega_p^2}{\omega^2 + \nu_{eH}^2} \right) + \frac{1}{2} \left[\left(1 - \frac{\omega_p^2}{\omega^2 + \nu_{eH}^2} \right)^2 + \left(\frac{\omega_p^2}{\omega^2 + \nu_{eH}^2} \frac{\nu_{eH}}{\omega} \right)^2 \right]^{1/2} \right\}^{1/2}. \end{aligned} \quad (1.3.9)$$

Considering now the attenuation and the phase coefficients from the expressions (1.3.6) and (1.3.7), it is possible to state that, in the collisional case, there is not a net separation between the two interaction regimes, but a more smoothed variation in the behaviour of the electromagnetic incident wave is realized. Thus in the collisional case, close to the condition $\omega = \omega_p$, we have not the condition of totally reflection or transit without attenuation, but a transition region with partially reflection and attenuation. The trends of reflexion and attenuation indexes are reported in figures 1.3.1 and 1.3.2.

As said before, close to the condition $\omega = \omega_p$, a variation both for the refractive and attenuation index occurs. This change is more gradual, more the ratio ν/ω is higher, that is, the plasma is far from the condition of collisionless case. One important note is that, in the case of $\nu/\omega \geq 1$, the refractive

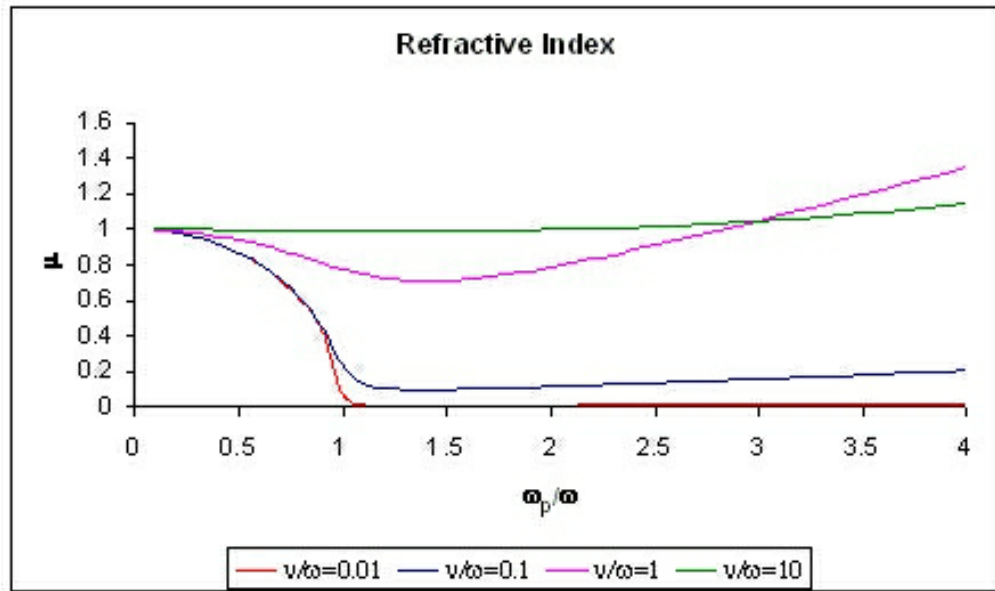


Figure 1.3.1: Refractive index at various electron heavy collision frequency.

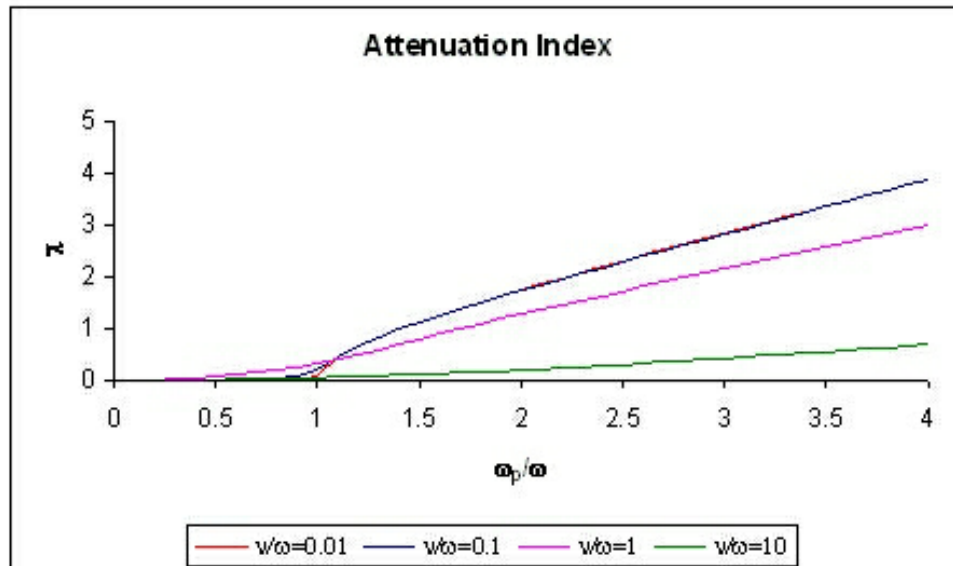


Figure 1.3.2: Attenuation index at various electron heavy collision frequency.

index can be greater than one, so the phase velocity results higher than the light velocity.

The measurement of these coefficients allows to the determination of the plasma frequency, i.e. the electron density, and the electron-heavy collision frequency.

As shown in figure 1.2.1 at page 6, for the plasmas studied in this work, the electron density is in the order of $10^{16} \div 10^{19}[\text{part}/m^3]$, so the plasma frequency is in the range of $1 \div 100[\text{GHz}]$, thus in the microwave regime.

For a microwave that impinges a bounded plasma (or a conductive medium) it must be considered that the attenuation leads to a finite penetration depth. Considering the wave equation for the electric field \mathbf{E} (B.0.12) at page 254 and the complex propagation coefficient expressed in the (1.2.9) it is possible to introduce an *attenuation length* δ defined as the inverse of the attenuation coefficient α . This coefficient represents the penetration depth at which the field amplitude falls to e^{-1} of its original value.

For the case of a conductive material, expressing the complex dielectric constant with the relation (1.2.6) and assuming that the conductivity σ is largely real and of high magnitude, the complex propagation coefficient results in

$$\check{\gamma} = \sqrt{-j\omega\mu\sigma} = \sqrt{\frac{\omega\mu\sigma}{2}} + j\sqrt{\frac{\omega\mu\sigma}{2}}. \quad (1.3.10)$$

The attenuation length becomes so

$$\delta = \sqrt{\frac{2}{\omega\mu\sigma}}, \quad (1.3.11)$$

that is the usual expression for the skin depth in metals. For a microwave of $12[\text{GHz}]$, the penetration depth is on the order of $2[\mu m]$.

For plasmas a complex conductivity normally holds, so the whole formulation of the complex propagation constant must be taken into account.

The evaluation of the electron density can be determined by means of the transmission measurements.

Lying in a partial transmission regime, the transmission factor T_f of an electromagnetic wave that is crossing a certain plasma volume can be defined

as

$$T_f = \frac{P_2}{P_1} = e^{(-\chi \frac{\omega}{c} \Delta x)} \quad (1.3.12)$$

where P_1 is the baseline transmitted power, i.e. the power transmitted without the plasma, P_2 is the transmitted power with the presence of the plasma and Δx is the plasma dimension saw by the microwave.

The transmission factor is a function both on plasma frequency and collisional frequency (see equation 1.3.9 at page 10), that are unknowns.

In figure 1.3.3 the transmission factors with fixed electron-heavy collision frequency and variable microwave frequency (left-hand side) and with fixed microwave frequency and variable electron-heavy collision frequency (right-hand side) are plotted.

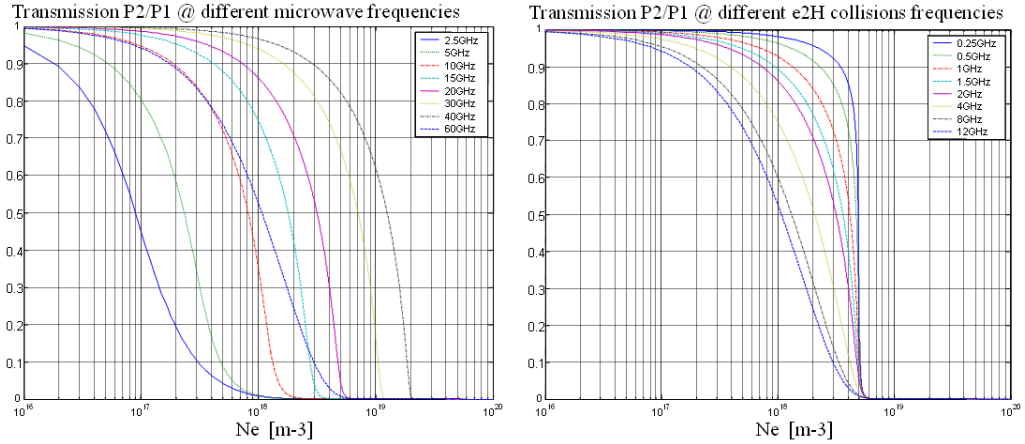


Figure 1.3.3: Transmission factor with an electron collisional frequency of 2[GHz] and variable microwave frequency (left-hand side), and with a microwave frequency of 20[GHz] and variable electron-heavy collision frequency (right-hand side).

The plots show how the condition at which there is no wave propagation ($T_f = 0$) is only a function of the electron number density.

By means of a variable microwave frequency source, the frequency at which does not correspond any wave transmission can be found.

Under the assumption of $\omega \gg \nu_{eH}$ (with constant ν_{eH}) the critical electron

number density corresponding to that frequency can be calculated using the expression 1.2.1 at page 5

$$n_{ec} = \frac{\omega^2 m_e \epsilon_0}{e^2} = \frac{4\pi^2 m_e \epsilon_0}{e^2} \nu^2 = 1.2404 \times 10^{10} f^2 \quad (1.3.13)$$

where f is the microwave frequency.

Then, the frequency can be lower down and allowing a partial transmission mode. From the known electron number density and the measured transmission factor, is then possible to calculate the electron collision frequency.

1.4 Microwave propagation theory

In the previous two sections and in Appendices A and B we dealt with the propagation of an electromagnetic wave and its interactions with a plasma. We also saw how, for the plasmas studied in this work, the interaction regime lays in the microwave frequencies.

In this section we will study more deeply the nature of the microwave propagation.

The most basic microwave circuit element is the transmission line, or waveguide. The microwave field is contained within conducting waveguide walls, and in the ideal case is propagated without reflections or losses. This ideal case is achieved for a waveguide of uniform cross section in the limit of infinitely conductive walls. The wave equations are solved by applying boundary conditions for the electric and magnetic fields along the perimeter of the wall.

Lets first consider the propagation of time-harmonic electric and magnetic fields which are governed by the Helmholtz equations (B.0.15) and (B.0.16) at page 255.

$$\nabla^2 \mathbf{E} - k^2 \mathbf{E} = 0, \quad \nabla^2 \mathbf{H} - k^2 \mathbf{H} = 0.$$

The type of solution for which we are looking for, corresponding to a

wave that propagates itself in a preferential direction, lets say along z . Since the Helmholtz equation is separable, in our study, solutions in the form $f(z)g(x, y)$, where f is a function of z only and g is a function of x and y , can be found.

The second derivative with respect to z enters into the wave equation in a manner similar to the second derivative with respect to time.

By analogy with $e^{j\omega t}$ time dependence, the z dependence can be assumed to be $e^{\pm j\beta z}$. This assumption will lead to wave solution in the form $\cos(\omega t \pm \beta z)$ and $\sin(\omega t \pm \beta z)$ which are appropriate to describing wave propagation along the z axis.

Whit an assumed z dependence $e^{-j\beta z}$ (i.e. a wave propagation in the positive z direction) the “*del*” operator can be decomposed as

$$\nabla = \nabla_t + \nabla_z = \nabla_t - j\beta\hat{\mathbf{a}}_z \quad (1.4.1)$$

since $\nabla_z = \hat{\mathbf{a}}_z\partial/\partial z$. Note that ∇_t is the transverse part and equals $\hat{\mathbf{a}}_x\partial/\partial x + \hat{\mathbf{a}}_y\partial/\partial y$ in rectangular coordinates.

Whit these considerations, the propagation constant β will depend on the waveguide configuration.

The decomposition of the fields into transverse and axial component and the separation of the z component, allows to considerable simplification of the Maxwell’s equations. Electric and magnetic fields can be expressed as

$$\mathbf{E} = (\mathbf{e}_t + \mathbf{e}_z)e^{j(\omega t - \beta z)}, \quad (1.4.2)$$

$$\mathbf{H} = (\mathbf{h}_t + \mathbf{h}_z)e^{j(\omega t - \beta z)}, \quad (1.4.3)$$

where the subscript term t refers to the transverse component, the subscript term z refers to the axial one. All the components depend only by the transverse coordinates x and y .

Finally the Maxwell’s equations become

$$\nabla_t \times \mathbf{e}_t = -j\omega\mu\mathbf{h}_z, \quad (1.4.4)$$

$$\nabla_t \times \mathbf{e}_z - j\beta \hat{\mathbf{k}} \times \mathbf{e}_t = -\hat{\mathbf{k}} \times \nabla_t e_z + -j\beta \hat{\mathbf{k}} \times \mathbf{e}_t = -j\omega \mu \mathbf{h}_t, \quad (1.4.5)$$

$$\nabla_t \times \mathbf{h}_t = j\omega \epsilon \mathbf{e}_z, \quad (1.4.6)$$

$$-\hat{\mathbf{k}} \times \nabla_t h_z + j\beta \hat{\mathbf{k}} \times \mathbf{h}_t = -j\omega \epsilon \mathbf{e}_t, \quad (1.4.7)$$

$$\nabla_t \cdot \mathbf{h}_t = +j\beta \mathbf{h}_z, \quad (1.4.8)$$

$$\nabla_t \cdot \mathbf{e}_t = +j\beta \mathbf{e}_z, \quad (1.4.9)$$

where, as introduced before, ϵ and μ are the permittivity and the permeability of the considered medium.

For a large variety of waveguides of practical interest it turns out that all boundary conditions can be satisfied by fields that do not have all components present.

Because of the widespread occurrence of such field solutions, the following classification of solutions is of practical interest.

- *transverse electric*, referred to as *TE* or *H modes*, for which $\mathbf{e}_z = 0$, $\mathbf{h}_z \neq 0$;
- *transverse magnetic*, referred to as *TM* or *E modes*, for which $\mathbf{h}_z = 0$, $\mathbf{e}_z \neq 0$;
- and *transverse electromagnetic*, or *TEM waves*, for which $\mathbf{e}_z = \mathbf{h}_z = 0$.

The transverse electric *TE* mode case is considered first. In this case, h_z plays the role of a potential function from which the rest of the field components may be obtained.

We recall now the Helmholtz equation for the magnetic field (B.0.16) at page 255.

$$\nabla^2 \mathbf{H} - k^2 \mathbf{H} = 0.$$

Separating the above equation into transverse and axial parts and replacing ∇^2 by $\nabla_t^2 - \beta^2$ yield

$$\nabla_t^2 \mathbf{h} + k_c^2 \mathbf{h} \quad (1.4.10)$$

where $k_c^2 = k_0^2 - \beta^2$ (see Appendix B equation (B.0.18) at page 256) and a z dependence $e^{-j\beta z}$ is assumed.

When this equation is solved, subjected to appropriate boundary conditions, the eigenvalue k_c^2 will be found to be a function of the particular waveguide configuration.

Solutions for equation (1.4.10) can be found by the separating variable method allowing to

$$h_z = (A \cos(k_x x) + B \sin(k_x x)) * (C \cos(k_y y) + D \sin(k_y y)) \quad (1.4.11)$$

where A, B, C, D are arbitrary constants.

We consider now a waveguide, sketched as in figure 1.4.1, propagating itself in the z direction.

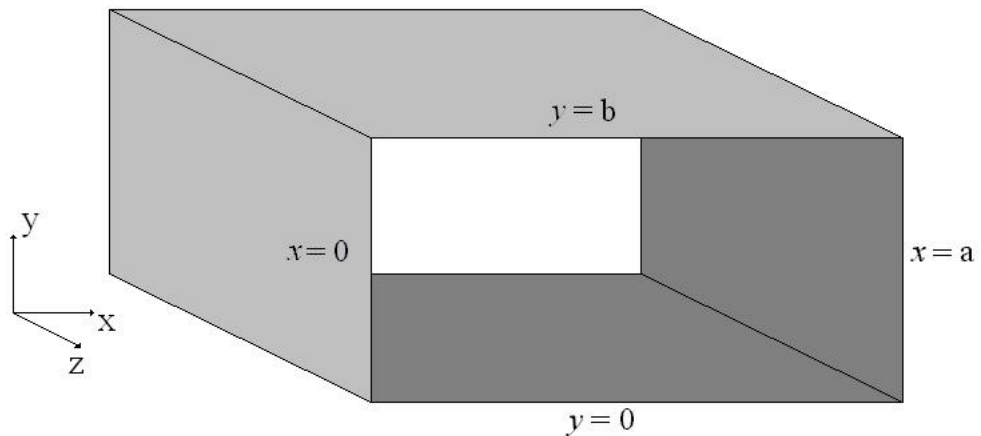


Figure 1.4.1: Hollow rectangular waveguide

Setting e_t and e_z equal to zero at the boundaries, the magnetic boundary conditions are found from equations (1.4.5) and (1.4.7).

$$\frac{\partial h_z}{\partial x} = 0 \quad @ \quad x = 0, a \quad (1.4.12)$$

$$\frac{\partial h_z}{\partial y} = 0 \quad @ \quad y = 0, b. \quad (1.4.13)$$

Applying these conditions to equation (1.4.11) we obtain

$$h_z = A_{nm} \cos\left(\frac{n\pi x}{a}\right) \cos\left(\frac{m\pi y}{b}\right) \quad (1.4.14)$$

only for integer values of n and m . The new coefficients for x and y are the eigenvalues of the propagation constants k_x and k_y . The remaining magnetic field components and the electric field components are found by the substitution of this result into equations (1.4.4) and (1.4.9). A solution with particular values for n and m is referred to as the TE_{nm} mode.

Lets now consider the TM modes.

Solutions to TM modes are found similarly, starting from the wave equation for the axial electric field:

$$\nabla_t^2 e_z + k_c^2 e_z = 0. \quad (1.4.15)$$

The boundary condition for which the tangential component of the electric field must go to zero at the wall is imposed:

$$e_z = 0 \quad @ \quad x = 0, a \quad \text{and} \quad y = 0, b, \quad (1.4.16)$$

which leads to a solution in the form

$$e_z = A_{nm} \sin\left(\frac{n\pi x}{a}\right) \sin\left(\frac{m\pi y}{b}\right). \quad (1.4.17)$$

The remaining electric field components and the magnetic field components are found from the equations (1.4.4) through (1.4.9) using this result

for e_z .

Note that in the solutions to the TE and TM waves, each mode corresponds to a different eigenvalue, k_c , determined by the relationship

$$k_{c,nm}^2 = \left(\frac{n\pi}{a}\right)^2 + \left(\frac{m\pi}{b}\right)^2. \quad (1.4.18)$$

We recall now that the constant k_c is defined by $k_c^2 = k^2 - \beta^2$. This relation for k_c and the definition $k = \sqrt{\omega^2\mu\epsilon} = 2\pi/\lambda$ (Appendix B, equation (B.0.17) at page 255) lead to the propagation constant γ to be determined as

$$\gamma \equiv j\beta = j\sqrt{k^2 - k_c^2} = j\sqrt{\left(\frac{2\pi}{\lambda}\right)^2 - \left(\frac{n\pi}{a}\right)^2 - \left(\frac{m\pi}{b}\right)^2}. \quad (1.4.19)$$

where λ is the wavelength of the wave. The propagation constant (as saw in previous Sections) can be either real or imaginary, depending on the sign of the quantity $k^2 - k_c^2$. The cutoff wavelength λ_c , defined for γ equal to zero, is given by

$$\lambda_c = \frac{2\pi}{\sqrt{\left(\frac{n\pi}{a}\right)^2 + \left(\frac{m\pi}{b}\right)^2}} = \frac{2ab}{\sqrt{n^2b^2 + m^2a^2}}. \quad (1.4.20)$$

At wavelengths less than λ_c , γ is imaginary and microwaves propagate with a sinusoidal variation in the z direction of $e^{-\gamma z}$. However, at wavelengths greater than λ_c , γ is real and the factor $e^{-\gamma z}$ corresponds to an exponentially decaying wave. This is what is meant by cutoff.

These results are the same obtained in the treatment of the propagation of an electromagnetic wave in a collisionless plasma (Section 1.2). Also in this case in fact the conductivity is set to an infinite value.

Because the propagation constants are different for each mode, some modes may be propagating while others are not. A standard rectangular waveguide typically has one dimension twice the length of the other, $a = 2b$. For this type of waveguide, the cutoff wavelengths for the first three modes

are listed in table 1.4.1.

nm	λ_c
10	$2a$
01	a
11	$2a/\sqrt{5}$

Table 1.4.1: Cutoff wavelengths for cavity modes.

Comparing equations (1.4.14) and (1.4.14) for TE and TM modes, it can be seen that the lowest order TM mode is the TM_{11} , since the trivial solution is obtained by setting n and m to zero. However, nontrivial TE modes exist for either n or m equal to zero. Between wavelengths of a and $2a$ only the TE_{10} mode propagates and all other modes are cut off. For this reason, the TE_{10} mode is known as the dominant mode, and it is in this single mode condition that microwave waveguides are typically operated.

The TE_{10} mode is sketched in figures 1.4.2, 1.4.3 and 1.4.4, showing the electric and magnetic field lines. Physically, the mode number for TE modes corresponds to the number of half wave oscillations of the electric field in the perpendicular and parallel directions, respectively. So for a TE_{10} mode, the electric field has a one half period sinusoidal oscillation perpendicular to the polarization vector, and is constant in the parallel direction.

A brief discussion of the third class of propagating wave solutions, the transverse electromagnetic wave TEM , is in order. Following the form of equations (1.4.4) through (1.4.9) and setting the axial components of the electric and magnetic fields equal to zero, the Maxwell's equations may be written as

$$\nabla_t \times \mathbf{e}_t = 0, \quad (1.4.21)$$

$$\beta \hat{\mathbf{k}} \times \mathbf{e}_t = \omega \mu \mathbf{h}_t, \quad (1.4.22)$$

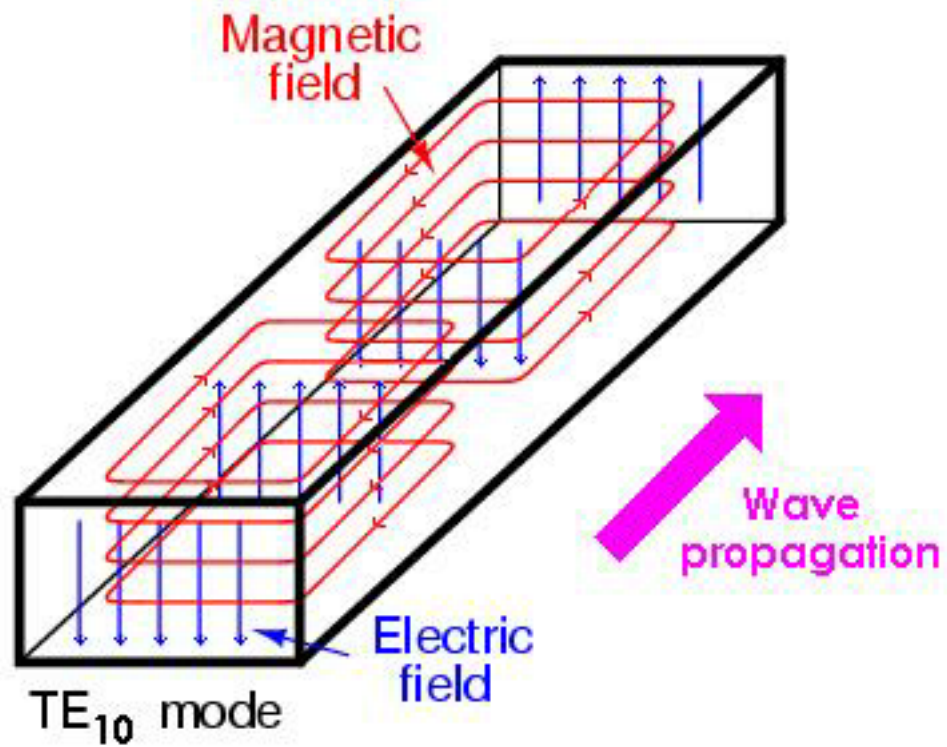


Figure 1.4.2: Electric and magnetic field lines for a TE_{10} mode.

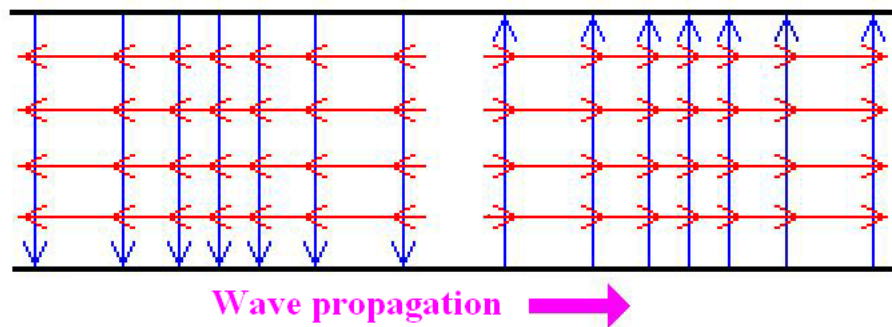


Figure 1.4.3: E-plane electric and magnetic field lines for the TE_{10} mode (side view).

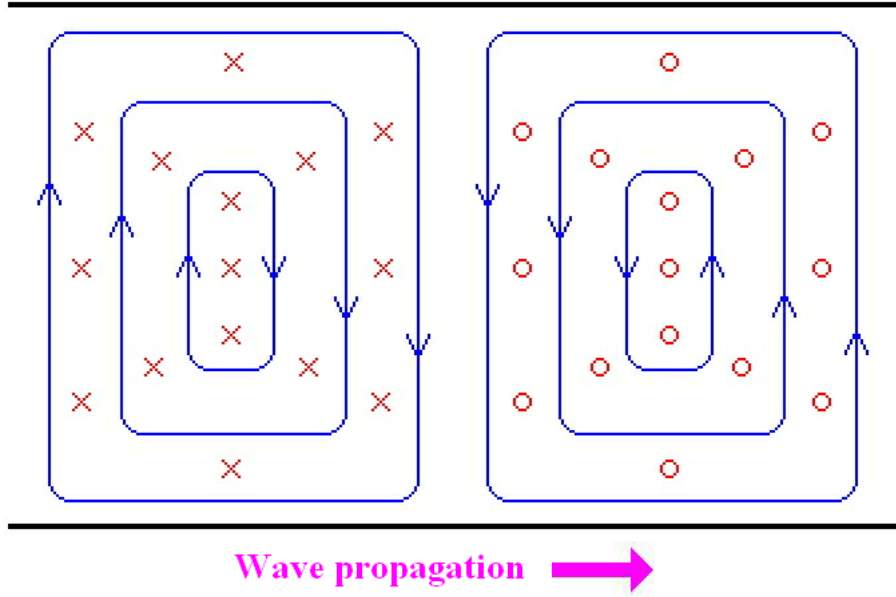


Figure 1.4.4: H-plane electric and magnetic field lines for the TE_{10} mode (top view).

$$\nabla_t \times \mathbf{h}_t = 0, \quad (1.4.23)$$

$$\beta \hat{\mathbf{k}} \times \mathbf{h}_t = \omega \epsilon \mathbf{e}_t, \quad (1.4.24)$$

$$\nabla_t \cdot \mathbf{h}_t = 0, \quad (1.4.25)$$

$$\nabla_t \cdot \mathbf{e}_t = 0. \quad (1.4.26)$$

Equation (1.4.21) shows that e_t must be the gradient of a scalar potential function. In order to satisfy also the equation (1.4.26), the scalar function must be a solution to Laplace's equation:

$$\nabla_t^2 \Phi = 0. \quad (1.4.27)$$

The boundary condition for \mathbf{E}_t implies that the gradient of Φ in the tangential direction must be zero along the boundary. The unique solution to Laplace's equation is then Φ equal to a constant. Physically, this is a statement that the voltage is uniform along the boundary, which clearly must be true for the infinitely conductive walls assumed in the problem. In this case $\mathbf{E} = -\nabla\Phi = 0$ everywhere inside the perimeter of the waveguide, and the only solution is the trivial one. Therefore, TE_M modes cannot be sustained by hollow conducting waveguides.

In a rectangular waveguide the propagation constant, for a TE or TM mode, may be determined from equation (1.4.19), and it is seen to depend upon the waveguide dimensions. A guide wavelength may be defined as

$$\lambda_g = \frac{2\pi}{\beta} = \frac{2\pi}{\sqrt{\left(\frac{2\pi}{\lambda}\right)^2 - \left(\frac{n\pi}{a}\right)^2 - \left(\frac{m\pi}{b}\right)^2}}. \quad (1.4.28)$$

In the case of a single propagating TE_{10} mode, this expression becomes

$$\lambda_g = \frac{2\pi}{\beta} = \frac{2\pi}{\sqrt{\left(\frac{2\pi}{\lambda}\right)^2 - \left(\frac{\pi}{a}\right)^2}} \quad (1.4.29)$$

and depends only on the larger dimension, a , of the rectangular guide. The guide wavelength is always greater than the free space wavelength, λ . It may vary between λ as $a \rightarrow \infty$, and infinity at $a \rightarrow \lambda/2$. A guide which has a varying cross section along its length will allow propagation with a similarly varying guide wavelength. If the guide should become smaller than the cutoff dimension, corresponding to $a < \lambda/2$, then the wave will cease to propagate and instead will decay exponentially as an evanescent wave over a characteristic length scale $1/\gamma$, where

$$\gamma = \sqrt{\frac{2\pi}{\left(\frac{\pi}{a}\right)^2 - \left(\frac{2\pi}{\lambda}\right)^2}}. \quad (1.4.30)$$

Chapter 2

Schlieren diagnostic

2.1 Introduction

Schlieren imaging is an optical diagnostic sensitive to the refraction of the rays of light. This technique enables the human eye (or the camera “eye”) to see the presence of pressure and temperature gradients.

This diagnostic has been largely utilized in past, and is still widely used to detect the presence of shock waves in supersonic flows. For MHD hypersonic experiments, this techniques can be suitable adopted to detect change in shock wave properties in presence or absence of the magnetic field.

For EHD experiments, the hot jet produced by means of the plasma actuators can be detected and evaluated in shape and velocity, leading to a better comprehension of the interaction plasma-neutral gas.

2.2 Light propagation in an inhomogeneous medium

As seen in the previous Chapter, a ray of light (i.e. an electromagnetic wave) propagates uniformly through an homogeneous media. If a change in the properties of the medium occurs, a consequent change in propagation speed of the light takes place. It is well known that the interaction between light

an matter slow down the propagation velocity of the light wave.

The *refractive index* $n = c_0/c$ defines this change in velocity as function of the speed of the medium c and the vacuum speed velocity c_0 . For air and other gases a simple linear relation between refractive index n and gas density ρ exists [1]:

$$n - 1 = k\rho \quad (2.2.1)$$

where k is the Gladstone-Dale coefficient.

Let's suppose to consider a ray of light traveling in the z direction in a x, y, z plane. It can be demonstrated that optical inhomogeneities refract or bend rays in proportion to their gradients of refractive index in a x, y plane (see Appendix C at page 259). The resulting ray curvature is:

$$\begin{aligned} \frac{\partial^2 x}{\partial z^2} &= \frac{1}{n} \frac{\partial n}{\partial x}, \\ \frac{\partial^2 y}{\partial z^2} &= \frac{1}{n} \frac{\partial n}{\partial y}. \end{aligned} \quad (2.2.2)$$

Integrating once, it is possible to obtain the *angular ray deflection* in the x and y directions.

$$\begin{aligned} \epsilon_x &= \frac{1}{n} \int \frac{\partial n}{\partial x} \partial z, \\ \epsilon_y &= \frac{1}{n} \int \frac{\partial n}{\partial y} \partial z. \end{aligned} \quad (2.2.3)$$

For a Schlieren set up with optic path in the z direction of length L , we deduce

$$\begin{aligned} \epsilon_x &= \frac{L}{n_0} \frac{\partial n}{\partial x}, \\ \epsilon_y &= \frac{L}{n_0} \frac{\partial n}{\partial y} \end{aligned} \quad (2.2.4)$$

where n_0 is the refractive index of the unperturbed medium. The Schlieren technique allows to detect these variations of the light path, due to changing in the refractive index.

2.3 Schlieren technique

The best way to understand in which way the Schlieren technique works, is to refer to an example of Schlieren setup (figure 2.3.1)

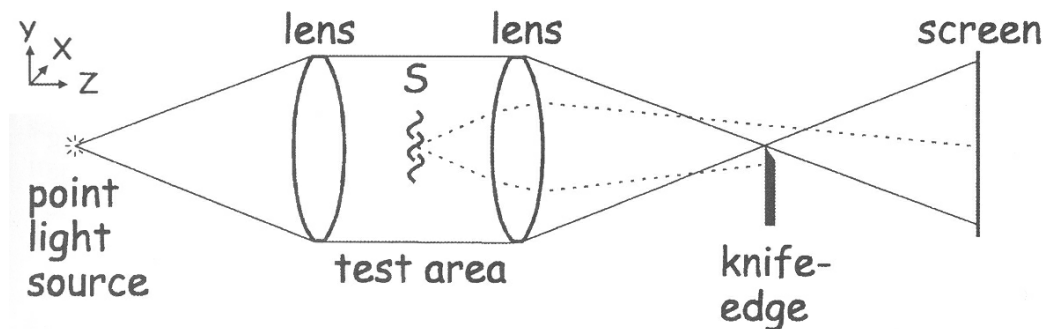


Figure 2.3.1: Schlieren setup with a point source [1].

The light source is supposed to act as a “point” source, and is collimated with the concave lens 1. This first lens generates a parallel beam of rays that impinges the test body. The second lens refocuses the beam in the point F where a knife edge (normally a real knife or razor blade) is mounted. Finally the beam proceeds to a viewing system (the human eye, a screen or a camera) where a real inverted image of the test area is formed.

If there are no change in refractive index in the test section, and the knife edge is open, all the light emitted from the source arrives undisturbed to the screen. If the knife is slightly closed, less light arrives to the screen, until all the rays are intercepted and the screen becomes dark.

If there are change in the refractive index, a certain amount of rays will be bent and pointed out of focus. In figure 2.3.1 some will be bent “over” the focus point, some “down”, so the firsts will pass impressing the screen in

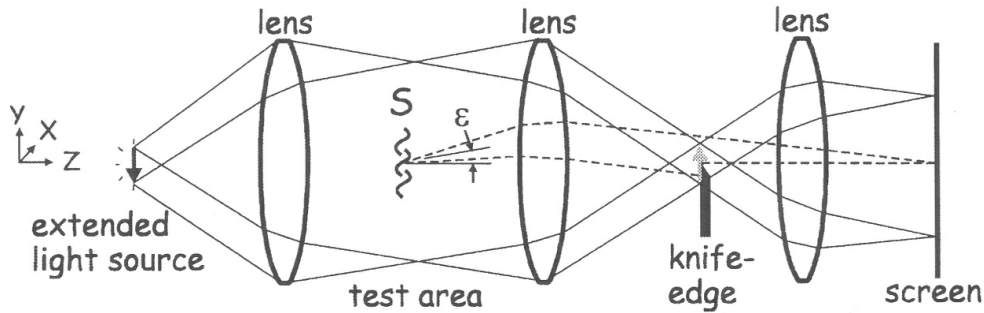


Figure 2.3.2: Schlieren setup with a real extended light source [1].

a different point in comparison with the rays unbent, the seconds will be stopped by the knife edge. On the screen it is now possible to observe regions that are more bright and others that are more dark.

In this Schlieren setup, a variations in the phase of the ray of light causes a vertical gradient of the refractive index, $\partial n/\partial y$. This gradient is converted in an amplitude difference in the brightness of the rays that impress the screen. Variation in the refractive index are so made visible.

Here only vertical (y) variation are visible because the knife edge is horizontal, it propagates in the x directions. In order to realize a suitable Schlieren setup is important to put the knife in the right orientation, thus perpendicular to the density variations of the gas. From this analysis, it can be assumed that the Schlieren diagnostic is sensible to the first derivate of the refractive index $\partial n/\partial y$.

In this setup, the point source is not so useful because allows only a on-off mode depending on the position of the knife edge. To take Schlieren images it is necessary to use an expended light source that allows more fine regulation of the knife edge because the focus “point” is not any more a point but a surface.

This more realistic setup, showed in figure 2.3.2, leads to a Grey color scale that enhances the contrasts and realize a more defined picture.

Each point in the test area contributes to create an entire element source

image to the composite image in the knife edge plane. If no Schlieren object is present, in order to block more of the composite source image, the motion of the knife blocks each elemental source image equally. Since every test-area point is therefore equally deprived of light, then the screen darkness uniformly. This is a fundamental characteristic of the Schlieren image and produce the Grey colored scale mentioned above.

A Schlieren object produces an image that is displaced from the undisturbed originally image, as can be seen in figure 2.3.3.

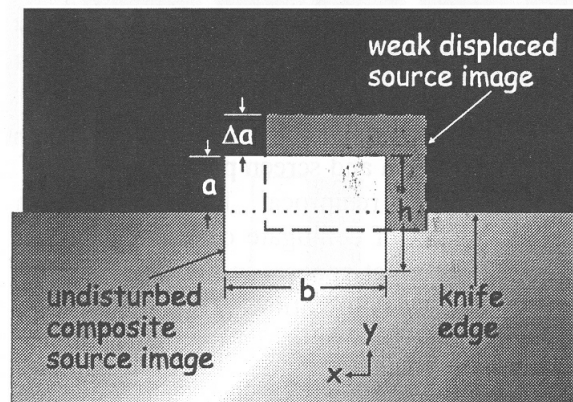


Figure 2.3.3: Diagram of the knife edge plane. Undisturbed and displaced light source [1]

The rays that are bent in the x direction are not intercepted by the knife edge. The amount of rays captured from the knife edge in the y direction depends on the knife position and influences the level of illuminance of the image projected on the screen. As mentioned above, the closing the knife edge allows to intercept more light, yielding a more sensitivity setup, as can be observed in figure 2.3.4.

Within the linear measuring range of the Schlieren setup, the image illuminance E , is proportional to the amount of the knife edge cut-off.

Another relation holds:

$$\Delta a = f_2 \epsilon_y \quad (2.3.1)$$

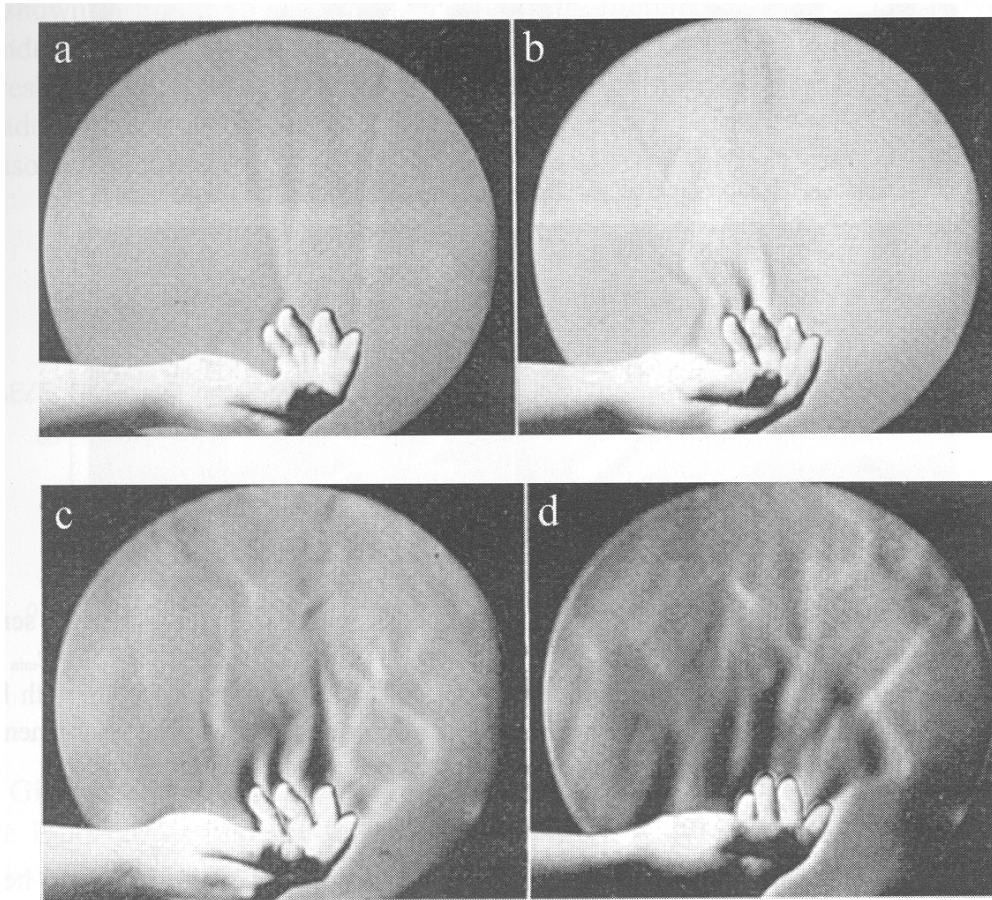


Figure 2.3.4: Schlieren image of a hand with knife edge gradually closed from *a* to *d*. It is possible to note the heat volutes. [1]

where f_2 is the focal length of the second lens. This relation shows how the illuminance E is proportional also at the y -component of the refractive angle ϵ_y .

2.4 Sensitivity of the Schlieren diagnostic

The sensitivity of each diagnostic setup is always of fundamental importance. In the case of Schlieren setup, the sensitivity represents the lowest change in refractivity that can be detected in the $2D$ output image.

Let's suppose a z -type configuration that is often used in Schlieren diagnostic (see figure 2.4.1).

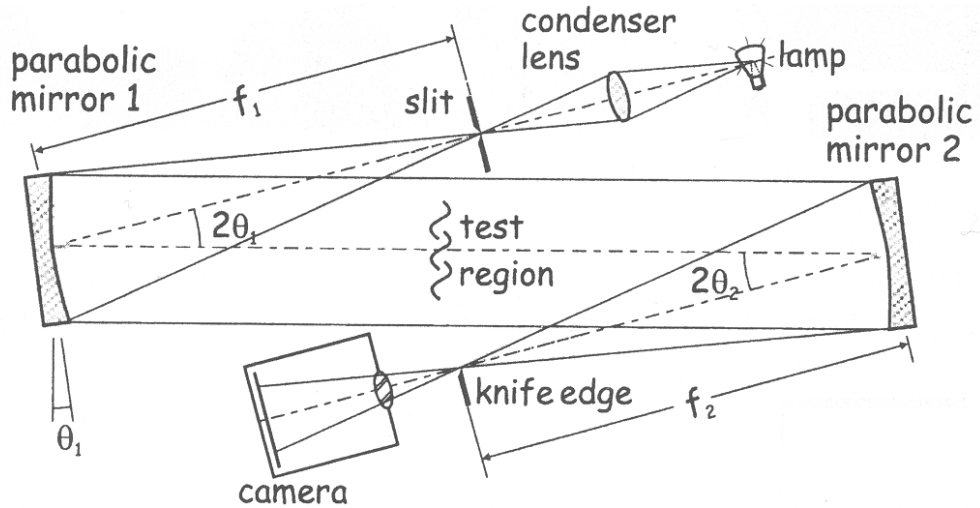


Figure 2.4.1: Z-configuration Schlieren setup scheme [1].

The illuminance E_0 that impinges the first mirror can be expressed as

$$E_0 = \frac{Bbh}{f_1^2} \quad (2.4.1)$$

where B is the luminance emitted by the light source (measured in $[candela/m^2]$), b and h are the breadth and height of the source slit and f_1 is the focal length of the first mirror.

The Schlieren image illuminance must take into account the magnification m introduced by the image size.

$$E_0 = \frac{Bbh}{m^2 f_1^2}. \quad (2.4.2)$$

Now it is time to introduce the presence of the knife edge. It inserts a window of height a that allows the passage of the light. Replacing h in the expression (2.4.2) with $(f_1/f_2)a$, that is the unobstructed height of the light source image, the background illuminance of a given Schlieren setup is determined as.

$$E = \frac{Bba}{m^2 f_1 f_2} \quad (2.4.3)$$

If we consider now a Schlieren object that refracts a certain amount of rays, an angle of refraction ϵ_y is introduced. Using the relation (2.3.1) and substituting Δa for a , it is possible to obtain the incremental gain of the illuminance ΔE at the corresponding image point due to a refraction of ϵ_y in the test area.

$$\Delta E = \frac{Bb\epsilon_y}{m^2 f_1} \quad (2.4.4)$$

Contrast in Schlieren photography refers to the ratio of the differential illuminance ΔE at an image point to the general background illuminance E :

$$C \equiv \frac{\Delta E}{E} = \frac{f_2 \epsilon_y}{a} \quad (2.4.5)$$

This image contrast C is the output of the Schlieren image. The input is a pattern of irregular rays deflection ϵ , resulting from variations in the refractive index in the test area. Hence the contrast (that is the relation between the variation of the input and the variation of the output) can be useful used to derive the Schlieren sensitivity S

$$S = \frac{dC}{d\epsilon} = \frac{f_2}{a} \quad (2.4.6)$$

The relation (2.4.6) attests as, in order to have big sensitivity, is necessary to have high focal length of the second lens (or mirror) and knife edge close to the full cut-off. On the other side, a knife edge almost closed highly reduces the amount of light that arrive into the screen, so an optimal value of a must be chosen in function of the entity of the gradient of the refractive index with which we are dealing, and the luminance of the light source.

Chapter 3

Spectroscopic diagnostic

3.1 Plasma thermodynamic equilibrium

A plasma is a fluid in which electrons, ions, and neutral particles coexist. The description of a plasma that lies in Thermodynamic Equilibrium (TE) is rather simple: its state is fully described by relative few quantities, such as mass density, temperature and chemical composition. Everything is ruled by statistic.

The velocity distribution is described by Maxwell, excited state distribution is described by Boltzmann, density relations between subsequent ionic states and electrons are predicted by Saha and the behaviour of the photons is given by Plank's law. In TE , all this contributes are governed by the same temperature.

The distribution laws valid in TE can be derived using the principle of the detailed balance (DB), as well as the opposite.

When the TE is no more valid, there is a violation for DB in at least one of the relations involving plasma state (Maxwell, Boltzmann, Saha or Plank); this leads to substitute the detailed balance with an improper one, since production and destruction of densities are no more equals.

Clearly there is a hierarchy in the rates of processes which causes departure from TE .

First of all, if radiation escapes from plasma, there is a violation of Plank's distribution law. However, if the overall loss of energy by escaping radiation is small if compared to the energy exchanged between material particles, Maxwell, Boltzmann and Saha are in equilibrium so the atoms, ions and electrons have the same temperature $T_H = T_i = T_e$.

At this stage of equilibrium, known as Local Thermodynamic Equilibrium (*LTE*), radiation has to be considered "decoupled" from matter. Moreover, also spatial and temporal decoupling are allowed in *LTE* ($\partial/\partial t \neq 0 \neq \nabla$). However, the excitation states in matter are all determined by the same temperature, defined as "excitational temperature" T_{EXC} .

A further departure from *LTE* is realized when different particles are subjected to different forces. Since the rate of energy transfer from electrons e to heavy particles H is not very efficient due to the large difference in mass ($m_H \approx 2000m_e$), the maxwellization of the same specie is much faster and reliable than between different groups.

In this situation, electrons and heavy particles are decoupled and their distribution function is related to two different temperatures.

This situation is referred as a "partial Local Thermodynamic Equilibrium" *pLTE*. Boltzmann and Saha equations still hold and two different Maxwell distributions, one related to the electron temperature T_e and one to the ion temperature T_i , must be considered.

The determination of the thermodynamic equilibrium of a plasma can be exhaustively realized by means of the emission spectroscopy.

The quantum theory developed behind the spectral emission of atoms is not the subject of this work and is nowadays well known.

In the next Section some references about atomic spectroscopy and a more complete treatment about diatomic molecular spectroscopy will be performed.

3.2 Atomic and molecular emission spectroscopy

The radiative transitions source of the electromagnetic emission generated by an atom can be associated to three principal phenomena:

- bound-bound radiation related to the de-excitation of an electron from two bound levels,
- free-bound radiation related to electron recombination processes,
- free-free radiation related to the changes in the momentum of the electron.

In the bound-bound spontaneous emission an electron in an upper energy level “falls” in one characterized by a lower energy and in this de-excitation a photon with energy $h\nu$ is emitted:

$$A^{(u)} \rightarrow A^{(l)} + h\nu \quad (3.2.1)$$

where A is the atom in an upper (u) and lower (l) energy state, h is the Planck constant and ν is the frequency of the emitted photon.

In the bound-bound stimulated emission an excited atom must interact with a photon characterized by an energy $h\nu$ equal to the one related to an allowed transition. After the de-excitation two photons with energy $h\nu$ are emitted.

$$A^{(u)} + h\nu_{lu} \rightarrow A^{(l)} + 2h\nu_{lu}. \quad (3.2.2)$$

The energy gaps between the electron levels are quantized and thus the frequency ν of the emitted photon can assume only a discretized series of values.

Bound-bound radiative transitions generate so only a discrete spectra with lines corresponding only to allowed transitions.

The free-bound radiation is generated by the recombination of an electron with a positive ion and the following electron transition in a lower energy level.

$$A^+ + e(\epsilon_e) \rightarrow A^{(l)} + h\nu. \quad (3.2.3)$$

In the equation (3.2.3) the value of the photon energy can be expressed as

$$h\nu = \frac{1}{2}m_e v_e^2 + \epsilon_{il} \quad (3.2.4)$$

where the first term in the right side of the equation represent the kinetic energy owned by the colliding electron and the second term is the energy gap between the ionization level i (i.e. the maximum energy held by an electron inside an atom) and the lower level l .

The energy ϵ_{il} is quantized but the kinetic energy can assume a continuous series of values. The total energy $h\nu$ and thus the frequency ν of the emitted radiation can assume a continuous range of values.

The free-free radiation is due to the deceleration of free electrons by means of the electric field, or to the centripetal acceleration due to the presence of a magnetic field. In the first case we are dealing with a bremsstrahlung radiation in the second one with a cyclotron radiation.

In free-free processes the energy gaps are not quantized and a continuous emission is allowed.

At the matter of facts, the whole spectra emitted by a plasma is generally composed by the contribution of discrete and continuous radiation.

The introduced radiation theory is valid both for atoms and molecules.

However for molecules the treatment becomes more complicated and a brief insight of the radiation processes of diatomic molecules may be useful for a better comprehension of the Nitrogen spectra subsequently used in this work for air plasma diagnostic.

When an atom is excited, it can “only” change its electronic arrangement. Otherwise a molecule owns more degrees of freedom and rotational and vibrational states can be excited. In fact, by means of the collisions, a molecule can start to rotate around a preferential axis or the atoms constituent the molecule itself can start to vibrate around their equilibrium positions.

Supposing that the amount of energy associated to each degree of freedom is $\frac{1}{2}kT$, for the linear H_2 molecule if the temperature is under the $80^\circ K$, only three degrees of freedom related to translational effects are excited and the energy is thus $\frac{3}{2}kT$. At ambient temperature the rotational energies are excited. Mathematically, there is a whole of three rotational degrees of freedom, one corresponding to rotation about each of the axes of three dimensional space.

However, in practice we shall only consider the existence of two degrees of rotational freedom for linear molecules. This approximation is valid because the moment of inertia about the internuclear axis is vanishingly small with respect other moments of inertia in the molecule (this is due to the extremely small radii of the atomic nuclei, compared to the distance between them in a molecule).

Quantum mechanically, it can be shown that the interval between successive rotational energy eigenstates is inversely proportional to the moment of inertia about that axis. Because the moment of inertia about the internuclear axis is vanishingly small relative to the other two rotational axes, the energy spacing can be considered so high that no excitations of the rotational state can possibly occur unless the temperature is extremely high.

The total energy can be so expressed as $\frac{3}{2} + \frac{2}{2}kT = \frac{5}{2}kT$.

If the temperature is afterward increased, also the vibrational states are excited. Considering that the total degrees of freedom in a tridimensional space are six, and by now three translational and two rotational degrees have been excited, linear molecules present only one vibrational degree of freedom.

Each vibrational mode develops both potential and kinetic energy, so the total vibrational energy can be expressed as $\frac{1}{2}kT + \frac{1}{2}kT = kT$.

The total internal energy of a linear molecule with all the modes excited is thus $\frac{7}{2}kT$.

The N_2 molecule, used in this work for spectroscopic analysis, is a linear molecule and presents a behaviour close to the aforementioned H_2 .

The excitation of these rotational and vibrational modes generates spectral

emission in the de-excitation phase.

For the rotational modes the quantum mechanics theory leads to a rotational energy expressed as

$$E_{rot} = \frac{J(J+1)h^2}{8\pi^2 I} \quad (3.2.5)$$

where J is the rotational quantum number ($J = 0, 1, 2 \dots n$), I is the moment of inertia of the molecule and h is the Plank constant.

The possible radiation transition frequencies are:

$$\nu_{J+1,J} = \frac{E_{J+1} - E_J}{h} = \frac{(J+1)h}{4\pi^2 I}. \quad (3.2.6)$$

Selection rules allows only variation in the rotational quantum number of $\Delta J = \pm 1$. The rotational spectra is so formed of a series of even-spaced spectral lines.

The energy rotational gaps are pretty close one to the others and rotational modes are the more easily excitable in nature. For an H_2 molecule, rotational modes are excited starting from a number of collisions with other molecules in the order of 350. For more heavy molecules this number quickly decreases. The collisional transport processes which lead translational temperature are related to similar dynamics. Rotational and translational relaxation times are so analogous and we can affirm that rotational and translational temperatures are equal:

$$T_{rotational} = T_{translational}. \quad (3.2.7)$$

The low energy levels, associated to rotational excitation, generate electromagnetic emission that normally lay in the microwave region.

Vibrational modes are related to higher energies. Assuming the approximation of simple harmonic oscillator, the vibrational energy can be expressed as

$$E_{vib} = (v + \frac{1}{2})h\omega = (v + \frac{1}{2})h \left(\frac{k}{m_{eff}} \right)^{\frac{1}{2}} \quad (3.2.8)$$

where v is the vibrational quantum number ($v = 0, 1, 2 \dots n$) and ω is the oscillation angular frequency related to the force constant of the bond k and the effective mass of the molecule m_{eff} . The total energy associated to a rovibrational transition is thus

$$E_{tot} = E_{rot} + E_{vib} = \left(\frac{J(J+1)h^2}{8\pi^2 I} + v + \frac{1}{2} \right) h\omega. \quad (3.2.9)$$

The corresponding transition frequency ν depends both from the rotational and vibrational quantum numbers.

A scheme of possible rotational-vibrational transitions is reported in figure 3.2.1.

In the figure the possible vibrational states are two ($v = 0, 1$) and the possible rotational states are six ($J = 0 \div 5$).

Transitions between vibrational levels may or not involve rotational transitions.

If the rotational quantum number decreases ($\Delta J = -1$) the so called “P-branch” transitions (or negative branch transitions) are formed. If the rotational quantum number increases ($\Delta J = +1$) the “R-branch” transitions (or positive branch transitions) are generated. Finally the “Q-branch” transitions are formed if the rotational quantum number remains unchanged ($\Delta J = 0$). From the selection rules formulation derives that the Q-branch is not always allowed. For Nitrogen molecules is not.

The name “branch” derives from the series of close spectral lines that rovibrational transitions generate (see figure 3.2.2).

The quantum mechanics theory provides us a “simple” formulation for the branches transition frequencies.

The ones for the P-branch are

$$\nu_P(J) = \nu - 2BJ \quad (3.2.10)$$

where B is the rotational constant equal to

$$B = \frac{h}{8\pi^2 cI} \quad (3.2.11)$$

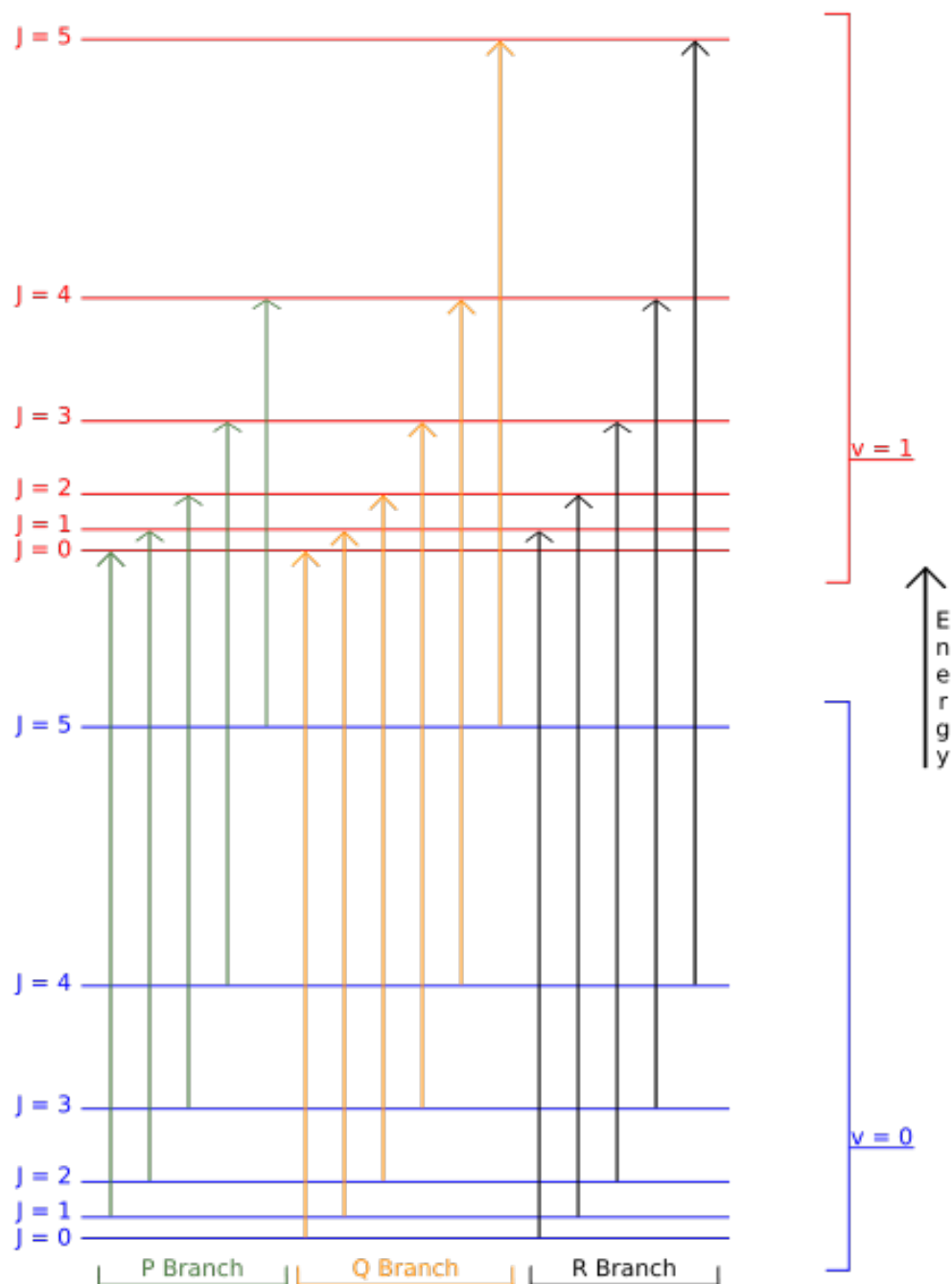


Figure 3.2.1: Scheme of the vibration-rotation energy levels for vibrational quantum number $v = 0 \div 1$ and rotational quantum number $J = 0 \div 5$.

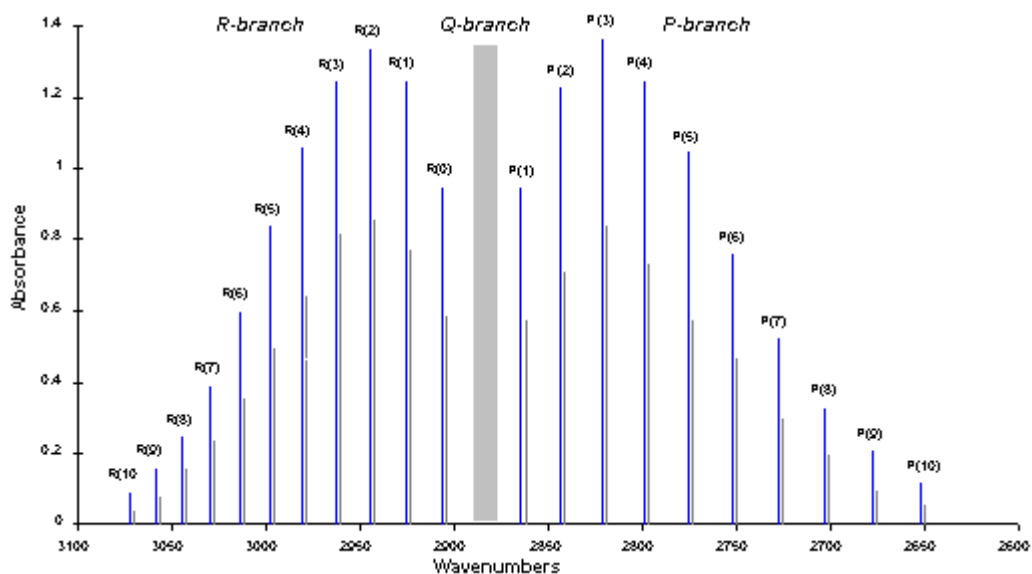


Figure 3.2.2: Scheme of the spectra of R , Q and P molecular branches.

where c is the light velocity. The equation (3.2.10) results from the approximation in which the inertial constant of the excited vibrational state B_v differs slightly from the one related to the ground vibrational state B .

For the Q-branch the transition frequencies are

$$\nu_P(J) = \nu. \quad (3.2.12)$$

In the case of the R-branch we obtain

$$\nu_P(J) = \nu + 2B(J + 1). \quad (3.2.13)$$

From equations (3.2.10), (3.2.12) and (3.2.13) it is possible to note how the relation $\nu_P(J) < \nu_Q(J) < \nu_R(J)$ holds. That behaviour is made visible in the already introduced figure 3.2.2.

Rovibrational spectra generally lays in the far-Infrared and in the Infrared regions.

If we consider now electronic excitation connected to higher energy states, the treatment developed till now must be reviewed. The assumption of an inertial constant B that is equal for all the excited energy levels is no more

valid because changes in the electronic arrangement determines variations in the moment of inertia of the molecule. We can introduce a new inertial constant B' proper of the excited state.

The rotational energy levels of the initial (J) and final (J') states are respectively

$$E(J) = hcBJ(J + 1), \quad E(J') = hcB'J'(J' + 1) \quad (3.2.14)$$

Recalling equations (3.2.10), (3.2.12) and (3.2.13) the wavenumber $\tilde{\nu}$ relative to a vibrational transition for the three branches cases is:

- P-branch ($\Delta j = -1$): $\tilde{\nu}_P(J) = \tilde{\nu} - (B' + B)J + (B' - B)J^2$.
- Q-branch ($\Delta j = 0$): $\tilde{\nu}_Q(J) = \tilde{\nu} + (B' - B)J(J + 1)$.
- R-branch ($\Delta j = +1$): $\tilde{\nu}_R(J) = \tilde{\nu} + (B' + B)(J + 1) + (B' - B)(J + 1)^2$.

We first consider the case in which the bond length in the electronically excited state is greater than that in the ground state, than $B' < B$ and $B' - B$ is negative. In this case the lines of the R-branch converge with increasing J and, when J is such that $|B' - B|(J + 1) > B' + B$, the lines start to appear at decreasing wavenumber. That is the R branch develops a so called “band head peak”.

When the bond length is shorter than that in the ground state, $B' > B$ and $B' - B$ is positive. In this case the lines of the P-branch begin to converge into a band head peak when J is such that $|B' - B|J > B' + B$.

The scheme of the energy transitions of P and R branches, in the case of electronic excitation, is represented in figure 3.2.3.

An example of partially resolved rovibronical R-branch spectra of the Second Positive System of the N_2 molecule is reported in figure 3.2.4.

Rovibronical spectra normally lays in the visible and ultraviolet regions. The already described atomic and molecular quantum mechanics theory, demonstrates how a hierarchy in the temperatures associated to different modes exists. We can assert that in a plasma this relation generally holds:

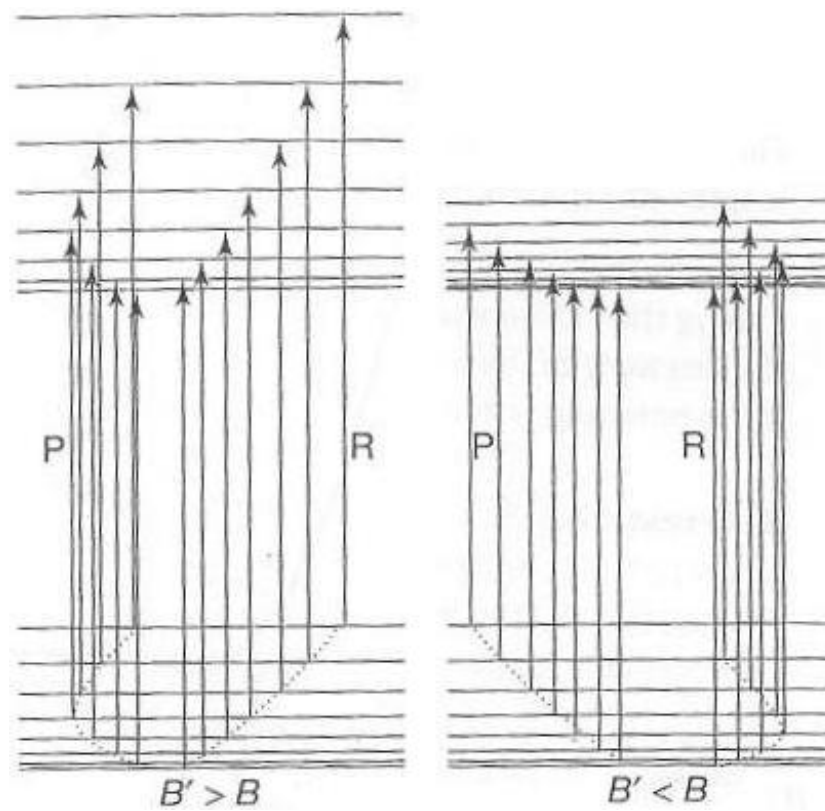


Figure 3.2.3: Scheme of the energy transitions of the P (left-hand side) and R (right-hand side) branches.

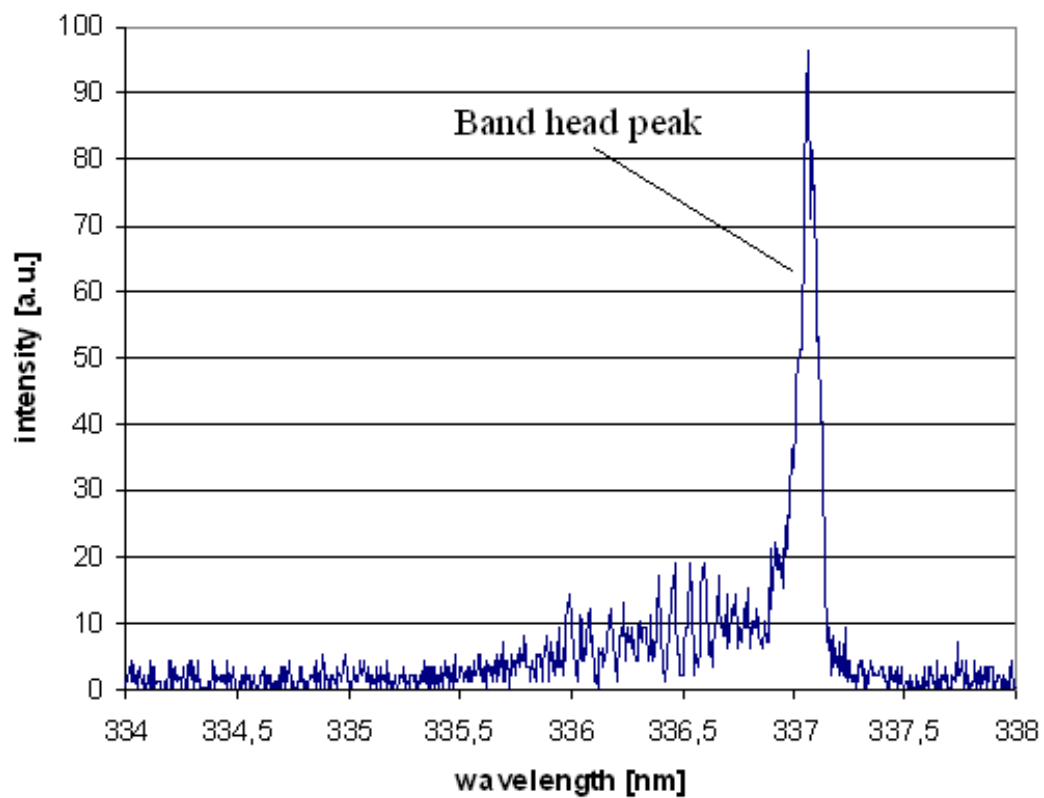


Figure 3.2.4: R-branch of the rovibronic spectra of the Second Positive System of the N_2 molecule. The band head peak is easily visible.

$$T_{EXC} \approx T_e \geq T_{vib} \geq T_{rot} \approx T_{transl}. \quad (3.2.15)$$

3.3 Plasma parameters spectroscopic evaluation

The two principal parameters that feature a plasma, the electron temperature and the electron number density can be evaluated by means of the emission spectroscopy. Moreover this methodology is very useful because it is a completely non intrusive diagnostic.

Hereafter the techniques used for the determination of these parameters in the plasmas subject of this work are presented.

Temperature evaluation

One of the most useful tools for temperature evaluation (electron, vibrational or rotational temperature) is the so called Boltzmann plot.

This plot is based on intensity measurements of the emitted spectra.

The radiation intensity of a generic emission line I_u , is proportional to the spontaneous emission probability $A^{u \rightarrow l}$ and to the population density of the upper level of the transition n_u :

$$I_u = C_1 A^{u \rightarrow l} n_u \frac{hc}{\lambda_u} \quad (3.3.1)$$

where C_1 is a constant depending on the considered atom, h is the Plank constant, c is the vacuum speed of light and λ_u is the wavelength of the emitted photon.

If excited electrons are distributed over the energy levels with Boltzmann distribution, the following relation holds:

$$\frac{n_u}{n_0} = \frac{g_u}{g_0} e^{-\frac{E_u - E_0}{kT_e}} \quad (3.3.2)$$

where n is the electron density, g is the statistical weight and E is the level energy respectively for the ground state (subscript l) and for the upper one (subscript u). At last T_e is the electron temperature and k the Boltzmann constant.

Obtaining the excited population density n_u from equation (3.3.2) and putting it into the (3.3.1) it is possible to derive the following expression:

$$y_u = \ln \left(\frac{I_u \lambda_u}{A^{u \rightarrow l} g_u} \right) = C - \frac{E_u}{kT_e}. \quad (3.3.3)$$

Each equation (3.3.3) represents a point $(E_n; y_u)$ in a semi-logarithm plot, the so called Boltzmann plot. The constant C takes into account all the constant quantities when element and ionization stage are chosen. In this way, the slope of the line fitting the data points, obtained by several emission lines of the same element and same ionization stage, is proportional to the inverse of the electron temperature.

If the points are perfectly aligned, the plasma is in partially local thermodynamic equilibrium (pLTE). Deviations from this equilibrium condition are reflected in the Boltzmann plot by a scattering of the points.

In atomic plasma, like the Argon one used in the MHD experiments presented in this work, the Boltzmann plot allows to the determination of the electron temperature by means of the lines intensity.

In air plasma, the rovibronical band head peaks are useful for the vibrational temperature evaluation.

The partially resolved rotational peaks are not available because of the limited resolution of the spectroscopic system further used. The rotational temperature will be thus esteemed by means of an approximated method based on the partially resolved rotational spectra [12].

Also continuum emission intensity is related to the electron temperature and a Boltzmann plot can be realized in this case too (see Griem [13]).

As mentioned above, continuum emission is generated by means of the recombination-emission and bremsstrahlung.

The recombination-emission is generated when a free electron and an ion re-

combine to a neutral atom or an ion with charge $Z-1$. For the Argon plasma in which continuum emission has been used, only singly ionized species will be present so that $Z=1$. The free-bound (*fb*) emission coefficient $\epsilon_{fb,\lambda}$ of this recombination emission is equal to

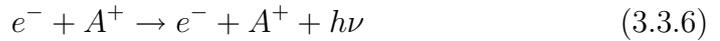
$$\epsilon_{fb,\lambda} = \frac{c_1 n_e n_i}{\lambda^2 \sqrt{T_e}} \left[1 - e\left(-\frac{hc}{\lambda k T_e}\right) \right] \xi_{fb}(\lambda, T_e) \quad (3.3.4)$$

where $\xi_{fb}(\lambda, T_e)$ is the free bound Bibermann factor which is a dimensionless quantity close to unity. For an argon plasma is equal to one and the spectral emission lies in the range $\lambda > 300[nm]$. In this equation n_i is the total density of ions. This number can be replaced by the electron number density n_e under the assumption that all ions are singly ionized and thus the plasma is quasi neutral. This assumption is also made for the rest of this study.

The constant c_1 is equal to:

$$c_1 = \frac{16\pi e^2}{3c^2 m_e \sqrt{6\pi n_e k} (4\pi\epsilon_0)^3} [Jm^4 k^{1/2} s^{-1} sr^{-1}]. \quad (3.3.5)$$

Bremsstrahlung originates from a change of the momentum of electrons caused by an interaction of electrons (*e*) with neutral atoms (*a*) or ions (*i*). We first consider the *e-i* interaction. The process of bremsstrahlung by the interaction of electrons with ions is represented by



During this Coulomb interaction, the energy of the electron is reduced and is transferred to the photon. The emission coefficient for the Coulomb interaction is represented by

$$\epsilon_{ff,\lambda}^{ei}(\lambda, T_e) = \frac{c_1 n_e^2}{\lambda^2 \sqrt{T_e}} e\left(-\frac{hc}{\lambda k T_e}\right) \xi_{ff}(\lambda, T_e) \quad (3.3.7)$$

In his equation, $\xi_{ff}(\lambda, T_e)$ is the free-free Bibermann factor, and the value of c_1 is equal to that of the free bound Bibermann factor.

The other component of the bremsstrahlung radiation is generated by the interaction of electrons and atoms and is represented by



The emission coefficient of the electron-atom (ea) interaction is given by

$$\epsilon_{ff,\lambda}^{ea}(\lambda, T_e) = \frac{c_2 n_e T_e^{3/2} n_a Q(T_e)}{\lambda^2} \left[1 + \left(1 + \frac{hc}{\lambda k T_e} \right) \right]^{(-\frac{hc}{\lambda k T_e})} \quad (3.3.9)$$

The parameter Q in equation (3.3.9) represents the cross section of momentum transfer from electrons to neutral atoms.

For argon, it can be approximated by

$$Q(\hat{T}_e) = \sqrt{\frac{40}{3\pi \left(1 + 19.73\hat{T}_e\right)^2} - 0.3 + 3.25\hat{T}_e^3 \cdot 10^{-20}} \quad [m^{-2}], \quad (3.3.10)$$

where the electron temperature \hat{T}_e is given in eV . Equation (3.3.10) only holds under the assumption that an integration of Q over the electron velocity can be replaced by taking the value of Q at the average electron velocity.

The coefficient c_2 is given by

$$c_2 = \frac{32e^2}{12\pi\epsilon_0 c^2} \left(\frac{k}{2\pi m_e} \right)^{3/2} = 1.026 \cdot 10^{-34} \quad [jm^2 K^{-3/2} s^{-1} sr^{-1}] \quad (3.3.11)$$

The measured continuum emission coefficient is determined by the sum of the various components, i.e.

$$\epsilon_{total,\lambda} = \epsilon_{fb,\lambda} + \epsilon_{ff,\lambda}^{ei} + \epsilon_{ff,\lambda}^{ea} \quad (3.3.12)$$

The total emission coefficient depends on the electron temperature and on the electron number density.

Considering a plasma characterized by a certain electron number density, from the ratio between continuum intensities of different spectral wavelengths,

the term relative to n_e disappears and a Boltzmann plot can be realized finding the electron temperature.

A Boltzmann plot can also be realized from the ratio of line to continuum intensities, but working with integrals line profiles instead of pure intensities [13]. Also in this case the only unknown is the electron temperature.

Some limitations on the use of the Boltzmann plot derive essentially from the assumption of pLTE for upper levels (that can be a strong assumption in some plasmas) and uncertainties in the values of the spontaneous emission probability coefficients.

Electron number density evaluation

The electron number density can be esteemed by several spectroscopic methods.

The first presented here is the ratio of two emission lines of the same element but proper to different systems (for example neutral and singly ionized). If the plasma is in local thermodynamic equilibrium (LTE), the neutral and singly ionized particle density, n_0 and n_+ respectively, are related together the by the Saha equation:

$$\frac{n_e n_+}{n_0} = \frac{2U_+}{U_0} \left(\frac{m_e k T_e}{2\pi h^2} \right)^{3/2} e^{-\frac{\chi_i - \Delta\chi_i}{k T_e}} \quad (3.3.13)$$

where χ_i is the ionization potential and $\Delta\chi_i$ is the lowering value of χ_i due to Coulombian interactions. Writing the relation (3.3.13) for a neutral and singly ionized line and combining their ratio with equation (3.3.2), the following relation for the electron number density is obtained:

$$n_e = \frac{A_{+k} g_{+k} \lambda_n}{A_n g_n \lambda_{+k}} \frac{2I_n}{I_{+k}} \left(\frac{m_e k T_e}{2\pi h^2} \right)^{3/2} e^{-\frac{E_{+k} - E_n + \chi_i - \Delta\chi_i}{k T_e}} \quad (3.3.14)$$

Finally, the neutral density n_0 , and then the ionization degree of the plasma, can be evaluated by means of the Saha equation (3.3.13).

The validity of this method depends on the validity of the condition of pLTE

for the levels of the considered transitions. It is well known from the theory of collisional-radiative processes that the upper levels of an atom reach a thermal distribution with the continuum of free electrons more easily than the lower levels. Thus, it is possible to define the levels of an atom as being in pLTE from level p if equation (3.3.14) applies to it and all higher-lying levels.

Many authors studied this problem. Griem [13], for example, studied how the emission of radiation affects the distribution with respect to excited states in hydrogen (or hydrogen-like ions) plasma. He found the following relation:

$$n_e = 7 \cdot 10^{18} \frac{z^7}{p^{17/2}} \left(\frac{kT_e}{z^2 E_H} \right)^{1/2} \quad [cm^{-3}] \quad (3.3.15)$$

where E_H is the hydrogen ionization energy and p is the effective principal quantum number defined as:

$$p = Z \sqrt{\frac{E_H}{E_{ion} - E_p}}. \quad (3.3.16)$$

For atoms or ions that are not hydrogen-like, as the ArII system is, the applicability of these criteria is a critical point. Experiments on ArII, in fact, show that the criterion reported in equation (3.3.15) is too restrictive and thus this method is not used in this work.

Another way to calculate the electron density is based on the continuum emission. If the electron temperature is already measured by means of some of the aforementioned methods, the electron number density can be evaluated measuring the continuum emission coefficient and using equations (3.3.4), (3.3.7), (3.3.9) and (3.3.12).

A more reliable method, that doesn't implies any thermodynamic equilibrium assumptions, is based on the line broadening theories.

A measured spectral line is actually not a proper line, but a certain broadening and an associated profile is present.

The three major broadening mechanisms are:

- natural broadening,
- Doppler broadening,
- pressure broadening.

The natural broadening is due to the uncertainty principle that relates the lifetime of an excited state (due to the spontaneous radiative decay) with the uncertainty of its energy. This broadening effect results in an unshifted Lorentzian profile. This kind of mechanism is always neglected in spectroscopic measurements because its insignificant relevance.

Doppler broadening is related to the thermal energy owned by the emitters. The atoms in a gas which are emitting radiation will have in fact a distribution of velocities. Each photon emitted will be “red” or “blue” shifted by the Doppler effect depending on the velocity of the atom relative to the observer. The higher will be the temperature of the gas, the wider will be the distribution of velocities.

Since the spectral line is a combination of all of the emitted radiation, the higher the temperature of the gas, the broader will be the spectral line emitted from that gas. This broadening effect is described by a Gaussian profile and there is no associated shift.

This kind of broadening mechanism is dependent only on the wavelength of the line, the mass of the emitting particle and the temperature, and can therefore be a very useful method for measuring the temperature of an emitting gas.

The Full Width at Half Maximum (FWHM) $\Delta\lambda_D$ of the Doppler profile is given by

$$\Delta\lambda_D = \sqrt{\frac{8kT \ln 2}{mc^2}} \lambda_0 \quad (3.3.17)$$

where λ_0 is the considered wavelength, m is the atomic weight in atomic mass units (amu) and c is the vacuum speed of light.

Pressure broadening is due to collisions between emitters with neighboring

particles. Pressure mechanisms are related to several reasons. In the weakly ionized argon plasmas studied in this work, the predominant one is the Stark pressure effect.

The Stark broadening, which is produced by means of the interaction of the emitter with an electric field, causes a shift in energy which is linear in the field strength. This mechanism is thus proportional to the coulombian interactions between particles and so proportional to the electron number density. While the Doppler broadening mechanism is readily understood, the development of an adequate Stark broadening theory it is a quite difficult task. The Lorentzian shape of this profile depends on the density of charged particles surrounding the emitters. Only with the recent development in computers science, a set of tables that is including both electrons and ion dynamics effects, leading to a more correct estimation of the electron number density [14], has been calculated.

For hydrogen lines the FWHM imputable to Stark effect is

$$\Delta\lambda_S = 2.5 \cdot 10^{-10} \alpha n_e^{2/3} \quad (3.3.18)$$

where α is a tabulated parameter that depends on the particular emission line and is slightly dependent on the temperature.

Another broadening mechanism doesn't mentioned till now is the one related to the instrumentation. Each instrument inescapably introduces a dispersion due to the limited resolution owned by the instrument itself. This broadening is characterized by a Gaussian profile.

The whole line profile is so the convolution of Gaussian and Lorentzian profiles and it is generally called Voigt profile (see figure 3.3.1).

The temperatures of the plasmas subjects of this work generate Doppler profiles negligible in compare with instrumental and Stark broadening. Measuring the shape of the line profile and performing a deconvolution, it is thus possible to separate the Gaussian part (due to the instrumentation resolution) and the Lorentzian one useful for electron density evaluation.

In order to accomplish a reliable estimation of the electron density, Stark

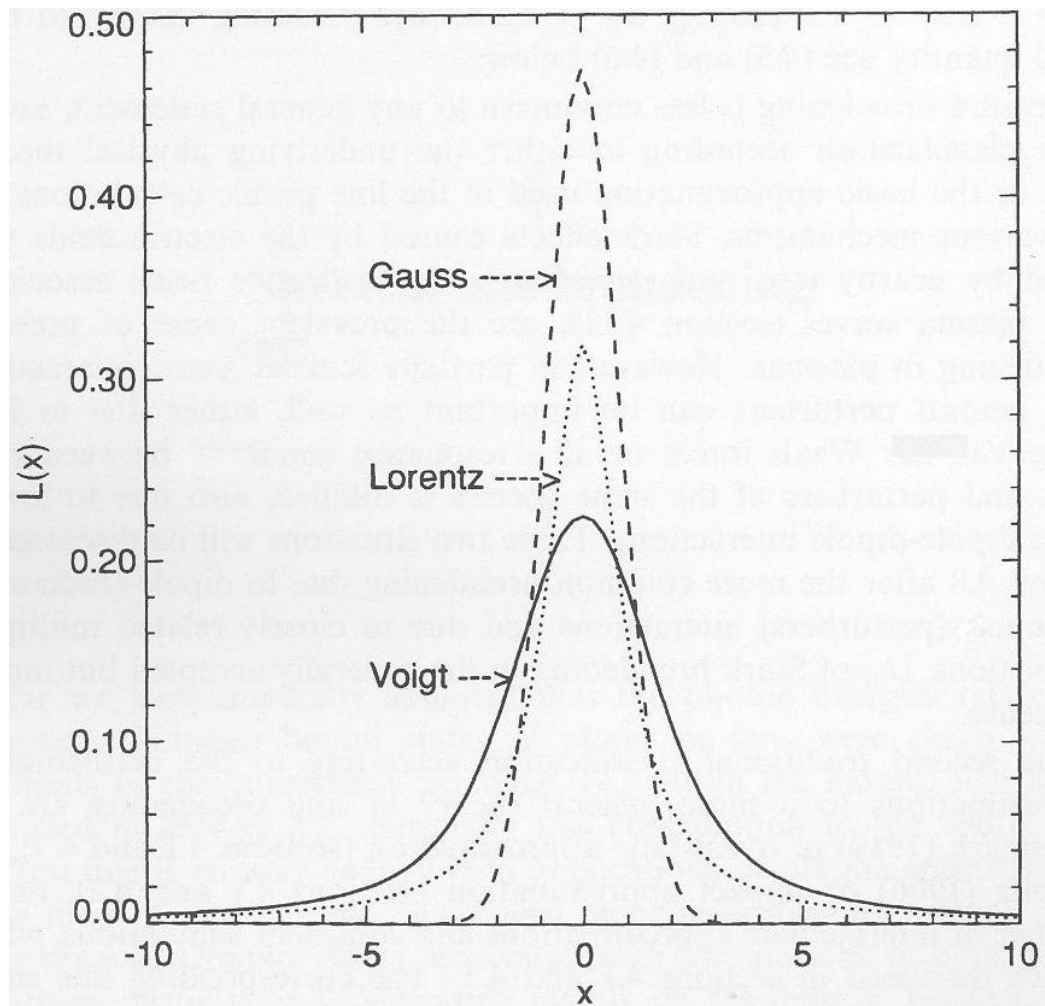


Figure 3.3.1: Normalized Gauss (Doppler) and Lorentz (Stark) profiles of equal FWHM. In continuous line there is the Voigt profile, convolution of these two profiles [2].

broadening must be at least one order of magnitude greater than instrumental broadening. For argon lines this condition is not realized, on the contrary instrumental broadening is predominant. Moreover a precise treatment of Stark effect in non hydrogen-like plasmas has not yet completely been realized.

Light atoms present higher Stark broadening, thus hydrogen is the best element under this point of view. Furthermore accurate Stark broadening parameters exist for hydrogen because of its simple structure.

In this work electron number density measurements have been performed using the line broadening of the hydrogen always present as impurity.

Chapter 4

Pitot tube diagnostic

The Pitot tube is an “old” kind of diagnostic that allows to determine the punctual velocity of a fluid (gas or liquid). In this work the Pitot tube is used in order to determine the velocity that a plasma aerodynamic actuator yields to the surrounding gas (the purpose of this kind of measurement and the plasma setup will be largely explained in section 8.3).

A Pitot tube, in its most simplified form, is composed of a thin “L” shaped tube (normally of several *mm* of external diameter) that is positioned against the flow direction as reported in figure 4.0.1.

Two different pressures are measured, one on the tip of the probe (the so called “nose”) and one in another part of the Pitot tube. A zoom of the nose (figure 4.0.2) shows as in the top aperture the velocity of the fluid is zero, because the tube is filled of fluid. In this point, a stagnation pressure that is higher than the static pressure of the fluid exists.

Referring on figure 4.0.2 we consider two sections of the conduct, one in the stagnation point (1), and the second one in another part of the tube (2). The general Bernoulli’s equation is

$$\frac{u_1^2}{2} + gz_1 + \frac{p_1}{\rho_1} = \frac{u_2^2}{2} + gz_2 + \frac{p_2}{\rho_2} \quad (4.0.1)$$

where g is the standard gravity constant and u , z and ρ are respectively the velocity, the high and the density of the fluid.

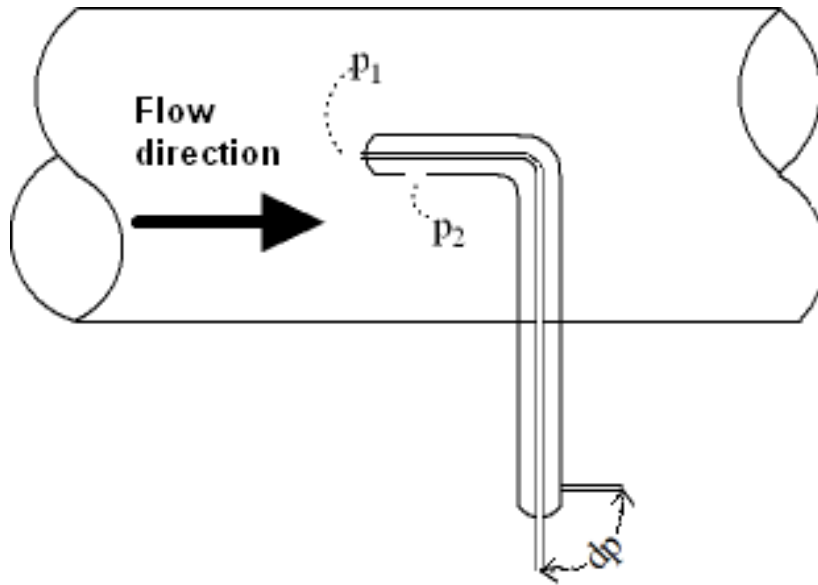


Figure 4.0.1: Pitot tube scheme

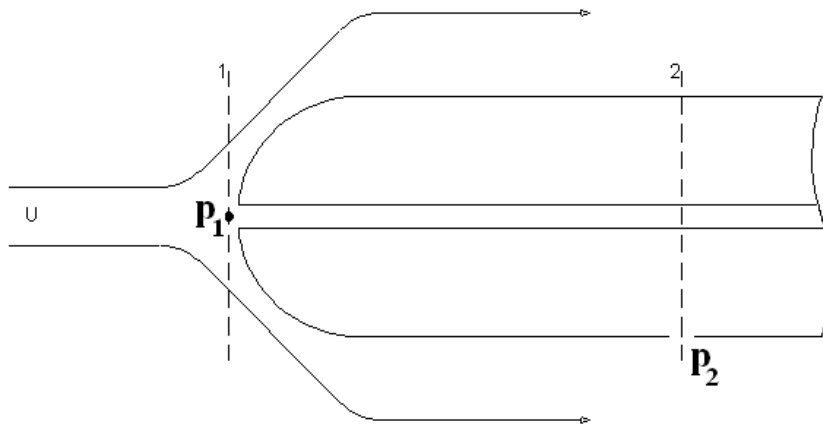


Figure 4.0.2: Zoom of the pitot nose

For the sections considered, we can state that

- $z_1 = z_2$ because the highs of the fluid are the same (the conduct is horizontal),
- $\rho_1 = \rho_2 = \rho$ because we are in condition of incompressible flow,
- $u_1 = 0$ because in the stagnation point the condition of still fluid holds.

With these assumptions equation (4.0.1) becomes

$$\frac{p_1}{\rho_1} = \frac{u_2^2}{2} + \frac{p_2}{\rho_2} \quad (4.0.2)$$

The velocity of the fluid in the section 2 of the pitot, u_2 , can so be esteemed with the following expression

$$u_2 = \sqrt{\frac{2(P_1 - P_2)}{\rho}} \quad (4.0.3)$$

Chapter 5

Electrostatic probes

Electrostatic probes are used, in this work, for the determination of the Hall field that is generated during the MHD experiments in the low density working plasma. We will see that this field is pretty important in order to understand the physics and the performances of the MHD experiments.

When a floating conductive object (i.e. each metallic body) is immersed into a plasma, electron and ion fluxes will move toward it charging its surface at some potential depending on the local plasma potential. In this way a so called Langmuir probe is realized.

Otherwise for Langmuir probes which are generally supplied with external variable voltage source, the electrostatic probes that we have adopted are completely float, thus one extremity of the probe is in direct contact with the plasma, the other side is “flying”.

In order to measure the potential reached by the probe, the “flying” terminal is connected to a scope and so linked to the ground by means of the $1[M\Omega]$ internal resistance of the scope (thus we can still assume the floating condition).

Positioning several probes in different location along the plasma path, the local potential can be evaluated and by means of the differences between these potential measurements, the Hall field can be estimated.

Part II

EHD interaction experiments

Chapter 6

Introduction to EHD applications

In last ten years the active flow control, i.e. the ability to direct manipulate a flow in order to create a wanted change, is in huge growth [15]. An efficient active flow control system could prevent or induce separation, could modify the laminar to turbulent transition inside the boundary layer, could stabilize or mix airflow in order to avoid unsteadiness which generates unwanted vibrations, noise and energy losses and could reduce the drag and enhance the lifts of airfoils [16].

The non-thermal plasma layer generated by means of the a Dielectric Barrier Discharge (DBD) is pretty suitable in order to produce a coupling between the created ionized gas and the neutral particles that surrounding the plasma itself. In this way, an Electro Hydro Dynamic (EHD) interaction is realized. The concept of ion wind is well know, but an increasing interest for this phenomenon is growing in the aeronautical [17, 18, 19, 20, 21] and astronomical [22, 23, 24] fields, and in the turbine blades area [25, 26, 7].

It is important to notice how the American Institute of Aeronautics and Astronautics (AIAA) held the “Flow Control Conference” in 2003, a meeting especially dedicated to this subject. The third and last one was held at San Francisco in June 2006.

Nowadays almost 30 research groups around the world are working in the plasma fluid dynamic actuator field.

The plasma jet generated by a DBD fluid-dynamic actuator is able to alter the velocity inside the boundary layer and can modify the interaction between fluid and body surface (a wing or a blade) without moving parts. Hence the EHD phenomenon allows to a direct conversion from electric into kinetic energy, without the meaning of mechanical moving parts and so with response times that can be considered negligible in compare to the characteristic times of the fluid system.

Furthermore a fully composed electric actuator with no moving parts could lead to reduced size, low input power, and the easy ability to simulate its effect in numerical flow solvers.

In this Part of the work, after an overview of the DBD plasma features and of the EHD interaction, two different series of experiments are presented.

The first is on a flat multi-electrodes panel driven by a 3-phase sinusoidal waveform. The second on a single actuator driven by a nanopulses plus DC or AC bias waveform.

Chapter 7

EHD interaction theory

7.1 The Dielectric Barrier Discharge

The EHD interaction is based, as said in the introduction of this Part, on the interaction between the plasma generated by a Dielectric Barrier Discharge and the neutral gas that surrounds the plasma itself. It is so useful to describe the way with which the plasma is formed and the features of this kind of plasma.

The Dielectric Barrier Discharge is a suitable way to generate a stable, confined and homogeneous plasma also at high pressure (i.e. at atmospheric pressure and so without the presence of a vacuum facility). The concept of the DBD is not new because it has been used by 1857 from Siemens [27] for ozone generation.

The typical configuration of a DBD actuator is sketched in figure 7.1.1. The basic configuration of a DBD actuator is composed by two parallel electrodes separated by a gap filled by a gas. One or both the electrodes are covered by a dielectric material.

Supplying the system with a DC bias, nothing happens because the dielectric material screens the free charges to reach the electrodes.

If a sinusoidal AC voltage is applied a displacement current is established and, if the supplying conditions are well chosen, the breakdown of the gas

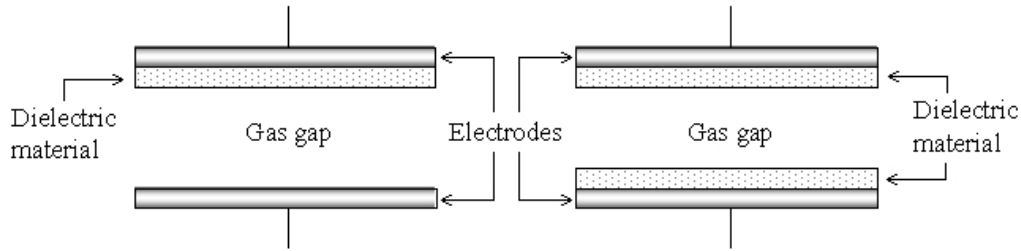


Figure 7.1.1: Example scheme of DBD setup configuration.

occurs leading to plasma formation. The presence of the dielectric forbids the transition into an arc regime, self-limiting the current. Typical values for voltage and supply frequency are respectively $1 \div 10 [kV]$ and $1 \div 10 [kHz]$. The formation of the plasma is based on the avalanche phenomenon. In the interelectrode space, a certain amount of free electrons, mostly due to UV radiation from the sun light or other phenomenon exists. When an electric field is applied, the electrons are accelerated along the field lines and during this motion they collide with neutral particles. If the energy owned by the electrons is high enough, they are able to ionize the neutral particles, and so they can extract from the molecules or atoms of the gas one or more “new” electrons. These electrons are themselves accelerated and are so potentially able to ionize more and more neutral particles. In this way an avalanche ionization is generated.

Under the influence of the imposed electric field, a separation of charge takes place because a fast cloud of electrons moves toward the anode and a negative one, formed by the positive ions, remains back because of the lower mobilities of ions ($m_i \cong 2000 m_e$). Positive and negative charges start to shield respectively the cathode and the anode. A stationary condition is so achieved and a steady regime is established and the ionization stops.

In presence of an AC field, the avalanche process can be repeated in the opposite direction and the plasma formation can be sustained.

The plasma formed by a DBD is reported in 7.1.2 and seems pretty homogeneous to the unaided eye.

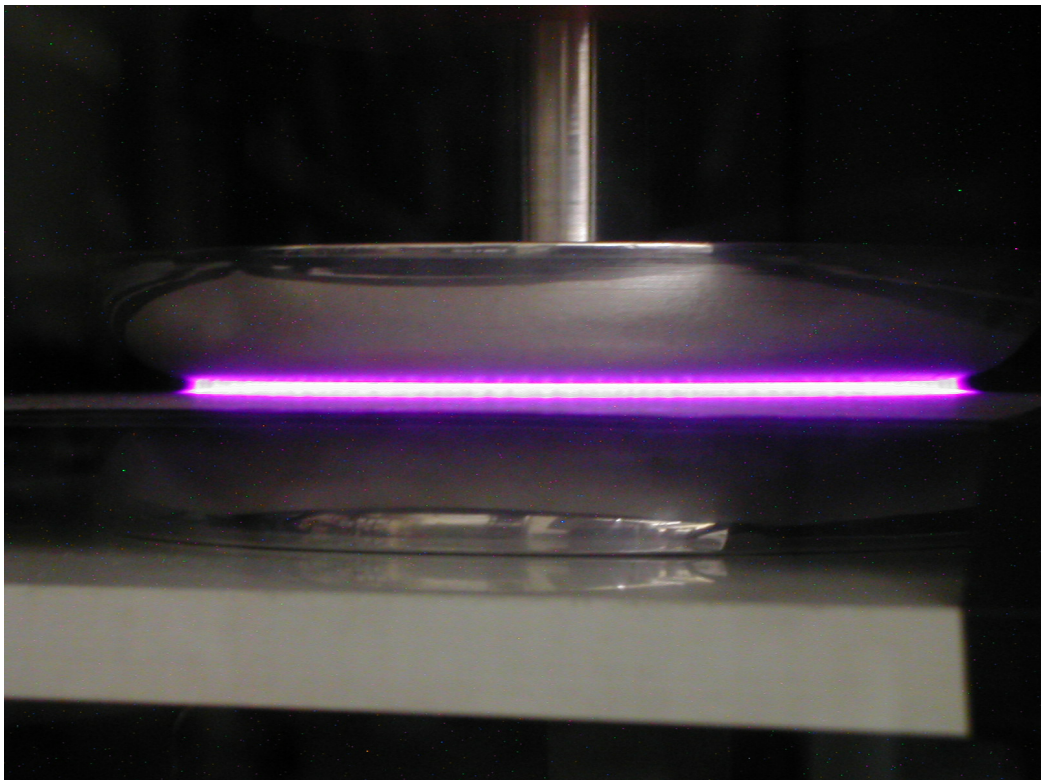


Figure 7.1.2: Plasma formed by a DBD in air at atmospheric pressure.

In reality the plasma is formed of a series of plasma-filaments, of the radius of the order of $100[\mu m]$, which move along the field lines with velocities in the order of $10^5[m/s]$.

The wire-like plasma starts where the conditions are more favorable (rough surfaces, higher local field or more initial electrons) and then propagates under the presence of its own field. Each filament is due to the charge neutralization of the ionizing channel due to the avalanche phenomenon [28].

The motion of the charges and the ionization process create a net current that extinguish itself when the electrons reach the dielectric surface that cover the anode. When the space charge reaches the anode an electromagnetic wave is formed and it propagates back toward the cathode and can originate a back current (with a mechanism close to that one of the lighting event).

The life time of a streamer is of the order of the tenth of nanoseconds and so, taking into account the typical supply frequencies, for each half period of the sinusoidal supply voltage, a huge number of streamers are formed.

The exchange of energy between the accelerated electrons and the other particles occurs both within and outside the microdischarges.

Almost the 90% of the energy owned by the weakly energized electrons is given, by collisions, to the heavy particles. This stored energy allows to the excitation of the internal energy of the species and limit the temperature of the plasma itself. That is why the plasma formed by a DBD is classified as a “cold” one.

The plasma generated by a DBD is in fact a weakly ionized gas, thus a gas in which the amount of charged particles is less than the 1% of the total particles population. The electrons gain a huge amount of energy in compare with the ions because of their lower mass, and so they are able to ionize the gas and activate radical species. The plasma created can be considered in partial Local Thermal Equilibrium (pLTE). Its behaviour can be described by two different Boltzmann particles distributions characterized by two different temperatures: an electron temperature T_e and an ion one T_i .

As introduced before, the electrons with high energy are able to ionize or

to excite the heavy molecules, and so new species (O_3 , CN , NO_x) can be created. That is the reason because one of the applications of the DBD is for ozone production or decontamination processes.

The deexcitation of the excited species generates spectral emissions that are useful for temperature measurements (see Chapter 3 for more details).

From an electrical point of view, the DBD plasma is characterized by electron density in the order of $10^{13} \div 10^{16} [part/m^3]$ and current density in the range of $100 \div 1000 A/cm^2$ [29, 30].

Typical voltage and supply current are showed in figure 7.1.3.

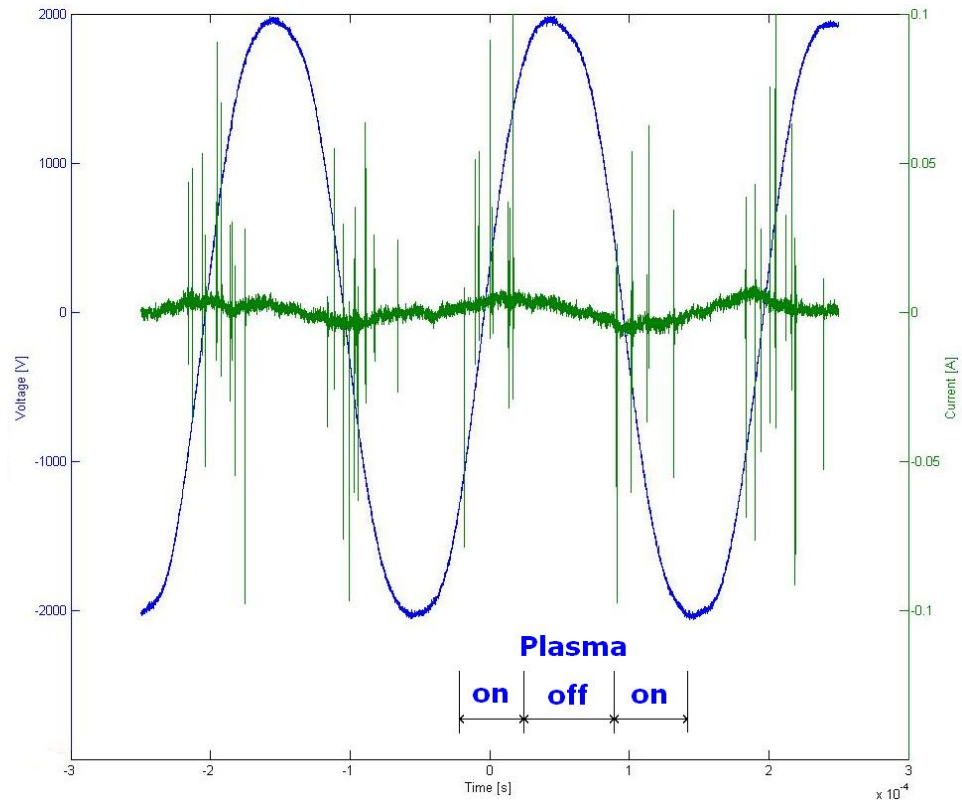


Figure 7.1.3: Voltage and current vs. time characteristic of a DBD. Supply voltage $2[kV]$ peak, $5[kHz]$.

The plasma is present only in two portion of the supply period and the current is characterized by two different contributes. One is a sine component with a phase shift of almost -90° , in compare with the voltage phase. That

is the displacement current due to the capacitive behaviour of the DBD. The second component is due to the net current generated by the streamers formation, and is composed of a dense repetition of steep peaks with high magnitude, related to the fast formation and quenching of the microdischarges.

In the next Section, the adjustment of the DBD actuator for the fluid-dynamics field will be described and investigated.

7.2 The EHD actuator based on the DBD

The use of an electric fluid-dynamic actuator characterized by means of no moving parts is not a new concept. The ion wind generated by a DC corona discharge is able to convert the electric field into ions, and subsequently, neutral flow that moves away from the high voltage electrode and reaches velocity on the order of several meters per second [31, 32, 33].

Without lengthen with the DC corona fluid actuators, some words must be said in this section.

The mechanism of the formation of the plasma is close to that one explained for the DBD.

Under the presence of an high electric field, an avalanche regime is formed and the multiplication of primarily energetic electrons is established. The positive ions that are created are then pushed away from the positive electrode.

The plasma that is formed can be classified as “cold”, in fact the majority of the electron energy goes into the formation of other energetic electrons, instead heating the surrounding gas [34, 35, 36, 37, 38].

Surface DC corona actuators (figure 7.2.1) have been studied and tested, and velocity in the order of several meters per second have been reached as showed in figure 7.2.2.

One of the biggest limitation of this kind of plasma is the glow to arc

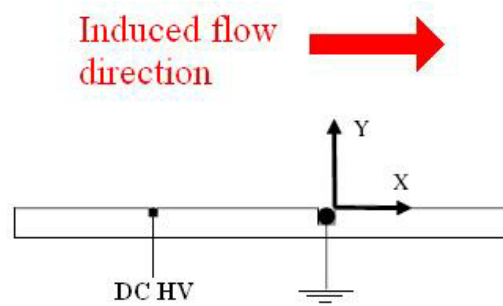


Figure 7.2.1: DC surface corona fluid-dynamic actuator design from [3].

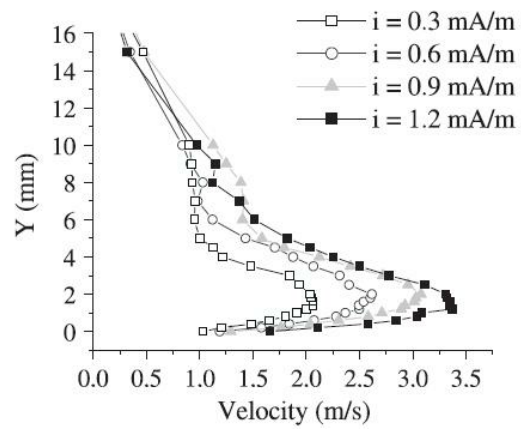


Figure 7.2.2: Velocity profile in still air for a DC Corona fluid-dynamic actuator with increasing current [4].

transition. As a matter of fact, if the voltage is constantly increased, in order to increase the velocity, an arc regime is established and the plasma becomes unstable, and more and more energy goes into thermal excitation of heavy particles. In these conditions, the efficiency of the actuator decreases and the heat generated starts to deteriorate the actuator itself.

In 1994 Roth's group refined a new kind of atmospheric fluid-dynamic actuator based on the plasma generated by means of a Surface Dielectric Barrier Discharge and he presented its work in 1998 at the AIAA Conference and 25th ICOPS [17, 39]. He demonstrated that such actuator was able to induce a flow tangential velocity on the order of several meters per second and that velocity was proportional to the magnitude of the AC applied voltage.

This geometrical actuator design was then followed by several research groups (Borghetti *et al.* [18], Moreau *et al.* [19], Corke *et al.* [20], Miles *et al.* [21]) and became the typical fluid-dynamic actuator arrangement based on the DBD (figure 7.2.3).

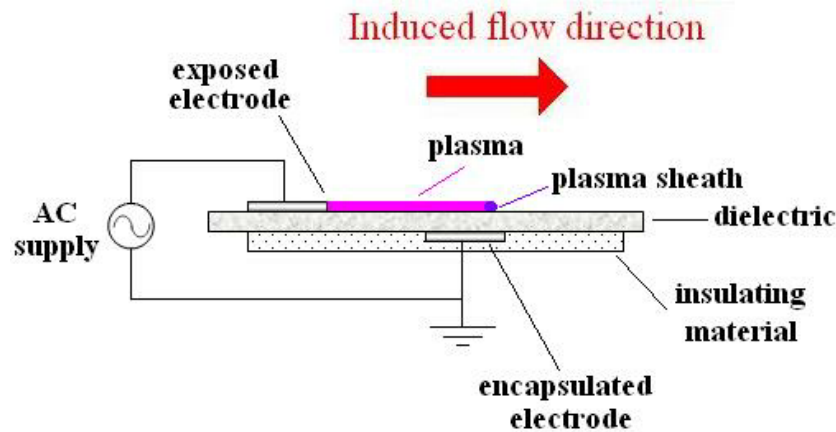


Figure 7.2.3: Typical EHD fluid-dynamic actuator arrangement.

A dielectric layer is interposed between two electrodes flush mounted, the upper one is in direct contact with the fluid, the other is embedded, in order to prevent the plasma formation on it. The principal characteristic is the asymmetry of the electrodes (a displacement gap between the electrodes can be eventually present as sketched in figure 7.2.3). Under the presence of an

appropriate electric field this asymmetry leads to the formation of a plasma only in the upper surface correspondingly over the embedded electrode. This design has demonstrated to create a net force in the neutral fluid that is, on the average, directed away from the exposed electrode [17].

The typical dimensions for this kind of actuator are: dielectric width in the order of $0.1 \div 5[mm]$, electrodes width in the order of $0.1[mm]$, length of the encapsulated electrode within $20[mm]$ (the length of the bare electrode is not influent in the EHD performance) and gap in the range $0 \div 20[mm]$ [40, 41]. The plasma interact with the boundary layer by means of the collisions between the ions and the surrounding neutral particles. The presence of high energetic electrons is not considered in the momentum coupling because of their low mass.

Taking into account that we are dealing with a weakly ionized plasma (the electron density is in the order of $10^{13} \div 10^{16}[part/m^3]$), we can assume that this EHD actuator operates as a porous piston because of the presence of few ions that “push” away the neutral surrounding particles [42]. That is in agreement with the relative low velocity of several meters per second induced in the neutral flow, in compare with the pretty high velocity owns by the ions that is on the order of $10^5[m/s]$.

Due to the nature of the DBD, the ions receive the push thousand times per cycles. Macroscopic measurements in the induced velocity (for example by means of a Pitot tube), show how the neutral flow “sees” a constant push directed away from the exposed electrode [40, 41, 43].

In figure 7.2.4 is reported a velocity scan of the boundary layer of still air for a DBD fluid-dynamic actuator at different supply conditions [40].

At this point the nature of the streamers formation and propagation, and the interaction between ions and boundary layer must be well considered. The streamers formation behaviour of an asymmetric DBD actuator can be studied starting from the typical current-voltage vs. time characteristic (figure 7.2.5).

As introduced before for a general DBD arrangement, the current is char-

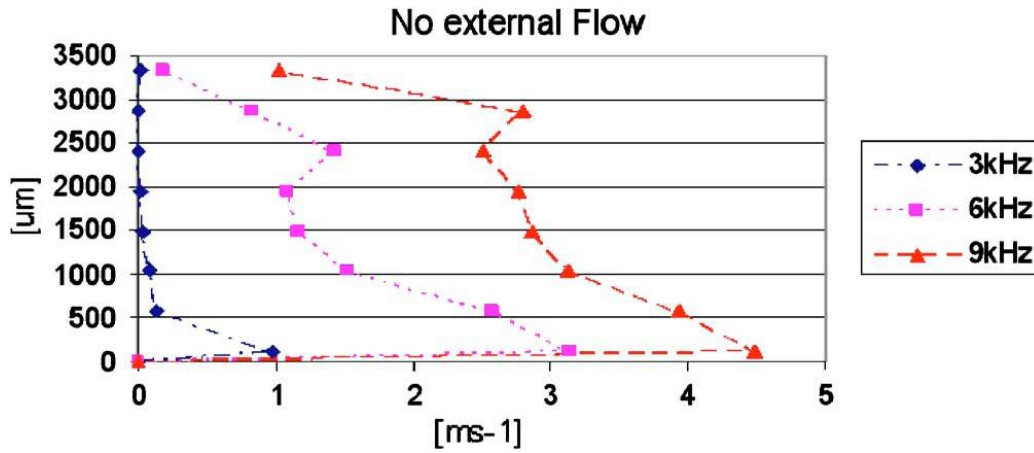


Figure 7.2.4: Pitot scan of the boundary layer induced velocity by a DBD fluid-dynamic actuator supplied by an AC voltage of $5[kVp]$ at different frequencies.

acterized by two contributes; a sine displacement current and a fast succession of symmetric current peaks due to streamers formation (figure 7.1.3 at page 71).

With an asymmetric electrodes design different current behaviours along the two half cycles are noticed. During the positive period, the plasma is characterized by a series of high current peaks of relative low frequency. During the negative half the plasma is more homogeneous and a series of low magnitude and high frequency streamers are formed. This behaviour is demonstrated both from experimental [44] and numerical [45, 46] works.

A possible explanation can be done as follow.

Supposing the bottom electrode grounded, during the negative half cycle electrons are emitted from the exposed electrode and deposited onto the dielectric surface. As the charge on the dielectric builds up, it opposes to the applied voltage on the exposed electrode decreasing the total electric field. The discharge will then stop choking itself, unless the magnitude of the applied voltage continues to increase. That happens during the period in which the magnitude of the applied voltage increases (in absolute value). This phenomenon stops when the voltage on the exposed electrode stops becoming more negative, which is needed to overcome the buildup of charge on the di-

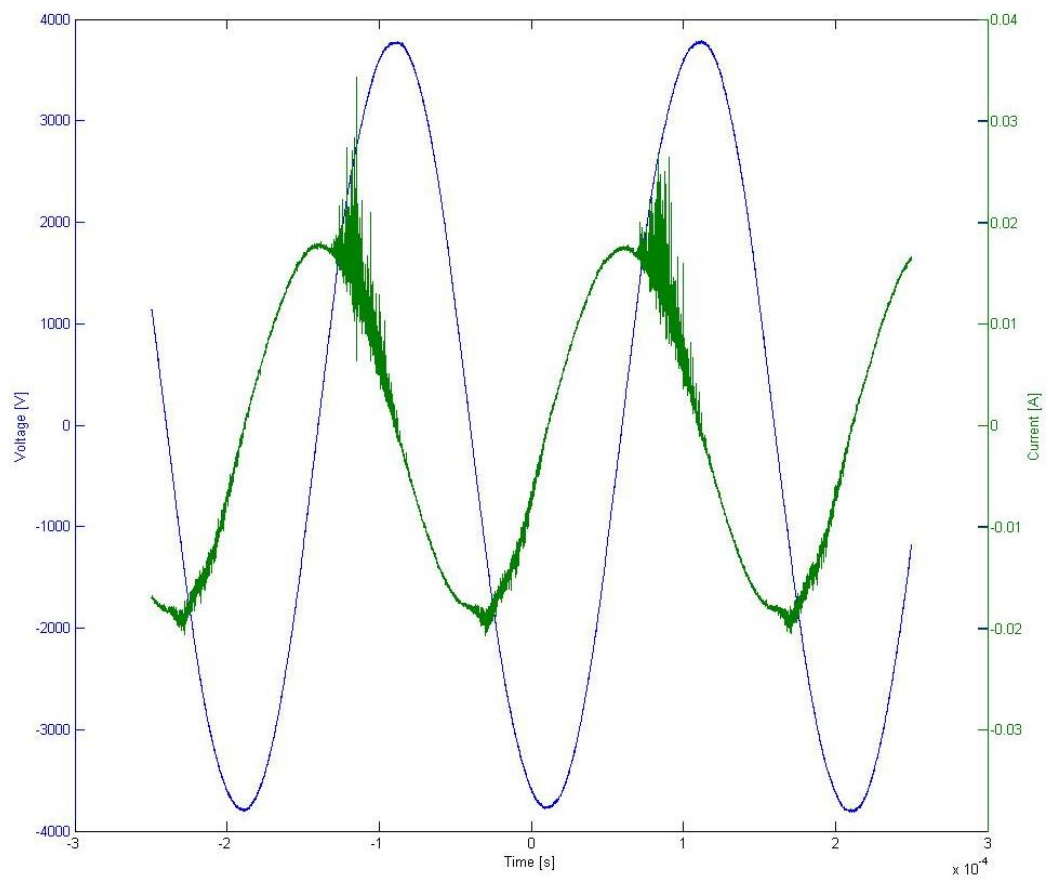


Figure 7.2.5: Voltage and current vs. time characteristic of an asymmetric DBD actuator. It is possible to note the asymmetric behaviour of the current.

electric. During this period, the exposed electrode acts as an infinite source of electrons. The discharges are so generated in a continuous and more uniform way.

The behaviour of the discharge is similar on the positive half of the ac cycle. In this case, the exposed electrode is more positive than the surface of the dielectric which is now holding the deposited electron charge of the previous period. When the potential difference is large enough, the electrons will be emitted from the dielectric surface directed toward the bare electrode. The ionization stops when the voltage at the bare electrode stops becoming more positive and the electric field falls below the breakdown requisite value. During this period the electrons begun available by the dielectric surface. This availability doesn't seem to come so readily or, when it comes, a big amount of electrons are collected and discharges of big magnitude are generated.

This behaviour has been also observed by Enloe [47] and Orlov [5] by means of measurements of the plasma emission using a photomultiplier. In figure 7.2.6 it is possible to notice as the measured light follows the streamers formation; high magnitude and low frequency signals have been observed during the positive half cycle and low magnitude, and high frequency light pulses have been measured during the half negative period.

These differences noticed in the plasma are also reflected in the actuator efficiency. As said before, higher is the plasma uniformity, higher is the induced airflow velocity. This behaviour has been found for positive and negative sawtooth AC supply signal. For the negative one, the rise time is higher and higher is the time in which the electrons are deposited on the dielectric surface, so higher is the time in which the plasma is more uniform. In this case the induced thrust is higher.

Furthermore we can affirm that a sawtooth signal is better than sine or rectangular waveform [47].

The other important aspect with which we are dealing now, is the ions-neutral particles interaction and the produced thrust.

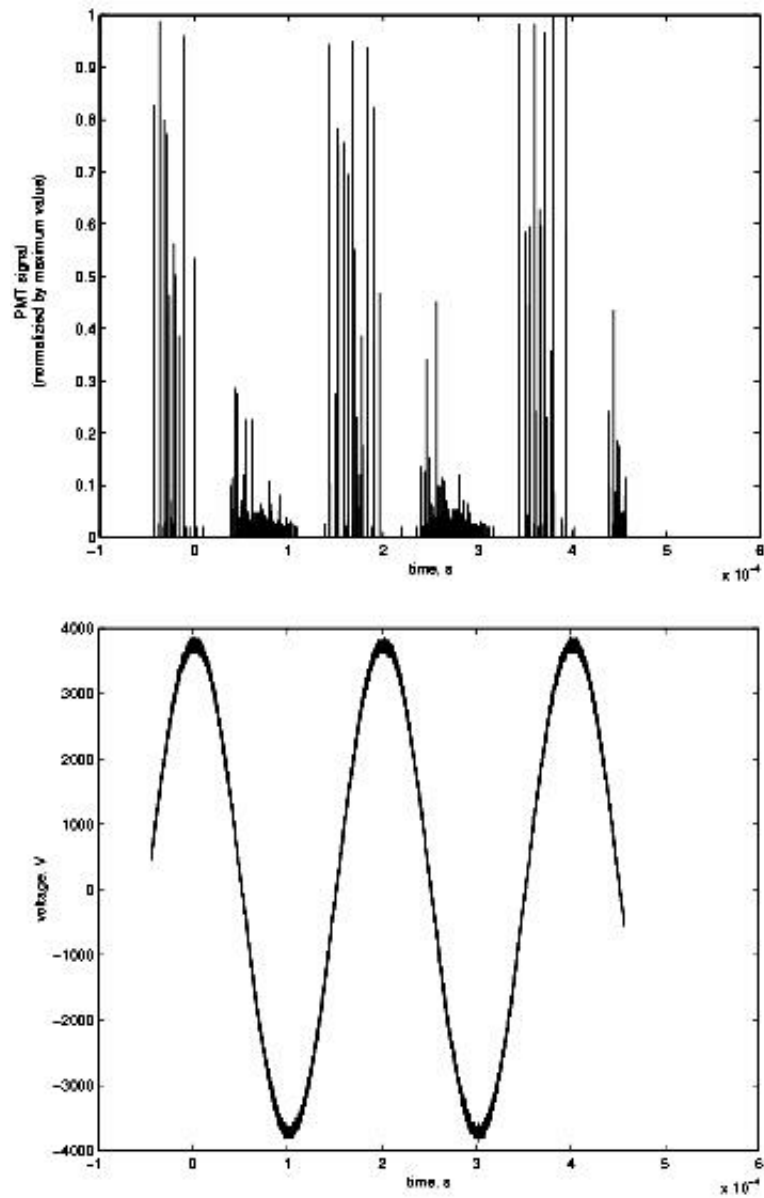


Figure 7.2.6: Photo Multiplier signal of ionized air measured over the bare electrode of a DBD actuator (top), and corresponding AC supply signal (bottom) [5].

One influential aspect is the DBD chemistry. In the previous Section, we saw how the DBD generates a plasma rich of a lot of chemical species and ions. The two major ions families that we must take into account are the N^+ and the O^- . In fact, the presence in the air of the electronegative O , generates a certain amounts of negative O^- ions.

Now, under the presence of a, as said, positive electric field, the positive ions will be repelled, the negative ones will be attracted. In this condition two opposite fluxes are generated and two contrary forces are produced. The presence of negative ions is probably one of the first reasons of inefficiency for the DBD fluid-dynamic actuators [42]. Both experiments and simulations demonstrate that the average force in the period is directed downstream, but about the instantaneous forces or at least the average ones in each period, the point is open.

The two major theories consist in a “PUSH-push” (big push in the positive period and lower push in the negative one) or in a “PUSH-pull” (big push in the positive period and little pull in the negative one) behaviour. Font [48] and Porter [8] found a PUSH-pull behaviour with a backward force in the pull phase in the order of the 20% of the push phase. Forte [49] did LDV measurements and found a PUSH-push behaviour. Further investigation must be done in this ambit.

By now we always talked about a surface thrust induced by the actuator on the neutral flow. Some experimental works with PIV [50] and LDV [49] measurements and numerical ones [45, 46, 42] have dealt with the tangential and normal component of the induced thrust.

Focusing now on the numerical work, it is important to note that the force is expressed only in the non-neutral regions of the plasma, in particular in the plasma sheath that travels, at a velocity in the order of $10^5 \div 10^6 [m/s]$, in the head of each stream. Two components of the force have been detected; one normal and directed toward the surface that creates a suction for the neutral fluid that surrounds the tip of the exposed electrode, and one tangential to the surface itself. The neutral gas is so sucked close to the top of

the bare electrode in the side displayed over the bottom electrode, and then it is pushed away tangentially to the surface forming then a vortex.

Moreover, Boeuf [45], for a nitrogen-like gas (only electrons, positive ions and neutral particles are considered), found that the force is produced not only during the streamer phase in which the current is high, but also during the low current corona phase that exists between two streamer phases. The produced forces are of the same magnitude and, when the cathode is below the dielectric, the force is mainly directed tangentially to the surface, and when the cathode is above the dielectric, the force is mainly normal to the surface. The entity of the induced thrust both from numerical and experimental [8] works, is in the order of the tenth of mN/m .

Thus, in order to improve the efficiency of the DBD plasma fluid-dynamic actuator, the important role of the dielectric as source of secondary electrons, the presence of both positive and negative ions, the design of the electrodes and the kind of supply signal must be taken into account.

7.3 EHD air flow control

The application of the DBD fluid-dynamic actuator in the aerodynamic flow control is in continuous development. Several numerical [51, 52] and experimental [53, 54, 55, 6] works have dealt on the application of EHD actuators over flat panels or airfoils.

In particular, the ability of the actuator to prevent or to induce separation and the possibility to reduce the drag and to enhance the lift of airfoils have been demonstrated.

Normally, both simulations and experiments operate on surfaces over which a certain numbers of electrodes are mounted perpendicular to the flow, in order to generate a downstream induced velocity.

In figures 7.3.1 and 7.3.2 the smoke visualization photographs of a flat panel and of an airfoil immersed in a subsonic low Reynolds number air flow are

respectively reported.

On the leading edge of both flat panel and airfoil a single DBD actuator is mounted. The supply system is characterized by a sine waveform with voltage of $10[kV]$ peak-to-peak and frequency of $4[kHz]$.

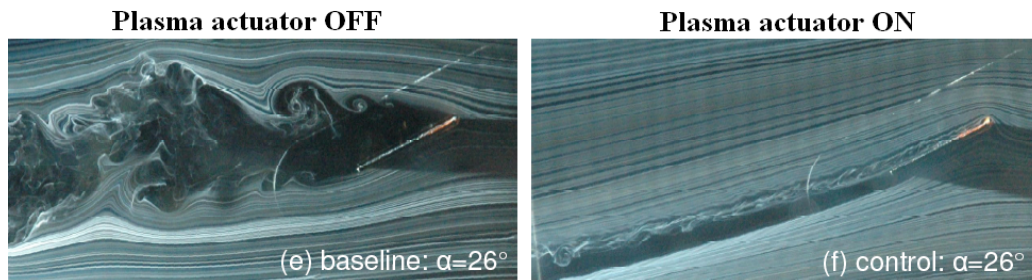


Figure 7.3.1: Smoke visualization photographs of a flat panel positioned with an angle of attack of 26° ($R_e = 3000$): baseline (left-hand side) and “steady plasma” control (right-hand) [6].

On the left side of figure 7.3.1 the actuator is turned off and a big separation region is present over the flat panel body. In the right-hand side the actuator is turned on and there is a complete reattachment of the flow. Analogous considerations can be expressed for the airfoil in figure 7.3.2. When the actuator is turned on, the detachment is strongly decreased.

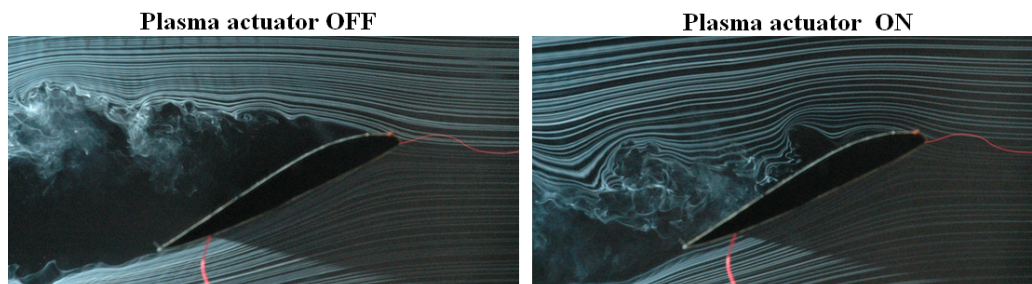


Figure 7.3.2: Smoke visualization photographs of an airfoil positioned with an angle of attack of 25° ($R_e = 20500$): baseline (left-hand side) and steady plasma control (right-hand) [6].

These flow visualizations are accomplished by lift measurements. In figure 7.3.3 it is possible to observe the lift coefficient vs. angle of attack of the flat plate, at two different free stream conditions in the two cases of actuator turned on or off.

For both the fluid-dynamic conditions the DBD actuator allows to a considerable enhancement of the lift coefficient. In particular, in the case with Reynolds number equal to 9000, the lift coefficient is increased till the 50% of its baseline value.

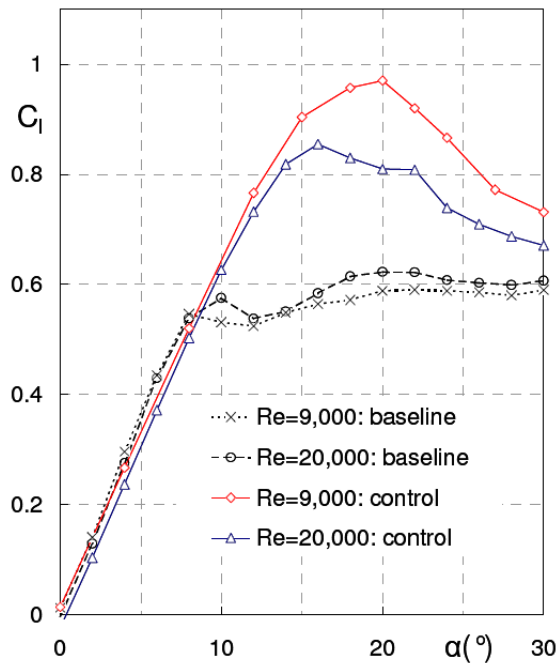


Figure 7.3.3: Effect of control on the flat panel performance at $Re = 9000$ and 20000 [6].

The other important field in which the fluid-dynamic DBD actuator could be positively used is on turbine blade surfaces.

One problem with turbine blades is the partial load regime, i.e. at low flow velocities, in which the blade exhibits flow separation on the suction side. Then a plasma actuator near the trailing edge, such as on an airfoil, can

prevent or reduce separation [7].

In figure 7.3.4 is reported an example of a DBD actuator applied to a blade stage of a gas turbine engine for high altitude cruise. On the left side is presented the position of the DBD actuator, and on the right one, are reported the flow velocity measurements over the blade surface by means of LDV [25].

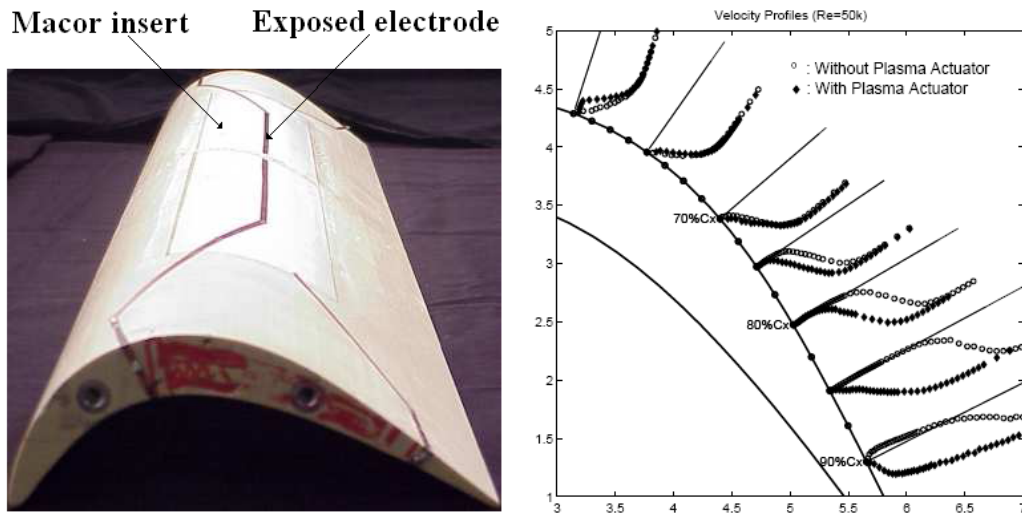


Figure 7.3.4: Pak-B blade with single DBD actuator photography on the left side and velocity measurements obtained using LDV on right one [7].

The velocity measurements show how, for the actuator off case, the separation location starts at $x/C = 0.72$ and finish at $x/C = 0.95$ (C is the cord length so x/C is the relative position on the cord). With actuator on, the re-attachment starts at $x/C = 0.85$ and the separation bubble is smaller.

The active flow control realized by a DBD actuator has demonstrated to have a strong impact in the flow separation and can produce big lift enhancement. Aside improvements in the efficiency of the plasma formation and its coupling with the neutral flow, further work must be done in order to optimize the position, the number and the supply conditions of the actuators.

Chapter 8

The EHD 3-phase actuator

8.1 The EHD 3-phase actuator setup

In Chapters 6 and 7 we dealt about the physics and the applications of the Electro Hydro Dynamic actuator. In this Section the base principles of a 3-phase multielectrodes actuator will be discussed.

The research group of the University of Bologna projected and realized a multielectrode flat panel fluid-dynamic actuator supplied by a 3-phase sine wave generator and checked the induced airflow in different supply conditions.

The multielectrode EHD actuator is based on the one introduced in the figure 7.2.3 at page 74, replied several times in order to sum the induced flow contribute of each single actuator.

In a monophasic multielectrode design, the plasma is subjected only to the field between one HV electrode and the corresponding closest grounded one. In a poly-phase supply system, there is also the contribution of the field between electrodes connected to different phases [56]. Assuming that the supplying frequency is sinusoidal and that V_0 is the phase to phase voltage, the electric field contribution of a single phase can be expressed by the equation (8.1.1):

$$|E_C| = -\nabla V = V_0 k \cos(\omega t - kx) [V/m] \quad (8.1.1)$$

where $k = 2\pi/\lambda$.

In our experiment, a 3-phase sine wave HV supply system has been used with a multielectrode flat panel actuator characterized by nine couple of electrodes [57] as shown in figure 8.1.1.

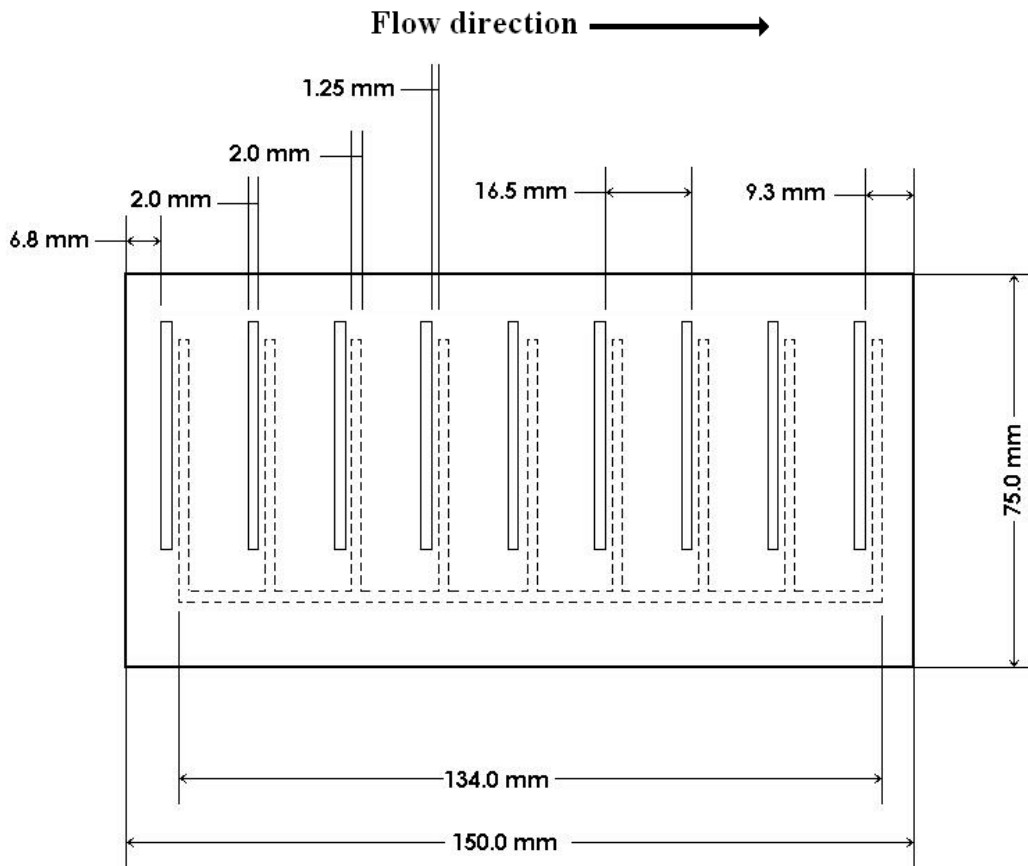


Figure 8.1.1: Top view of the 3-phase multielectrode flat panel. In continuous lines there are the top HV electrodes. In dashed the lower embedded grounded electrodes.

Each electrode has been realized by means of a $100[\mu m]$ thick, $50[mm]$ long and $2[mm]$ wide adhesive copper strip: all the electrodes are placed

orthogonally to the flow. The lower electrode comb is shifted by $1.25[mm]$ horizontally as regards to the position of the upper one. It has been chosen a phase to phase distance of $15.5[mm]$, in order to avoid a phase to phase discharge that could damage the power supplying system (figure 8.1.2).

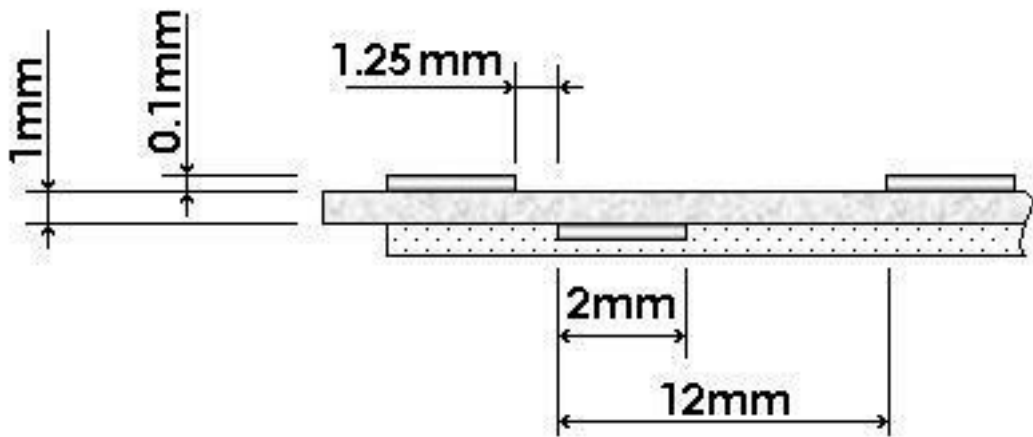


Figure 8.1.2: Transversal section of a couple of electrode of the 3-phase multi-electrode configuration.

The choice of the insulating material is crucial to obtain a reliable plasma between electrodes. The insulating material must have a good dielectric strength, must be chemically inert, must sustain thermal stresses and must have a small dielectric constant in order to minimize the dielectric losses between electrodes.

The material that better matches these requirements is Teflon (Polytetrafluoroethylene, PTFE); it has a dielectric strength of $100[kV/mm]$ and a relative dielectric constant that lies between 2.0 and 2.1 depending on the frequency. The actuator design and the supply conditions allow to the formation of a plasma that extend itself for a length (determined by eyes) of $\sim 3[mm]$. The power supply unit has been specifically designed for this application. It has been realized by means of a triphasic PIC based signal generator and three power amplification units, connected to three high voltage - high frequency transformers (figure 8.1.3).

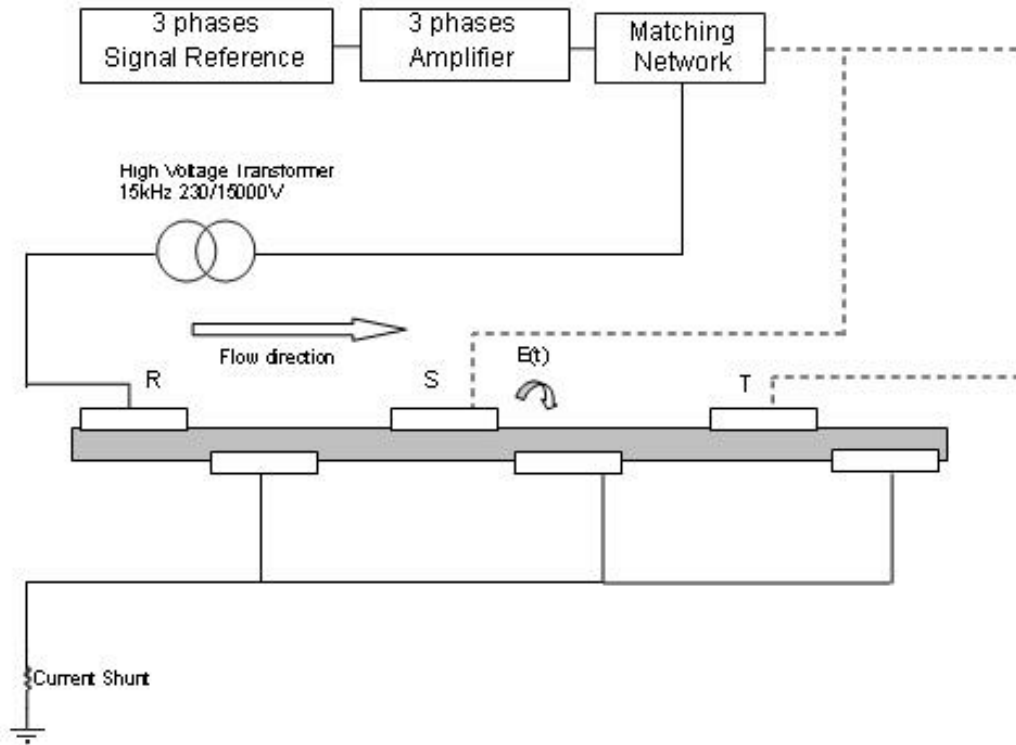


Figure 8.1.3: Scheme of the 3-phase EHD panel supply system. For phases *S* and *T* the scheme is the same that for phase *R*.

The signal generator, as it is possible to see in figure 8.1.4, has been built around a Programmable Integrated Circuit (PIC) where a specific firmware has been developed.

The PIC must satisfy two requirements: firstly it has to set each sinusoidal generator and calibrated attenuator to the value in frequency and amplitude settled by the user, secondly it has to synchronize the three sinusoidal generator at 120° one to each other, in order to achieve a symmetric system.

The sinusoidal signal was obtained by an analogue component that generates it, while a comparator controls the calibrated attenuator in order to obtain three signals at the same level.

The power amplification unit has been realized by means of a commercial

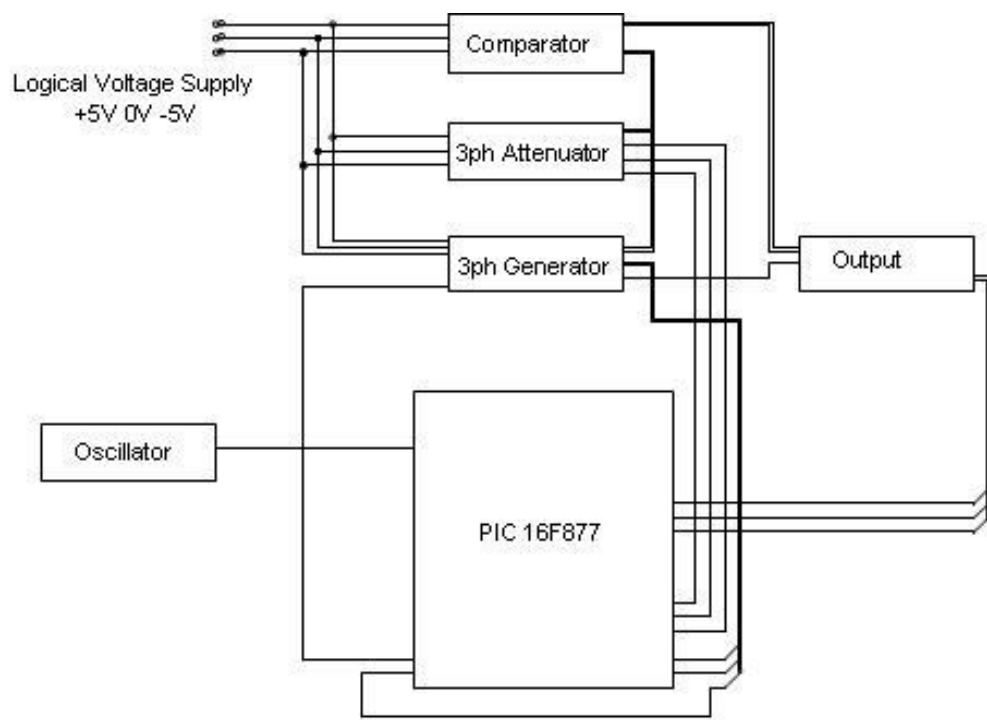


Figure 8.1.4: Three-phase signal generator layout

MOSFET amplifier.

The amplifier that has been chosen is a Prism Audio LA 450 M, with a continuous output power of 450[W] for each of the three branches needed for realizing the triphasic system. In order to obtain a reliable behaviour of the amplifier, it has been used a phase shifting branch realized with some inductors and resistance, and inserted in parallel to the load. With this expedient it has been possible to have a $\cos \varphi < 0$.

In the end, in order to avoid any possible voltage spike reflected from the load or the phase shifting branch, a surge arrester was also placed in parallel at the exit of the audio amplifier (figure 8.1.5).

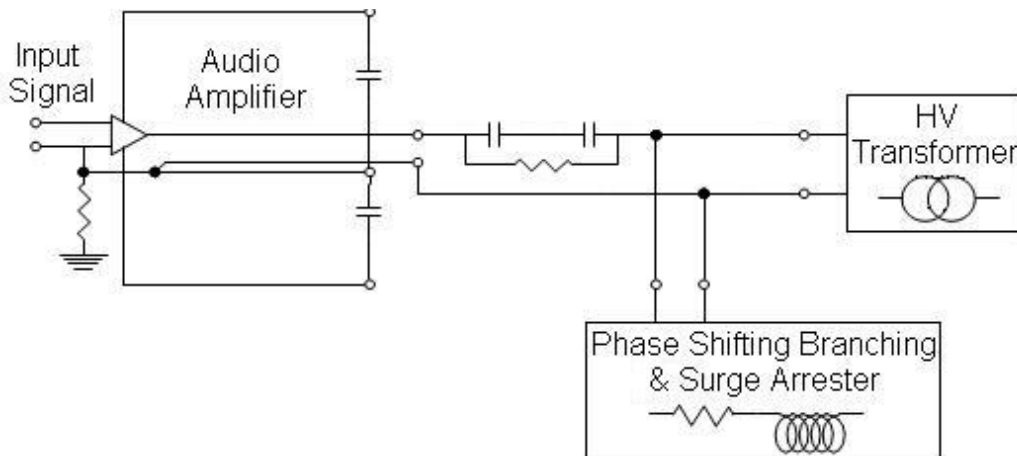


Figure 8.1.5: Single Monophasic Power amplifier branch. The actual design uses three of this branches, with a “*dye*” configuration on high voltage transformers.

Each amplifier needs to be supplied by a dual DC voltage, that is provided by a 50[Hz] industrial transformer and a rectifier bridge with some capacitors banks to flatten the voltage ripple. The 50[Hz] transformers were down-rated in power respect the amplifier in order to protect the MOSFETs. At the exit of the power amplification system, a triphasic system with frequencies ranging from 3[kHz] to 14[kHz], and a maximum rated voltage of $\pm 90[V]$ can be obtained.

The required kilovolt voltage range was then obtained by means of an high

voltage ferrite transformer. It has been realized an array of three monophase dedicated transformers, connected together in “*dye*” configuration in the high voltage side. This reference voltage has been connected to the bottom electrodes comb, while the three others transformer electrodes have been connected to the upper face of the plasma panel.

In all conditions, the plasma panel was voltage driven. This has been done to compensate plasma load variations during thermal transients.

The plasma panel has been placed in the test section of an open circuit blowing wind tunnel (figure 8.1.6). A 1.8[kW] centrifugal blower, driven by a PWM inverter, accelerates the flow to a speed between 0 and 20[m/s].

Several screens in the settling chamber have been used. However the flow is not completely uniform across the 120×140 [mm²] test section. The shape of the boundary layer is slightly affected by the flow non-uniformity.

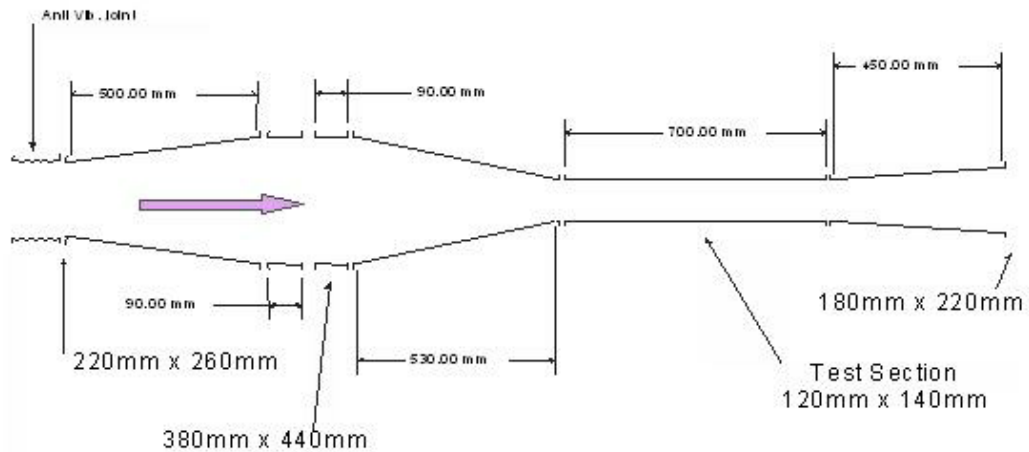


Figure 8.1.6: Scheme and quotation of the wind tunnel used for the 3-phase EHD experiments.

Four fluid dynamic conditions corresponding to four free stream velocities have been used (table 8.1.1).

The aim of the experiment has been to evaluate the influence of different supply conditions on the induced flow. In particular both voltage and supply frequency have been varied. Moreover also the influence of the different

<i>Measured stream Velocity</i> [m/s]	<i>Reynold Number</i> (Laminar)	<i>Boundary Layer Thickness</i> [mm]
1.001	$1.21 \cdot 10^4$	8.177
4.884	$5.86 \cdot 10^4$	3.718
11.29	$1.35 \cdot 10^5$	2.445
19.46	$1.24 \cdot 10^6$	1.854

Table 8.1.1: Wind tunnel working conditions

tangential field presents between phase and the following one has been considered.

For this reason two different phase configurations have been tested.

One is with the phases in the *RST* sequence, the other with a phase transposition resulting in a *SRT* sequence.

A more exhaustive discussion will be done in Section 8.3 “Interpretation of the results”.

8.2 Diagnostic setup

The evaluation of the induced thrust and the comparison between the different electrical supply configurations, have been evaluated using electrical, fluid-dynamical and optical measurements.

Electrical setup

For each phase, the voltage and current delivered to the actuator have been measured, the first, by means of a *Tektronix P6015A* capacitive compensated high voltage probe positioned between the HV terminals of the ferrite transformer and the ground electrode, the second by means of a *Stangenes Industries Current Transformer 2-0.1W* and a shunt resistor of 1Ω positioned on each phase.

These measurements allow to the determination of the instantaneous power delivered to the DBD actuator.

Fluid-dynamic setup

The free stream velocities and the ones modified by the presence of the plasma actuator have been appraised by a Pitot probe realized by means of a small insulating glass tube, with an outer diameter equal to $1.2[mm]$ and an internal one of $0.3[mm]$.

The tube has been connected to a *DCAL401GN* analogical differential ultra low pressure sensor characterized by response time of $0.5[ms]$ and a sensitivity of $4.076[mV/Pa]$.

It has been chosen to probe the air velocity field at the closest vertical position to the panel (zero high) and $5[mm]$ after the last electrodes couple, where the plasma influence is higher (figure 8.2.1).

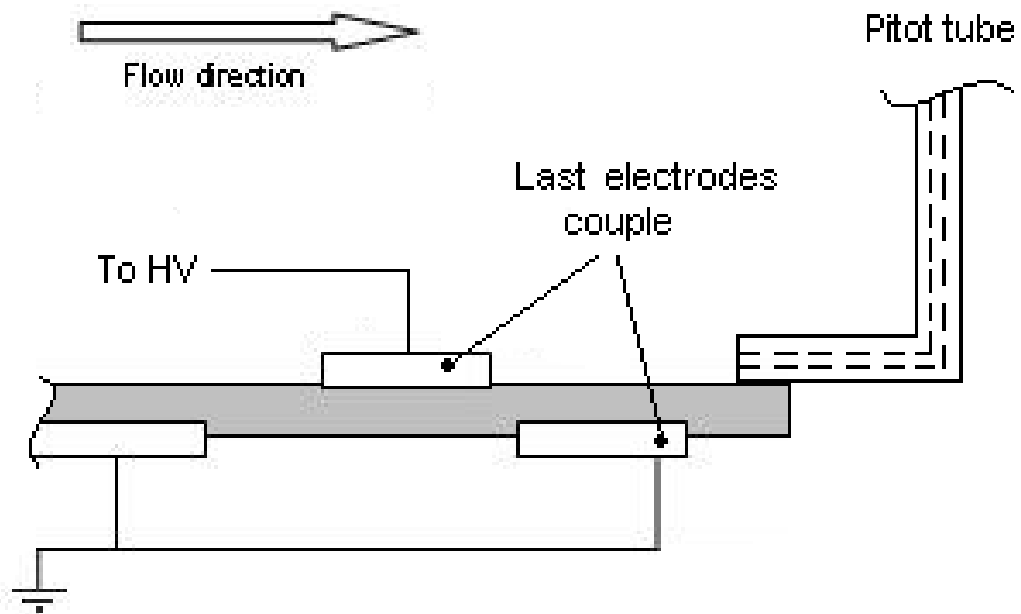


Figure 8.2.1: Pitot tube position in the three phase EHD setup.

The Pitot tube influence in the plasma behaviour has been verified both by eyes, in the plasma extension and homogeneity, and by electrical measure-

ments of the power delivered to the actuator. With and without the Pitot tube, the overall behaviour of the actuator has been the same (within the measurement errors).

Spectroscopic setup

The spectra emitted by the plasma has been detected in order to determine the rotational and the vibrational temperatures of the plasm itself.

The light has been collected by means of a collimating lens positioned over a region of plasma formation, and so correspondingly over a grounded electrode (figure 8.2.2). The lens has a focal ratio equal to $f4$, with a focal length in the order of $40[mm]$.

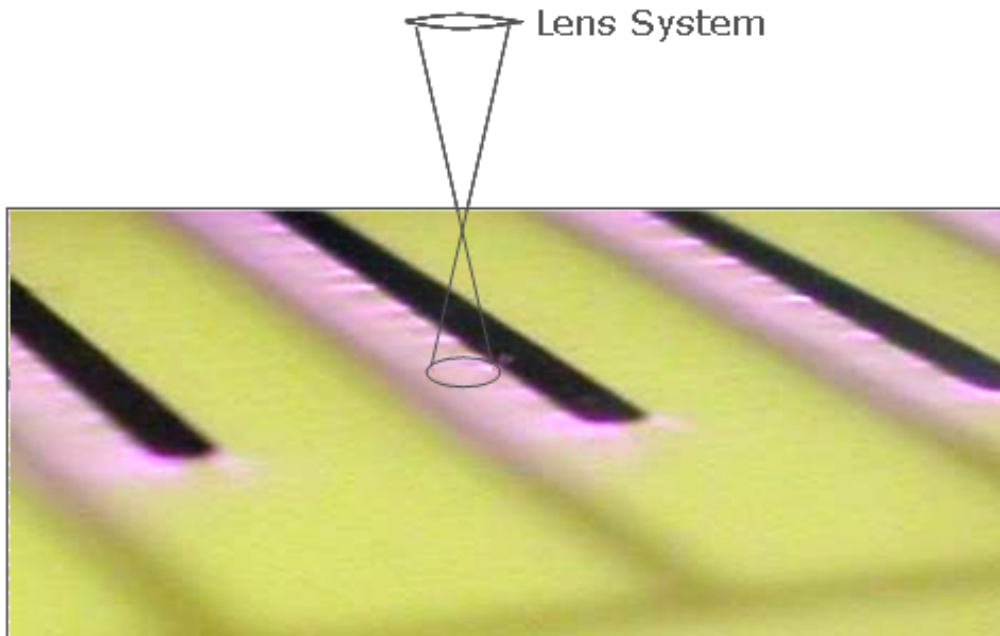


Figure 8.2.2: Position of the lens over the plasm.

The signal, trough out a $600[\mu m]$ fiber optic, has been delivered to the entrance of the spectrograph.

The spectrograph was a *Jobin-Yvon HR-460* monochromator, with a focal

length of 460[mm] and a focal ratio of $f5.3$.

The monochromator's exit was coupled with a fast shutter PCO CCD camera, with a SVGA resolution and a pixel size of $6 \times 6[\mu m]$. The peak quantum efficiency of this camera is in the order of 55% at 380[nm]. The grating used was a JY holographic with 1200[lines/mm], in order to collect a wider spectral window. The entrance slit was settled at an intermediate position of 0.1[mm]: this allows to obtain the best union between resolution and intensity of the spectral peaks.

The spectrograph was then calibrated both with a Mercury-Argon and a Deuterium-Halogen lamps.

The monochromator, the CCD camera and all the spectral collected data, have been controlled by means of a Personal Computer.

The signal detected was not so intense so the CCD camera has been set at the maximum exposure time (10[ms]) and several spectra have been acquired and averaged at each condition, in order to gain a better signal to noise ratio.

All the electrical and fluid-dynamic measurements have been checked and stored by means of a *DL-1740* and *DL-1640* 200MS/s Yokogawa scopes.

The whole scheme of the actuator panel, supply system and the diagnostic apparatus is sketched in figure 8.2.3.

8.3 Interpretation of the results

Flow velocity measurements

In order to gain information on the plasma properties and its influence on the boundary layer, different power supplying conditions have been considered. As it is possible to see in table 8.3.1, two voltage levels and seven frequency conditions have been chosen. Furthermore, as introduced before, also two different electrodes connections have been realized.

In the first one, named *123*, the triphasic system generates a phase to phase

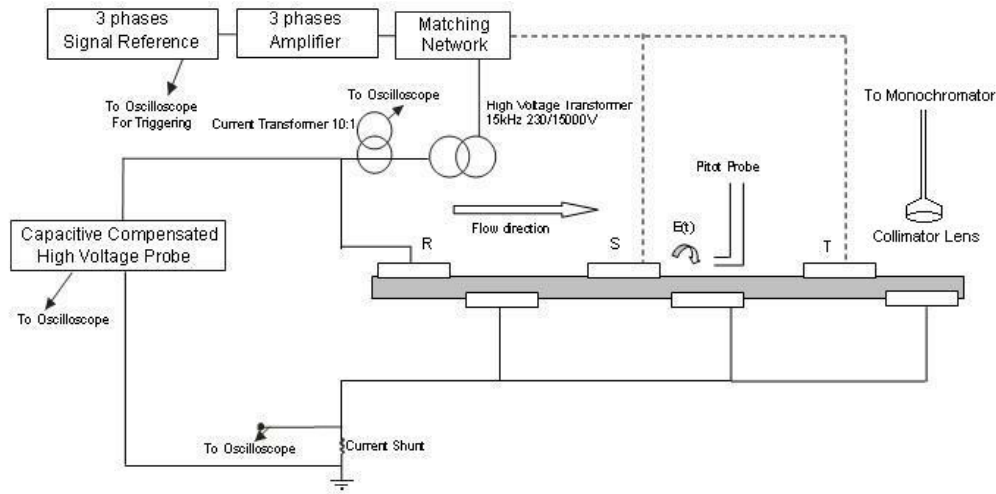


Figure 8.2.3: Plasma Panel Experimental set-up. For phases S and T there is the same probe set-up as for phase R .

E-field wave that force the ions moving upstream respect the external air field. In the second one, two phases have been transposed (named 213): with this expedient the traveling wave reverses its polarity and ions are forced downstream.

	123 <i>Electrode Configuration</i>	213 <i>Electrode Configuration</i>
5 [kV]	From $4kHz$ to $10kHz$ with $2kHz$ steps	From $4kHz$ to $10kHz$ with $2kHz$ steps
6 [kV]	From $4kHz$ to $10kHz$ with $2kHz$ steps	From $4kHz$ to $10kHz$ with $2kHz$ steps

Table 8.3.1: EHD 3-phase experiment: power supply conditions.

For first instance let's consider the induced flow by means of the plasma actuator.

In figure 8.3.1 the induced velocities at different electrical supply conditions and different free stream velocities are showed.

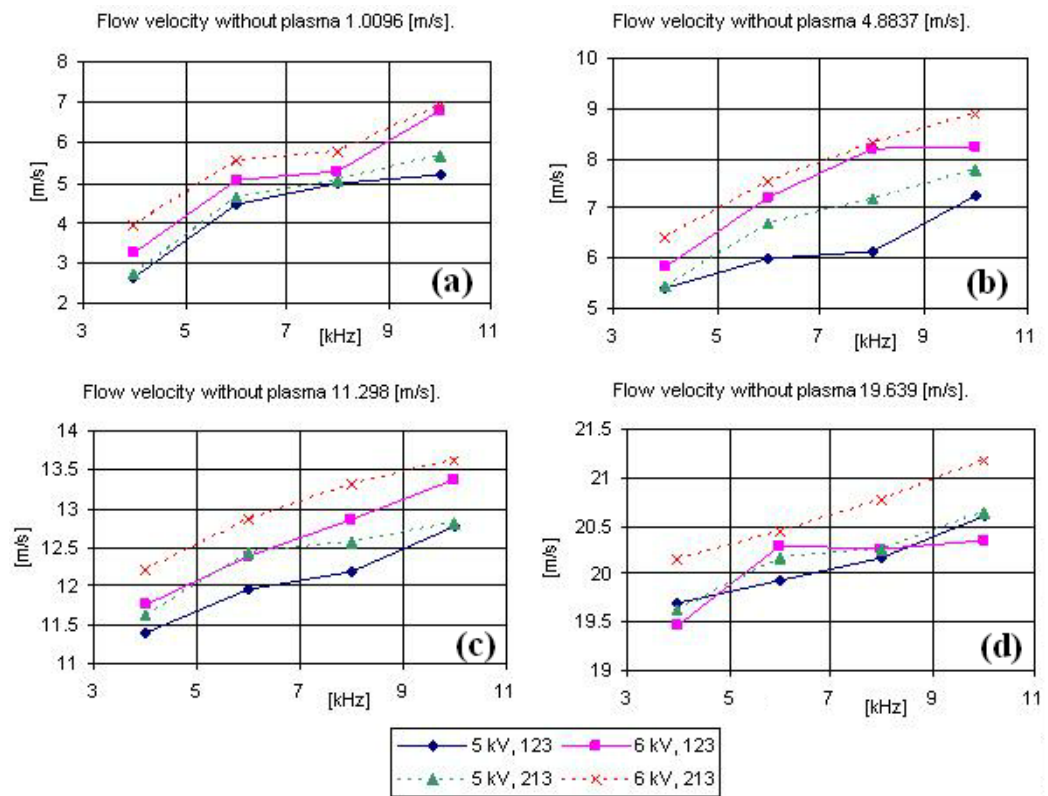


Figure 8.3.1: Induced flow velocities at different frequencies and for the four wind tunnel conditions: 1[m/s] (a), 4[m/s] (b), 11[m/s] (c), 20[m/s] (d).

The higher is the power supplying frequency or the applied voltage, the stronger is the effect on the momentum given to the fluid. At higher frequencies or voltages, the electron number density and the net charge accumulation in the sheath and in the insulating material are larger than those obtained at lower ones: consequentially the electrical fields close to the panel surface are stronger, and this leads to an higher effect on the fluid.

The EHD effect has showed to be much more efficient when the external air field is slower. When the free stream velocity is around $1[m/s]$ (figure 8.3.1-a), the plasma is able to accelerate the fluid up to $6[m/s]$ with a net speed gain on the order of $5[m/s]$. On the contrary, at the higher stream velocity tested in the wind tunnel, EHD effect can give only $1[m/s]$ to the fluid in this more energetic condition, as it is possible to see in figure 8.3.1-d.

This behaviour has been experienced also on a monophasic plasma panel [18], and has been explained by means of a plasma volume contraction caused by the external airfield, as Schlieren photographs in figure 8.3.2 confirmed. In the case of still air, the plasma thickness is on the order of $100[\mu m]$, on the contrary in presence of an external fluid velocity of $16[m/s]$, its thickness is visibly diminished.

The influence of the phase to phase electric field polarity is also evident. At all the frequencies-voltage conditions and external air fields a remarkable difference between the two different connections can be found. The *213* configuration, that accelerates ions downstream, has been showed to be more efficient in giving momentum to the fluid rather than the *123* connection, as expected.

From the electrical measurements, it is possible to obtain the classical Voltage-Current vs time characteristic (figure 8.3.3).

As previous described, the plasma is present as succession of streamers and exists only in almost two quarter of the sine period.

The measurements of voltages and currents, allow to the determinations of active and reactive power absorbed by the actuator during a period.

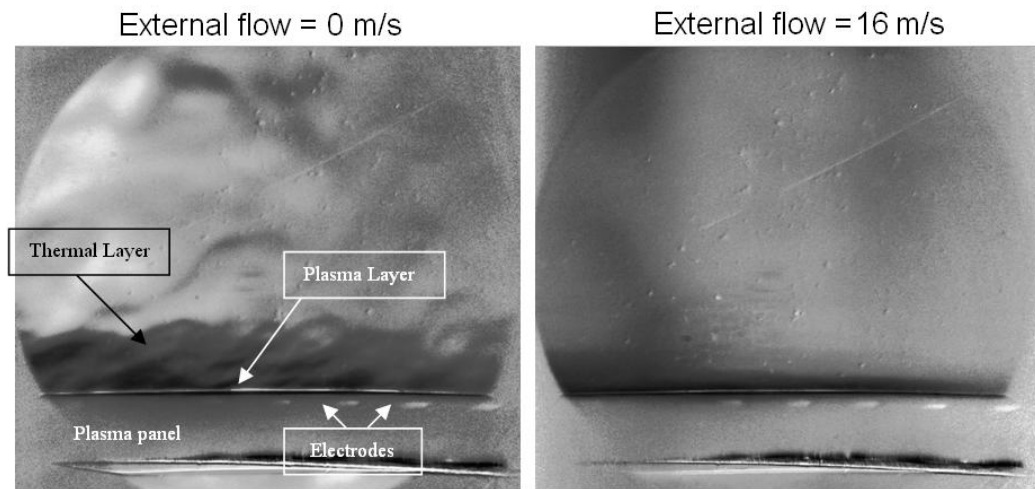


Figure 8.3.2: Schlieren image close to the actuator surface with a supply voltage equal to $5[kVp]$ and frequency of $9[kHz]$: left-hand side the external flow velocity is of $0[m/s]$, in the right-hand one is $16[m/s]$.

Plasma absorbed active power has been showed to be a function both on voltage and supplying frequency, as it is possible to see in figure 8.3.4.

Total reactive power exchanged by the plasma panel load showed the same behaviour. The $\cos \varphi$ has been measured to lie between a value of 0.04 and 0.1, depending on frequency and applied voltage.

Absorbed active power has not showed to depend on external flow: for all the wind tunnel free stream velocity conditions the active power variation lie inside instrumental measuring tolerance.

On the contrary, it has to be pointed out that the active power is a function of the electrodes connection order: at an higher momentum delivered to the fluid corresponds an higher active power absorbed by the plasma.

From the velocity and absorbed active power measurements it has been noticed that a polyphase system with a proper electrodes connection scheme acts more efficiently respect than a monophasic. The explanation of this phenomenon can be searched into the phase to phase electric field, that pushes

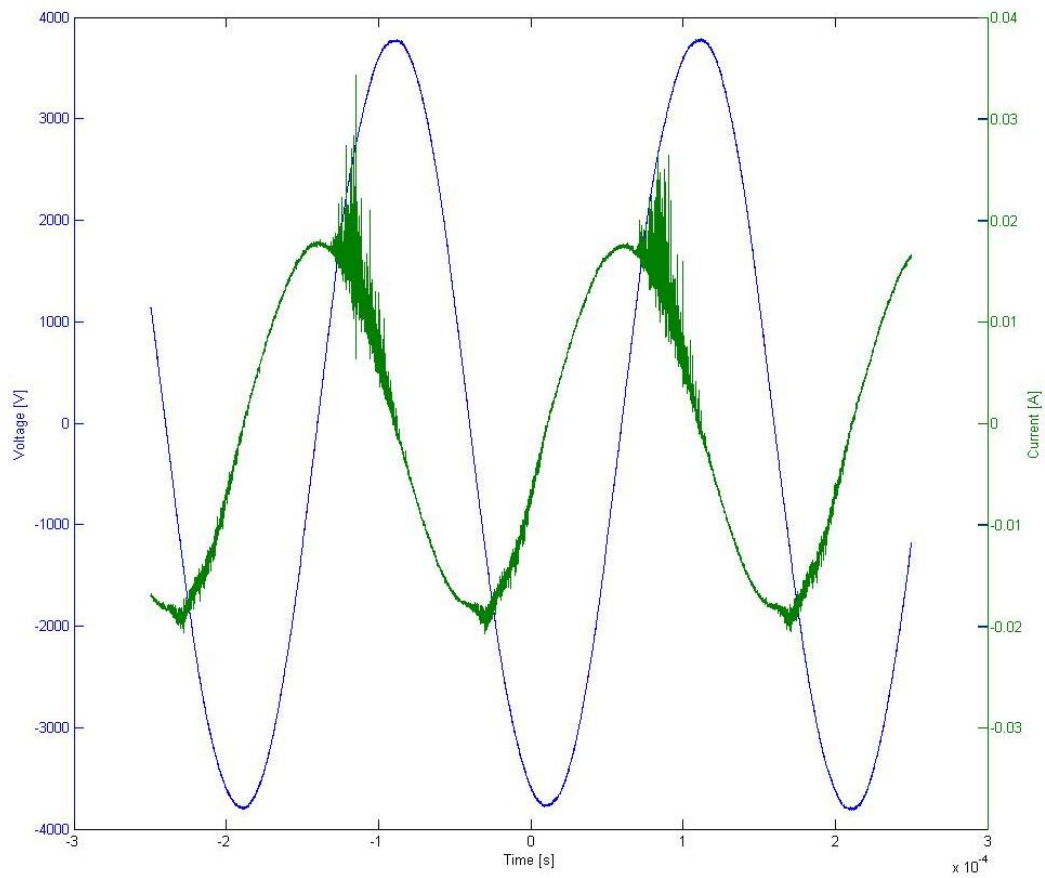


Figure 8.3.3: Voltage and current vs. time characteristic of one phase of the asymmetric 3-phase DBD actuator.

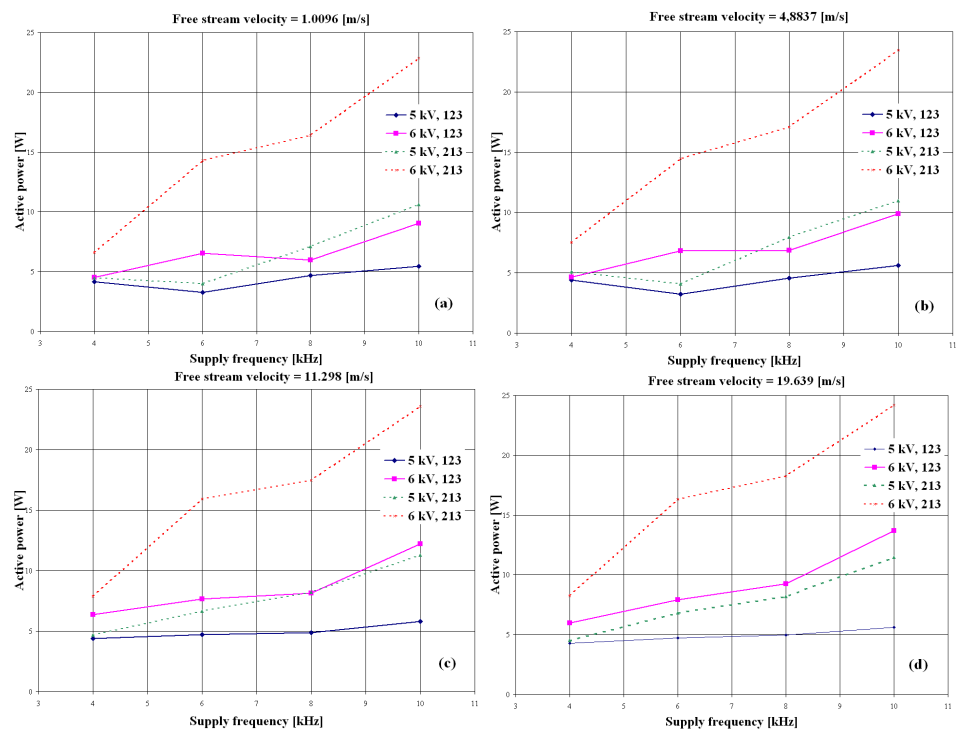


Figure 8.3.4: Active power at different supply frequencies and for the four wind tunnel conditions: 1[m/s] (a), 4[m/s] (b), 11[m/s] (c), 20[m/s] (d).

more ions.

Plasma formation period occurs only when the module of the electrical field is rising; moreover, the plasma panel design is asymmetric, and the discharge can be produced only downstream the edge of the electrodes.

As it can be seen from figure 8.3.5, for each electrodes pair of every phase, plasma is present only for a certain amount of time.

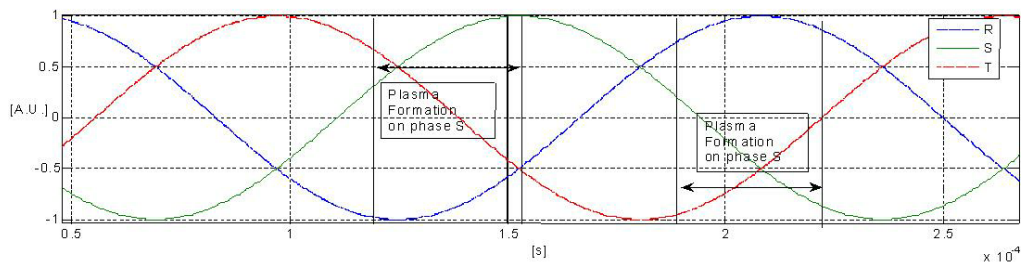


Figure 8.3.5: Three phases supply voltage. Periods in which the plasma is formed for the phase *S* are emphasized.

By means of the two phases connections, it has been possible to set the system in such a way that downstream to the electrode related to phase *S*, both an electrode referred to phase *T* (*123* configuration) or *R* (*213* configuration) can be connected. It is easy to see from figure 8.3.5 that the average phase to phase electric field during the plasma formation period is far higher in the second case rather than in the first one.

In order to visualize this phase to phase effect, a numerical analysis of the electrical field on the plasma panel has been performed.

A numerical code based on an electrostatic finite element method has been used. As it appears in figure 8.3.6, the influence of the plasma bulk and sheaths on the electric field has been neglected. The numerical simulations show that iso-potential lines are different when subsequent electrodes are or are not at the same potential.

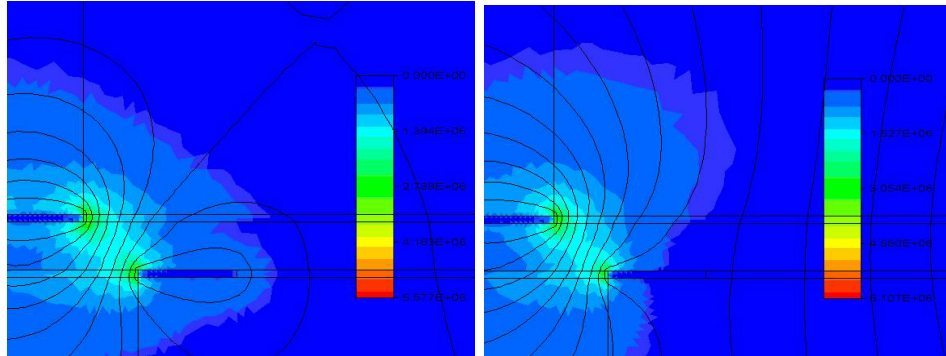


Figure 8.3.6: FEM simulation of two different supply conditions for the *RST* phases. In the left-hand side $R = -[6kV]$, $S = [3kV]$ and $T = [3kV]$, in the right one $R = [3kV]$, $S = [3kV]$ and $T = -[6kV]$. E-field and iso-potential line are showed.

Temperature measurements

The spectra emitted by the plasma has been used to determine the vibrational and rotational temperatures of the plasma itself.

These measurements allow to the determination of the thermal condition of the plasma.

As it is shown in figure 8.3.7, the emission spectrum is dominated by the molecular bands of N_2 , and by some weak molecular bands of N_2^+ . This spectra has been taken by means of a low resolution *Avantes* spectrometer and is not suitable for rigorous temperature measurements.

All the spectra useful for temperature determination have been detected by means of the Jobin-Yvon monochromator.

As explained in Chapter 3, the intensity of the line peaks are useful (under the assumption of a Boltzmann distributions of the levels) for the creation of the so called Boltzmann plot and the determination of the associated temperature.

The vibrational temperature has been estimated by means of the Boltzmann plot of the $\Delta\nu - 2$ sequence of the Second Positive Band of N_2 ($N_2 C^3\Pi_u \rightarrow$

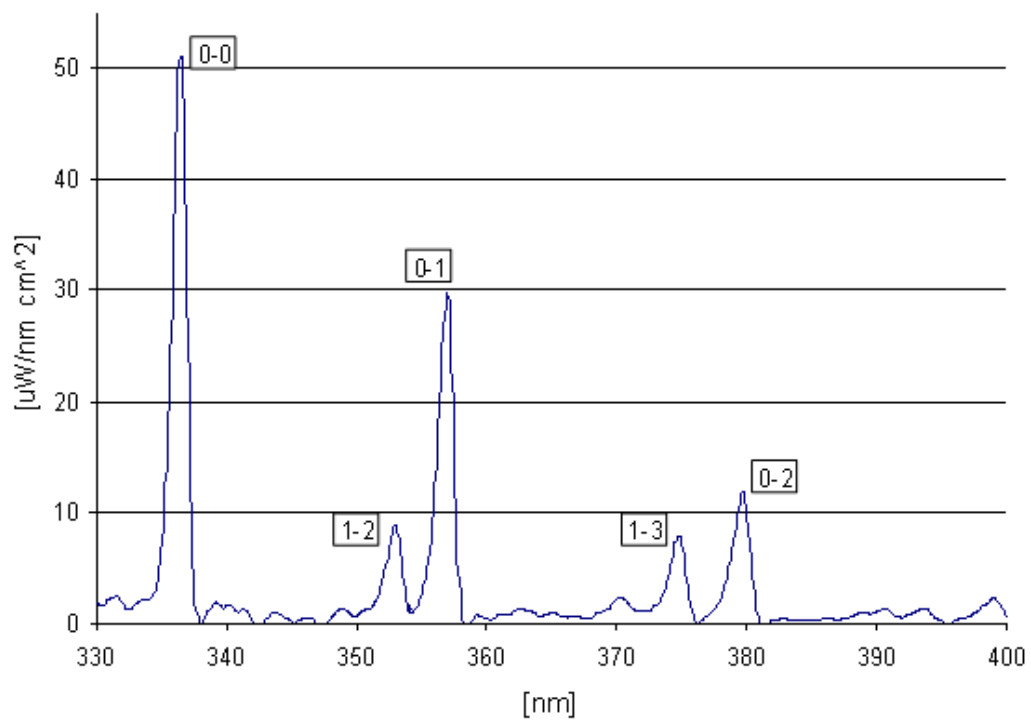


Figure 8.3.7: Low resolution spectra of the Second Positive System of the N_2 molecule ($C^3\Pi_u \rightarrow B^3\Pi_g$).

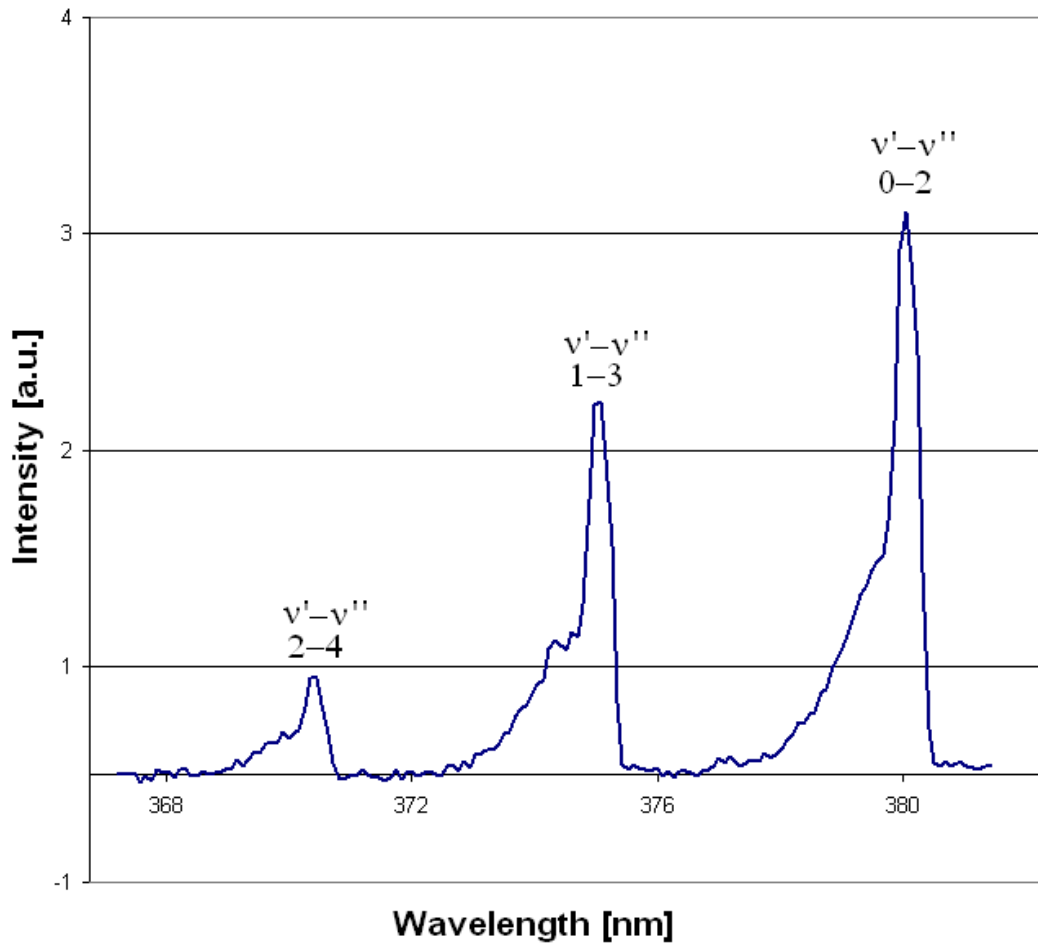


Figure 8.3.8: Spectra of the $\Delta\nu - 2$ sequence of the Second Positive System of N_2 molecule ($C^3\Pi_u \rightarrow B^3\Pi_g$).

$B^3\Pi_g$) [58] in the range $365 \div 382$ [nm] (figure 8.3.8). The three band-head peaks are positioned at 371.06 [nm], 375.55 [nm] and 380.49 [nm].

The relative Boltzmann plot is showed in figure 8.3.9. The alignment of the points is pretty good indicating that the plasma is not far from a pLTE condition.

The graphics in figure 8.3.10 show that the vibrational temperature increases with descending the power supply frequency.

The relation between the vibrational temperature and the electron-heavy

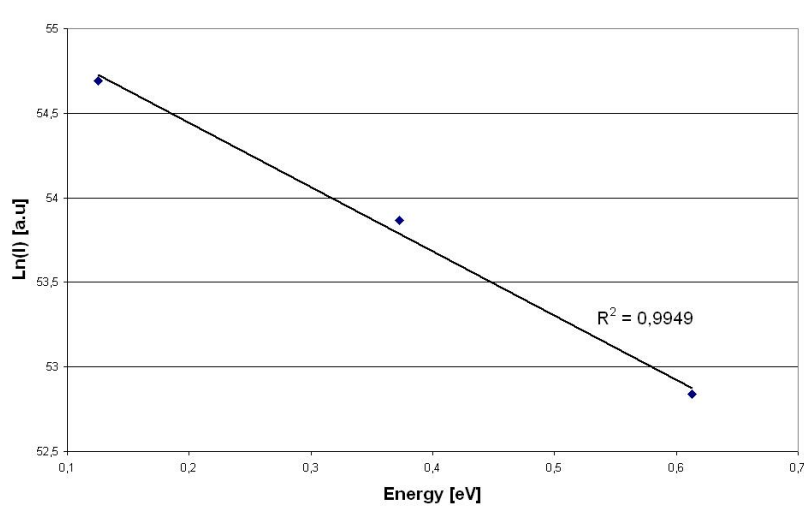


Figure 8.3.9: Example of Boltzmann plot of $\Delta\nu-2$ sequence of the Second Positive Band of N_2 ($N_2 C^3\Pi_u \rightarrow B^3\Pi_g$).

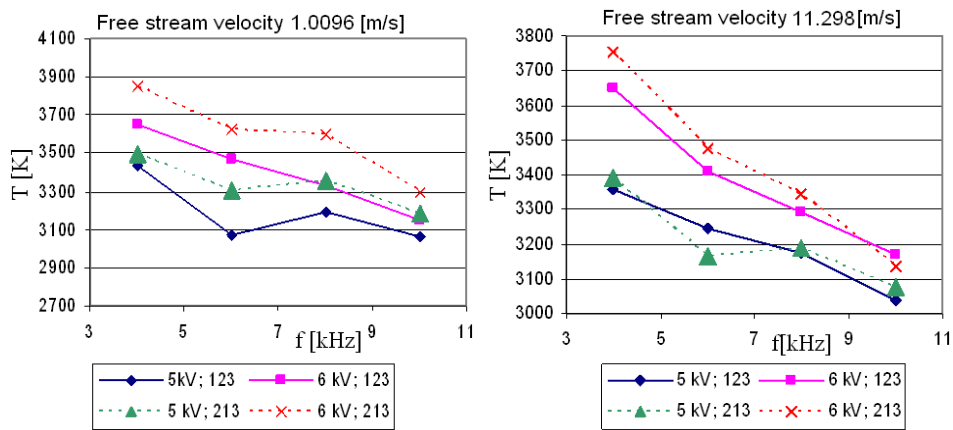


Figure 8.3.10: Vibrational temperature as a function of power supplying frequency and voltage with 1[m/s] and 11[m/s] free stream velocities.

collisional processes can explain this effect. The observed phenomenon seems to be due to a reduction of the electron-ion collision rate as the frequency increases. At low frequencies, the electron oscillation length and the energy delivered to the electrons, due to the applied electric field, are relatively high. Thus the collisional processes between electrons and heavy particles are more frequent. This results in a relatively highly energetic excitation of vibrational modes and consequently, in an high vibrational temperature [59].

Vibrational temperature is also a function on applied voltage. Also this effect can be explained by the straight relation between the vibrational temperature and the collisional processes heavy particles-electrons. Electron number density and electron energy increase when the voltage grows.

Vibrational temperatures have showed to be slightly higher with a *213* electrodes configuration respect than the *123*. This fact could be explained because of the phase to phase superimposed field that rises the overall value of the electric field during the plasma formation period and heats consequentially the electrons.

The dependence of the vibrational temperature on the external flow velocity is currently under investigation. The variations that have been measured are on the order of magnitude of the measuring tolerance: for this reason more precise experiments are needed.

The rotational temperature has also been evaluated. The spectral resolution of the spectrograph has not showed to be sufficient to completely resolve the rotational spectrum. Consequently, rotational temperatures have been evaluated by means of an approximated method that considers the partially resolved First Negative System of N_2^+ ($B^2\Sigma_u^+ - X^2\Sigma_g^+$) [12] with bandhead peak at $391.4[nm]$ (figure 8.3.11).

The rotational temperature has been evaluated only at a voltage of $6[kV]$, because the light emission from the plasma at $5[kV]$ has been showed being too much weak.

The rotational temperature as a function of the flow velocity at different

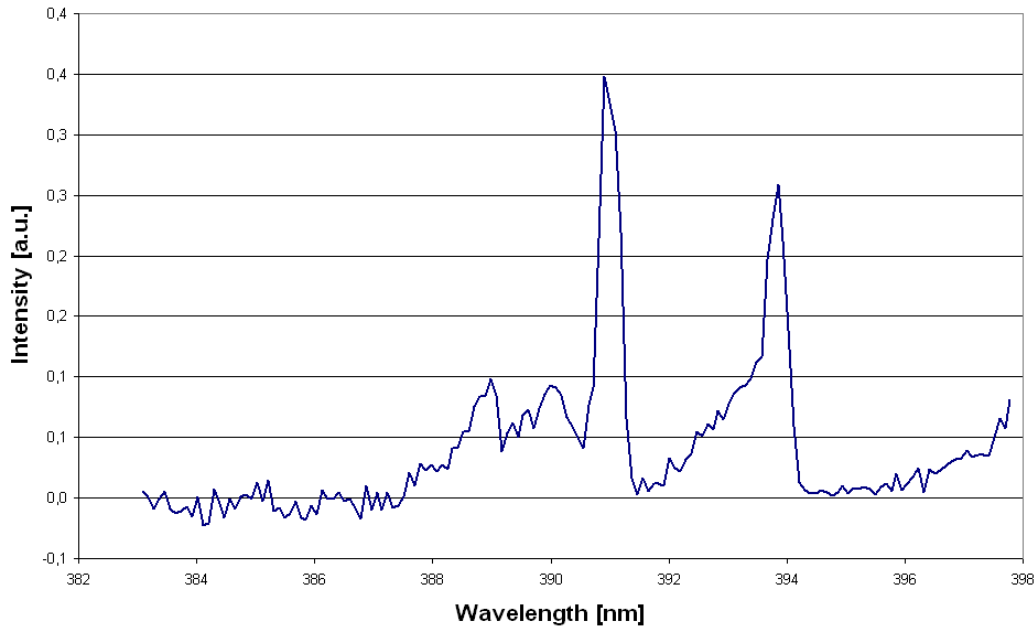


Figure 8.3.11: Partially resolved First Negative System of N_2^+ ($B^2\Sigma_u^+ - X^2\Sigma_g^+$).

frequencies is shown in figure 8.3.12.

The rotational temperature is strongly related to the gas temperature. A dependence of the rotational temperature in function of the supply frequency is expected as the active power dissipated in the plasma is, as seen before, function of the frequency. When the power injected into the plasma increases, the temperature increases also.

It could be expected that, with an increase of the external air field velocity, the rotational temperature decreases as the plasma is cooled by the flow.

The measurements of figure 8.3.12 shows an opposite behaviour.

This phenomenon has been already explained because the plasma volume is reduced by increasing the externally applied airflow speed [59].

The plasma optical depth is comparable to the plasma characteristic dimension Without external flow, the plasma volume is larger and the gradient of the temperature is lower. The temperature measured is strongly determined by the external layers of the plasma, where it is colder than in the core.

When external flows attain higher speeds, the plasma volume contracts and

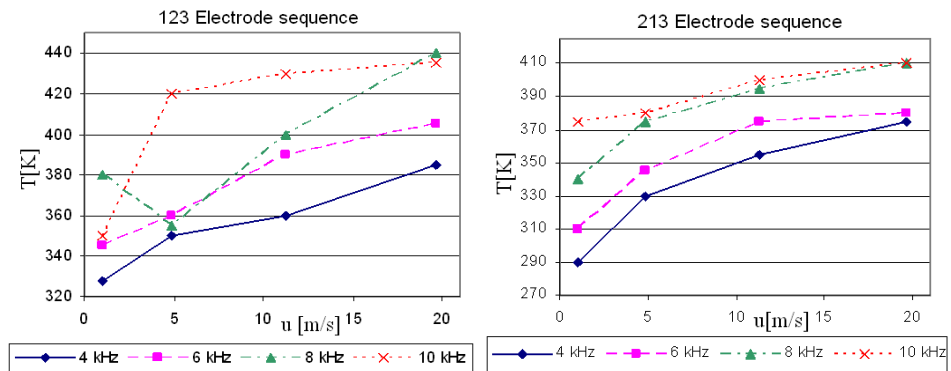


Figure 8.3.12: Rotational temperature as a function of the airflow velocity at different supplying frequencies with the two different electrodes configuration.

the temperature gradient is steeper. In this case the light recorded is emitted by the core of the plasma where the temperature is higher.

Rotational temperature seems not to be affected by the electrode phase order. This behaviour needs further investigations.

Chapter 9

Nanopulses driving system for a DBD actuator

All the data presented in this section are propriety of the Mechanical and Aerospace Department of the Princeton University (NJ).

9.1 Nanopulses DBD actuator setup

One of the most important features concerning the EHD phenomenon, is the supply waveform.

Nowadays almost all the works on this subject have dealt with sine (pretty easy to obtain) or triangular waveforms.

In this way, the plasma is generated when the needful breakdown voltage is achieved and the formed ions are pushed away by means of the same applied voltage.

Recent numerical studies, with a detailed model based on full plasma kinetics coupled with the dynamics of the electric field developed by Likhanskii *et al.* [42, 60], provided consistent physical explanations for the observed phenomenon and suggested ways for improvement of actuator performances.

Specifically, for a single DBD actuator, it was shown that a waveform consisting by the repetition of high-voltage nanosecond pulses has the potential

to produce a stronger effect on the flow than a conventional sinusoidal voltage. Additionally, it was predicted that adding a positive bias voltage to the pulses should increase the velocity of the induced wall jet.

The basic principle of this voltage performance is the creation of an ionization wave during the short pulse.

When a negative pulse is applied, the electrons are created near the edge of the top electrode due to the high electric field in this region, then they move along the electric field lines, ionizing the gas, and finally they attach to the dielectric surface, creating a virtual cathode.

Since a large number of electrons are attached to the dielectric surface and the pulse time is too short to make positive ions move, a positive ion cloud is formed above the dielectric surface.

After the pulse, this positive cloud is pushed from the electrode toward dielectric surface by an applied positive DC bias and by the harpoon attraction of the electrons stored on the dielectric.

Another possible way of pushing gas in a DBD plasma actuator is by applying high voltage repetitive positive pulses plus a positive DC bias.

The physics of the downstream force acting on the gas, in this case, is quite different from the one with negative pulses.

When a positive nanosecond pulse is applied to the upper electrode, at some voltage the electric field near the edge of the electrode will be sufficient for the initiation of cathode directed streamer propagation. During the pulse, the streamer propagates along the dielectric until the electric field at the leading edge (head) of the streamer is not sufficient to produce further ionization in front of it. At that point the streamer stops.

From the theory of streamers and from the calculations, it is well-known that the body of the streamer is quasi-neutral, but the head of the streamer carries a positive charge in order to displace the electric potential and to produce the ionization in front of it. Therefore after the pulse there will be a positive ion cloud in the front part of the decaying streamer.

The application of a positive DC bias, after the pulse, forces this cloud to

move downstream and to push the gas.

This new kind of supply waveform (nanopulses plus DC bias) introduces big improvements in the plasma actuator.

First of all, there is the separation from the formation mechanism of the plasma, generated by means of the nanopulses, and the push of the ions due to the bias.

Furthermore, the nanosecond pulses are the best choice in terms of ionization efficiency and they allow to a complete control on the plasma formation in compare with a conventional sinusoidal system in which the plasma creation is subjected to the air conditions (i.e. temperature, humidity and pressure). High efficiency and more degrees of freedom are so the key points of this new kind of DBD supply system.

The purpose of the experiments was to provide a better understanding of the physical processes involved in the induced flow generated by a DBD actuator driven by this nanopulses supply system. Moreover comparison between experimental and numerical results have been done.

All the experiments have been led with a single dielectric barrier discharge actuator sketched in figure 9.1.1.

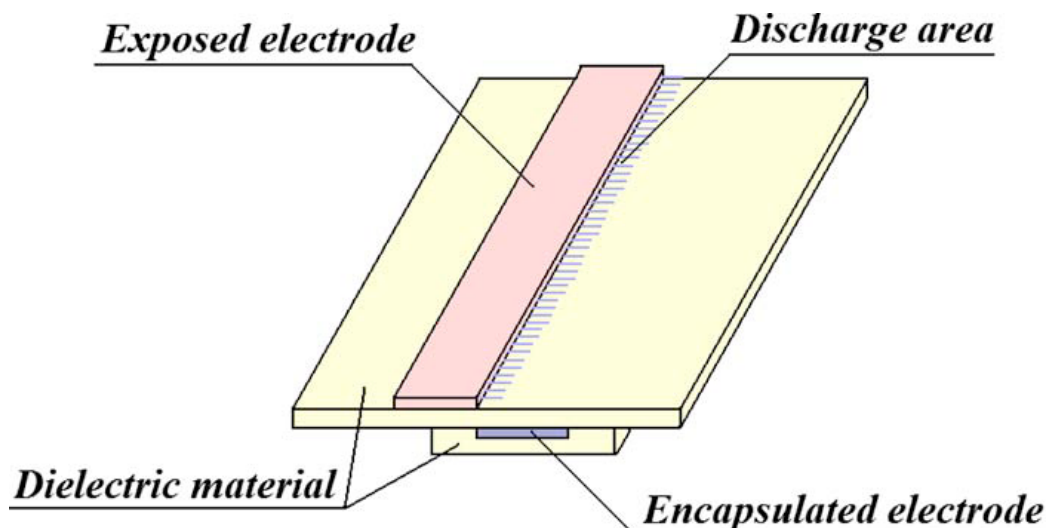


Figure 9.1.1: Scheme of the single dielectric barrier discharge actuator.

The plasma actuator consisted of two electrodes placed asymmetrically on either side of the dielectric, with one electrode encapsulated, and the other exposed to the atmospheric air. The electrodes were made of copper foil. The width of the electrodes was equal to 25[mm] and their spanwise dimension was 50[mm]. No gap between the electrodes was present. A 100[μ m] thick kapton tape was used as dielectric.

The discharge was ignited by applying high voltage to one of the electrodes. The other electrode was grounded. A photo of the DBD actuator on is reported in figure 9.1.2.

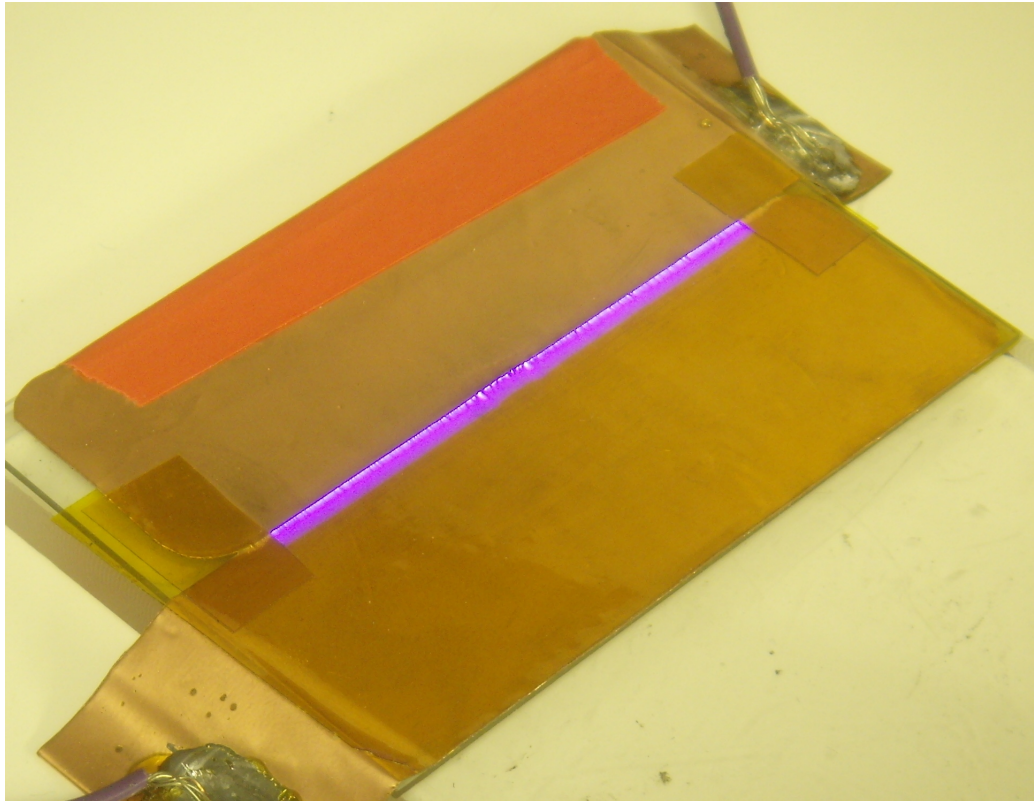


Figure 9.1.2: Photo of the DBD actuator on.

The actuator was placed inside a sealed cylindrical aluminum chamber (45[cm] high and 40[cm] in diameter) to eliminate the interaction between the plasma induced flow (~ 1 [m/s]) and air in the room and to enable ex-

periments at different pressures and with different gases.

In all the experiments, we used a voltage waveform consisting of repetitive nanosecond pulses in burst mode superimposed on a bias voltage. Although during the experiments the bias voltage waveform evolved from constant to sinusoidal [61].

The basic electric scheme of the supply setup is reported in figure 9.1.3.

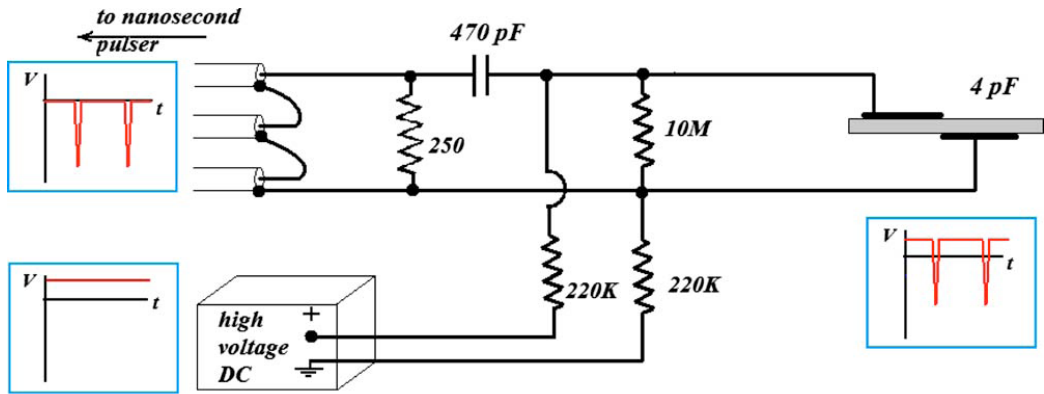


Figure 9.1.3: Electrical scheme of the nanopulses driven DBD actuator. The circuit is designed so as to combine short pulses with a low frequency bias voltage without interferences between the pulser and the low frequency power supply. In experiments with sinusoidal bias, the DC power supply was replaced by an high-voltage transformer.

The circuit is designed in order to superimpose short pulses on a constant or low frequency bias voltage without interference between the pulser and the low frequency power supply.

The addition of a $470[pF]$ capacitor in series with the actuator, shielded the pulser from the bias voltage. Since the capacitance of the actuator was only $4[pF]$, the main voltage drop occurred just on the plasma actuator.

The $220[k\Omega]$ resistor did not let the pulse go to the low frequency power supply. The charging time for the capacitor through the corresponding resistor was $\tau = RC = 220[k\Omega] 470[pF] \approx 100[\mu s]$, which corresponds to $10[kHz] \gg 60[Hz]$.

The $10[M\Omega]$ resistor was put in parallel with the actuator for safety rea-

sons. It discharged the high-voltage electrode after experiments. Its high impedance did not influence the circuit in any way.

Also, a noninductive $250[\Omega]$ resistor was added in parallel with the actuator to minimize the pulse reflection.

The pulser used in the experiments was a *FID Technology 4[ns]* full width at half maximum (FWHM) pulser capable of running with pulse repetition rate (PRR) up to $100[kHz]$, and triggered by a $\approx 10[V]$ pulse from a *Stanford Box*.

The peak output voltage of the pulser was up to $10[kV]$ which was fed to three separate $3[m]$ long $75[\Omega]$ coaxial lines.

The three copropagating pulses were converted into a single pulse by taking advantage of the short physical “length” of the pulses (less than $1[m]$). By connecting the center conductor of the first coaxial line to the outer conductor of the second and the center conductor of the second to the outer conductor of the third, an amplified pulse is produced between the center conductor of the third line and the outer conductor of the first one. This is essentially a transformer made of sections of transmission lines, and it is well described in the literature [62].

As source of constant bias voltage we used an *High Voltage DC Supply model 412 by John Fluke MFG Co, Inc.*, capable of producing output voltages up to $2[kV]$ both polarities.

The development of the experiments led us to switch from DC bias into alternative bias. The first step has been the passage to an AC $60[Hz]$ high voltage sine waveform supplied by a transformer directly connected to the net.

The encouraging results that we obtained induced us to the choice of a *Trek model 20/20C HV Amplifier* driven by a *Tenma 72-7210* function generator ables to produce sine, rectangular, triangular, positive and negative sawtooth waveform.

By now we will refer almost only to the DC bias case because it was introduced as first. During the exposition of the work, all the supply conditions

will be exhaustively explained.

Lets start now to describe the possible supply conditions with the nanopulse generator plus the DC bias.

The pulser was able to produce pulses of negative polarity only. The terminology used in this work came from the numerical simulations, where the encapsulated electrode was supposed grounded, and the voltage waveform was applied to the exposed electrode.

Following the same terminology, we consider the encapsulated electrode to be at zero potential.

That means that the term “positive” refers to a case in which the electric field is directed from the exposed electrode to the encapsulated one.

The term “negative” is used when the field is in the opposite direction.

Thus, applying negative pulses to the lower (encapsulated) electrode we will refer to a positive pulse.

Further, applying negative bias voltage to the top (exposed) electrode will be called a negative bias, whereas applying negative bias voltage to the lower (encapsulated) electrode will be referred to as positive bias. See figure 9.1.4 for further examples.

One of the major troubles with a very short pulse supply system is the matching between the generator and the load. If no match impedance is realized, harmful pulses reflection can be created.

For this reason, special attention was paid to the electric pulse waveform. It was measured by a LeCroy high-voltage probe PPE6 kV (400MHz bandwidth, 50MΩ input resistance, < 6pF input capacitance) connected to a Tektronix digital oscilloscope TDS 380 (400MHz bandwidth).

Since the pulses were only several nanoseconds long, they were reflected back from the plasma actuator and then reflected again by the pulser toward the actuator. Therefore, each pulse lastly looked like a series of damped pulses.

To reduce this phenomenon, a computer code incorporating the actuators and the probes capacitances was developed. The code calculated the reflection of a pulse from a RLC load. The code was based on Kirchhoff's laws

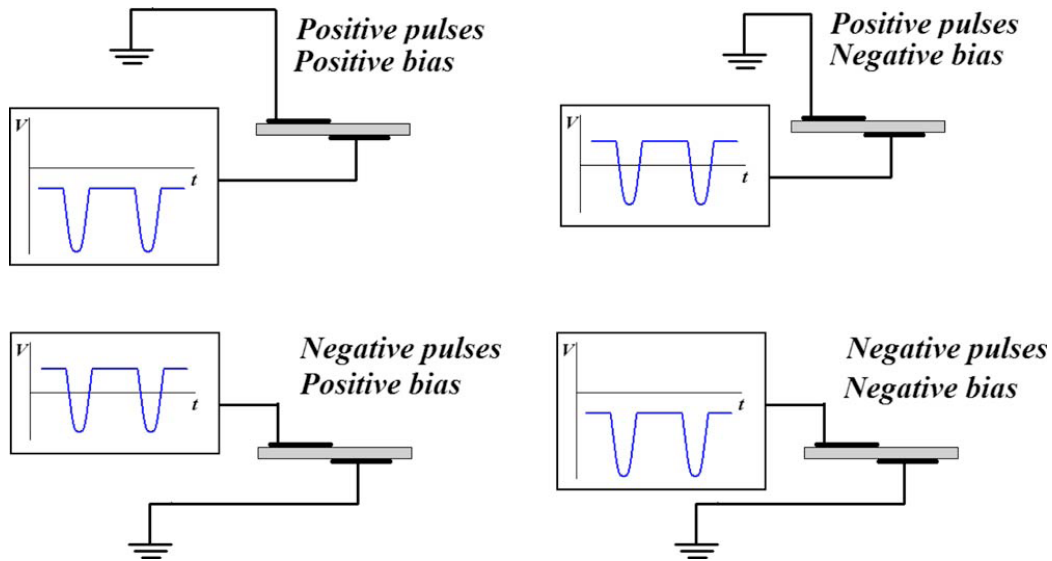


Figure 9.1.4: Terminology used in the paper for the pulse and bias voltage polarities. The encapsulated electrode is always considered to be at zero potential. The sign potential of the exposed electrode relative to the encapsulated one, determines the pulse and bias polarity.

written for an LRC load connected to a $3 \times 75[\Omega] = 225[\Omega]$ cable.

A scheme of the transformer made of sections of transmission lines connected to a RLC load is shown in figure 9.1.5.

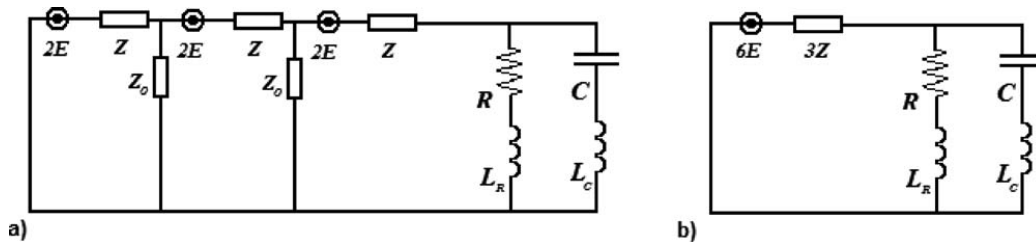


Figure 9.1.5: An equivalent scheme of the transformer made of sections of transmission lines connected to the RLC load. In the left-hand side there is the full circuit (a), in the other side there is the reduced one (b).

Z is the cable impedance, Z_0 is defined by parasitic impedances and/or impedance of cable connecting wires, C is the capacitance of the actuator and the voltage probe, R is the resistance of a noninductive matching resistor,

and L_R and L_C are the inductances of the connecting wires.

Usually, the relation $Z_0 \gg nZ$ holds (n is the number of the cables). With this assumption, it is possible to simplify the circuit in figure 9.1.5-a in the one in 9.1.5-b.

For this circuit, the following Kirchhoff's laws hold.

$$6E = 3Z_0 (I_{RL} + I_{LC}) + I_{RL}R + L_R \frac{dI_{RL}}{dt}, \quad (9.1.1)$$

$$6E = 3Z_0 (I_{RL} + I_{LC}) + V + L_C \frac{dI_{RC}}{dt}, \quad (9.1.2)$$

$$V = \frac{1}{C} \int_0^t I_{LC} d\tau. \quad (9.1.3)$$

From these equation set, we get the following set of two integrodifferential equations for the currents:

$$\frac{dI_{RL}}{dt} = \frac{1}{L_R} (6E - 3Z_0 (I_{RL} + I_{LC}) - I_{RL}R), \quad (9.1.4)$$

$$\frac{dI_{LC}}{dt} = \frac{1}{L_C} \left(6E - 3Z_0 (I_{RL} + I_{LC}) - \frac{1}{C} \int_0^t I_{LC} d\tau \right). \quad (9.1.5)$$

Solving this set of two equations using first order explicit Eulers method, we obtain the dependence of the currents on time. From that, the time-dependent voltage of the plasma actuator and of the reflected pulse can be calculated as

$$V_{Reflected} = 3Z_0 (I_{RL} + I_{LC}) - 3E \quad (9.1.6)$$

With this equation, in absence of a reactive load, it is possible to calculate the value of the resistance which enables the establishment of a regime without the presence of reflection. In our case we obtain $225[\Omega]$.

We must now consider the real experiment and regard that we must deal with connecting wires characterized by finite dimension, i.e. with related

inductances. The inductances value can be esteemed by an approximate expression, used for circular loop inductance.

$$L_{circle} \approx R\mu_0 \left[\ln \left(\frac{8R}{a} \right) - 2 \right] \quad (9.1.7)$$

where R is the radius of the loop, a is the radius of the wire and μ_0 is the permeability of the free space.

In the experiments, the wires connecting the resistance formed a loop with $\sim 1[cm]$ radius, while the wires connecting the actuator were longer and the corresponding radius was $\sim 5[cm]$.

The corresponding inductances are $L_R = 38[nH]$ and $L_C = 294[nH]$.

Substituting these numbers into the numerical code, the pulse reflection can be calculated.

Calculations showed that at these values of inductances, there is almost no difference if a $250[\Omega]$ resistor is used as the matching impedance instead of the $225[\Omega]$ one. Therefore, in the experiments, $250[\Omega]$ resistor was used due to its availability in the laboratory.

Unfortunately, the reflection of the pulse from the pulser back to the actuator could not be calculated because of the complex internal structure of the pulser itself.

Therefore, the numerical results are for single reflection only, whereas the experimental ones show all the reflections which take place between the actuator and the pulser. Note that the increase of the actuator's capacitance leads to a lower peak voltage and to an increased pulse duration.

The voltage over the actuator and the reflected pulse is shown in figure 9.1.6. By choosing the right resistance, we were able to reduce the ratio of the reflected pulse to the voltage over the actuator from 60% to 40%. The main reason for the 40% reflection is the inductance of the connecting wires. The numerical model also predicted a pulse duration increase from 4 to $\sim 5.5[ns]$ in the matched case, in compare with a doubling of the time pulse duration in the non-matched condition.

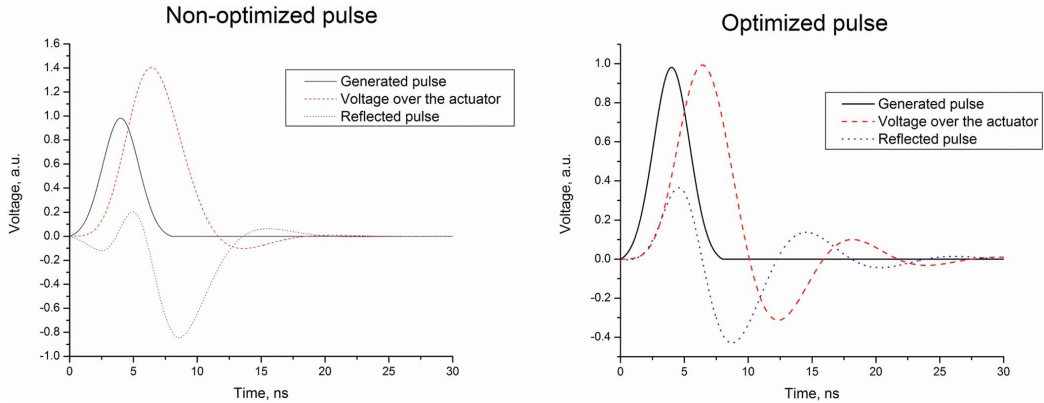


Figure 9.1.6: Numerical calculation of the nanosecond pulses. The plots show profiles of the pulse originally generated by the pulser, the voltage profile over the actuator, and the pulse reflected back into the cables. Left plot is for non-optimized load. Right plot is for optimized load with $250[\Omega]$ noninductive resistor.

These numerical results well agree with the experimental measures. In figure 9.1.7 a measure of the pulse profile before and after optimization is shown. In the matched case, the duration and the overshooting of the pulse are both reduced.

Experiments also showed that covering the exposed electrode by a kapton tape, thus preventing the discharge ignition, changed the amplitude of reflected pulse by only a few percent. Thus it was concluded that the plasma impedance plays an insignificant role in the impedance matching problem.

The aim of the experiments has been the study of the inner interaction between plasma and boundary layer, trying to understand the complex physics phenomenon that are at the basis of the EHD interaction. These evaluations has been done by means of a photograph Schlieren technique able to visualize the hot wall jet generated by the DBD plasma actuator.

The results of the Schlieren photographs lead us to surface charge measurements and to the realization of a modified DBD actuator [63].

Moreover measurements of the induced thrust have been performed in order to compare different supply conditions.

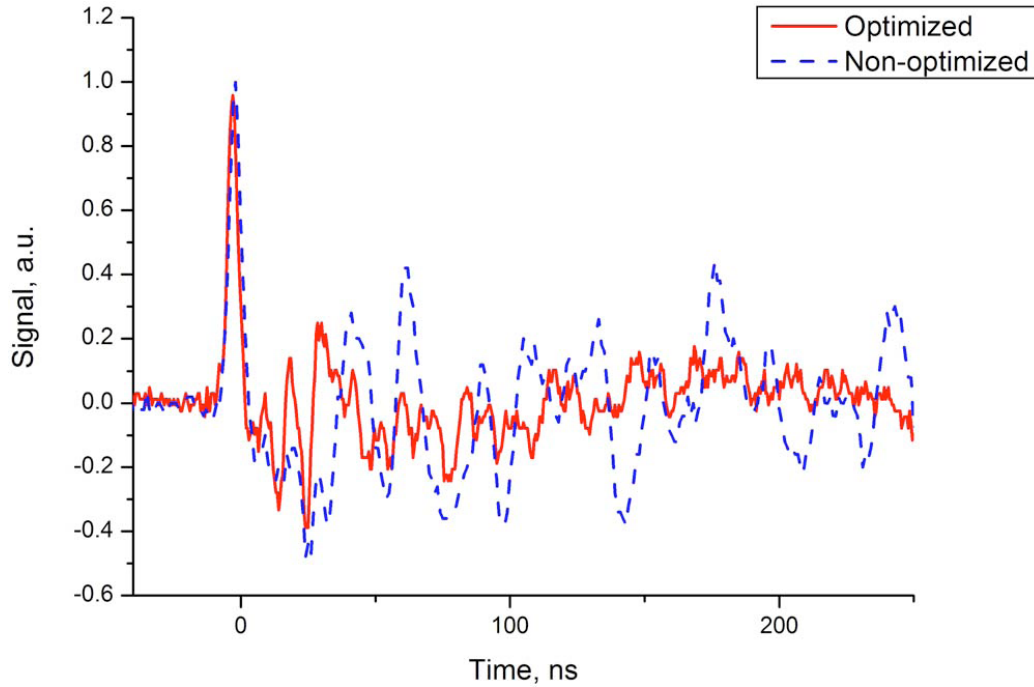


Figure 9.1.7: The measured pulse profile before and after optimization.

9.2 Diagnostic setup

The major purposes of this work are the evaluation of the shape and the velocity of the induced flow paying particular attention to the interaction physics phenomenon, and to the induced thrust.

We first introduce the Schlieren diagnostic used in order to visualize the induced flow, because it was firstly adopted to understand the effect of this new kind of nanopulses supply system on the boundary layer. Then we will describe the experimental setup used for thrust measurements and at the end we will show the setup needed for the surface discharge measurements.

Schlieren setup

On regard the induced flow diagnostic of an EHD actuator, many difficult arise from its small (approximately centimeter) scale, low speed ($\sim m/s$) and

closeness to the plasma and to the dielectric surface.

Most common techniques to diagnose the induced wall jet include Particle Image Velocimetry (PIV), Laser Doppler Velocimetry (LDV), smoke visualization, Pitot probes, etc. Unfortunately, these methods are intrusive and must be used with great care.

For example, in PIV measurements the particles may get charged in the plasma and may not only depict the flow incorrectly but may also affect the plasma dynamic and the gas flow.

The main disadvantage of Pitot-probe measurements is low sensitivity. The measurements have to be taken at some distance downstream from the actuator in order to not perturb the plasma. Pitot measurements are also local, and to obtain the entire flow pattern, a scan through the entire flow region should be performed. The task becomes much more complicated with non-stationary flows.

The use of a non intrusive laser diagnostic, as LDV works, gives only punctual velocity measures and needs great work for the difficult interpretations of the measurements.

The use of the Schlieren technique for DBD induced flow measurements was yet used by Leonov [64] and Sosa [65].

In the first work [64], the authors used conventional Schlieren technique for flow visualization. The technique is based on following thermal disturbances in the jet and extracting the flow speed from that.

However, the authors found this insufficient for quantitative speed measurements and used Schlieren streak video instead. Another, similar, application of the Schlieren technique to DBD plasma actuator was developed in [65].

In this work, turbulent eddies were treated as tracers in the flow. A new, helium based technique of Schlieren image processing was suggested to observe the flow field. In the region outside the turbulent flow an helium jet was injected in order to produce the necessary contrast. The helium jet, however, can disturb the plasma and the flow field.

All of the above techniques are based on disturbances and/or turbulences in

the induced flow. As noted in [65] the technique is not applicable for laminar flows.

In our experiment, we used a new approach both for the induced flow visualization and the velocity measurements.

Since the discharge slightly heats the air, it is possible to visualize the induced wall jet. The principal feature of our Schlieren technique, distinguishing it from other studies, is the modulation of the voltage waveform applied to the discharge so that the plasma actuator is operated in pulse-burst mode.

The pulse-burst mode means that the supply waveform is formed by a series of pulses (a pulse train) and a period in which no pulses are applied. In this way each vortex can be relate with the corresponding pulse train.

In the burst mode, separate pulse jets are created by each burst. The advantage of the proposed technique is the ability to visualize two-dimensional (2-D), laminar, low speed, small, nonstationary plasma induced jets. An advantage with the study of quiescent air is that it is possible to notice some features, of the induced flow, which otherwise would be covered by an external superimposed flow.

A numerical model based on 2D Navier-Stokes equations predicts similar structures and allows us to extrapolate the entire flow pattern by matching the Schlieren images of a single vortex. The numerical modeling also allows us to infer the magnitude of the body forces exerted by the DBD actuator on the gas.

As will be largely discussed in the Section 9.3 “Interpretation of the results”, the Schlieren imaging in the pulse-burst mode demonstrated that the DBD actuator produces vortices.

Note that similar structures were observed in DBD experiments using smoke visualization [66] and Schlieren technique [67], in DBD induced flow numerical simulations [68, 69] and also in plane wall jet experiments and numerical simulations [70, 71, 72].

However, in this work, we demonstrate that the strength of the vortices and frequency of their generation can be controlled by means of the voltage wave-

form, which has interesting practical implications.

The Schlieren setup used is reported in figure 9.2.1.

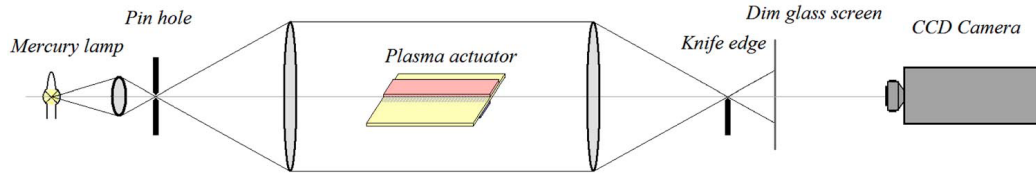


Figure 9.2.1: Schlieren setup.

The light source is a mercury lamp with a $50[\mu m]$ pinhole. The two lenses are characterized by a focal length of $25[cm]$ and diameter of $6[cm]$. A vertical knife edge was put into the focus of the second lens. The image was projected on a ground glass screen and then captured by a *Princeton Scientific Instruments 4-D* charge coupled device camera. The camera took 28 consecutive images with $1[ms]$ exposure time and no significant delay between the images.

The camera has been triggered by means of the Stanford Box generator in order to relate the vortex morphology with the supply conditions.

Thrust measurement setup

The thrust imparted by the DBD actuator has been measured by means of a *PL303 Mettler Toledo balance*. The maximum capacity of the balance is $310[g]$, readability $0.001[g]$, typical settling time $3[s]$.

The actuator was placed perpendicular to the balance in such a way it pushes toward the balance itself.

Difficulties arose because the balance was electrically operated, and nanosecond pulses used for driving the DBD created a lot of electro-magnetic noise. This noise distorted the force readings significantly.

A Faraday cage was thus constructed to shield the balance, and the actuator was mounted on a dielectric post as shown in figure 9.2.2.

A set of experiments was conducted in order to verify the accuracy of the measurements.

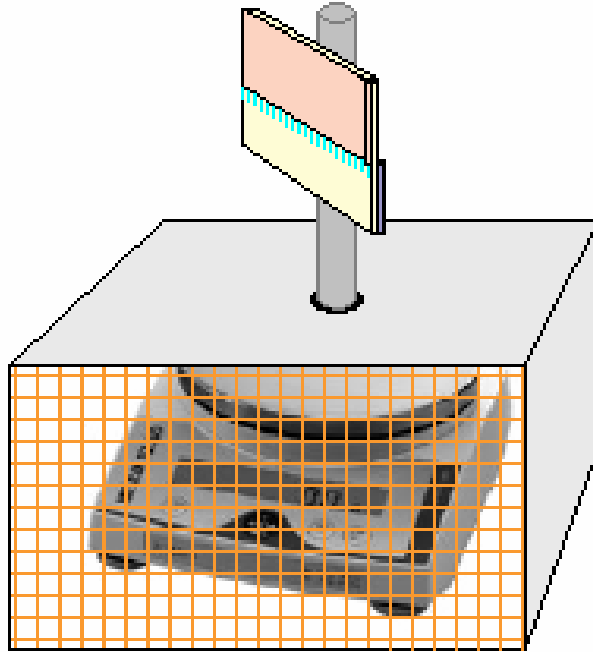


Figure 9.2.2: Balance in a Faraday cage and actuator position.

First of all, we confirmed that the connecting wires do not alter the readings. This was done by placing a known weight on the actuator with connected wires. The weights ranged from $5[mg]$ to $50[g]$ and the error introduced by the connecting wires was not more than $1[mg]$, i.e. within the reading accuracy of the balance. Furthermore it was noticed that the balance did not measure weights less than $5[mg]$.

Second, the fact that electro-magnetic noise created by the discharge did not affect the readings was checked by fixing the actuator (so it did not act on the balance) and running the plasma. The balance readings remained zero when the plasma was *ON*.

Third, the actuator was mounted upside down and observed to create the same force on the balance but in the opposite direction. Thus we can conclude that the setup works properly and measures the actuator induced thrust.

Surface charge measurement setup

Since the surface charge plays an important role in DBD physics it requires a special attention and study. For non-contacting surface potential measurements we used *Trek Model 247-3 Electrostatic Voltmeter* with *Trek Model 6000B-13C Electrostatic Voltmeter Probe*. It has high resolution, fast response time (less than $3[ms]$ for a $1[kV]$ step) and an operating range from 0 to $\pm 3[kV]$ DC or peak AC.

Figure 9.2.3 shows a $1[kV]$ step potential measured by the probe for calibration of the spatial resolution. For this calibration measurement a $1[kV]$ positive potential was applied to the exposed electrode of a DBD plasma actuator whereas the encapsulated one was grounded. It can be deduced that spatial resolution of the probe is around $1[mm]$.

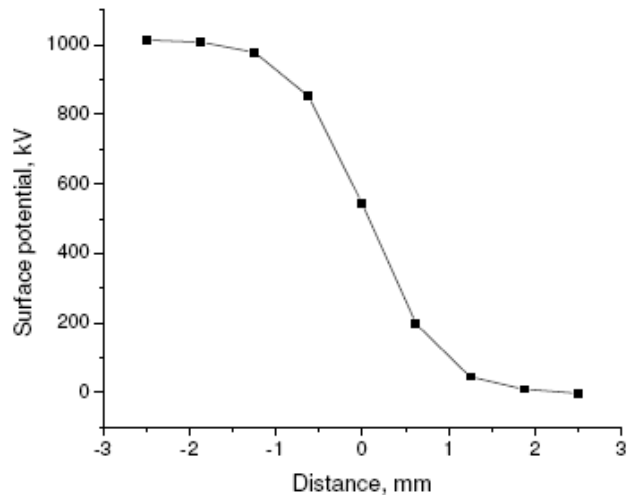


Figure 9.2.3: Electrostatic probe spatial resolution. $1[kV]$ step-like potential.

9.3 Interpretation of the results

In this section we first present the results from the Schlieren visualization. Then we will deal with the thrust measurements and in the end we will introduce the surface discharge measurements and the modified DBD actuator.

Schlieren measurements results

As mentioned in previous Sections of this Chapter, the Schlieren technique used in this work allows to the visualization of the vortexes formed by the DBD actuator.

In figure 9.3.1 the scheme of the actuator and a typical Schlieren photograph are reported.

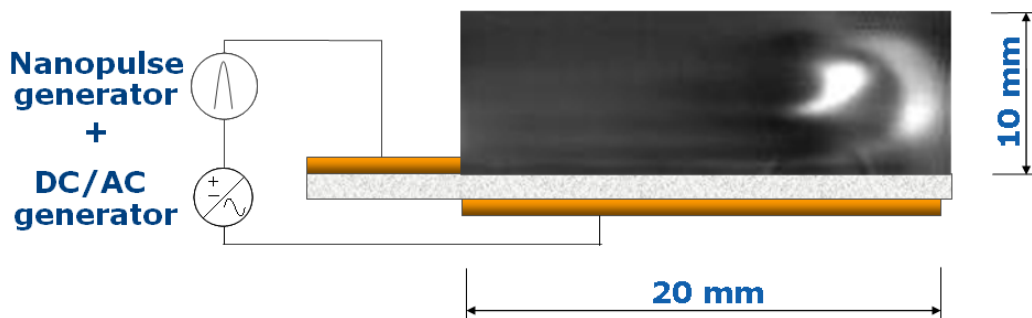


Figure 9.3.1: Schlieren photograph of the induced wall-jet of the DBD actuator run in pulse-burst mode and position of the actuator respect the photograph itself.

The photograph shows the presence of an hot vortex that propagates away from the top electrode of the actuator. The dimension of the photograph and the relative position with the actuator are the same for all the conditions reported in this work: frame of $20 \times 10[mm]$ and low left corner positioned in the junction top electrode-dielectric surface.

The Schlieren technique allows to visualize the coupling between plasma and boundary layer, and the first step of the work has been the comparison between numerical and experimental measurements.

The plasma model predicts the heating rate and the force exerted on the gas. The output parameters from the plasma calculations can be then used as an input for a time-accurate numerical computational fluid dynamics (CFD) model based on 2D Navier-Stokes equations.

The experiments showed that the DBD actuator run in pulse-burst mode generates periodic wall jets which evolve into vortical structures. The numerical model predicts similar structures and allows us to reconstruct the entire

flow pattern by matching the Schlieren images of a single vortex.

The 2D NavierStokes equations were solved using second order accurate MacCormack scheme. The computational domain was $5 \times 2[cm^2]$. The time step was determined by the Courant-Friedrichs-Lewy (CFL) condition.

The gas constants have been taken from [73].

The modeling has been performed for quiescent air at initial temperature of $300^\circ[K]$. The dielectric surface temperature $1[mm]$ downstream from the exposed electrode was considered to be $350^\circ[K]$.

We considered the plasma region to be $100 \times 500[\mu m]$. The force on the gas was considered to act only in horizontal direction downstream and to be uniformly distributed in the interaction region.

In the simulations, the force magnitude and heating in the interaction region were varied.

In the experiment the pulser was run in burst mode at 50 kHz PRR and 50% duty cycle, giving $10[ms]$ bursts with 500 pulses in each burst every $20[ms]$. The pulse voltage was $5[kV]$.

In addition $2[kV]$ bias voltage was applied to the electrodes.

Lets consider now the flow induced by the DBD plasma actuator in pulse-burst mode. When the DBD is on, the plasma is generated and the gas in the interaction region is heated and receives momentum in the downstream direction (in our representation of the results, from left to right) The motion of the gas generates pressure gradient in the vicinity of interaction region. The gas is being sucked in that region from the left and from above, creating an upstream vorticity. At the same time another vortex is generated by the induced gas jet (figure 9.3.2).

There are important differences between the two vortices.

One of them is the sign of vorticity. The vorticities of upstream and downstream vortices are negative (clockwise) and positive (counter clockwise), respectively.

Another principal difference is the gas density in these vortices. The upstream vortex involves motion of the quiescent air at room temperature, thus its tem-

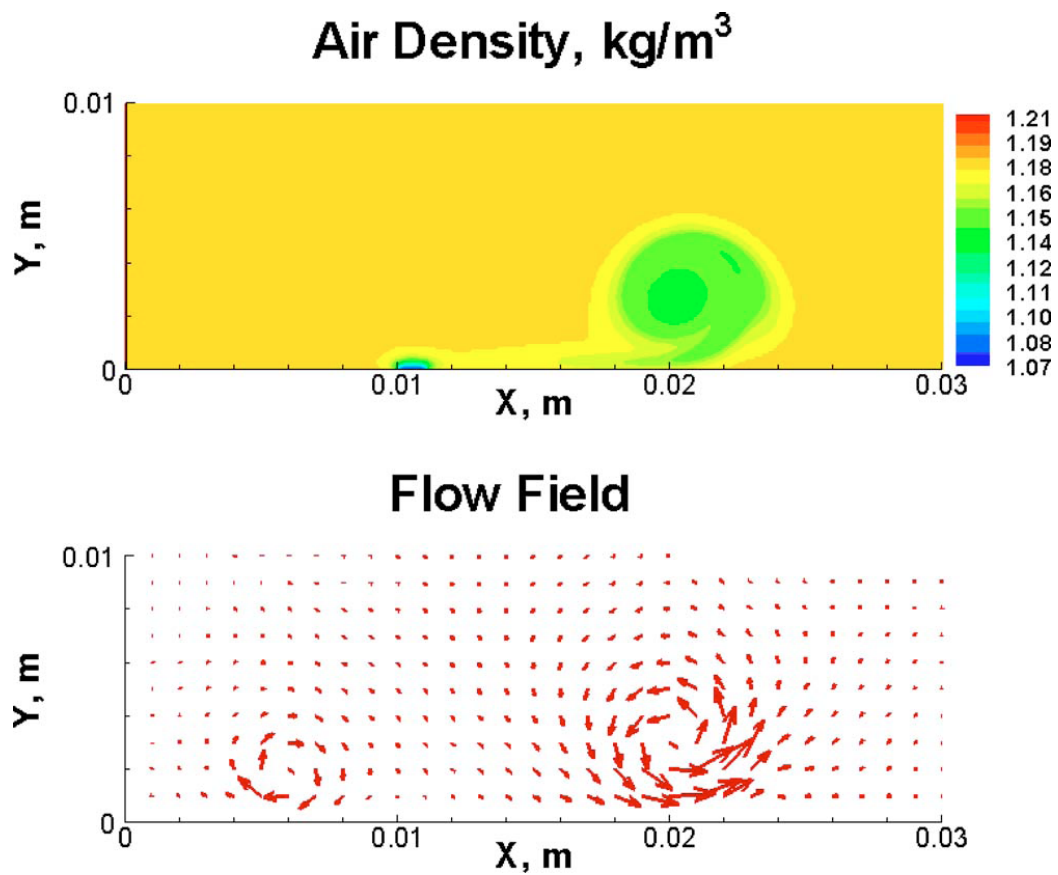


Figure 9.3.2: Numerical results of the air density and velocity distribution 14 ms after the burst.

perature is constant. In contrast, the downstream vortex is generated due to the motion of heated gas jet. Thus, it is characterized by well-defined temperature and density profiles.

In the Schlieren experiments on DBD induced flow, only density gradients can be visualized, i.e., the downstream vortex is observed and the upstream one is not detected.

These results can be important in theoretical investigations of the flow separation control using DBD: the gas flow will interact not only with the observed downstream vortex but also with the “hidden” upstream one.

Representative examples of such vortical structures, both experimental and reproduced in the numerical modeling, are shown in figure 9.3.3.

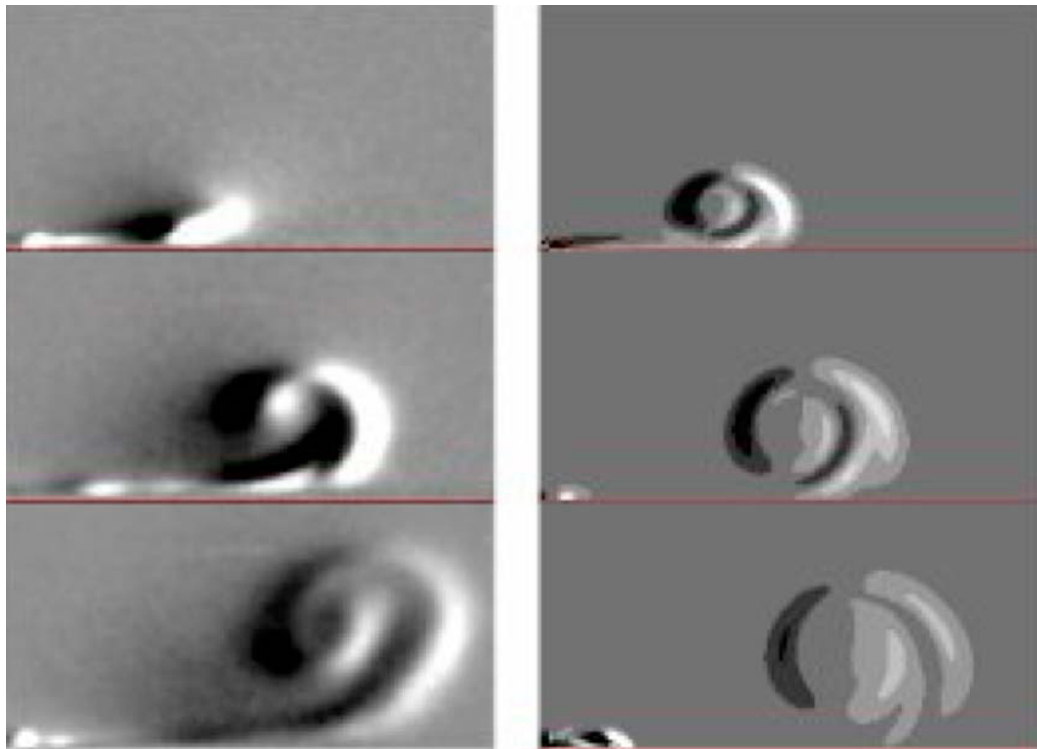


Figure 9.3.3: An example of experimental (left) and simulated (right) Schlieren images of the DBD plasma jets. The images are $20 \times 10 [mm^2]$ each and correspond to 7, 14, and 21[ms] after the burst start.

The agreement between experimental and computational results is excel-

lent and it allows to reconstruct the entire evolving flow pattern and to derive both the induced velocity field and the magnitude of plasma induced body force.

For this example the motion of the vortex was around $0.5[m/s]$, $17[mm]$ downstream and that vorticity was driven by a surface jet with a velocity of $7[m/s]$ in the plasma vicinity.

In previous works [74, 75] Likhanskii calculated the integral momentum transferred to the gas by means of positive and negative nanosecond pulses with DC bias, as well as the heating rate in the interaction region. These data have been extracted and used as an input to the Navier-Stokes solver. An important assumption in the modeling was that there are no saturation effects due to surface charging. This is a crucial point because we will see that the build-up of the charges in the dielectric is a fundamental phenomenon for the DBD actuator performances.

The pulser was considered to operate at $500[kHz]$ repetition rate.

The computed vortex propagation velocity as a function of distance from the exposed electrode is shown in figure 9.3.4.

If we consider the results for momentum transfer from [75] for positive $3[kV]$ pulses ($4[ns]$ FWHM) with $1[kV]$ DC bias and distributing it equally in the interaction region, we get a force of $1.4 \cdot 10^5[N/m^3]$.

The numerical results for this calculation are between the green (round) and blue (square) data points in figure 9.3.4.

The other curves correspond to the different force magnitudes in the interaction region at constant heating rate. It can be clearly seen that the translational vortex velocity significantly drops with the propagation along the surface. This fact is very important, since using the Schlieren technique in the experiments we can extract the density gradients at several temporal points and thus determine the vortex propagation speed.

The developed model allows thus to deduce the induced flow velocity right at the edge of the plasma and the force magnitude in the interaction region by matching the experimental pictures with numerically obtained ones.

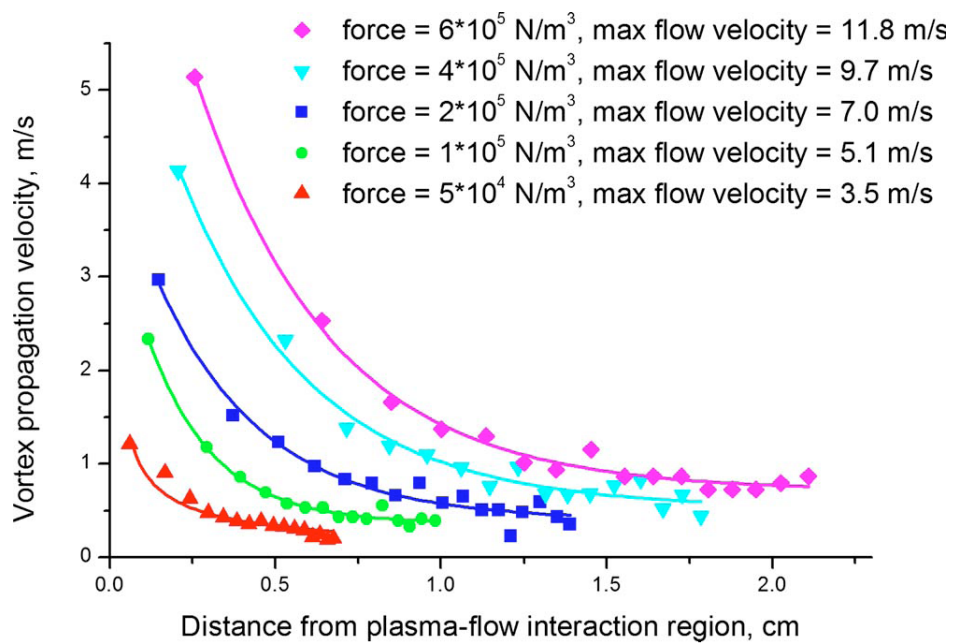


Figure 9.3.4: Vortex propagation velocity as a function of the horizontal distance from the exposed electrode at different forces in the interaction region. The maximum velocities of the induced flow at the vicinity of interaction region are designated as “max flow velocities”.

The effect of heating was also investigated; however, the results showed that the vortex size has almost no dependence on the heating in the interaction region.

Only the temperature of the gas within the vortex varies. Note that the gas temperature cannot be measured by the Schlieren technique, and additional measurements with other techniques should be used to provide an additional insight into the plasma-flow interaction.

To examine experimentally how the actuator induced flow speed depends on the constant bias voltage, we ran experiments with fixed pulse voltage and different DC bias voltages, as shown in figure 9.3.5.

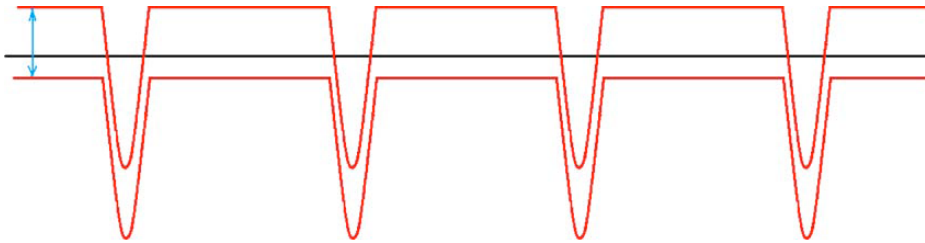


Figure 9.3.5: Variation of the DC bias maintaining constant pulses amplitude.

As introduced before, following the movements of the heated regions and knowing the frame rate of the CCD camera, it is possible to determine the velocity of the vorticities.

The vortex translational speed versus coordinate at different bias voltages is shown in figure 9.3.6 for both polarities of the pulses.

The experiments showed that, in the case of negative pulses, there is only a weak, within the error bars, dependence of the induced flow velocity on the bias voltage. Bias voltage of either polarity increased the induced jet speed only slightly. For the positive pulses, there was no clear dependence on the bias voltage.

These results did not agree with the expectations based on the numerical plasma model that predicted significant increase in the induced flow velocity with the bias voltage

However, during the experiment, an interesting phenomenon was noticed:

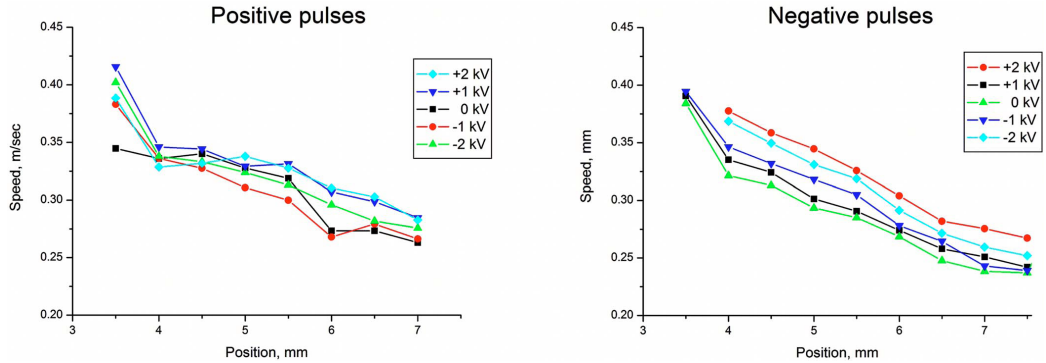


Figure 9.3.6: Induced tangential flow speed vs distance at different constant bias voltages. The error bar is $\sim 0.04[m/s]$.

a rapid switch of the bias polarity increased the jet velocity for the first several pulse bursts. To observe the details of the first vortices after the bias switch, the camera was triggered at the very beginning of every run so that it captured the first bursts.

The actuator was thus run at some value of the bias voltage for $5[s]$, and then the pulses were turned off. After $10[s]$ off, the pulses were turned on again, and the first burst of this second run was captured.

This second run was done at either the same or a different values of the bias voltage compared to the first run.

As in previous experiments, the pulser was run in burst mode at $50[kHz]$ PRR and 50% duty cycle, giving $10[ms]$ bursts with 500 pulses in each burst every $20[ms]$. The pulse voltage was $5[kV]$, and the bias voltage was changed from -2 to $+2[kV]$.

The results are presented in figure 9.3.7. The columns represent images taken 7, 14, and $21[ms]$ after the burst started. Different rows represent different bias conditions. The electrode arrangement is indicated.

The results show that switching the polarity of the bias voltage has a dramatic effect on the DBD operation: much faster jets and vortices are generated compared to the constant bias cases.

An interesting feature can also be seen when switching from positive to negative bias. The induced wall jet from the first burst makes what looks like a

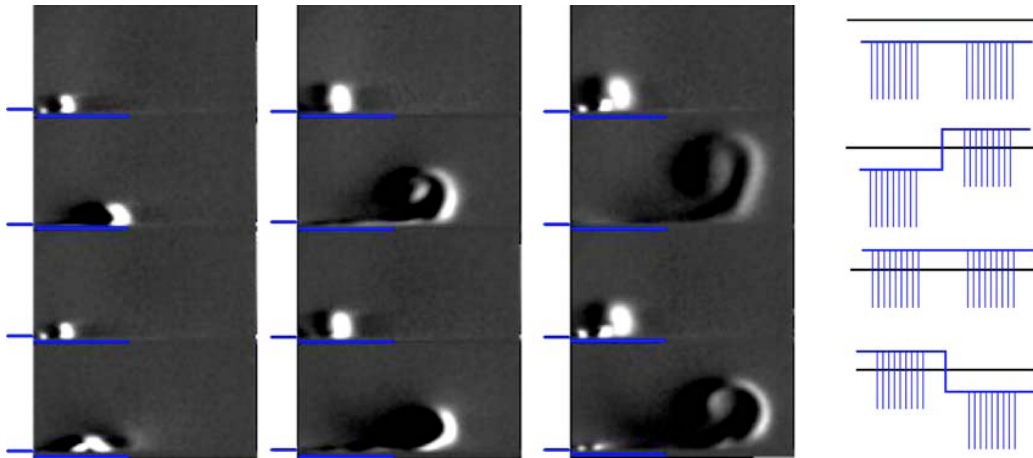


Figure 9.3.7: DC bias voltage switch experiments. The columns represent images taken 7, 14, and 21[ms] after the burst started. Different rows represent different bias profiles (sketched aside). The electrode arrangement is indicated. The results are presented for 5[kV] negative pulses, 50[kHz], 50% duty cycle. The bias voltage was ± 2 [kV]. The view field is 20×10 [mm²].

jump. The jet created by the second burst, however, does not “jump” anymore. The location of the jump is around the region where the plasma ends. In the case of positive pulses, a similar jump can be observed when switching from negative to positive bias voltage. In addition, in that case the second vortex also “jumps”.

The same behaviour was observed during switches from -2 to 0, 0 to -2, 0 to +2, and +2 to 0[kV] for both polarities of the pulses. However, the jet velocity increased and the jump were not as strong as in the cases of switching between negative and positive polarities of the bias voltage.

Likely explanation for the observed behaviour is accumulation of surface charge on the dielectric.

During the run, the dielectric surface is charged, and a shielding of the applied bias electric field occurs, reducing the force on the gas and the jet velocity. This explains why, in the first series of experiments in which the wall-jet was weak, the EHD effect was determined by the difference between the peak voltage and the bias voltage and not so much by the peak voltage

or the bias voltage separately.

Switching the polarity of the bias removes the surface charge and enhances the actuator performance for a short time, until the surface charge builds up again.

One reason for the jump behaviour could be an interaction of residual space charge present in the wall-jet with the surface charge.

To check the presence of charges on the surface of the dielectric, the next series of experiments have been done.

The conditions were similar to the previous experiments. First the actuator was run for 5[s]. Then after some time being off it was run again without switching the bias voltage.

The first burst of the second run was captured by the camera. The aim was to see how the generated vortex depends on the time delay between the runs. The experiments were done for -2, 0, and +2[kV] bias voltages with 5[kV], 50[kHz], 50% duty cycle positive pulses and time delays of 10, 20, and 60[s]. Another run was done with 10[s] time delay during which the charge was removed from the surface. The surface charge removal was done with a wet grounded cloth.

The water provided a good contact with the entire surface, and after a wipe the surface was slightly wet and quickly dried out by itself. The whole procedure took less than 10[s] at the end of which the surface was dry and discharged (wiping the surface with a dry cloth to remove the water might lead to charging through friction).

The results are presented in figure 9.3.8.

The vortex-generating performance persists for the times up to 1 minute. If the observed behaviour was due to some heating effects, there would not have been such a long hysteresis as 1 minute. This provides evidence in favor of the surface charge.

Also the wiped-surface runs with bias look like a switch from zero bias voltage. This shows that the effect does occur due to the surface charge which depends on the bias voltage.

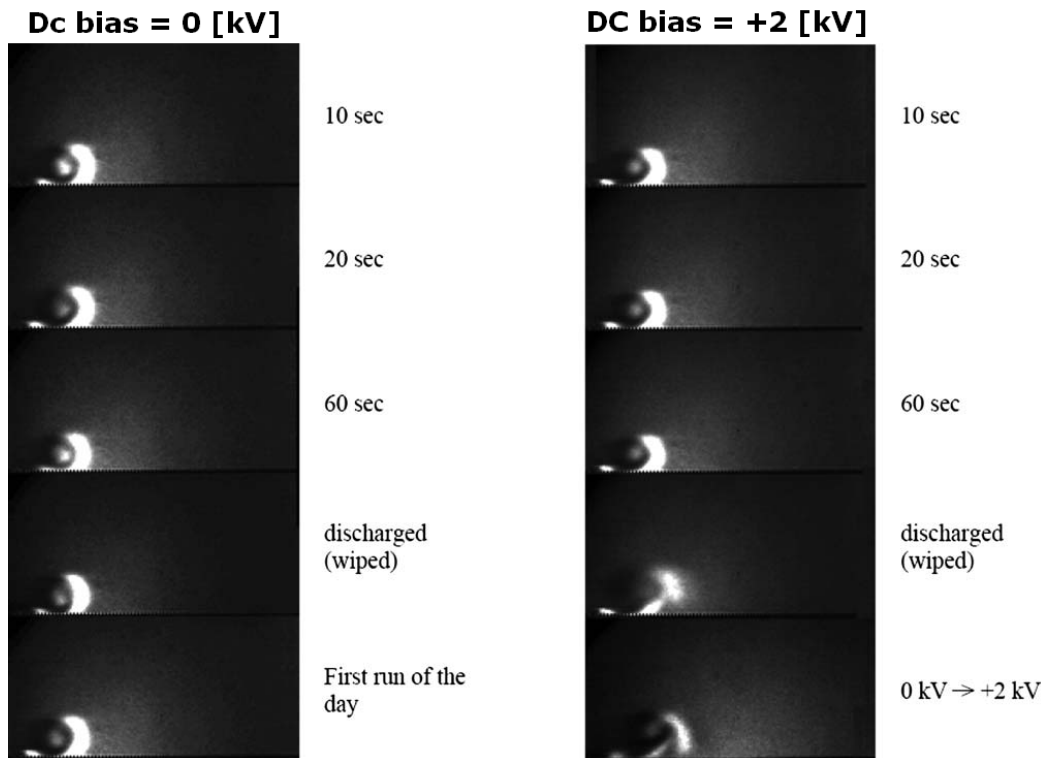


Figure 9.3.8: Surface wipe experiments with $0[kV]$ (left column) and $+2[kV]$ (right column) bias voltages both with $5[kV]$, $50[kHz]$, 50% duty cycle positive pulses and time delays of 10 , 20 , and $60[s]$. Wiped runs were done with $10[s]$ time delay. The last picture in the left column shows the very first run of the day, when the surface was still charge-free. The last picture in the right column shows a bias switch experiment in which the bias voltage was changed from 0 to $+2[kV]$. The images were taken $12[ms]$ after the burst start. The field of view of each image is $20 \times 10[mm^2]$.

Moreover it can be seen that the vortex is very similar to the one from the wiped-surface run, which means that both the wipe and the run at 0[kV] bias voltage discharge the surface. Again it can be seen that the surface charge shields the applied bias voltage. However, if the surface charge is removed, the plasma feels the bias voltage, but only until new charge builds up on the dielectric surface.

It was not possible to conduct similar experiments with the negative pulses. As mentioned above, the bias voltage was applied to the same electrode as the pulses, i.e., for the negative pulses that would be the exposed electrode. Manually wiping the surface to remove the charge in the close vicinity of the electrode at a few kilovolts potential would be unsafe.

After these results, we decide to better investigate the possibility of charge accumulation on the dielectric surface. A series of experiments has been done and they are described in the 'Surface charge measurement results' at page 158.

We return now to the Schlieren results.

Since the jet-enhancement effect disappears as soon as the charge builds up on the dielectric and shields the bias field, to let the effect go on continuously, one needs to keep switching the bias.

Thus, a new voltage waveform was used in the subsequent experiments: high-voltage sinusoidal signal (2.6[kV] peak to peak, 60[Hz]) plus nanosecond pulses (50[kHz], 5[kV], positive or negative).

Three versions of the voltage waveform were examined:

- (a) 100% duty cycle pulses + sinusoidal bias voltage

- (b) 50% duty cycle pulses, bursts near the peak of the sinusoidal voltage + sinusoidal bias voltage

- (c) 50% duty cycle pulses, bursts at the slopes of the sinusoidal voltage + sinusoidal bias voltage.

These supply configuration have been compared with the pulses without any bias voltage: (d) configuration 50% duty cycle pulses with no bias.

Since this set of experiments involved $60[Hz]$ sinusoidal signal, a new modulation of the pulses had to be used.

The pulses were generated in bursts with 208 pulses per burst and 120 bursts per second in such a way to synchronize pulses and bias.

The results are presented in figure 9.3.9.

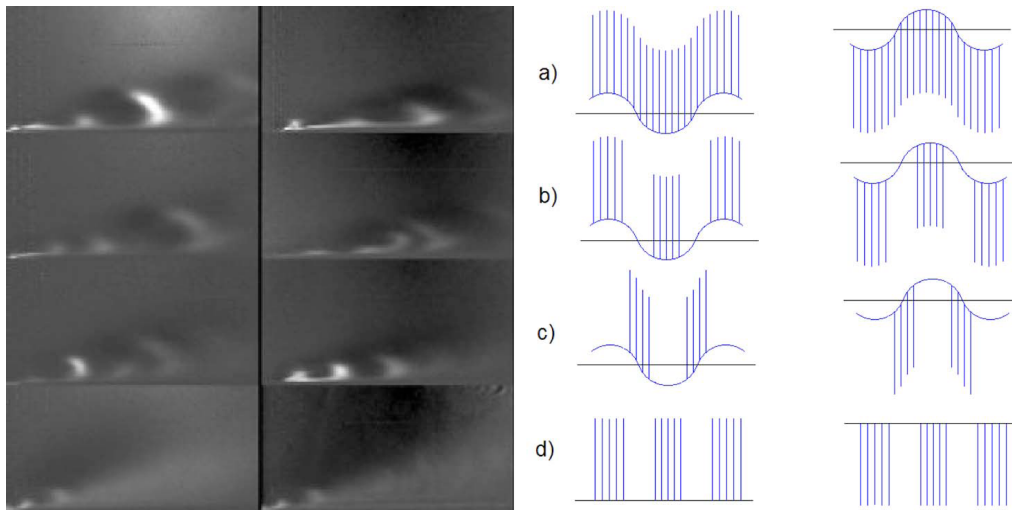


Figure 9.3.9: Nanosecond pulses combined with sinusoidal bias voltage. $5[kV]$, $50[kHz]$ positive (left column) and negative (right column) pulses combined with $2.6[kV]$ peak-to-peak $60[Hz]$ sinusoidal bias voltage. The field of view of each image is $20 \times 10[mm^2]$.

From the experimental results we can see that the sinusoidal bias significantly improves the actuator performance (last row in compare with the others). The jet speed increases from $\sim 30[cm/s]$ near the discharge in case (d) to $\sim 80[cm/s]$ at 10 mm downstream in case (a).

Thus, even a relatively low bias voltage (1.3 kV amplitude comparing to 5 kV of the pulses) has a great effect on the DBD actuator operation. Note that the bias voltage itself could not ignite the plasma in the absence of the

pulses, so as already introduced, the pulses generate the plasma and the bias pushes away the ions.

Also, vortices are still observed in case (a) despite the fact that the pulses are on all the time. This means that the induced wall jet speed strongly depends on instantaneous bias voltage as well as on the surface charge on the dielectric.

In addition, vortices coming out of different bursts, i.e., of bursts at different bias voltages, are different. The vortex speed and size depend on whether it was generated during positive/negative bias/slope of the bias voltage.

For further investigation we selected voltage waveform with pulses near the peaks of the bias voltage, since this waveform was more effective than the one with the pulse bursts at the bias voltage slopes. Additionally, with this waveform, it can be determined unambiguously which burst the vortex came from, which makes the data easier for interpretation.

DBD actuator operation dependence on the new voltage waveform parameters was investigated. As a baseline voltage waveform, we chose 5[kV] pulses at 50[kHz] and 50% duty cycle near the peaks of a 10[kV] peak-to-peak 60[Hz] sinusoidal bias voltage. We choose an higher voltage value of the AC bias because we expect an higher induced flow velocity.

Then varying one of the parameters at a time (the bias voltage, pulse voltage, and pulse repetition rate) we observed the vortices for each polarity of the pulses. As mentioned above, the vortices coming out of different bias half-cycles differ in speed and size. Thus plots for both kinds of vortices are presented in the figures when possible.

Consider first the actuator performance dependence on Pulse Repetition Rate (PRR) for positive pulses (figure 9.3.10).

The vortex coming out of the positive bias half-cycle is slow. It does not move far away from the plasma region by the time the next vortex appears. The next vortex, which comes out of the negative bias half-cycle, is very fast. It actually does not evolve into a vortex immediately; it is still in its jet phase and thus is hard to notice. Then, upon collision with the earlier generated

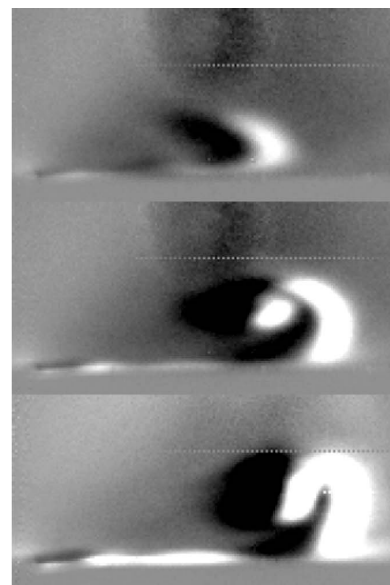
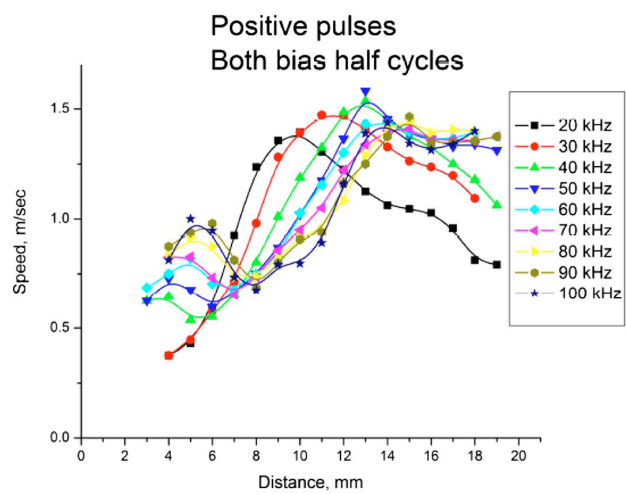


Figure 9.3.10: Vortex speed vs distance for different PRRs with positive polarity of the pulses. The Schlieren images were taken at the same moment of time for 20, 50, and 100[kHz]. A slow vortex is created by a jet from positive bias half-cycle, then from $\sim 5 \div 7$ [mm] it is accelerated by a jet from the negative bias half-cycle burst. The field of view of each image is 20×10 [mm²].

slow vortex, it also becomes a vortex. Thus, actually there is only one vortex in the Schlieren image at a time. As seen in figure 9.3.10, there is some weak dependence on the PRR.

The dependence of vortex parameters on PRR for negative pulses (figure 9.3.11) is different.

The vortices created during the negative bias half-cycles consist of two parts. The head part is not observed for pulses repetition rate lower than $30[kHz]$. Its speed is relatively high and does not depend on the PRR.

The tail part is brighter (so hotter) and much slower. The vortex created during positive bias half-cycle is faster. Its speed strongly depends on the PRR, as seen in figure 9.3.11.

The next parameter varied in the experiments was the pulse voltage. The results for the positive pulses are presented in figure 9.3.12.

The speed of positive (i.e., generated during the positive half-cycle of the bias voltage) vortices weakly depends on the pulse voltage. However, their brightness (temperature) strongly depends on the pulse voltage.

The pulse voltage has a dramatic effect on the speed of negative (i.e., generated during the negative half-cycle of the bias voltage) vortices. For the negative polarity of the pulses, the vortex speed is quite high, and the only effect of the higher pulse voltage is stronger heating. The details are shown in figure 9.3.13.

Among all the parameters, the sinusoidal bias voltage has perhaps the strongest influence on the DBD plasma actuator operation. The results for the positive pulses are presented in figure 9.3.14.

Again, positive vortices are rather slow, and it is unclear if changing the bias voltage has any effect on them because they propagate only several millimeters before the vortices from the negative bias half-cycles hit them from behind. The speed of vortices from the negative half-cycles depends strongly on the bias voltage.

For negative pulses, the increase in bias voltage leads to a significant increase in effect in both half-cycles of the bias voltage. The results are presented in

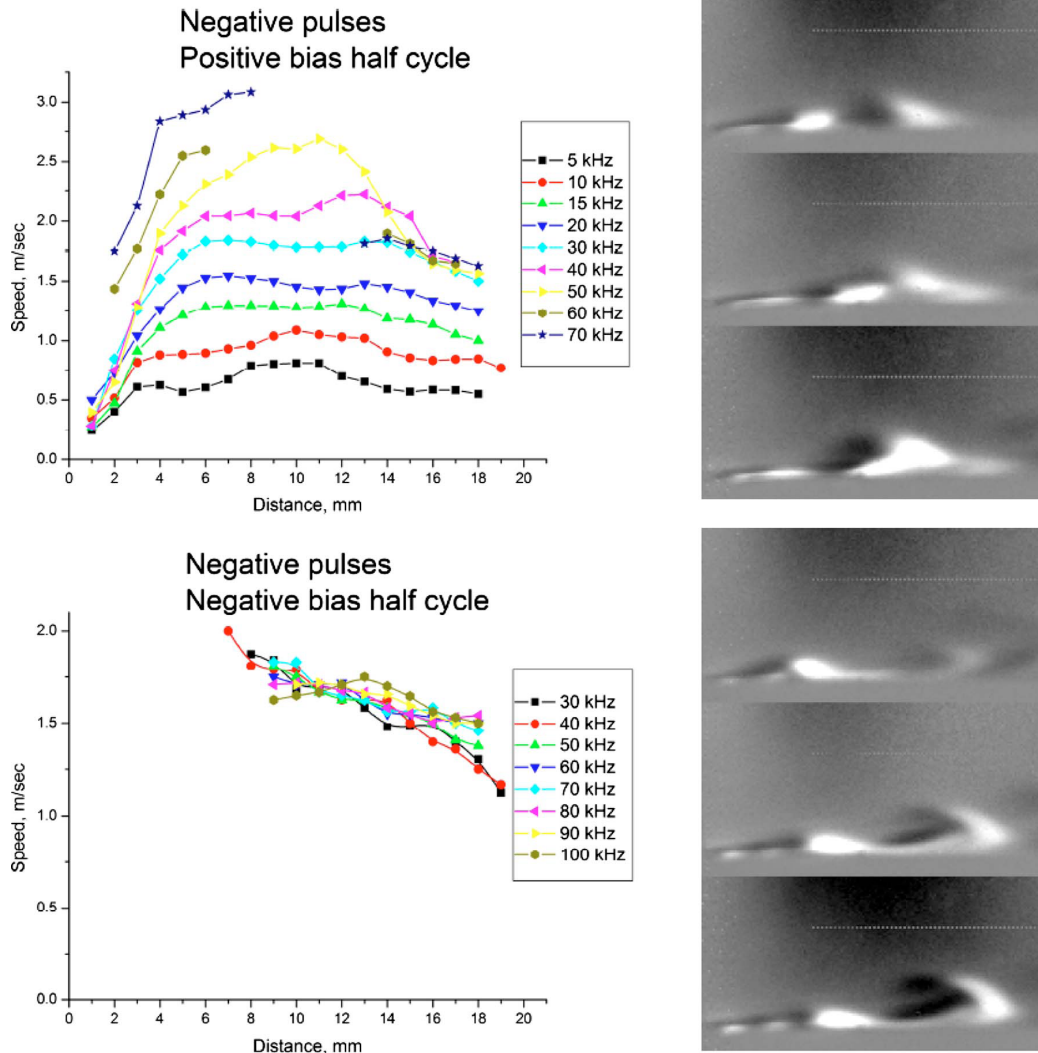


Figure 9.3.11: Vortex speed vs distance for different PRRs with negative polarity of the pulses. The Schlieren images were taken at the same moment of time for 30, 50, and 70[kHz]. In the bottom images, a vortex from the negative bias half-cycle is shown. The vortex consists of two parts: “head” vortex and “tail” vortex. In the top image, jet from positive bias half-cycle hitting the tail part of the negative vortex is shown. The speed of the positive vortex greatly depends on the PRR, while the speed of the negative one does not. The field of view of each Schlieren image is $20 \times 10[mm^2]$.

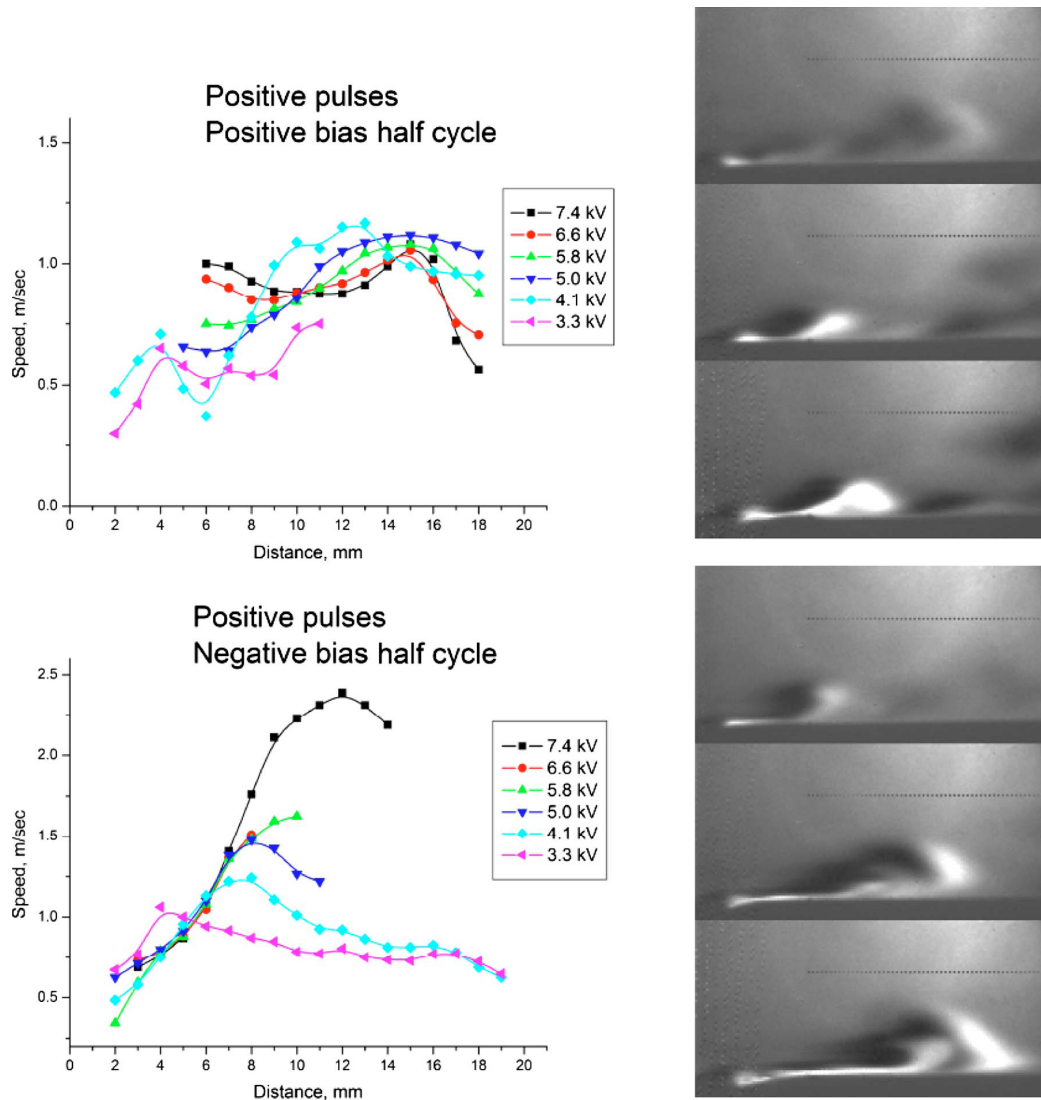


Figure 9.3.12: Vortex speed vs distance for different pulse voltages with positive polarity of the pulses. The Schlieren images were taken at the same moment of time for 3.3, 5.0, and 7.4[kV]. In the top images, slow jet from positive bias half-cycle is shown. In the bottom images, a vortex from the negative bias half-cycle is shown. The speed of this vortex is high and depends strongly on the pulse voltage. In the pictures for 5.0, and 7.4[kV], this vortex is colliding with the positive one. The field of view of each Schlieren image is $20 \times 10[mm^2]$.

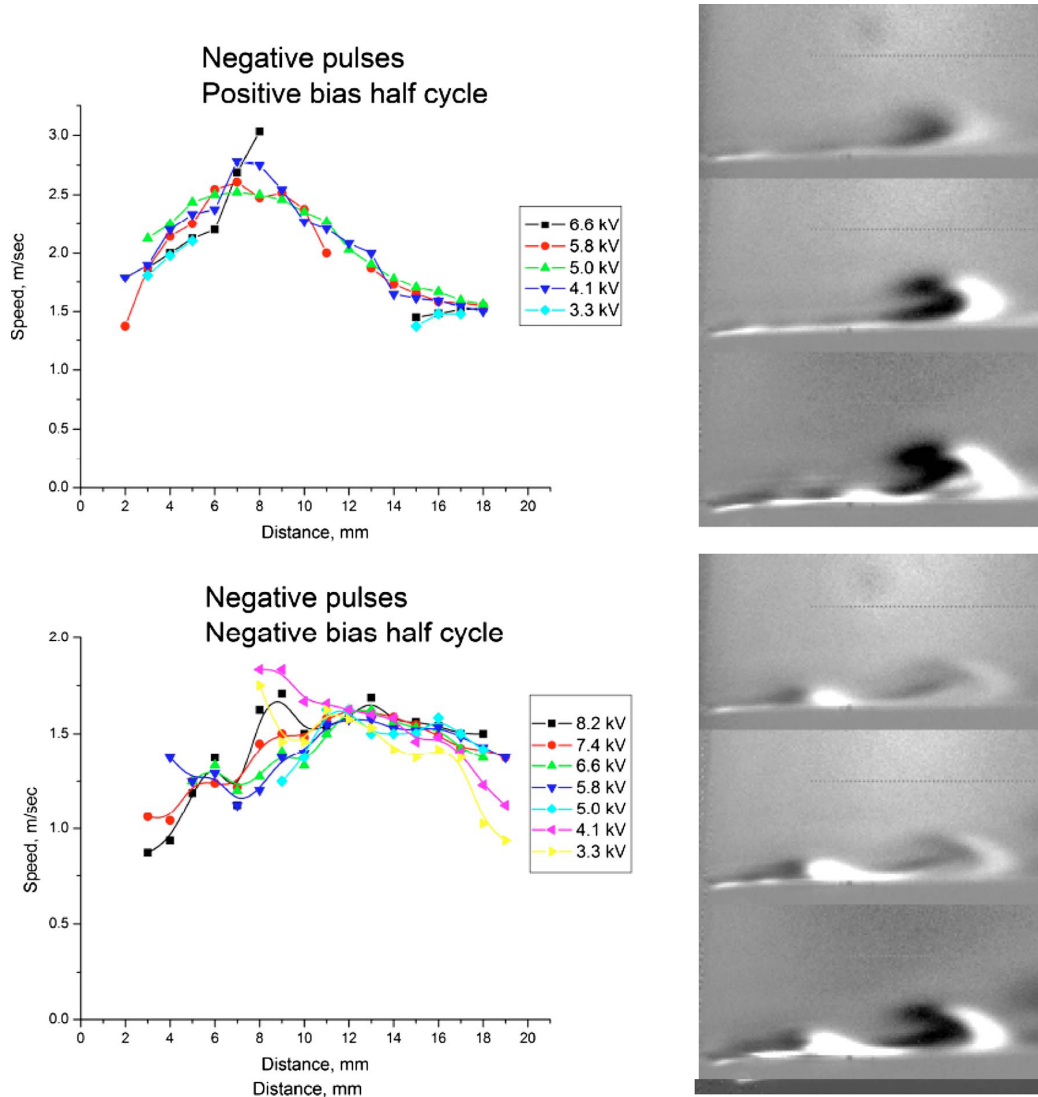


Figure 9.3.13: Vortex speed vs distance for different pulse voltages with negative polarity of the pulses. The Schlieren images were taken at the same moment of time for 3.3, 5.0, and 7.4[kV]. In the top images, jet from positive bias half-cycle is shown. In the bottom images, a jet from the negative bias half-cycle is shown, consisting of two parts: head vortex and tail vortex. There is no dependence of the speed of the vortices on the pulse voltage. The field of view of each Schlieren image is $20 \times 10[mm^2]$.

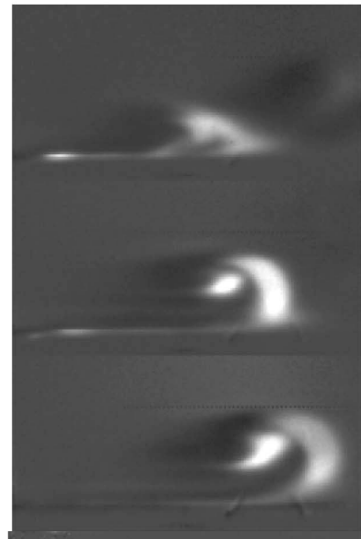
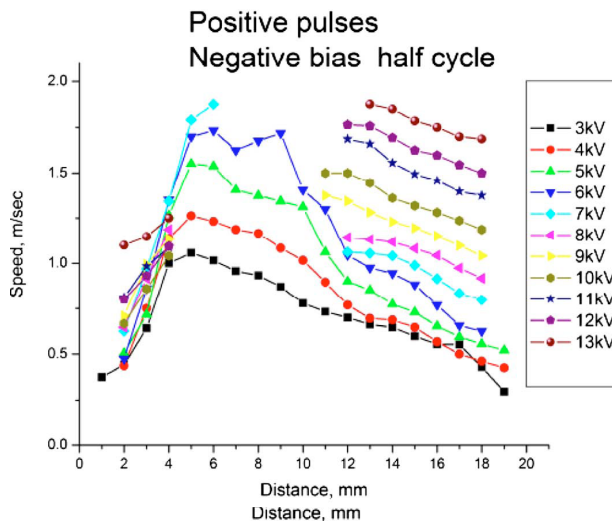
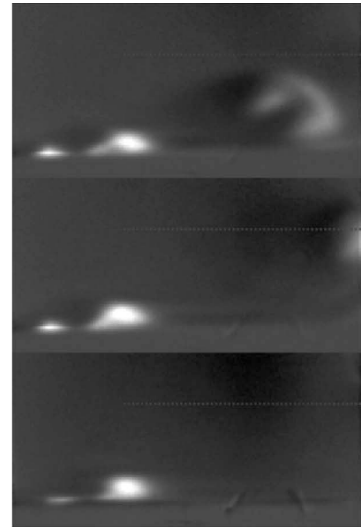
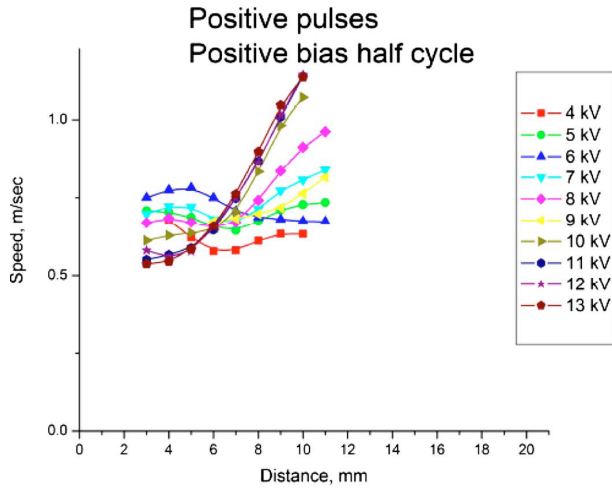


Figure 9.3.14: Vortex speed vs distance for different peak-to-peak sinusoidal bias voltages with positive polarity of the pulses. The Schlieren images were taken at the same moment of time for 5, 10, and 13[kV]. In the top images, a slow jet from positive bias half-cycle is shown; when a strong jet from the negative half-cycle arrives, it pushes the positive jet forward, which explains the acceleration in $6 \div 11[mm]$ range. In the bottom images, a vortex from the negative bias half-cycle is shown. Its speed is high and strongly depends on the pulse voltage. In the pictures for 5.0 kV, the collision is still in progress, which explains the complex shape of the vortex. The field of view of each Schlieren image is $20 \times 10[mm^2]$.

figure 9.3.15.

Starting from 5[kV] peak-to-peak bias voltage, self-sustained discharge was ignited in the absence of the high-voltage pulses. This discharge could remove the surface charge by itself improving the actuator performances.

The variations of all the parameters has shown the presence, for positive pulses, of a fast vortex that collides in a previous bigger but slower one creating a unique fast and big eddy.

In the case of negative pulses the two vortexes are both fast and little and propagate themselves more close to the surface.

In all the configurations, the vortexes are faster if the polarity of the pulses is contrary respect the one of the bias. We tried so to supply the actuator only applying pulses only when this condition was realized. Thus experiments were run with the pulses during half-cycles of one polarity only. The voltage waveforms are shown in figure 9.3.16.

The results of the experiments are shown in figure 9.3.17 where a comparison between the case with pulses present at both positive and negative top of the AC bias (pulses at every top) and pulses present in the top AC bias in which the polarity was inverted in compare with the pulses (pulses at positive tops only or pulses at negative tops only) is reported.

In all the conditions, the absence of the pulse burst during the other half-cycle leads to wall jet speed from two to three times lower. Also from the Schlieren photograph it is possible to note a slower and less far propagation of the vortexes if pulses are not present at every top of the AC bias.

This means that although some of the pulse bursts do not create a strong wall jet, they still play an important role in the DBD operation. Their task is to discharge/recharge the dielectric surface and thus to increase the efficiency of the other bursts.

The experiments also clearly showed that the wall jets induced by negative pulses evolve into two-vortex formations, whereas the ones from the positive pulses do not. The mechanism of this behaviour should be investigated in future studies.

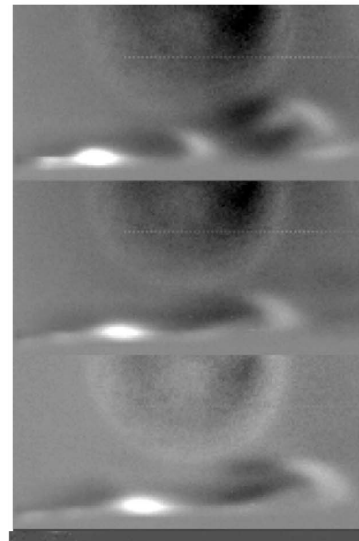
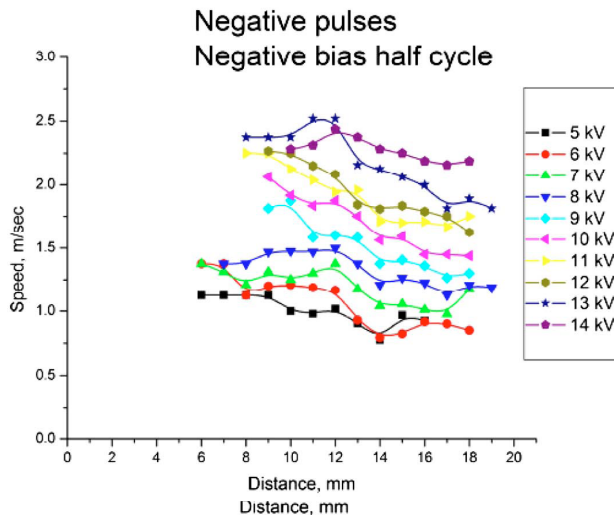
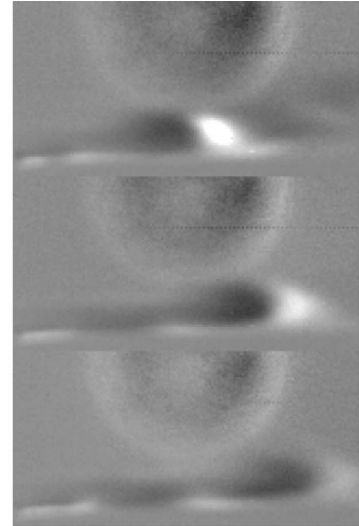
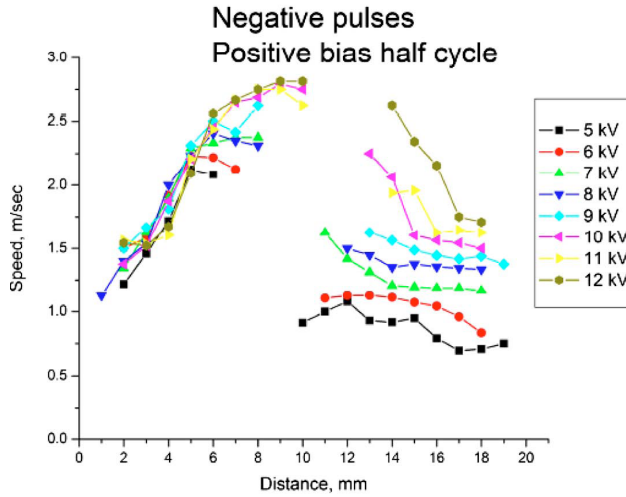


Figure 9.3.15: Vortex speed vs distance for different peak-to-peak sinusoidal bias voltages with negative polarity of the pulses. The Schlieren images were taken at the same moment of time for 5, 10, and 13[kV]. In the top images, jet from positive bias half-cycle is shown. The vortex speed strongly depends on the negative pulse voltage. The field of view of each Schlieren image is $20 \times 10[mm^2]$. The circle in the images is due to water condensation in the camera.

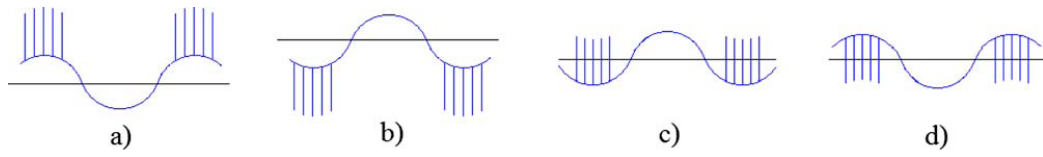


Figure 9.3.16: Voltage profiles with pulses near the bias voltage peaks of one polarity only.

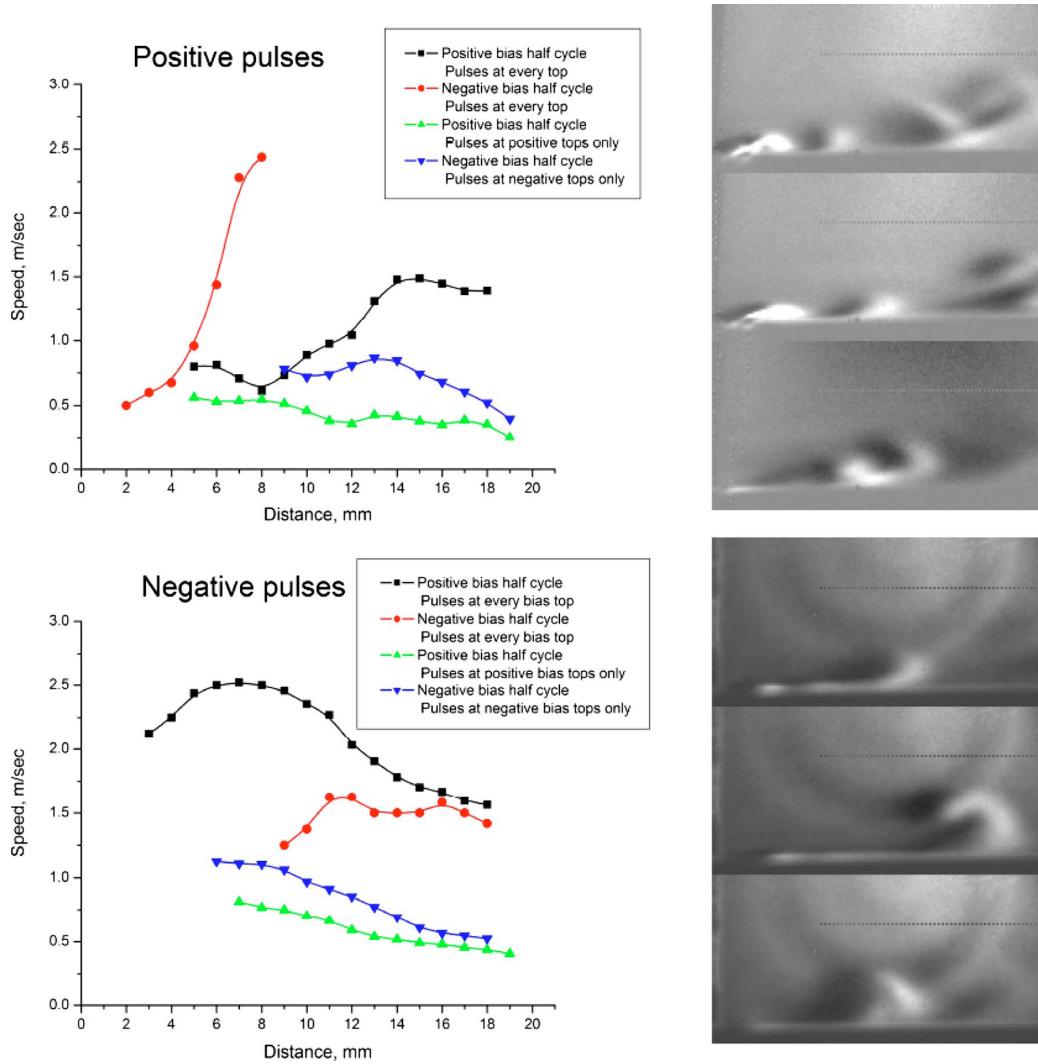


Figure 9.3.17: Vortex speed vs distance for different voltage waveforms. The Schlieren images were taken at the same moment of time for pulses during negative half-cycle only, both half-cycles, and positive half-cycle only. The field of view of each Schlieren image is $20 \times 10 [mm^2]$.

Thrust measurement results

As largely introduced in previous Sections, after the first Schlieren photograph campaign acted both to a physical comprehension of the EHD phenomenon and the measurements of flow velocity, we realized a series of thrust measurements comparing different bias profiles.

For first comparison, all the bias waveforms were characterized by 10[kV] peak-to-peak, 100[Hz] and the pulses were 3[kV], 25[kHz] 100% duty cycle, positive or negative.

From the results presented in figure 9.3.18 we can see that rectangular wave bias profile provides the highest thrust.

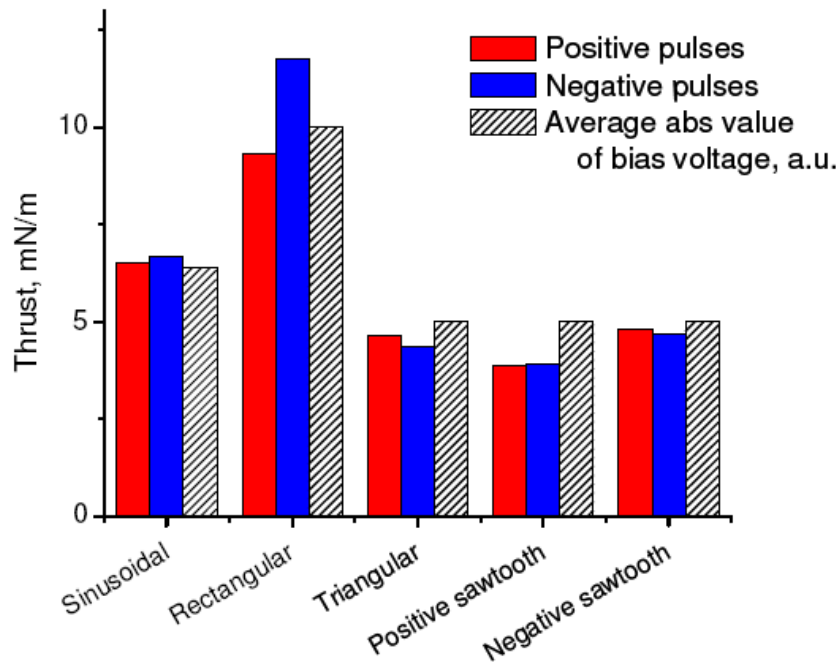


Figure 9.3.18: Thrust measurements for different bias profiles. Bias 10[kV] peak-to-peak, 100[Hz]; Pulses 3[kV], 25[kHz] 100% duty cycle.

The produced thrust correlates very well with the average of the absolute value of bias voltage (which is proportional to 0.64 : 1 : 0.5 : 0.5 : 0.5 respectively for sinusoidal, rectangular, triangular, positive and negative sawtooth respectively) and is almost the same for both polarities of the

pulses.

Some deviation from this rule is observed in the case of the rectangular bias profile where negative pulses produce higher force. The question of why the thrust of negative and positive pulses is different for the rectangular bias and is the same for other bias profiles is still open.

Based on these results, all further experiments were conducted with rectangular bias voltage profile.

Firstly, the effect of bias positive and negative duty cycles was investigated. In these experiments the frequency and voltage of the bias profile were fixed and the relative time duration of positive and negative periods was varied. The results are presented at figure 9.3.19.

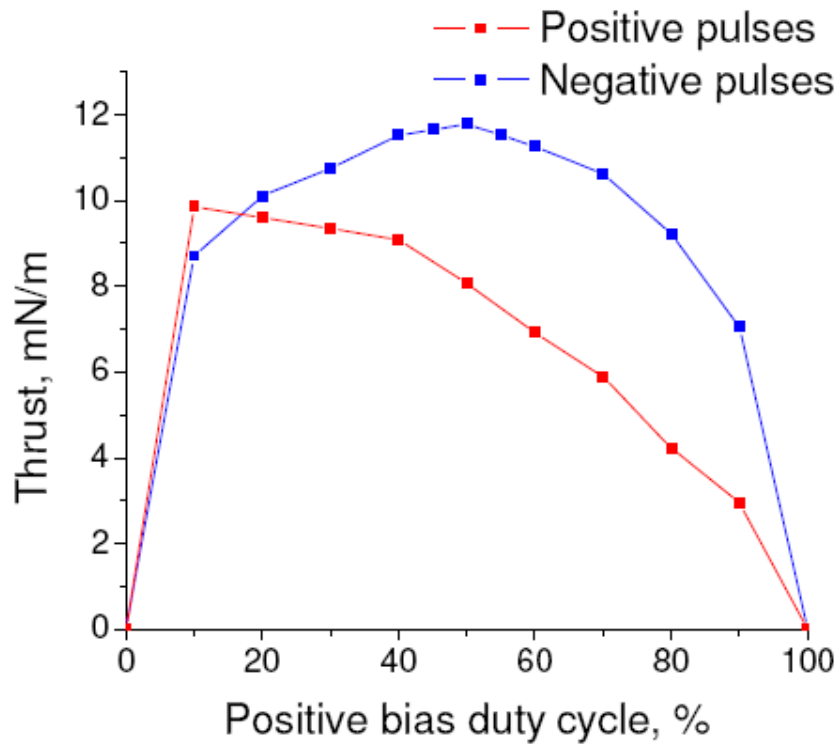


Figure 9.3.19: Thrust measurements for different bias duty cycles. Bias: rectangular, $10[kV]$ peak-to-peak, $100[Hz]$; Pulses $3[kV]$, $25[kHz]$ 100% duty cycle.

For case of positive ionization pulses the optimum regime was found to be when the bias is positive for less than 10% of the time and negative the other

time. For case of negative ionization pulses 50% duty cycle is most efficient one. The results agree with ones obtained by means of the previous Schlieren visualizations.

As seen before, in case of positive ionization pulses the plasma actuator induced a very strong wall jet in the negative half cycle of bias voltage and a relatively weak one in positive half cycle.

In case of negative ionization pulses, the induced wall jets of both half cycles are approximately of the same strength.

Also the effect of ionization pulse duty cycle was investigated. Keeping the total number of ionization pulses the same we increased pulse repetition rate and decreased the *ON* time.

From the results shown at figure 9.3.20 we can state that the uniform distribution of pulse in time is most efficient. Reducing the duty cycle down to 50% decreases the effect by 30%.

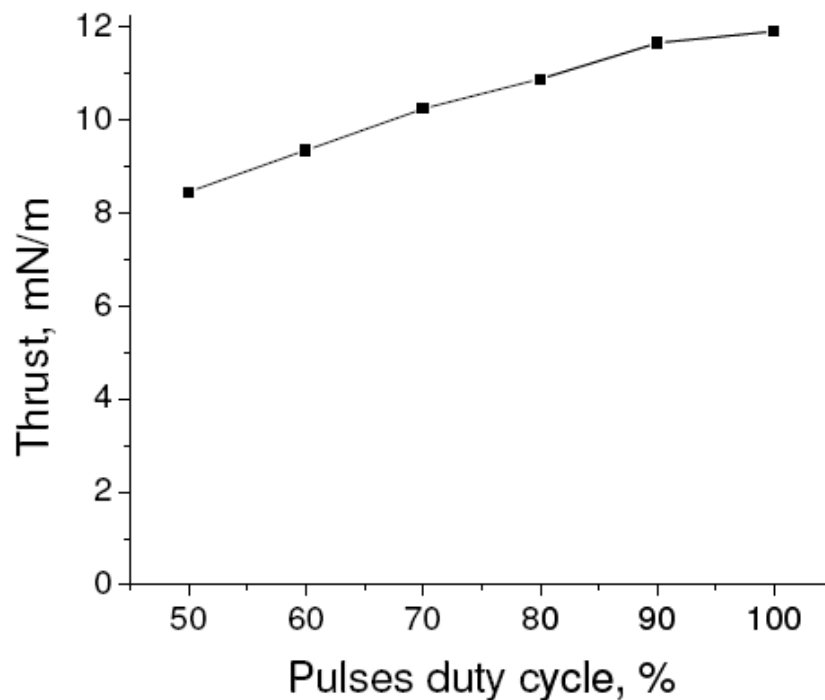


Figure 9.3.20: Thrust measurements for different pulses duty cycles. Bias: rectangular, 10[kV] peak-to-peak, 100[Hz]; Pulses 3[kV], 25[kHz] 100% duty cycle.

Thrust dependence on the pulse repetition rate, pulse voltage, bias frequency and bias voltage was investigated. The results for both polarities of the pulses are presented at figures 9.3.21 and 9.3.22.

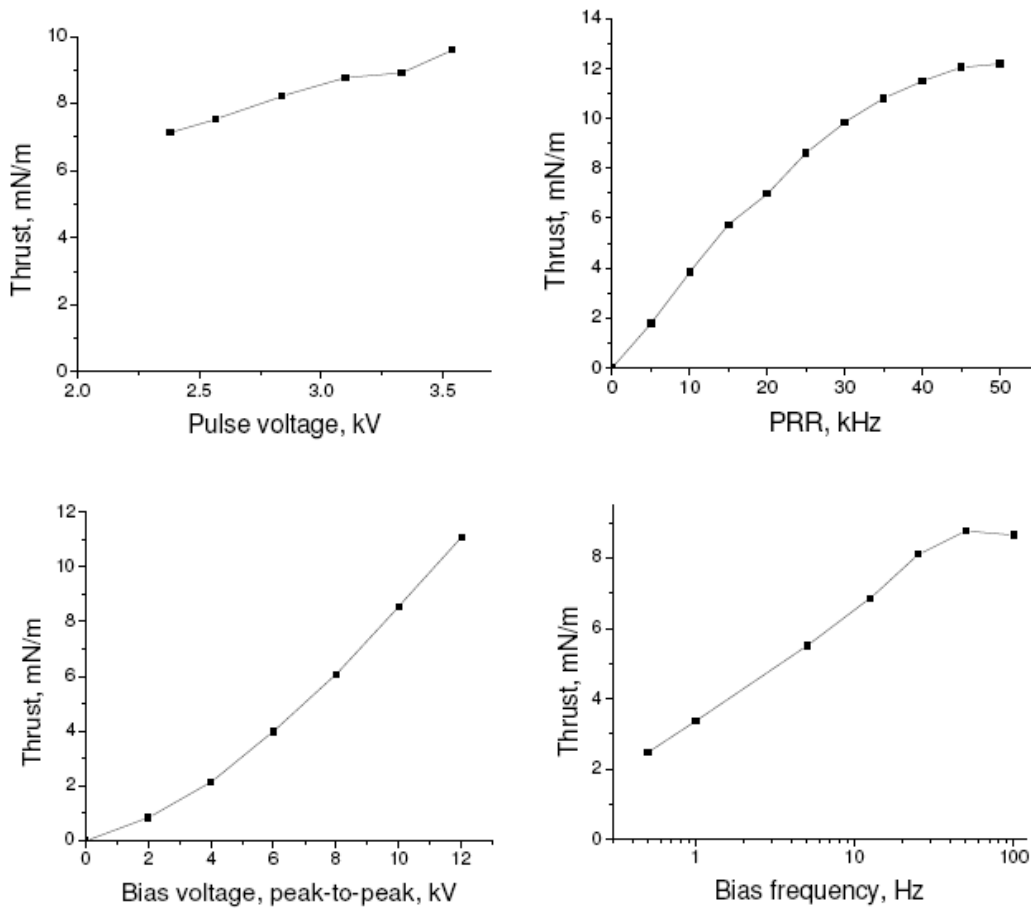


Figure 9.3.21: Thrust dependence on applied voltage parameters. Negative pulses. Bias: rectangular, 10[kV] peak-to-peak, 100[Hz]; Pulses 3[kV], 25[kHz] 100% duty cycle.

For these measurements a baseline was chosen: bias voltage 10[kV] peak-to-peak, 100[Hz] frequency, rectangular waveform, ionization pulse voltage 3[kV], 25[kHz] and ionization pulse repetition rate in continuous mode. Then one parameter at a time was varied.

As can be seen from the figures, the bias voltage has greatest impact on the induced thrust. With no bias applied, the thrust is zero (within the er-

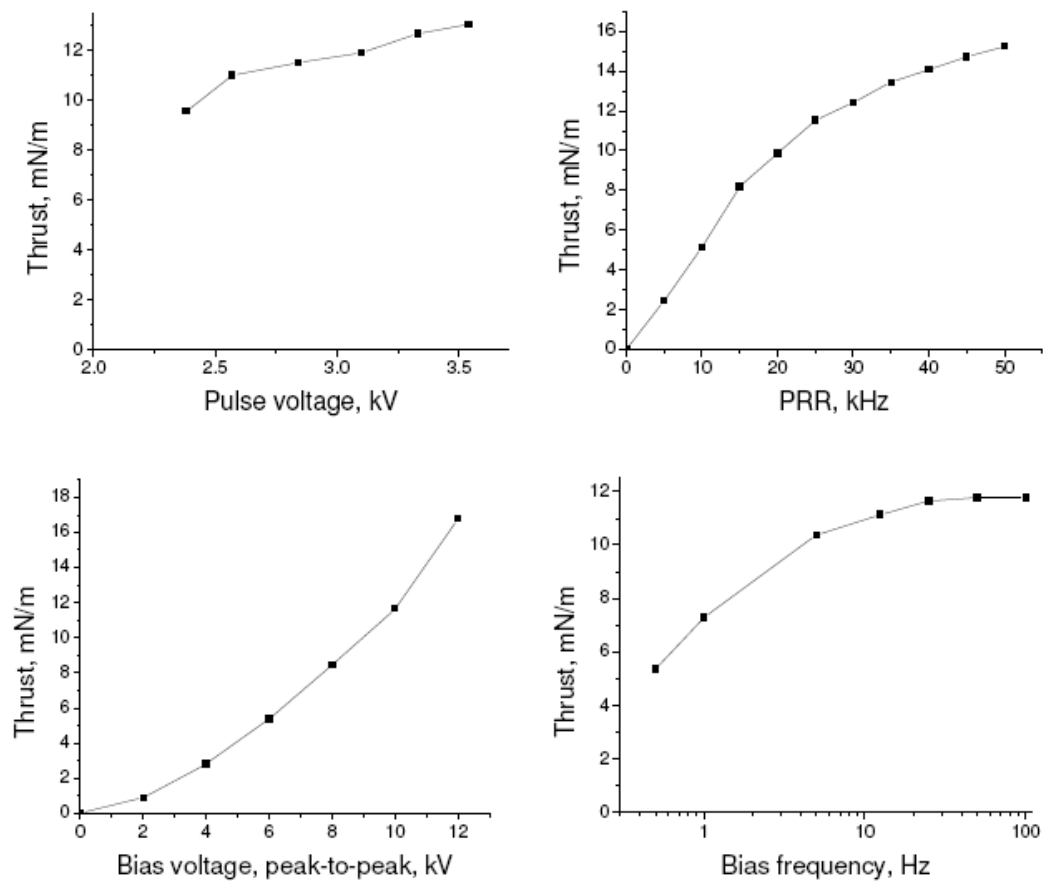


Figure 9.3.22: Thrust dependence on applied voltage parameters. Negative pulses. Bias: rectangular, 10[kV] peak-to-peak, 100[Hz]; Pulses 3[kV], 25[kHz] 100% duty cycle.

ror bar). Increasing the bias voltage, an increase of the thrust of more than $1[mN/m]$ each $[kV]$ is obtained.

An increase of the other parameters also leads to an increase in force but not so fast.

When the bias frequency is varied, a saturation effect is reached around $50[Hz]$.

These results have been compared with other thrust measurements realized by classical sine supply waveform.

At the present time a few groups have performed thrust measurements for DBD plasma actuators [8, 76, 77] for different voltage profiles and dielectric parameters.

Some of the literature data plotted together with our results for comparison are presented in figures 9.3.23 and 9.3.24 .

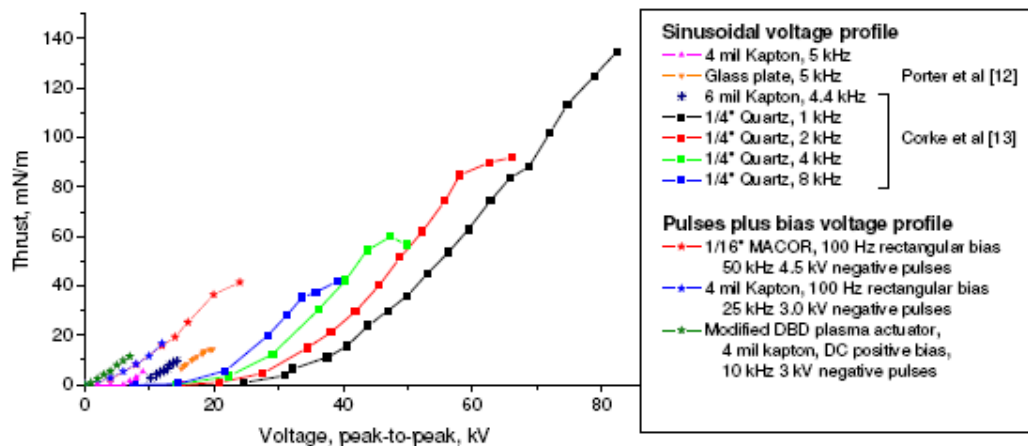


Figure 9.3.23: “Pulses plus AC bias” versus sinusoidal voltage: comparison of tangential body forces. Comparison data were taken from [8, 9].

Most of the data were obtained for sinusoidal voltage profiles. In the case of the pulses plus AC bias profile, the peak to peak bias voltage was used to characterize the amplitude of the applied voltage. The pulses plus DC bias profile was characterized by the value of the DC voltage.

These results appear to show that the “pulses plus sinusoidal bias” method

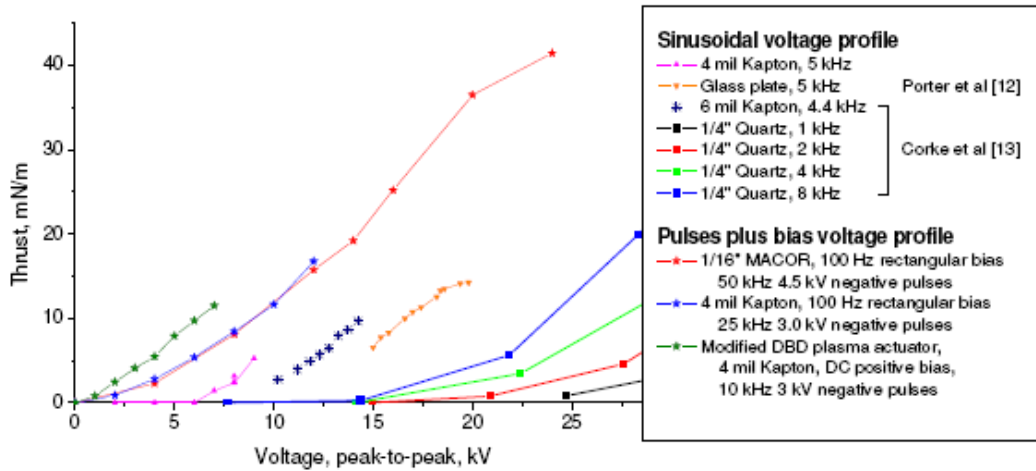


Figure 9.3.24: Pulses plus AC bias versus sinusoidal voltage: comparison of tangential body forces (zoomed in). Comparison data were taken from [8, 9].

generates a much stronger tangential force than the conventional sinusoidal voltage at the same voltage amplitude.

Of course the comparison is not so easy to do because, since we have pulses, their amplitude also effectively adds to the “overall” voltage amplitude. However, we can claim that the amplitude of neither the sinusoidal bias nor the ionization pulses need be very high to achieve an equivalent performance to that of DBD with a conventional sinusoidal voltage.

We can also say that there is a clear trend to improved performance with thicker dielectrics (both for us and for T. Corke [9]) that allow the use of higher voltages, besides there is a trend of improved performance when the bias frequency and ionization pulse repetition frequency are increased. We are optimistic that, if all those parameters are increased, the performance of the “pulses plus sinusoidal bias” system can be significantly higher than that of the conventional devices.

This trend is also confirmed by the thrust measurements of the “modified” actuator, that are included in figure 9.3.23 and 9.3.24. This kind of actuator will be introduced in next section. By now we can declare that it is able to realize higher thrust at lower voltages, so improvements of both supply

parameters and actuator design could lead to higher performances.

Surface charge measurement results

Schlieren measurements demonstrated that the accumulation of charge on the dielectric surface drastically decreases the DBD actuator performances. To check the presence of this charge accumulation, a set of measurements has been realized by means of an electrostatic probe (see page 127 for probe details). A first series of experiments have been performed with a sinusoidal voltage profile $10[kV]$ peak-to-peak, $3[kHz]$. Since the sinusoidal profile is widely used in DBD experiments it is interesting to compare its surface potential distribution with the one obtained in pulsed DBD.

The actuator was run for 15 seconds and then the surface potential was measured. The result is presented at figure 9.3.25.

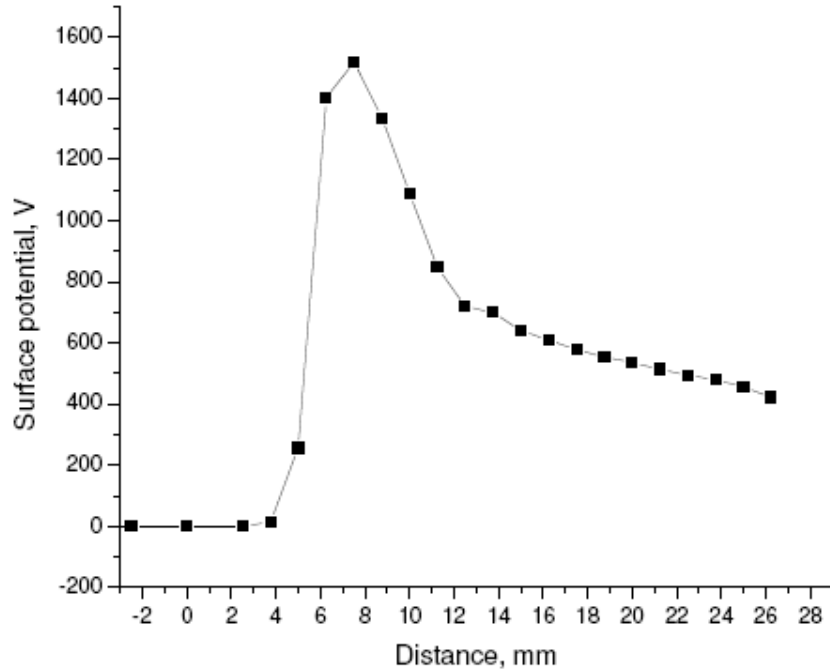


Figure 9.3.25: Surface potential distribution. Applied voltage profile: sinusoidal, $3[kHz]$, $10[kV]$ peak-to-peak. Electrodes edge at 0.

As can be seen in the figure, there is a significant charge build up on the dielectric in the region far downstream of the plasma. The plasma extends only a few millimeters downstream of the edge of the exposed electrode whereas the dielectric charges centimeters away from it.

The maximum surface potential ($1.5[kV]$) is comparable with the applied peak voltage ($5[kV]$). This means that the electric field of the surface charge can dramatically distort the electric field produced by the voltage applied to the electrodes.

Also, even though the applied voltage is symmetrical (sinusoidal with no bias voltage) the surface charge has a positive polarity. This may be due to the much higher mobility of electrons compared to positive ions which leads to a much higher electron current into the exposed electrode during the positive half cycle of the sinusoidal voltage compared to the positive ion current into the exposed electrode during negative half cycle. With this reasoning one might conclude that there is a total negative current into the exposed electrode and positive current flow from the DBD to infinity with the induced gas jet.

This picture is consistent with results from two further experiments.

In one, a $167[pF]$ capacitor was inserted in the circuit between the power supply and the exposed electrode (i.e. in series to the plasma). From the results, presented in figure 9.3.26, we can see that the potential of the exposed electrode (negative values of distance) is negative and maximum positive potential value decreased. It proves that on average there is a negative current to the exposed electrode.

In the second experiment a copper plate was placed in the plasma induced gas jet $3[cm]$ downstream the plasma. The plate was suspended in the air so it did not touch the actuator, and an electrostatic voltmeter was used to monitor its potential versus time. The result is shown in figure 9.3.27.

The figure reports that the plate gains a significant positive potential of $600[V]$. This is consistent with the positive current flux to a virtual electrode at infinity as in the case of an asymmetric RF discharge [78]. In addition the

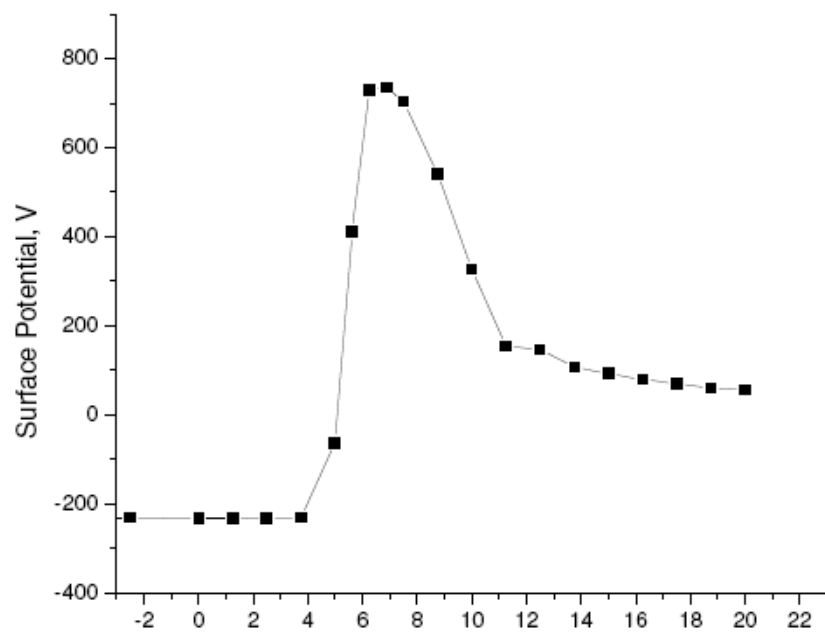


Figure 9.3.26: Surface potential distribution. Applied voltage profile: sinusoidal, $3[kHz]$, $10[kV]$ peak-to-peak. $C = 167[pF]$ in series with the plasma actuator. Electrodes edge at 0.

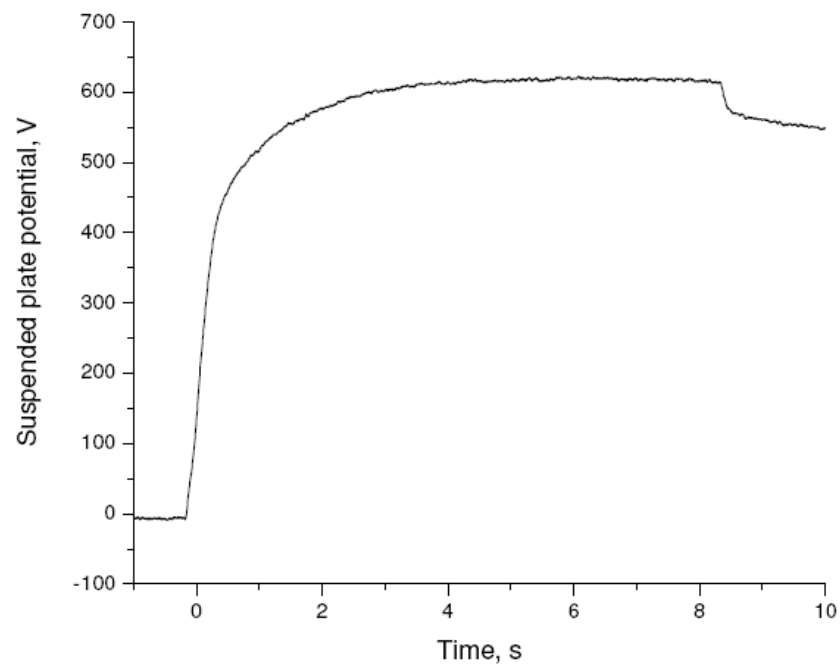


Figure 9.3.27: Suspended plate in the induced flow potential. A metallic plate with a surface of $S = 35[cm^2]$, put in the induced flow $3[cm]$ downstream gets positive charge. Applied voltage profile: sinusoidal, $3[kHz]$, $10[kV]$ peak-to-peak.

role of positive and negative oxygen molecular ions in the plasma, their attachment to the surface, and surface dominated mechanisms of charge build up and charge removal may be important. These effects need to be further studied.

We did then similar surface charge measurements with the actuator driven by pulses+bias.

In this set of experiments the voltage profile consisted of $3[kV]$ nanosecond ionization pulses superimposed on $\pm 2[kV]$ DC bias voltage. The ionization pulse repetition rate was $10[kHz]$ and the plasma was run for 15 seconds.

Results of surface potential measurements are presented at figure 9.3.28.

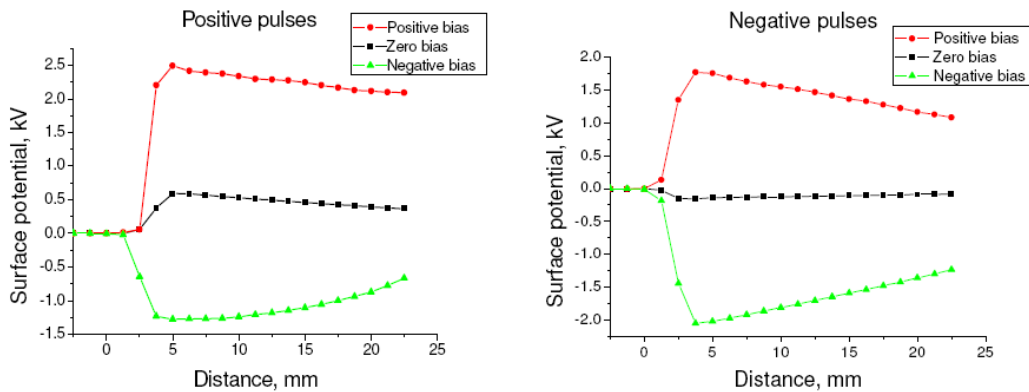


Figure 9.3.28: Surface potential distribution. Applied voltage profile: pulses + DC bias, $2[kV]$ DC bias, $3[kV]$ pulses at $10[kHz]$ PRR.

As in the case of a sinusoidal voltage, the charge builds up far downstream the plasma region. As we can see, the magnitude of the surface potential is primarily determined by the bias voltage. The ionization pulse voltage has a little effect on it. Even in presence of negative pulses the surface potential is due only to the applied bias.

We also examined how quickly the surface charge builds up.

At a selected DC bias voltage a pre-determined number of pulses were sent to the actuator and then the surface potential was measured. The results are shown at figure 9.3.29.

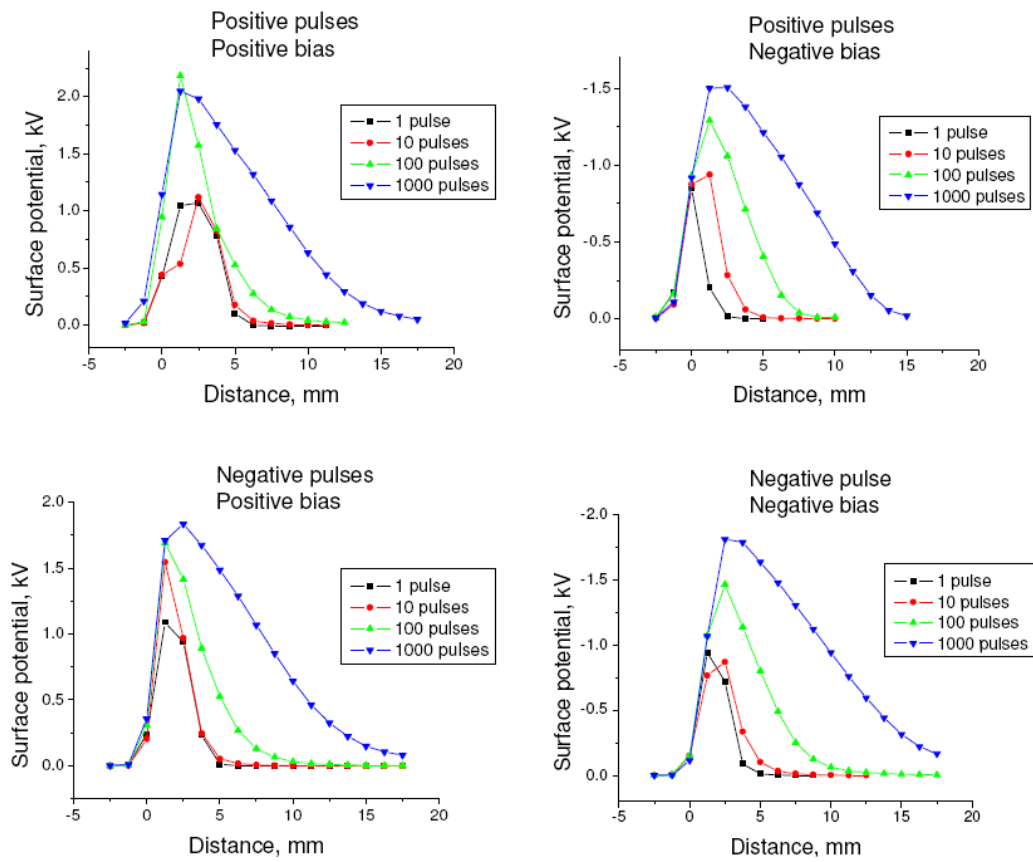


Figure 9.3.29: Surface potential for a fixed number of pulses. Applied voltage profile: pulses + DC bias, 2[kV] DC bias, 3[kV] pulses at 10[kHz] PRR.

Even though for a small number of pulses the accuracy of measurements is low, it can be seen that a single pulse creates a noticeable surface charge. As the number of pulses increases the surface charge builds up and moves farther away from the plasma.

The purpose of the next set of experiments was to study the evolution of the surface charge with time. The actuator was run for 30 seconds and then the surface charge was measured. The results are presented at figure 9.3.30.

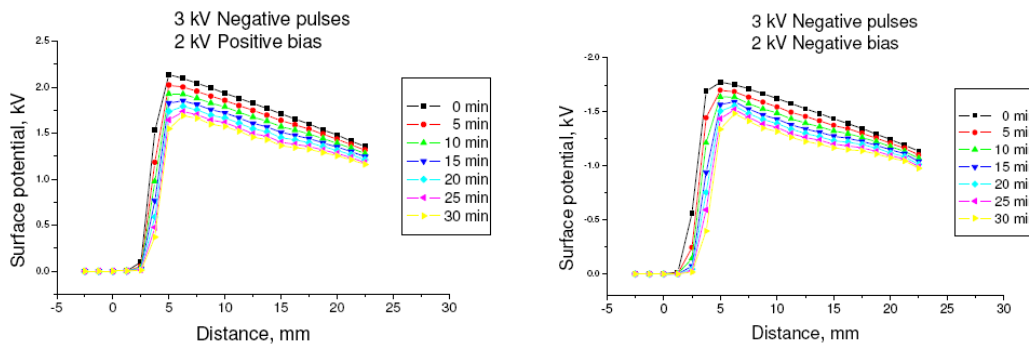


Figure 9.3.30: Surface potential versus time for positive (left side) and negative (right side) surface charges.

We can see that the charge stays on the surface for a very long time. In 30 minutes it depletes only by 15 ÷ 20 per cent. There is an uniform slow depletion from the surface in the region of low gradients of the charge concentration (far away from the actuator) and a relatively fast depletion close to the exposed electrode in the region of the high concentration gradients. Also, since the depletion occurs at the same rate for both positive and negative charge we can assume that the charged particles at the dielectric surface are positive and negative ions from the gas, but not electrons or holes.

Modified DBD actuator

All the above mentioned surface potential measurements both for sinusoidal or pulses supply waveform showed how there is a big amount of charge that

is stored on the dielectric surface. This charge shields the applied potential and decrease the actuator performances.

One possible way to remove the charge is applying an AC bias. Both Schlieren photograph and thrust measurements have demonstrated big improvements in the DBD actuator induced flow.

Here we present another way to remove the surface charge acting on the actuator design. In this configuration the dielectric covers only part of the lower electrode, for example 1[cm], leaving the rest of the electrode (another centimeter) exposed, as shown in figure 9.3.31. In such a case the surface charge can not build up far downstream and the DC bias voltage is not shielded.

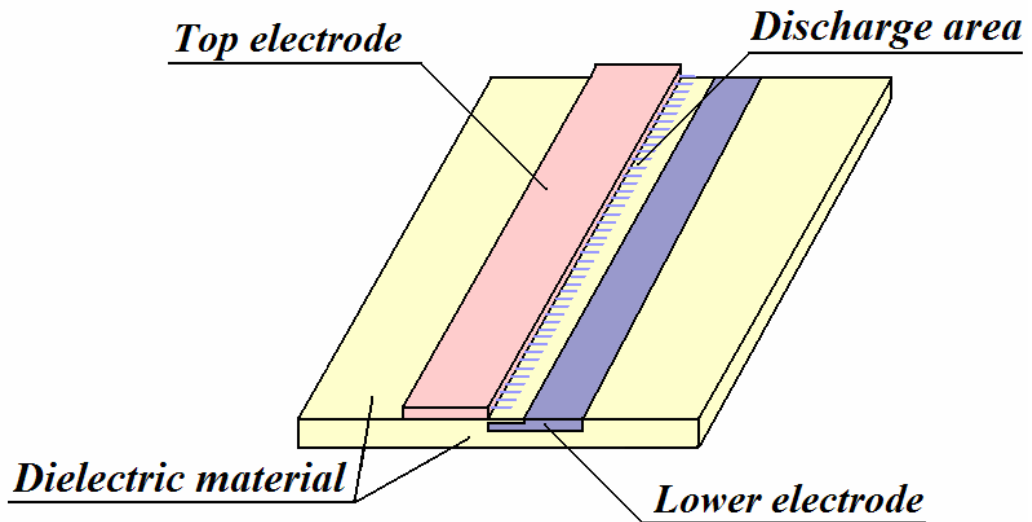


Figure 9.3.31: Modified DBD plasma actuator scheme.

Some preliminary results for 4[kV] positive DC bias voltage and 3[kV] negative pulses at 10[kHz] PRR are shown in figure 9.3.32.

Comparison between the thrust performances of this modified actuator and the “classical” one driven with different waveform has already been showed and commented in figure 9.3.24 at page 157. This figure is here reported for a better comparison.

First of all, the induced thrust has similar values as DBD plasma actuator

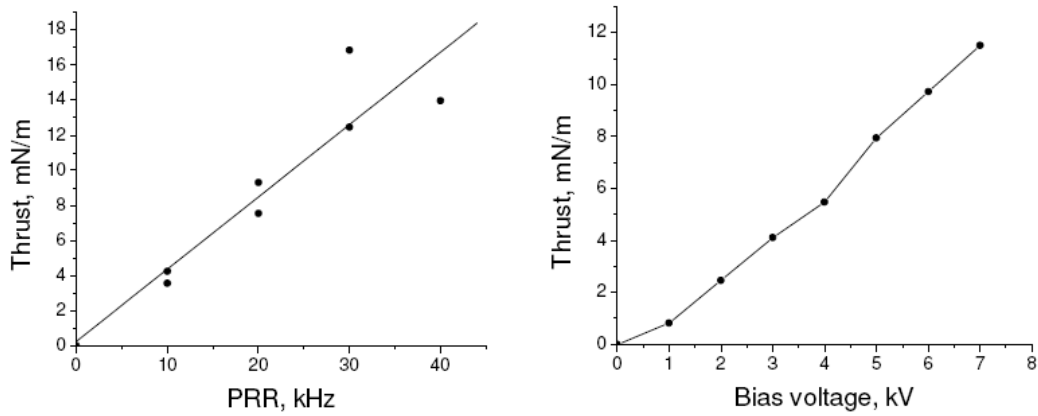


Figure 9.3.32: Modified DBD plasma actuator. Thrust versus PRR at 4[kV] positive DC bias voltage, 3[kV] negative pulses (left). Thrust versus bias voltage at 10[kHz] PRR, 3[kV] negative pulses (right).

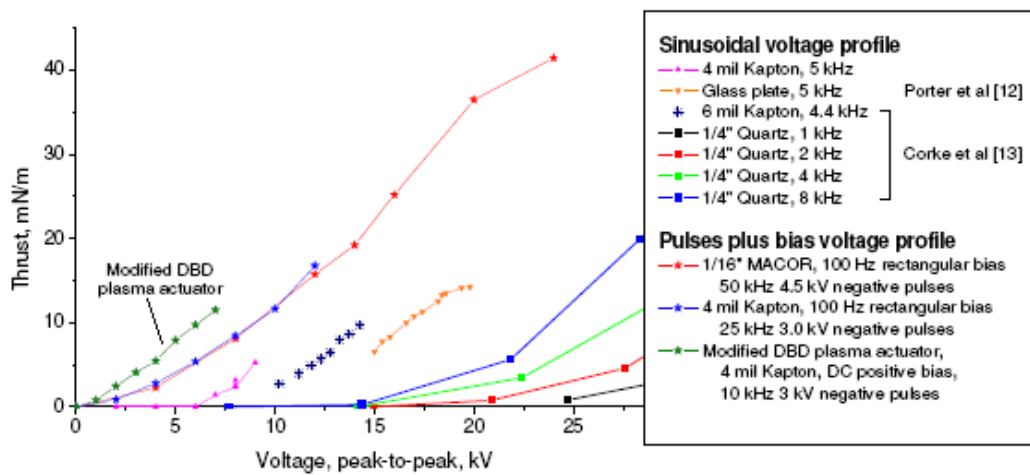


Figure 9.3.33: Pulses plus AC bias versus sinusoidal voltage: comparison of tangential body forces (zoomed in). Comparison between the modified actuator and the “classical” one. Comparison data were taken from [8, 9].

driven by repetitive pulses added to low frequency bias. Secondly, the effect scales linearly with the bias voltage and pulse repetition rate.

One of the advantages of such an actuator is a simpler bias voltage profile (DC but not AC). One should be careful with applying too high voltages, which can lead to an arcing over the dielectric. An inductance connected in series with the lower electrode might alleviate this problem.

Note that if a relatively thick dielectric layer is used, then simply cutting the dielectric layer off over a part of the lower electrode would produce a “step” which can be detrimental to aerodynamic drag. A simple modification of the idea would then be to put a third electrode on the surface and to electrically connect this electrode with the encapsulated electrode, rather than cutting the dielectric off.

Chapter 10

EHD experiments conclusions

In this chapter we present the conclusion remarks on the three-phase multi-electrodes actuators and then the ones related to the single DBD actuator driven by nano-pulses with a DC or an AC bias.

The EHD interaction effect and the momentum transfer caused by it inside the boundary layer on the surface of the actuator immersed in a subsonic air flow at atmospheric pressure had been experimentally investigated. The actuator in the first case was a three-phase multi-electrodes dielectric barrier discharge panel. The momentum transfer is observed to cause an acceleration of the flow in the boundary layer that increase with increases of the supply voltage and the frequency.

The acceleration of the flow produced by the actuator is stronger when the external flow velocity is lower. For a free stream velocity on of $1m/s$, gains of about $5m/s$ have been measured. This gain fell to $1m/s$ when the external flow velocity was $20m/s$. Moreover the three-phase system has been showed to be more reliable in boundary layer modification than one-phase ones. In this three-phase supply system the phase sequence has been varied showing the importance of the order of the phases in the momentum transfer efficiency.

A spectroscopic investigation allowed the determination of the rotational and vibrational temperatures of the plasma laying in the range of $320 \div 440^\circ K$

and of $3000 \div 3900^\circ K$ respectively. Thus a deviation from thermodynamic equilibrium has been found.

In the second experiment, the performances accomplished by means of a single electrode pair DBD plasma actuator driven by repetitive ionization pulses superimposed to DC or low frequency AC bias voltages in quiescent air have been studied. This supply system generates a non-self-sustained discharge in which the plasma is generated by repetitive short pulses, and the push action on the gas occurs mostly due to the low frequency bias voltage.

A non intrusive Schlieren diagnostic allowed to visualize the wall jets and the vortexes generated by the actuator driven in the burst mode. Both the nano-pulses and the DC bias voltage tests showed a low efficiency of the EHD interaction effect on the neutral gas because of the charge built up on the dielectric surface. The use of an AC bias allowed to remove the space charge and a larger effect of the actuator performance was observed.

The vortex behaviour and their velocity propagation have been studied when changing the polarity of the nano-pulses and the amplitude of both the nano-pulses and the bias voltage.

Several bias waveforms and the produced thrusts have been measured by means of a scales and compared with experimental data reported on the literature. Similar voltage amplitudes led to larger thrusts in our experiments when utilizing the nano-pulses supply system.

Furthermore, surface charge measurements led us to the realization of a modified DBD actuator able to obtain similar EHD interaction performances in comparison with the usual ones. In our case a DC bias in the place of a AC one had been utilized.

These EHD experiments show how the cold plasma, generated by an dielectric barrier discharge actuator, is able to modify substantially the boundary layer of a subsonic flow. The supply voltage waveform resulted to be one of the most important elements, able to increase the efficiency of the actuator EHD interaction effect.

Part III

MHD interaction experiments

Chapter 11

Introduction to MHD applications in the hypersonic flight

Hypersonic flight is nowadays receiving big improvements both in aeronautical and astronautical fields.

The Mach 10 flight of the concept unmanned aircraft *X43-A* performed in November 2004, is the demonstration of the possibility to realize a hypersonic atmospheric vehicle.

On parallel plane, the development of a Single Stage To Orbit (SSTO) vehicle is actually one of the main pre-requisite for the commercial exploitation of the space flight.

When aircrafts flies at high altitudes and high speeds, a gas-dynamic shock in front of the vehicle occurs. This causes a compression of the gas and a strong heating of it. The temperature reaches values up to $10000^{\circ}[K]$ or even larger than this value (especially for re-entry vehicle into the atmosphere). Close to the fuselage surface the temperature is sufficient to cause ionization of the gas and a weakly ionized plasma is formed. The presence of free charged particles suggested the use of electromagnetic forces able to modify the fluid-dynamics around the aircraft.

This purpose may be realized by means of the Magneto Hydro Dynamic interaction (MHD). Applying strong magnetic fields (of the order of the Tesla), the generation of body forces on the gas particles surrounding the plane is indeed possible [79, 80, 81, 82, 83, 84, 85, 86, 87].

In the last years several studies on the interaction of hypersonic flows with plasmas and with the MHD process have been realized [88, 89, 90, 91]. These studies mainly dealt with the control of the fluid dynamic phenomenon in the region between the shock front and the surface of the vehicle, and acquisition of knowledge about hypersonic shock layers.

In re-entry vehicles, MHD interaction could decrease thermal fluxes toward the fuselage walls and this may result in a thermal protection by means of an active magnetic shield [92, 93]. Moreover the aerodynamic drag and the vehicle trim will be modified.

Generally, in hypersonic aircrafts, flight control without the meaning of moving parts and the active control of shock waves inside air-breathing engines for a better combustion could be realized.

In the Russian *AJAX* project MHD techniques are utilized to by-pass kinetic energy of the working fluid inside the engine, from the supersonic diffuser to the nozzle [94, 95]. By doing this, the flow velocity in the combustion chamber is reduced to acceptable values, even for high Mach numbers.

The knowledge of the physics of the MHD-hypersonic flow interaction is essential for the application of this technology to the hypersonic flight.

So far, experimental investigations on the MHD interaction at high velocities have been performed in hypersonic wind tunnels by means of few research groups.

Bityurin *et al.* realized experiments on a blunt body with air as working fluid [96, 97]. Borghi *et al.* performed experiments in Argon studying the MHD fluid-dynamics modification over a wedge [10].

In this work we present a series of MHD experiments realized on an axial symmetric test body immersed in an argon Mach six plasma flow.

In the first part a complete aero-thermodynamic and electrical characteriza-

tion of the plasma flow is performed comparing experimental and numerical results.

In the second part imaging, pressure and electrical results on the MHD interaction measurements are reported.

Finally a numerical investigation is realized in order compare MHD results coming from measurements and simulations, in order to validate the numerical code developed by means of the Bologna University team.

Chapter 12

Non-intrusive nozzle characterization

12.1 Hypersonic wind-tunnel facility

The MHD hypersonic tests have been all performed inside the Alta High-Enthalpy Arc-heated hypersonic wind Tunnel (HEAT) facility that is able to produce Mach 6 flows in a low to medium Reynolds number range ($10^4 \div 10^6$). The characterization of the hypersonic plasma produced by HEAT is of fundamental importance for the numerical rebuilding of the experiments and for the interpretation of the experimental results.

In this section we will deal with the description of the wind-tunnel facility and its aero-thermodynamic characterization realized by the Alta team. The electrical characterization of the plasma jet will be largely discussed in the next two sections.

The core of the facility is the arc-heater chamber. A scheme of the fundamental components of this section is reported in figure 12.1.1.

In the wind-tunnel heating chamber, the gas is heated by means of an arc discharge powered by a $260[kW]$ DC power supply, delivering arc currents of up to $630[A]$ during running times of $20 \div 300[ms]$. A total specific enthalpy of up to $6[MJ/kg]$ with stagnation pressures of up to $9[bar]$ can be obtained.

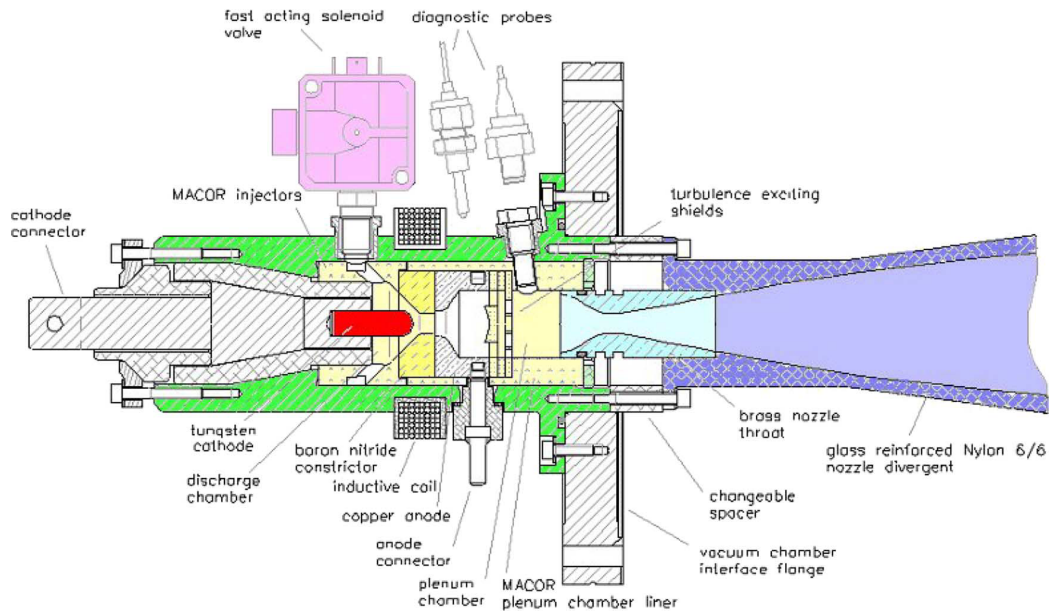


Figure 12.1.1: Arc-heater scheme.

The gas heater can be operated with air, nitrogen, argon, and CO_2 in a pulsed quasi-steady mode. At the exit of the settling chamber, a nozzle is mounted. A conical 5° nozzle with a throat diameter of $12[mm]$ was utilized. At the exit of the nozzle, the section diameter was $60[mm]$.

The wind tunnel (gas heater and nozzle) is installed on a vacuum test section of $600[mm]$ diameter. In the test section, there are optical accesses from all sides. This section is connected to a vacuum chamber with a volume of $4.1[m^3]$. Nozzle and vacuum chamber are shown in figure 12.1.2.

Before each run, the chamber is evacuated by means of four rotary pumps to reach an ultimate pressure of $10[Pa]$. The test gas used in this experiment is Argon. The nozzle Mach number was six.

A series of preliminary tests allowed the identification of the best conditions for the arc discharge. The arc voltage was between 55 and $65[V]$ for all the test conditions. Three typical test conditions with a heating-chamber pressure ranging between 0.5 and $0.7[bar]$ are considered. Pressure fluctuations are observed at pressures below $0.5[bar]$. This is due to the turbulence created in the heating chamber.



Figure 12.1.2: Nozzle mounted at the exit of the heating chamber (left-hand side) and Vacuum chamber of HEAT.

Four test conditions are reported in table 12.1.1.

Conditions	A	B	C	D
Mach number [-]	6.16	6.19	6.10	6.08
Mass flow rate [g/s]	4.46	5.34	6.43	14.51
Arc voltage [V]	55.30	58.61	64.55	90.60
Arc current [A]	518.5	509.4	520.0	515.0
Stagnation pressure [mbar]	523	589	653	1170
Stagnation temperature [K]	4456	3936	3344	2109

Table 12.1.1: Flow characteristic for the test conditions.

In the first three columns of the table, the three typical conditions chosen for the MHD experiments, with the Mach number, the mass flow rate, the arc voltage and current, and the stagnation pressure and temperature, are reported. The fourth condition which is reported in the table, refers to an ulterior test for the characterization of the plasma.

The stagnation pressure and temperature are given by the pressure measured in the heating chamber.

For the aero-thermodynamic characterization of the produced flow, the following set of instruments was used:

- two absolute *Kulite XCS-062* sensors in the tunnel settling chamber

(one with a 250[psi] FSO and one 100[psi]),

- a supersonic pitot probe equipped with a *Kulite XCS-062-5A* miniaturised pressure sensor for high frequency Mach number retrieval [98],
- a hemispheric stagnation point temperature probe equipped with a *MEDTHERM* coaxial thermocouple for the stagnation enthalpy and total enthalpy retrieval through the Sutton-Graves relations [99].

Due to the relatively high variance of the flow conditions during the hot runs (about 15%), at each gas condition in table 12.1.1, the runs were repeated from five to ten times, and the average values of the measured signals were considered. Accuracies of about 3% were obtained in all pressure measurements.

The total enthalpy was evaluated from the arc-discharge power and compared with the values obtained from the stagnation temperature measured in the test section. The total-enthalpy error was $\pm 5\% \div 10\%$.

The plasma jet has been fluid-dynamic characterized by the Alta team. The results are showed as follow.

The mapping of the nozzle flow was done for the four conditions in table 12.1.1.

The characterization activity allowed to the determination of the core-flow dimensions, the axial-symmetry degree of the flow, the fluctuations of the Mach number, and the temperature and repeatability of the test conditions. In figure 12.1.3, a typical radial profile of the Mach number is shown. Here, normalized values are reported.

In figure 12.1.4 it is shown the map of the Mach number in the exit region. Both figures are obtained at condition *A*.

In general, for all of the considered conditions, the flow can be considered axial symmetrical and uniform for a diameter of about 40[mm] (the Mach

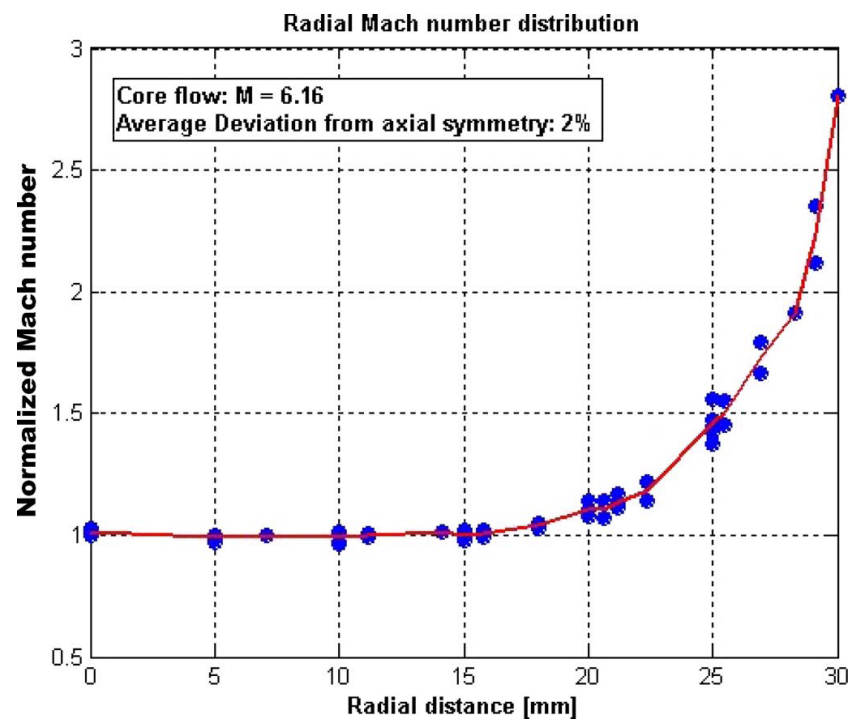


Figure 12.1.3: Mach number radial profile at the nozzle exit for condition A: (blue dots) measured values and (red line) mean profile.

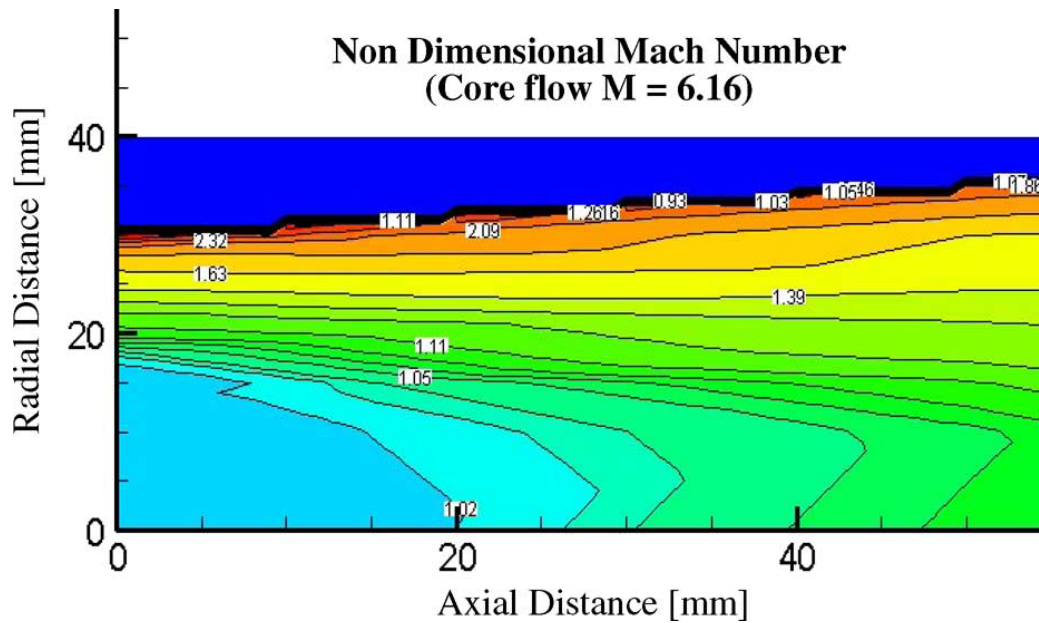


Figure 12.1.4: Experimental Mach number mapping in the test section after the nozzle exit at condition A.

number at 20[mm] is always within 9 ÷ 10% higher than the value of the core flow), with a slight non-symmetry starting at 18[mm] (maximum value of the asymmetry 4%).

The flow expansion continues in the test section with an increase of 5 % in the first 50[mm]. Relatively high differences in total enthalpy level can be individuated comparing different runs, probably due to the complicate flow pattern that is created in the settling chamber at this low pressure levels.

Relatively high differences in total-enthalpy level can be individuated by comparing different runs, probably due to the nonuniform flow pattern created in the heating chamber at this low pressure levels. This leads to the need of several repetitions of the runs (at least five) at each test condition in order to gather statistically significant samples.

12.2 Diagnostic setup

The fluid-dynamic measures of the plasma jet gave us information about velocity, pressure and temperature of the Mach six flow.

For a more complete comprehension of the feature of the plasma, an electrical characterization have been realized in order to infer important plasma parameters as the electron temperature and electron number density.

Two different plasma diagnostics have been applied to characterize the system.

In the arc heater plenum chamber, optical emission spectroscopy has been utilized to obtain both electron excitation temperature and electron density. Excitation temperature, which has been measured by means of the Boltzmann plots of continuum and lines spectra, can be considered a good estimation of electron temperature. Electron number density has been evaluated from H_α and H_β Stark broadening and from continuum.

At the nozzle exit, pressure and temperature are quite low, and the plasma develops a strong non equilibrium behaviour. Most notably, the electron distribution function develops a strong non-maxwellian behaviour. Thus, the measurements obtained by means of emission spectroscopy are hardly interpretable and necessitate a plasma kinetic modeling.

Consequently, microwave absorption diagnostic technique, as it shows a very weak dependence to electron energy distribution, has been adopted to measure the electron number density at the exit of the nozzle.

Spectroscopic setup

The spectroscopic setup is the same used for the 3-phase EHD actuator (see page 94 for instrumental and scheme details).

The light has been collected by two identical lenses with focal ratio equal to $f4$, one positioned inside the plenum chamber, the other one at the exit of the nozzle inside the vacuum chamber. In this way the plasma has been characterized before and after the expansion (figure 12.2.1).

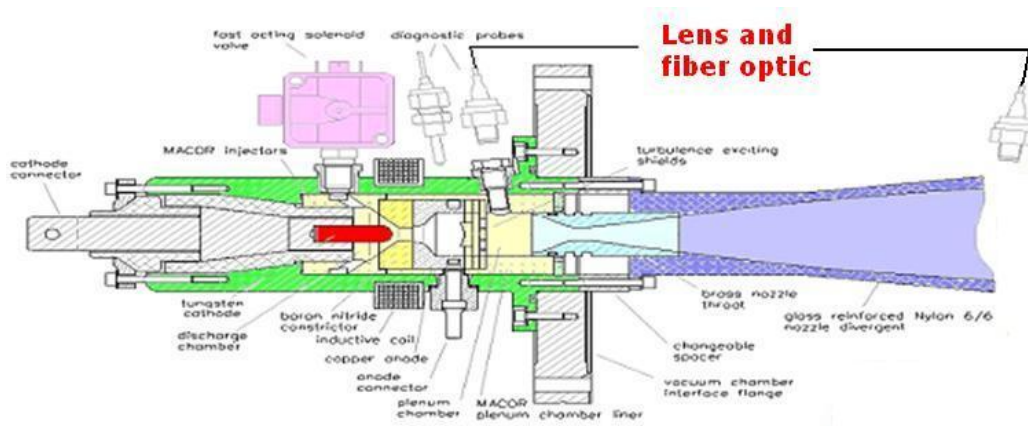


Figure 12.2.1: Position of the lenses for the spectroscopic measurements.

Both lenses delivered the light to the spectrograph by means of fiber optic. For the lens inside the vacuum chamber, a vacuum fiber optic feed-through has been necessary.

In all the conditions an holographic $1200[\text{lines}/\text{mm}]$ grating has been used, apart in the case of H_α and H_β emission lines in which the higher possible resolution was necessary and a $2400[\text{lines}/\text{mm}]$ grating was utilized.

For all the plasma conditions several spectra have been captured in order to obtain statistically significant samples.

For conditions *A*, *B*, and *C*, a $4[\text{ms}]$ exposure time after $100[\text{ms}]$ from the arc heater ignition was chosen. For condition *D*, the same exposure time was recorded at $100[\text{ms}]$, at $200[\text{ms}]$ and $290[\text{ms}]$ delay from the arc ignition, in order to time scan the behaviour of the plasma into the plenum chamber.

Microwave absorption setup

The absorption of microwave by means of the plasma jet has been detected putting two $15[\text{dB}]$ horn antennas, designed for an optimal working frequency between 12 and $18[\text{GHz}]$, inside the vacuum vessel at the two sides of the plasma flow at about $50[\text{mm}]$ to the nozzle exit (figure 12.2.2).

The aperture of the antenna was $76 \times 80[\text{mm}]$ with a length of $160[\text{mm}]$.

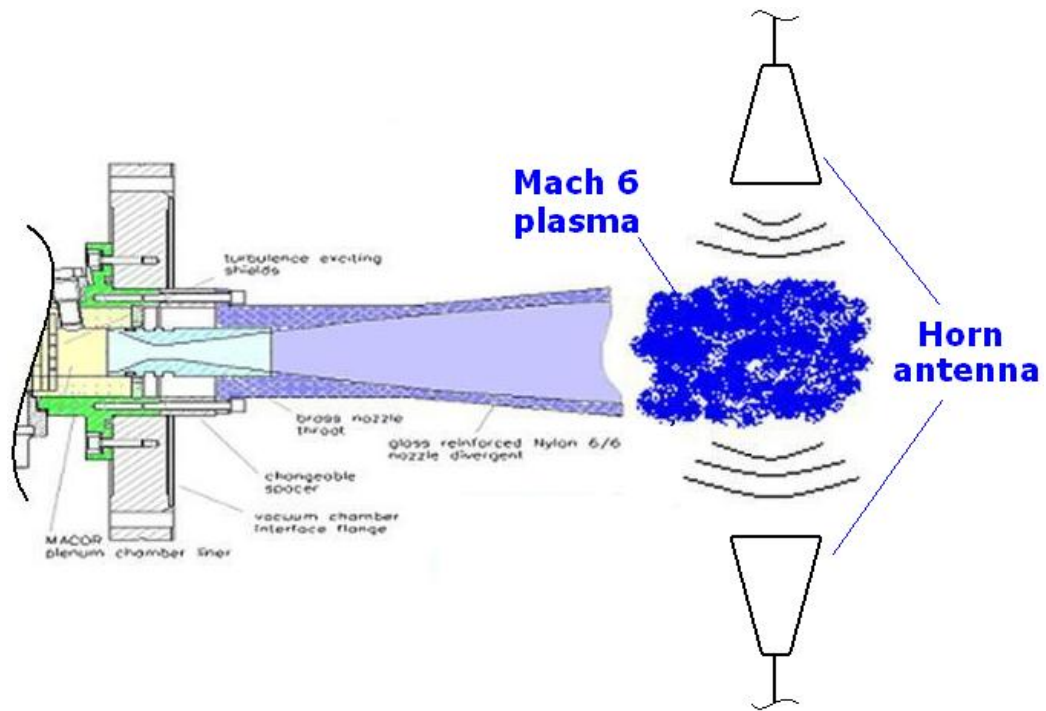


Figure 12.2.2: Horn antenna position for microwave absorption measurements.

The distance from one antenna to the other has set to $100[mm]$ that was the lower possible distance considering a plasma flow diameter in the order of $80[mm]$.

One antenna was used as source of microwave and was connected to a *Gigatronics 1018-009* microwave generator, able to produce a non-modulated microwave signal from $50[MHz]$ to $18.5[GHz]$ with a power exit of $10[dBm]$. The other antenna, used as a receiver, has been connected to an *HP8472A* crystal detector, with a pass band between $10[MHz]$ and $18.5[GHz]$. The crystal detector signal was carried out by a BNC cable and read by a digital oscilloscope, in order to time resolve the signal. The time response of this detector is in the order of tens of nanosecond, several order of magnitude higher than the sampling frequency of the oscilloscope.

In order to enhance the signal to noise ratio, at all the microwave conditions the processed transmission factor was the average of seven different signals, recorded at the same arc heater condition.

12.3 Interpretation of the results

Inside the plenum chamber electron density and electron temperature have been evaluated by means of spectroscopic measurements (the only one that are allowed).

In the free stream, both spectroscopy and microwave absorption have been used in order to estimate the electron density. Unfortunately for the first three conditions chosen for the experiments only spectroscopy is suitable.

The fourth condition *D* has been chosen in order to compare both spectroscopic and microwave absorption measurements.

Measurements in conditions *A*, *B* and *C*

An estimation of the electron temperature is given from the analysis of the emission spectra. It was measured by discrete emission of Ar I and Ar II lines, by the continuum radiation and by a line to continuum method [100]. Ar I lines seems not to be useful for any analysis, because they showed to be self-absorbed.

A typical spectra captured in the plenum chamber is showed in figure 12.3.1.

Ar II Boltzmann plots are quite well aligned (figure 12.3.2), pointing out that the plasma should not be far from a pLTE (Partial-Local-Thermodynamic-Equilibrium) condition.

Temperature measured by continuum is not far from the one measured by Ar II (table 12.3.1).

The temperature values obtained from line to continuum ratio was about 20% higher with respect to the calculated temperature by means of other methods in all conditions. A deviation from the Maxwellian distribution can be responsible of the incoherence of this last result.

Data from Ar II lines and continuum measurements were in well agreement

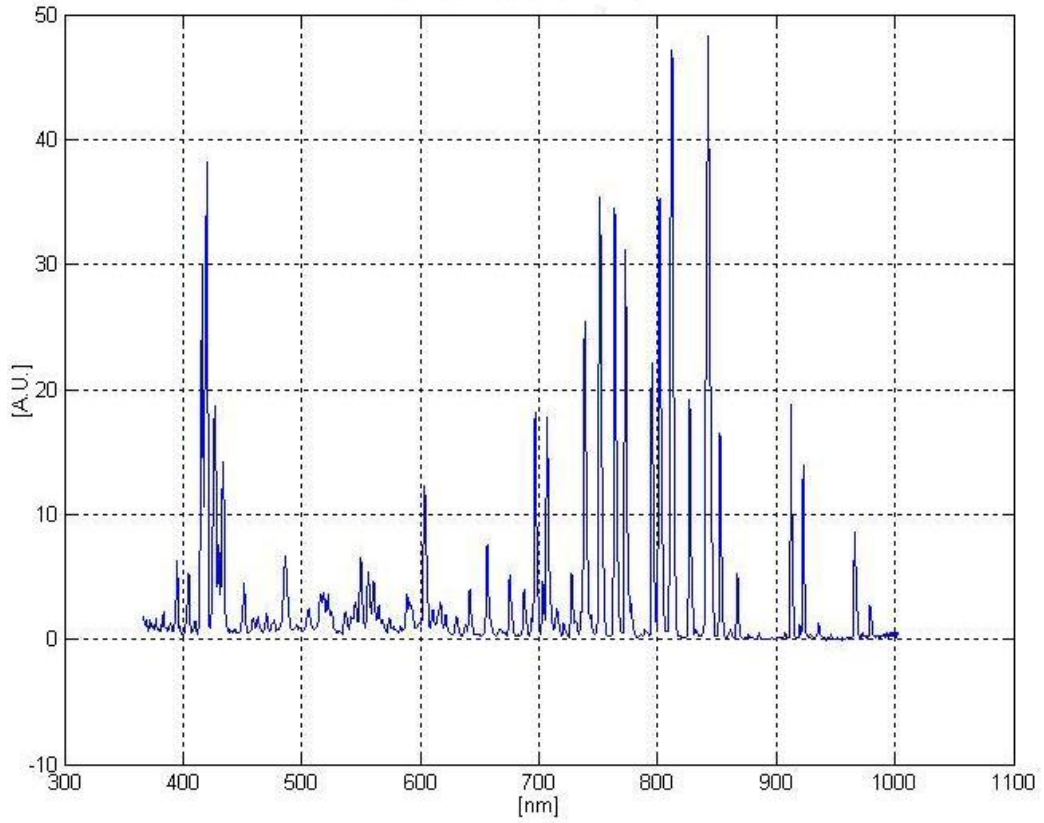


Figure 12.3.1: Argon spectra of the plenum chamber.

Conditions	Ar II [eV]	Continuum [eV]	Ar I (430[nm]) to continuum [eV]
A	0.737968	0.745046766	0.920372285
B	0.698636	0.70043570	0.80317132
C	1.06438	0.646607617	0.749741468

Table 12.3.1: Electron temperature in the plenum chamber for the conditions *A*, *B* and *C*. Delay time 100[ms].

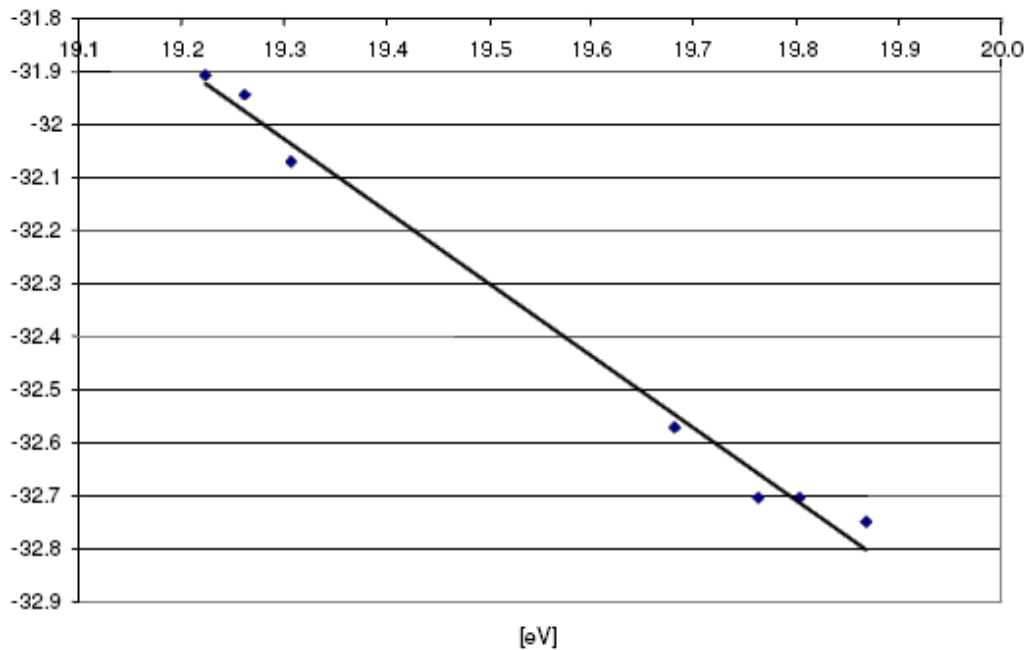


Figure 12.3.2: Boltzmann Plot for Ar II, at the plenum pressure condition A.

the ones with the others. The values lied between 0.6 and 0.8[eV], being the temperature higher for lower plenum chamber pressure.

Also the electron number density has been evaluated by means of several methods.

One is the Stark broadening of hydrogen (always present as impurity) lines. In figure 12.3.3 is showed an H_{β} line profile.

Of the various line-broadening mechanisms those due to the Doppler effect and Stark effect have attained practical importance for plasma diagnostic.

While the mechanism of Doppler broadening was readily understood, the development of an adequate Stark-broadening theory proved to be quite difficult. The shape of this profile depends on the density of charged particles surrounding the emitters: only with the recent development in computers science, it was possible to calculate a set of tables that is including both electrons and ion dynamic effects, leading to a more correct estimation of

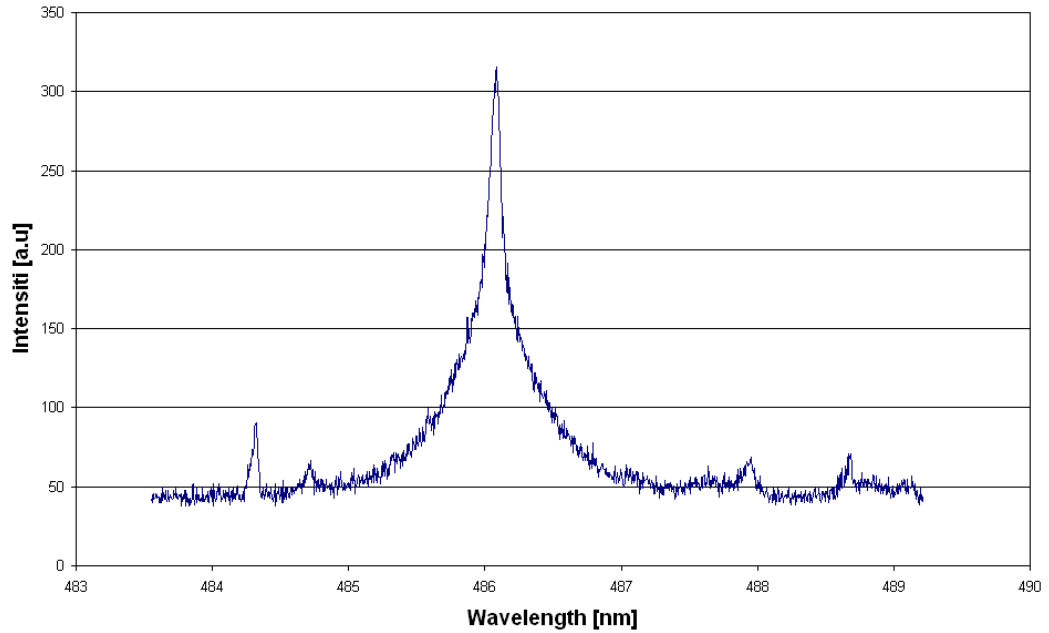


Figure 12.3.3: Spectra captured in the plenum chamber in the condition *A*. The H_{β} line at $486.1[\text{nm}]$ is easily visible.

the electron number density [101].

The line profiles has been deconvolved to subtract the Gaussian broadening due to the instrument and to the Doppler effect. In the working condition inside the plenum chamber, the lorentzian part of the line profile due to Stark effect is higher than the broadening due to the other mechanisms by more than an order of magnitude, allowing a precise processing of the measurements results. Various data tables are available in literature for the interpretation of hydrogen lines.

Electron number density has been also measured from continuum emission. For the estimations of n_e , the electron temperature has to be known: the temperature obtained by averaging the Ar I and the continuum measurements has been used.

Finally the electron number density has also been evaluated utilizing the Saha equation. The good agreement obtained validate the temperature and number density measurements. The measured values of the electron number

density stretch in the low $10^{21}[m^{-3}]$ range for conditions A , B , and C , as shown in table 12.3.2.

Conditions	H_α	H_β	Griem H_β	Continuum	ArI to continuum	Saha
A	$8.50 \cdot 10^{21}$	$2.81 \cdot 10^{21}$	$3.00 \cdot 10^{21}$	$3.20 \cdot 10^{21}$	$1.55 \cdot 10^{22}$	$3.35 \cdot 10^{21}$
B	$8.05 \cdot 10^{21}$	$2.38 \cdot 10^{21}$	$2.70 \cdot 10^{21}$	$2.80 \cdot 10^{21}$	$1.39 \cdot 10^{22}$	$1.89 \cdot 10^{21}$
C	$6.12 \cdot 10^{21}$	$1.84 \cdot 10^{21}$	$1.90 \cdot 10^{21}$	$1.30 \cdot 10^{21}$	$1.20 \cdot 10^{22}$	$8.00 \cdot 10^{20}$

Table 12.3.2: Electron number density [$part/m^3$] in the plenum chamber for the conditions A , B and C . Delay time 100[ms].

The evaluation of electron number density from Stark broadening can be done by means of some diagnosis tables: the coefficient of that tables are far well know for H_β line, but are not for H_α . So the most accurate measures should be the one coming from H_β and continuum radiation. Difference between H_β and Griem H_β are due to the use of two different diagnose tables. The table confirmed these assumptions: electron density from H_β and continuum are in well agreement with the electron density calculated by means of the Saha equation.

A spectroscopic investigation suitable for electron density evaluation, has been realized also in the plasma plume. Here it was measured an hydrogen broadening that was narrower than the one related to an electron number density of $10^{20}[part/m^3]$. With this value of electron density, Stark mechanism is not the ruling broadening effect, so this is the validity limit of the tables used.

Moreover, line broadening starts to become comparable to the instrument broadening caused by the resolution of the spectrograph.

We can so affirm that the value $10^{20}[part/m^3]$ is the lower limit in the elec-

tron number density evaluable with our spectroscopy setup.

In order to measure the electron density, microwave absorption has been used.

In all the conditions and with all the microwave frequencies (also with the highest one of 18[GHz]) the microwave signal was totally absorbed by the plasma (figure 12.3.4).

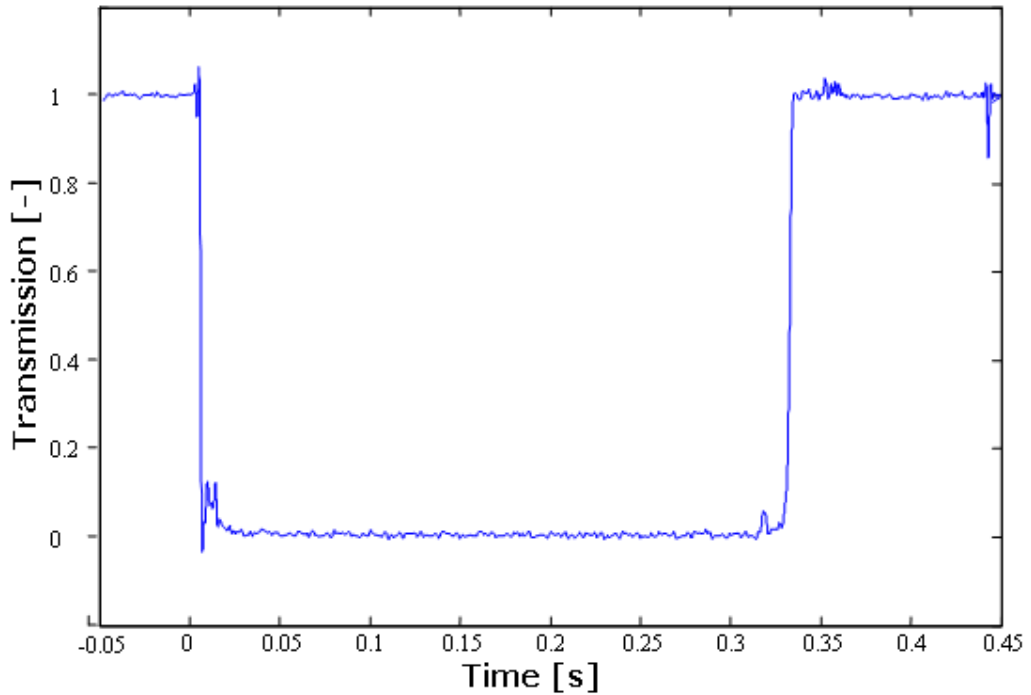


Figure 12.3.4: Microwave transmission signal for conditions *A*, *B*, *C*. At time equal to zero the plasma is ignited.

A total absorption does not allow to an electron density measurement. The only thing that we can say is that its value is greater than the critical electron density.

From the expression at page 14 and considering a maximum microwave frequency of 18[GHz], the critical electron density is $4.24 \cdot 10^{18}[\text{part}/\text{m}^3]$.

For condition *A*, *B* and *C* it was only possible to state that the plume electron number density lay between $4.24 \cdot 10^{18}[\text{particles}/\text{m}^3]$ and $10^{20}[\text{part}/\text{m}^3]$.

For a comparison between spectroscopic and microwave absorption electron

density evaluation, we introduced the condition D .

Measurements in conditions D

At the D condition it was possible to record at the same time the electron number density both at the throat of the nozzle and at its exit. With an higher mass flow rate, the gas was colder and consequently the electron number density was lower.

As the microwave diagnostic allows to time scan the electron density, for the emission spectroscopy three different delay time from the arc ignition were chosen, in order to complain a time dependence of the plasma parameters. It was possible to measure electron excitation temperature only by means of continuum emission: the plasma emission was much more weaker than at the conditions A , B and C . For this reason, it was not possible to record all the lines needed for a reliable Boltzmann plot. The electron temperature in the plenum chamber for the D condition is reported in table 12.3.3.

	Continuum
[ms]	[eV]
100	0.580711
200	0.5885506
290	0.597995

Table 12.3.3: Electron excitation temperature in the plenum chamber for the D condition esteemed by continuum emission.

Electron number density has been measured in the plenum chamber by means of the same techniques mentioned earlier. Again there was the validation from the Saha equation, estimated by means of the measured excitation temperature.

In the plasma jet the microwaves have been partially absorbed so a time

resolved electron number density could be measured.

From the complete absorption of the microwave beam at a certain frequency it was then computed the electron number density in the plasma plume. Came out that the electron collision frequency had a very weak time dependence: it changed from 2.9 to 3.2[GHz], according to the electron excitation temperature and gas pressure.

The time resolved electron density in the plasma plume obtained by means of microwave absorption is reported in figure 12.3.5. At the three lower frequencies of 9.97, 10.5 and 14.5[GHz] the microwave beam is completely absorbed. At the higher values of 17.72 and 18.5[GHz] there is partially absorption. It was so possible to obtain a correct measurement, correlating out the informations from the saturated signals to the ones with a partial absorption. A non stationary time behaviour of the electron density can be easily recognized.

Unfortunately, arc heater conditions were not exactly the same for all the experiments.

As the arc heater warm up, the power injected into the arc rose up, as it is possible to see in figure 12.3.6. So electron number density is never the same, both in the plenum and in the plume.

This fact could give a reason on the difference between the measure obtained from 18.5[GHz] and 16.72[GHz], that in principle should be the same at least in the first transient of the experiment (from 0 to 200[ms]), where the 16.72[GHz] microwave is far from the critical density.

Electron densities measured inside the plenum chamber and the ones detected in the free stream plasma are showed in table 12.3.4.

Evaluating the ratio between the electron density in the plenum chamber and at the nozzle exit, one obtain a value ranging between 90 and 120, depending on which evaluation method is chosen for the electron density in the plenum chamber.

According to the classical theory of the nozzles, the ratio between the inlet

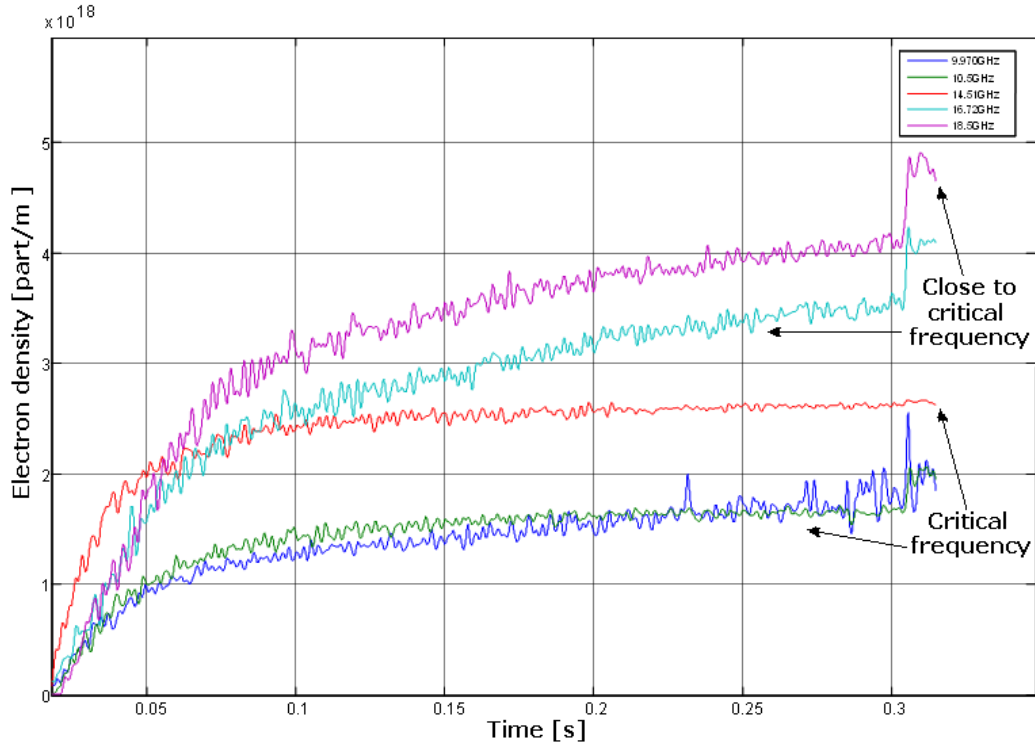


Figure 12.3.5: Time resolved electron number density in the plasma plume measured by means of different microwave frequencies. The electron-heavy collision frequency is in the range $2.9 \div 3.2 [GHz]$.

Run time [m/s]	Plenum chamber			Nozzle exit
	H_β	Griem H_β	Saha	Microwave
100	3.67×10^{20}	3.54×10^{20}	3.04×10^{20}	3.15×10^{18}
200	4.60×10^{20}	4.90×10^{20}	3.42×10^{20}	3.82×10^{18}
290	5.13×10^{20}	5.30×10^{20}	4.61×10^{20}	4.30×10^{18}

Table 12.3.4: Electron number density measured in plenum chamber and the nozzle exit for condition D .

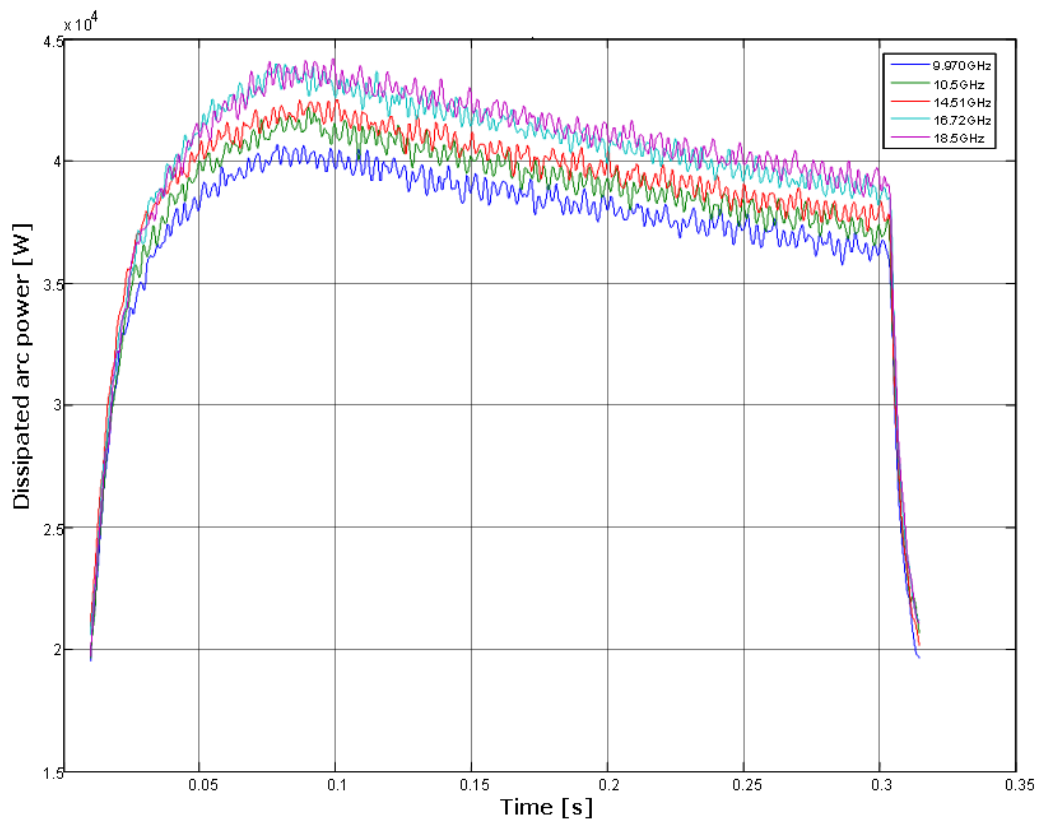


Figure 12.3.6: Dissipated arc power and microwave frequency used for the electron density estimation.

and exit mass density is given by the equation:

$$\frac{\rho_0}{\rho} = \left(1 - \frac{\gamma - 1}{2} M^2\right)^{1/(\gamma-1)}. \quad (12.3.1)$$

For the D condition the ratio is around 80. Comparing this result with the corresponding ratio for the electron densities, a condition of frozen ionization degree along the expansion in the nozzle can be deduced.

Nozzle simulation

In this section we are trying to reproduce, at least qualitatively, the experimental data obtained in the HEAT apparatus for the conditions listed in table 12.1.1 at page 179.

The numerical model solves the quasi two-dimensional steady Euler equations for the nozzle expansion using the method described in [102].

The model has been coupled with the state to state kinetics for different mixtures, for example air [103, 104] and Argon [105].

The internal state kinetics has been coupled with the Boltzmann equation for free electrons [104, 105]. Using this approach we can calculate internal state and electron distributions, allowing also non-Boltzmann and non-Maxwell behaviours.

In such cases it is not possible to describe the distribution properties using one or more temperatures. An important consequence is that for strong non equilibrium distributions the global rate coefficients, calculated as the mean over the distributions, does not follow the Arrhenius trend.

This contribution is more effective when metastable states are considered [103], resulting in appreciable variations (up to 20%) at the nozzle exit for fluid dynamic quantities, such as pressure and Mach number.

Nevertheless, due to the high pressure at the nozzle inlet, a global equilibrium is always considered.

Recent experiments [10, 106] seem to be incompatible with the assumption of

global equilibrium in the plenum chamber, showing that the electron concentration on a ramp positioned at the nozzle exit is higher than that predicted by calculations considering equilibrium at the nozzle inlet. As a consequence we perform calculations considering non-equilibrium electron concentration and temperature in the plenum chamber [10, 106]. This assumption was not supported by direct observation, but was able to predict the anomalous electron concentration. For arc heated wind tunnels, this assumption is not exotic, because an electric arc produces a plasma with electron temperature much higher than the gas, resulting also in non equilibrium ionization.

For molecular plasmas, electron impact induced processes related with molecule-molecule and atom-molecule collisions. For this reason the plasma has the time to reach global equilibrium before it enters the nozzle.

On the other hand, for noble gas plasmas, only electron-atom collisions and radiative processes are effective, therefore the time necessary to instaurate equilibrium is longer than the time the plasma needs to reach the nozzle, resulting in a non-equilibrium regime at the nozzle inlet.

These non equilibrium conditions have been observed by direct measurements in the plenum chamber, as discussed in the previous Section.

Here we will characterize the nozzle flow starting from the conditions measured experimentally in the plenum chamber.

The model will consider three species: Ar , with ground and the metastable state, Ar^+ and electrons. Electron impact and atom-atom excitation and ionization are considered as processes. The initial composition and electron and internal temperatures, listed in table 12.3.5, are taken from experimental measurements (see table 12.1.1 at page 179).

Parameters	A	B	C	D
n [$10^{23}/m^3$]	8.7376	11.4411	14.5521	39.077
n_e [$10^{20}/m^3$]	54.900	36.7001	13.000	3.0400
$T_i = T_e$ [K]	8642.0	8120.0	7505.2	673936

Table 12.3.5: Initial simulation conditions in the test cases listed in table 12.1.1

The initial distributions are supposed to be as Maxwell and Boltzmann at the given internal (T_i) and electron (T_e) temperatures. To allow the assessment of the distributions to a pseudo-stationary state, we prolonged the nozzle inlet of one centimeter with a constant section equal to that one at the nozzle inlet.

Next calculation should reproduce conditions in the plenum chamber.

The electron energy distribution function (eedf) along the nozzle, for cases *A* and *D*, is reported in figure 12.3.7. The molar fractions of the Ar metastable and electrons for all the cases are showed in figure 12.3.8.

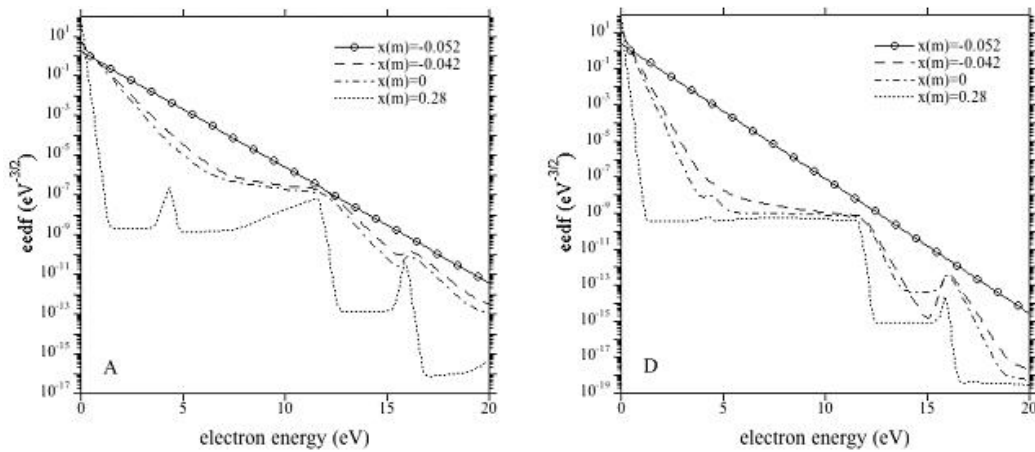


Figure 12.3.7: Electron energy distribution functions along the nozzle for cases *A* and *D* (input data from table 12.3.5). $X = 0$ is the throat position, $x = -0.042$ is the nozzle inlet, $x = 0.28$ is the nozzle exit.

The calculations show us how, in the nozzle inlet, there are, at least, two different leading temperatures (at least two different exponential behaviour are visible). One that characterize the low energy distribution and one related to the excitation temperature of the metastable state, which affect the distribution tails.

The metastable temperature cannot be considered the temperature of the radiative levels but it should be higher.

In table 12.3.6 we report the electron temperature calculated as the characteristic electron energy [107] and the metastable temperature at nozzle inlet

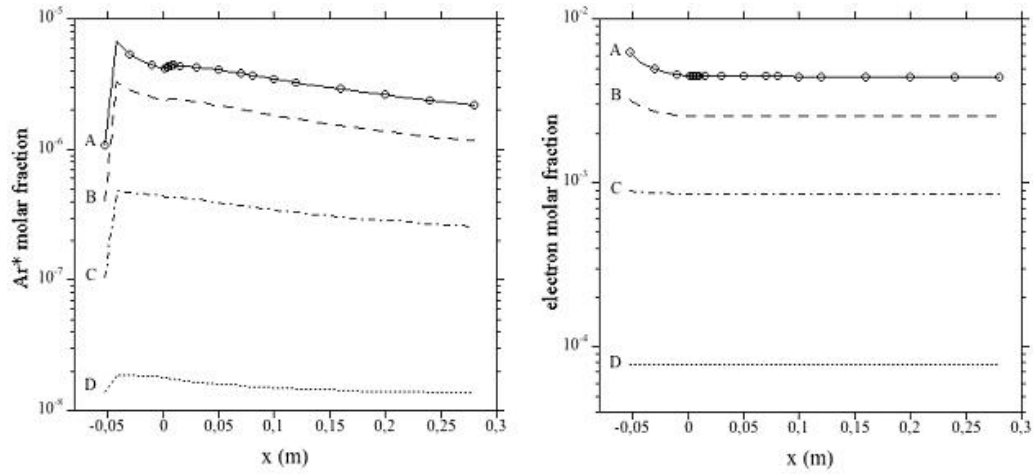


Figure 12.3.8: Molar fractions profiles of Ar metastable and electron (input data from table 12.3.5)

and at the nozzle exit. Moreover we present also the electron number density at the nozzle exit.

The two temperatures are different from each other because the processes that determine them are different, elastic collisions for the electron temperature and the inelastic and superelastic processes for the excitation temperature.

Parameters	A	B	C	D
T_e inlet [ev]	0.50612	0.44715	0.38882	0.254379
T_i inlet [ev]	0.84365	0.80249	0.70697	0.58966
T_e exit [ev]	0.21615	0.22150	0.22684	0.22985
T_i exit [ev]	0.78032	0.74787	0.68124	0.58051
n_e exit [$10^{18}/m^3$]	75.111	58.399	24.679	3.9235

Table 12.3.6: Inlet and exit electron (T_e) and excitation (T_i) temperatures and electron concentration at the nozzle exit in the test cases listed in table 12.1.1.

The trends of the electron temperatures and the electron density at the nozzle exit reproduce the experimental results qualitatively (see tables 12.3.1,

12.3.2 and 12.3.4 for a comparison).

The differences can be attributed to many factors.

The most important, apart the experimental errors, are due to the difficulties in reproducing exactly the experimental conditions. In fact, the measured temperatures are based on the assumption that the distributions are Boltzmann, in contradiction with the calculations.

Moreover experimental results contain informations about non-equilibrium distributions. In fact in table 12.3.1 the inlet electron temperature measured by Boltzmann plot from discrete lines and by continuum emission are different; it should be considered that the continuum spectrum is due determined by radiative recombination, which involves low energy electrons, while line spectrum is determined by the electrons above the excitation energy.

We could consider as an index of excitation the metastable temperature. Under these assumptions the T_e and T_i reproduce qualitatively the two measured temperatures.

The different meaning of temperatures makes the plenum chamber conditions difficult to determine. Some improvements to this approach could be to extend the state-to-state kinetic model also to radiative states.

Chapter 13

MHD conical test body experiment

13.1 Test body magnetic configuration

In the previous chapter, the plasma Mach six flow have been characterized both from the aero-thermodynamic and the electrical point of view. The three examined conditions A , B and C will be then used for the MHD experiments. The determination of the shape and the magnetic configuration of the test body is a crucial point.

In order to simulate the re-entry of a hypersonic vehicle into the atmosphere the test body had been designed for the operation at low plasma densities.

In these conditions the plasma is characterized by high values of the electron mobility and, thus, of the Hall parameter. Hence it is advisable to exploit the Hall component of the electric field (i.e. the component of the electric field parallel to the flow velocity) to sustain the current density which generates the MHD interaction.

In order to do this and to obtain a strong Lorenz force against the shock front, the Faraday current has to be as high as possible. This can be realized by means of the short circuiting of it.

In a recent work [10], the experimental results of the MHD interaction in

hypersonic regimes on a test body with an Hall electrodynamic configuration have been presented. A plane test body placed oblique against the flow and with an external magnetic field perpendicular to its surface was used. A set of electrodes parallel to the Faraday direction (the direction perpendicular to the plain containing the magnetic flux density and the flow velocity) had been placed on the test body surface to short-circuit the Faraday component of the current (figure 13.1.1).

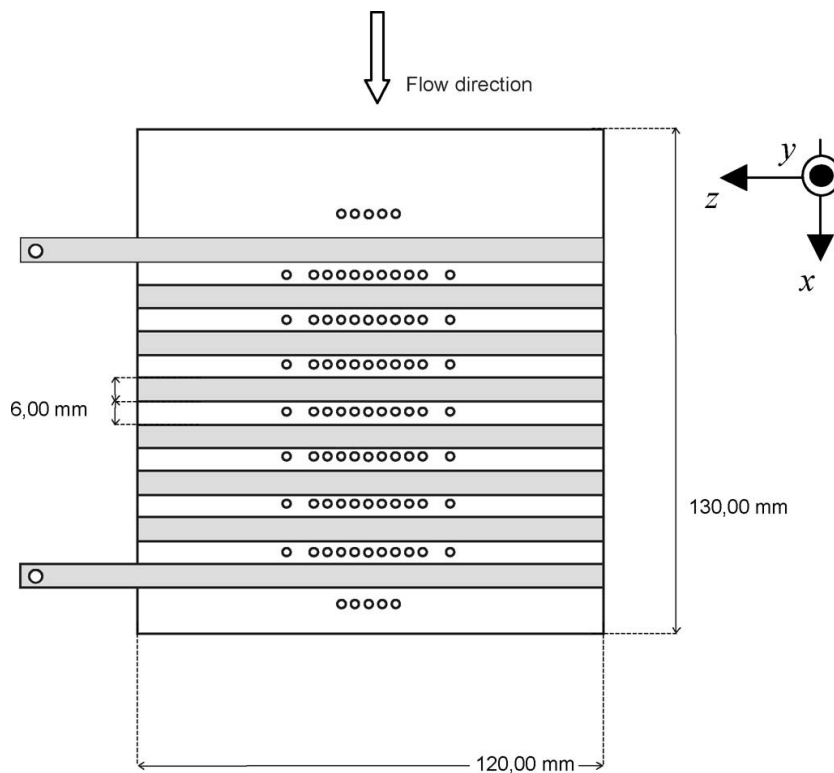


Figure 13.1.1: Wedge test body scheme [10].

In this configuration the short-circuited current flowed through the plasma of the shock layer, then passed to the electrodes through the boundary layer near the walls and went again to the plasma.

The measured electric potential on the test body surface revealed that the Faraday component of the electric field was not equal to zero. Hence the short-circuiting was not realized.

The boundary layer, which is characterized by a low electrical conductivity,

opposed an high electric resistance to the current flowing between the test body surface and the core flow. As a consequence the short-circuiting in the Faraday direction was inhibited and the effect of the MHD interaction was reduced.

In the present work, to avoid the high resistance of the plasma in the electrode region, the shorting of the Faraday current is completely realized inside the plasma by using a conical test body.

The axial symmetry of the test body allows to investigate a two dimensional geometry. The proposed design had been previously studied by means of a numerical code developed by the Bologna University team [108].

The experiments have been performed in two steps.

In the first one, a conical body with a diameter of the cone base of 60[mm] (large test body) has been utilized. During the tests the dimension of the region with a uniform hypersonic flow smaller than the dimensions of this test body has been observed.

Therefore a smaller test body with the base diameter of the cone of 40[mm] (small test body) has been constructed and tested.

Both the cones are realized with the same magnetic concept, an array of permanent magnets and ferromagnetic material. In order to keep the axial component (Hall component) of the current equal to zero, a conical electrical insulating shield of glass reinforced Nylon 6/6, with a thickness of 1[mm], is placed above the conical test body (figure 13.1.2). This cover has been also useful for the limitation of the heating fluxes toward the permanent magnets that are pretty sensible to temperature increases.

Aside the magnetic cones, two non-magnetic bodies with similar geometry in compare with the magnet ones, have been realized for non-MHD tests used as “baseline”.

The use of permanent magnets was necessary because numerical simulations showed that the high magnetic field needful for the creation of the MHD interaction, if created by means of electromagnets, will lead to current densities too much high, not reproducible in our test conditions [109].



Figure 13.1.2: Electrical insulation shield for the large body. A hole used for pressure measurements is visible.

The large test body assembly is shown in figure 13.1.3.



Figure 13.1.3: Large test body assembly. Magnetic and iron sections are visible.

The magnets had been arranged alternating the three truncated conical permanent magnet sections with ferromagnetic ARMCO iron sections to form a cone with an half-vertex angle of 22.5° and a $60[mm]$ base diameter.

The magnetic flux density distribution has been calculated by means of a finite element magnetostatic numerical code. In figure 13.1.4 the scheme of the magnetic structure with a plot of the magnetic lines is given.

As it results from the mentioned analysis, the components of the magnetic field perpendicular to the conical surface as functions of the distance from the cone vertex along the shield wall (red line), the end surface of the boundary layer (green line) and the shock front surface (blue line), are plotted in figure 13.1.5.

A comparison between magnetic field component perpendicular to the

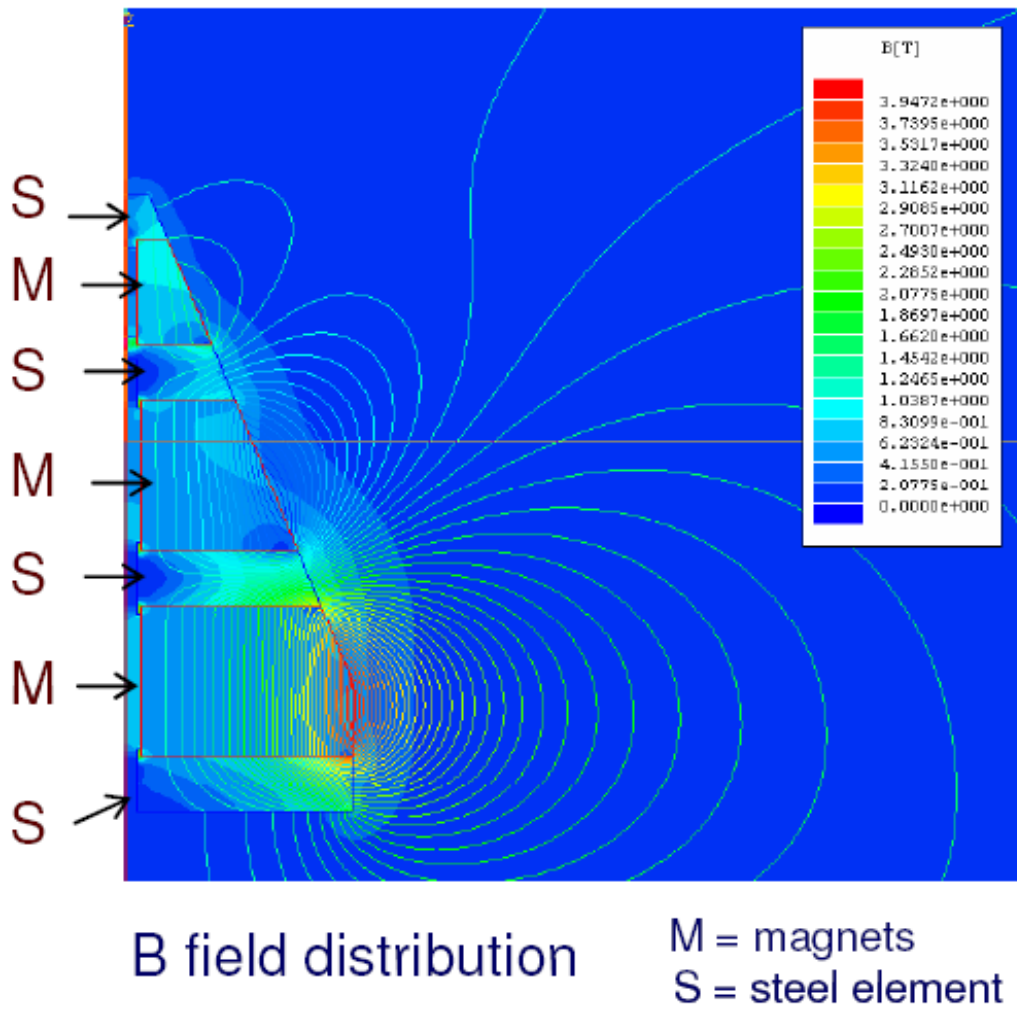


Figure 13.1.4: Large body scheme and B field distribution.

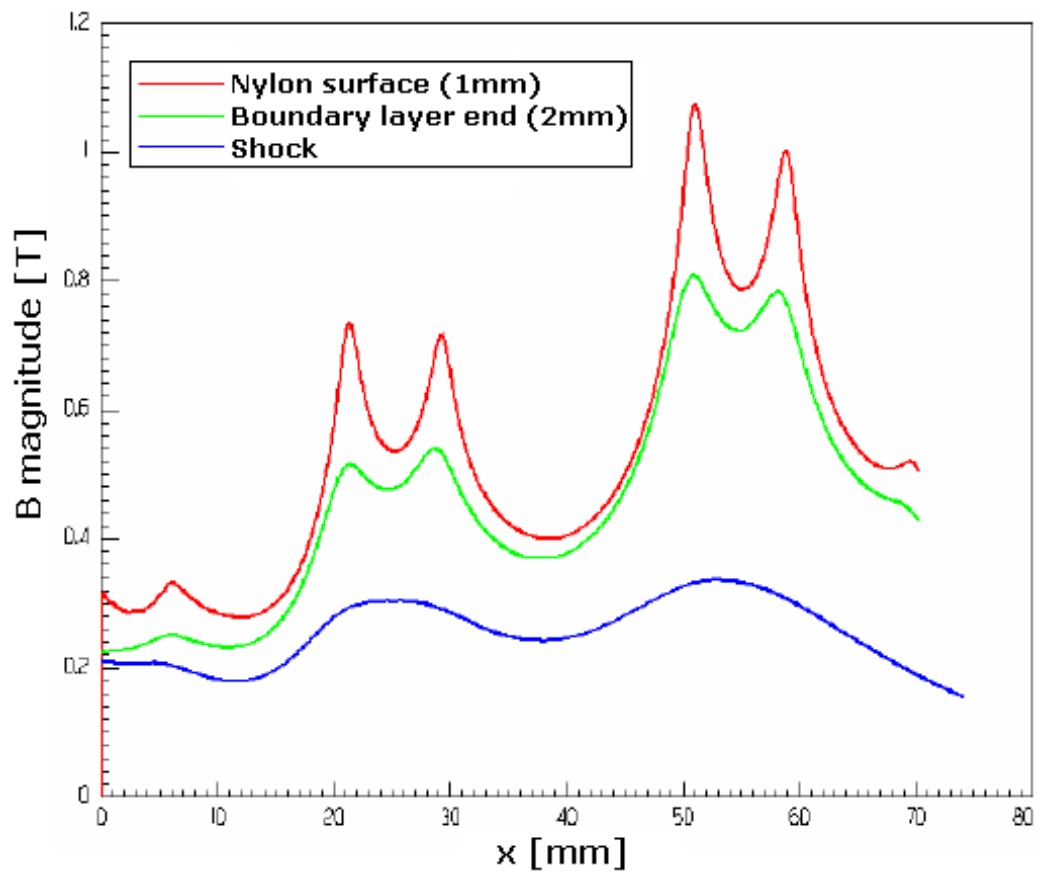


Figure 13.1.5: Magnetic flux density modulus on the shield wall (red line), at the end of the boundary layer (green line) and at the shock front surface (blue line).

conical surface measured and calculated on the body surface (zero distance), is reported in figure 13.1.6. The agreement is excellent.

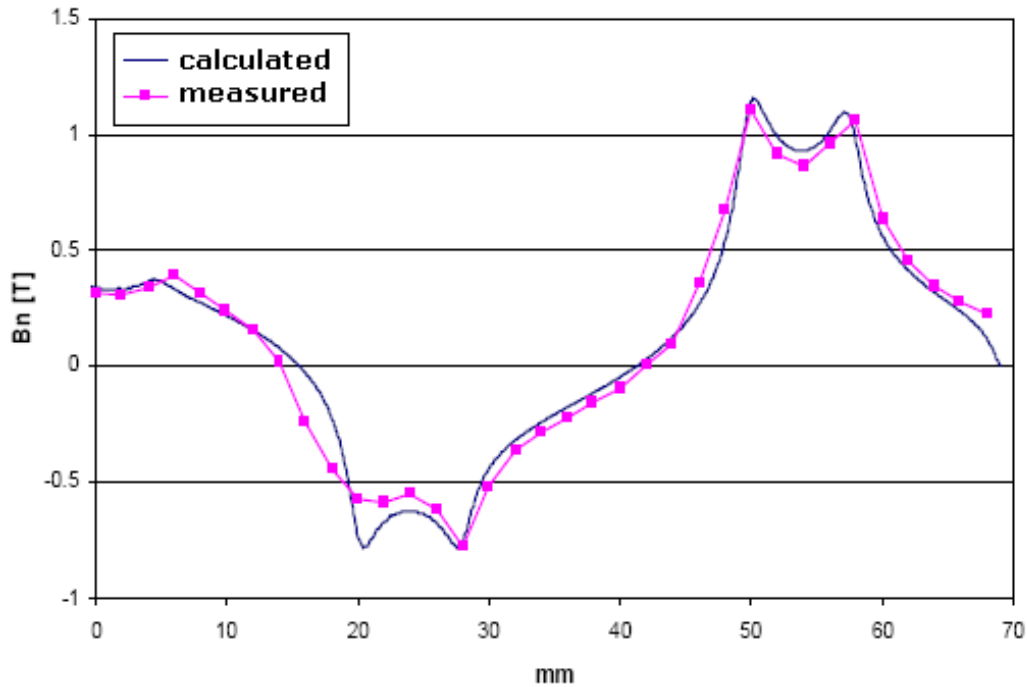


Figure 13.1.6: Comparison between design and measured values of the normal component of the B field along the cone surface.

The small test body, in the magnetic and non-magnetic version, is shown in figure 13.1.7.

The magnetic test body is made of two parts.

The first one is a cone with an half-vertex angle of 22.5° and base diameter of $40[mm]$.

The second part is a cylinder at the base of the cone with a length (height of the cylinder) of $48.3[mm]$. The cylindrical section was added in order to allow the placement of a third bigger magnet.

It has been assembled in a similar manner in compare with the large body: an array of three annular permanent magnets positioned in the cone central part, at the cone base and in the cylinder central part. Four annular sections of ARMCO iron alternate the magnets and are placed at the cone vertex, at



Figure 13.1.7: Magnetic (left-hand side) and non-magnetic (right-hand side) small test body. In the magnetic cone, magnetic and iron sections are visible.

the central part of the cone, at the central part of the cylinder and at the base of it.

The B field distribution generated by the permanent magnets as resulting from the analysis performed by means of the finite element magnetostatic numerical code, is shown in figure 13.1.8.

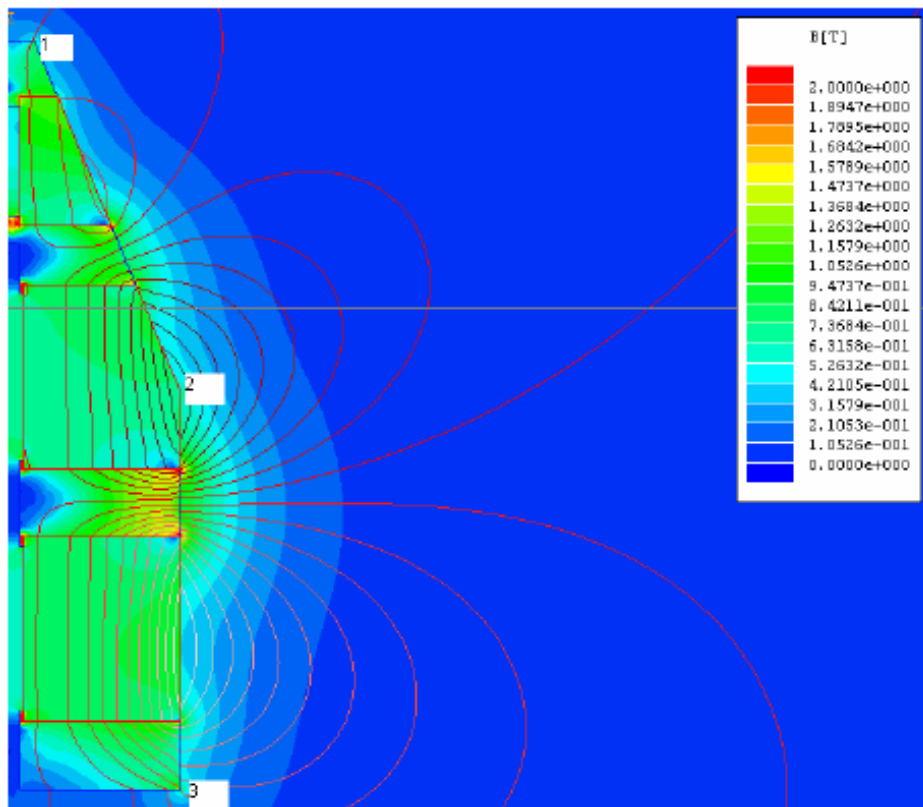


Figure 13.1.8: Small body scheme and B field distribution.

All the experiments have been performed mounting the test body (the large or the small one) at one centimeter away from the exit of the nozzle with the axis of the cone in the direction of the gas flow.

For both the cones, the MHD simulations predict the formation of azimuthal Faraday currents where the MHD interaction is stronger, thus where the B field lines are of big magnitude and perpendicular to the flow. These regions are sketched in the left-hand side of figure 13.1.9. In the right-hand side the

presence of Hall currents that decrease the body force is reported.

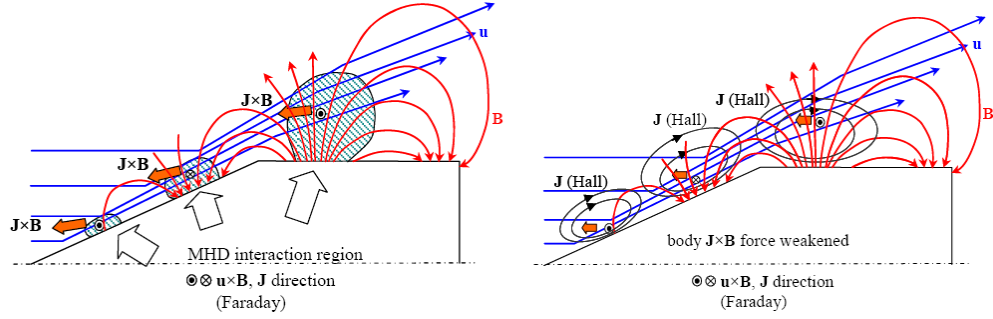


Figure 13.1.9: MHD interaction regions (left-hand side) and Hall currents (right-hand side).

The whole MHD phenomenon has been analyzed utilizing a two dimensional, low R_{em} model [110]. The advection of the magnetic field is so relatively unimportant, and it will tend to relax towards a purely diffusive state, determined by the boundary conditions rather than the flow motion. The fluid-dynamic equations are given by the continuity equation for mass, momentum and energy, and by the state equations of gas as follows:

$$\frac{\partial \rho}{\partial t} + \nabla \cdot (\rho \mathbf{u}) = 0, \quad (13.1.1)$$

$$\frac{\partial \rho \mathbf{u}}{\partial t} + \nabla \cdot (\rho \mathbf{u} \mathbf{u} + p \mathbf{I} - \tau) = \mathbf{J} \times \mathbf{B}, \quad (13.1.2)$$

$$\frac{\partial \rho e_i}{\partial t} + \nabla \cdot [(\rho e_i + p) \mathbf{u}] - \nabla \cdot (\tau \cdot \mathbf{u}) + \nabla \cdot \mathbf{F}_T = \mathbf{J} \cdot \mathbf{E}. \quad (13.1.3)$$

The physical model of the electrodynamic has been obtained assuming the condition $R_{em} \ll 1$. Under this assumption, some useful approximations can be applied [110].

Most notably, when an externally generated magnetic flux density \mathbf{B}_0 is applied to the plasma flow (i.e. a magnetic flux density produced by electric current), the magnetic flux density \mathbf{B}_j due to the current density in the plasma can be neglected.

Thus, the total magnetic flux density \mathbf{B} may be considered equal to the externally applied field \mathbf{B}_0 . Furthermore, assuming that the applied magnetic flux density does not vary in time, or it varies slowly, one can neglect the time derivative term in the Faraday Lenz's law:

$$\nabla \times \mathbf{E} = 0. \quad (13.1.4)$$

Another convenient approximation can be utilized, assuming that the characteristic time for the macroscopic variations is much greater than the inverse of the plasma frequency:

$$t_c \gg 1/\omega_p. \quad (13.1.5)$$

When equation (13.1.4) holds, the displacement current density, given by the time derivative of the electric displacement field \mathbf{D} , may be neglected compared to the conduction current density [86]. The Ampere Maxwell law can then be rewritten as follows:

$$\nabla \times \mathbf{H} = \mathbf{J}. \quad (13.1.6)$$

According to equation (13.1.5), the curl free electric field \mathbf{E} may be expressed as the gradient of a scalar potential Φ :

$$\mathbf{E} = -\nabla\Phi. \quad (13.1.7)$$

Applying then the divergence operator to equation (13.1.6), the following equation can be written as well:

$$\nabla \cdot \mathbf{J} = 0. \quad (13.1.8)$$

The electrodynamic model is completed by the generalized Ohm's law, which is here reported neglecting the ion Hall parameter and the electron pressure gradient (both considered of a second order importance):

$$\mathbf{J} = \sigma(\mathbf{E} + \mathbf{u} \times \mathbf{B}) - \beta_e \frac{\mathbf{J} \times \mathbf{B}}{B} \quad (13.1.9)$$

where

$$\beta_e = \mu_e B. \quad (13.1.10)$$

Assuming a reference system where the gas velocity \mathbf{u} and the magnetic flux density \mathbf{B} lie on the r - z plane, and the electromotive force $\mathbf{u} \times \mathbf{B}$ is directed along the φ -axis, equation (13.1.9) can be rewritten as follows:

$$\mathbf{J} = \bar{\sigma}(\mathbf{E} + \mathbf{u} \times \mathbf{B}). \quad (13.1.11)$$

Now the conductivity is expressed by means of the tensor

$$\bar{\sigma} = \frac{\sigma}{1 + \beta_e^2} \begin{bmatrix} 1 + \beta_z^2 & \beta_z \beta_r & \beta_r \\ \beta_z \beta_r & 1 + \beta_r^2 & -\beta_z \\ -\beta_r & \beta_z & 1 \end{bmatrix} \quad (13.1.12)$$

and the two components of β are described as

$$\beta_z = B_z \frac{\beta_e}{B} = \mu_e B_z, \quad \beta_r = B_r \frac{\beta_e}{B} = \mu_e B_r.$$

For the solution of the magnetohydrodynamic problem, a two dimensional model has been developed [106].

In order to get an insight of the electrodynamic in the proposed geometry, an annular flow may be considered as in figure 13.1.10, where the gas flows in the z direction with velocity \mathbf{u} , the \mathbf{B} field lies in the r direction, and $E_\varphi = 0$.

As the magnetic flux has to be conserved, the \mathbf{B} decreases with the radius:

$$B_r(r) = B_{r_0} \frac{r_0}{r}. \quad (13.1.13)$$

The equation (13.1.11) allows now to the determination of the three components of the current:

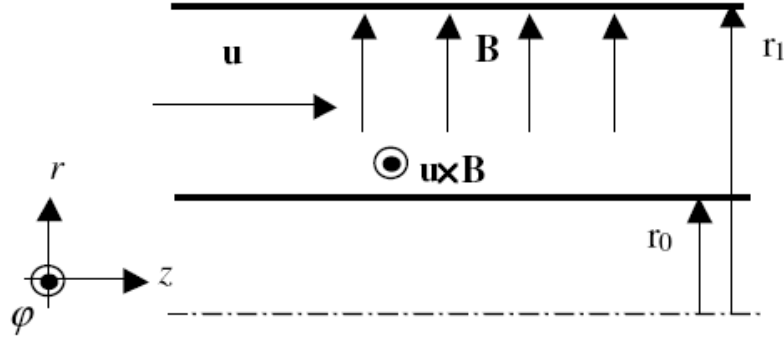


Figure 13.1.10: Annular channel in an axial symmetric geometry.

$$\begin{aligned}
 J_z &= \frac{\sigma}{1 + \beta_e^2} (E_z + \beta_e u B), \\
 J_r &= \beta_e E_r, \\
 J_\varphi &= \frac{\sigma}{1 + \beta_e^2} (-\beta_e E_z + u B). \tag{13.1.14}
 \end{aligned}$$

Assuming that the insulating wall of the channel does not allow the current density to flow in the r direction (as in our experiment in which there is the presence of the insulating nylon shield), the condition:

$$E_r = 0$$

holds.

As a consequence, the scalar electric potential is constant along the r direction and is only function of the z variable.

In order to maximize the azimuthal current density J_φ , one should set the total current flowing in the z direction equal to zero:

$$I_z = \int_{r_0}^{r_1} J_z r dr \approx \sigma \int_{r_0}^{r_1} \frac{(E_z + \beta_e u B) r}{\beta_e^2} dr = 0 \Rightarrow E_z = -\frac{2\mu_e u (B_0 r_0)^2}{r_0^2 + r_1^2} \tag{13.1.15}$$

From the obtained expression of the electric field in the Hall direction, the azimuthal component of the current density can be evaluated as:

$$j_\varphi \approx \frac{2\sigma u B_0 r_0 r}{r_0^2 + r_1^2} \quad (13.1.16)$$

Equation (13.1.16) shows that in the axial symmetric geometry, the azimuthal component of the current density is ideally not affected by an high Hall parameter when the current flow in the z direction is not allowed.

Equation (13.1.15) shows that an Hall electric field is needed to sustain the Faraday current density given by (13.1.16).

The two dimensional proposed model has been so characterized by a calculation domain positioned in the r - z plane.

In the reference system fixed with the body, the gaseous medium flows with hypersonic velocity \mathbf{u} lying on the r - z plane. The magnetic flux density \mathbf{B} , that generates the MHD interaction, lies on the r - z plane too. Thus the electromotive force $\mathbf{u} \times \mathbf{B}$ is directed along the φ -axis (as introduced in figure 13.1.10).

As seen before, the current density \mathbf{J} has an azimuthal component along the φ -axis and an Hall one on the r - z plane.

A cell-centered finite volume formulation has been adopted for the spatial discretization of the fluid dynamics.

Fluxes are evaluated by means of a centered scheme, corrected by an Osher scheme. A second order accuracy is obtained by a combination of upwind and centered discretization of the gradient.

Time integration is performed utilizing an explicit scheme, based on a fourth-order Runge-Kutta method.

Electrodynamics may be considered to vary as a sequence of steady state solutions driven by the evolution in time of the fluid dynamics. This is because, in the whole of the assumptions described above, the electrodynamics has a negligible characteristic time compared to the fluid dynamics.

Electrodynamic quantities are accordingly assumed to adapt themselves instantaneously to the time variation of the flow field.

The steady state electrodynamic problem defined by equations (13.1.7), (13.1.8) and (13.1.11) is solved by means of a finite element approach.

On the discretized domain a piecewise approximation Φ^* of the scalar potential Φ can be introduced, by means of the shape functions $\{N\}$:

$$\Phi^*(x, y) = \{N\}^T \{\Phi\} \quad (13.1.17)$$

where $\{\Phi\}$ is a vector containing the nodal value of the unknown electric scalar potential.

An expression for the approximate electric field and current density may be written, introducing equation (13.1.10) in equations (13.1.3) and (13.1.7):

$$\mathbf{E}^* = -[\nabla N]\{\Phi\}, \quad (13.1.18)$$

$$\mathbf{J}^* = -\bar{\sigma}([\nabla N]\{\Phi\} + \mathbf{u} \times \mathbf{B}). \quad (13.1.19)$$

Applying the divergence theorem to the vector $N\mathbf{J}^*$, the following equation can be written:

$$\int_{\Omega} N \nabla \cdot \mathbf{J}^* d\Omega + \int_{\Omega} \nabla N \cdot \mathbf{J}^* d\Omega = \int_{\partial\Omega} N J_n^* d(\partial\Omega). \quad (13.1.20)$$

Setting to zero the weighted residual of equation (13.1.8):

$$\int_{\Omega} N \nabla \cdot \mathbf{J}^* d\Omega = 0, \quad (13.1.21)$$

and introducing equations (13.1.18) and (13.1.19), the final FEM formulation for the electrodynamic problem can be rewritten as

$$-\int_{\Omega} \nabla N \cdot \bar{\sigma}(\mathbf{u} \times \mathbf{B}) d\Omega - \int_{\partial\Omega} N J_n^* d(\partial\Omega) = \int_{\Omega} \nabla N \cdot \bar{\sigma}[\nabla N]\{\Phi^*\} d\Omega. \quad (13.1.22)$$

The solution of the linear system obtained from equation (13.1.22), yields the nodal values of the electric scalar potential once the conductivity tensor, the flow velocity and the magnetic flux density are given.

The coupling between the fluid and the electrodynamics is accomplished quite straightforwardly.

As previously stated, the time dependent behaviour of the model is governed by the fluid dynamics. At the generic n^{th} time step, the fluid dynamic solver evaluates the source terms in the continuity equation for momentum and energy utilizing the values of \mathbf{E} and \mathbf{J} calculated at the previous time step. The steady state electrodynamic model then utilizes the value of \mathbf{u} at the n^{th} step to compute \mathbf{E} and \mathbf{J} .

These quantities will be utilized as input for the $(n + 1)^{th}$ time step of the fluid dynamic solver.

13.2 Diagnostic setup

The presence of the MHD interaction as been evaluated by means of imaging, pressure and electrical measurements.

Imaging setup

A *PCO SensiCam* 1280×1024 interline CCD color camera, with a minimum exposure time of $100[ns]$, has been utilized for the imaging of the MHD interacting plasma. The CCD quantum efficiency peak is nearly 53% at a wavelength of $380[nm]$.

The camera has been driven by means of a personal computer in order to have a complete control on the trigger.

Pressure setup

In order to perform the pressure measurements, a one miniaturized *Kulite* fast pressure transducer (model *XCS-062-5A*) was mounted halfway along the lateral surface of the large test cone.

For the small test body two of these sensors have been placed, one in the middle of the lateral cone surface and the other one in the cylindrical part.

Due to the expected low level of the pressure to be measured, the signal was sent to an amplifier circuit based on the *Analog Devices SSM2019 chip* which allows 10, 100 and 1000 times DC gain.

The signals were stored by means of a HEAT Data Acquisition (DAQ) system, which is based on the *LabVIEW 7* environment and a *National Instruments 6071* board.

Electrical setup

The presence of the Hall component of the electric field has been measured by means of a two sets of five electrical probes mounted on the shield wall as reported in figure 13.2.1.

Each probe is made of a strip of conductive paint insulated for all its length by means of a Kapton tape except a tip area of $2 \times 2[mm]$.

The two sets of probes have been used in order to measure the Hall potentials along two different axial direction and an evaluation of the symmetry of the flux has been allowed.

The electric potential measured by the probes have been detected by means of a *DL-1740* and a *DL-1640 200MS/s* Yokogawa scopes.

13.3 Interpretation of the results

In this section the measurements and the results of the large and the small test body are presented.

Large test body

Pressure measurements are presented as first.

The first important task to realize is the calibration of the pressure sensor. More exactly the influence of the magnetic field, due to the presence of the permanent magnet, on pressure sensors must be checked.



Figure 13.2.1: Electrical probes positioned on the conical insulating shield of the large test body.

A series of cold runs, i.e. without arc in the heating chamber, were done with the magnetic test body and with the non-magnetic one.

In figure 13.3.1, the pressure signals as functions of time, which are measured by means of the fast pressure transducer on the test-body lateral surface, are shown. After 150[ms] from the beginning of the flow time, equal signals were recorded. In the figure, the “effective-time” interval between 200 and 300[ms] is the interval for the average of the pressure data.

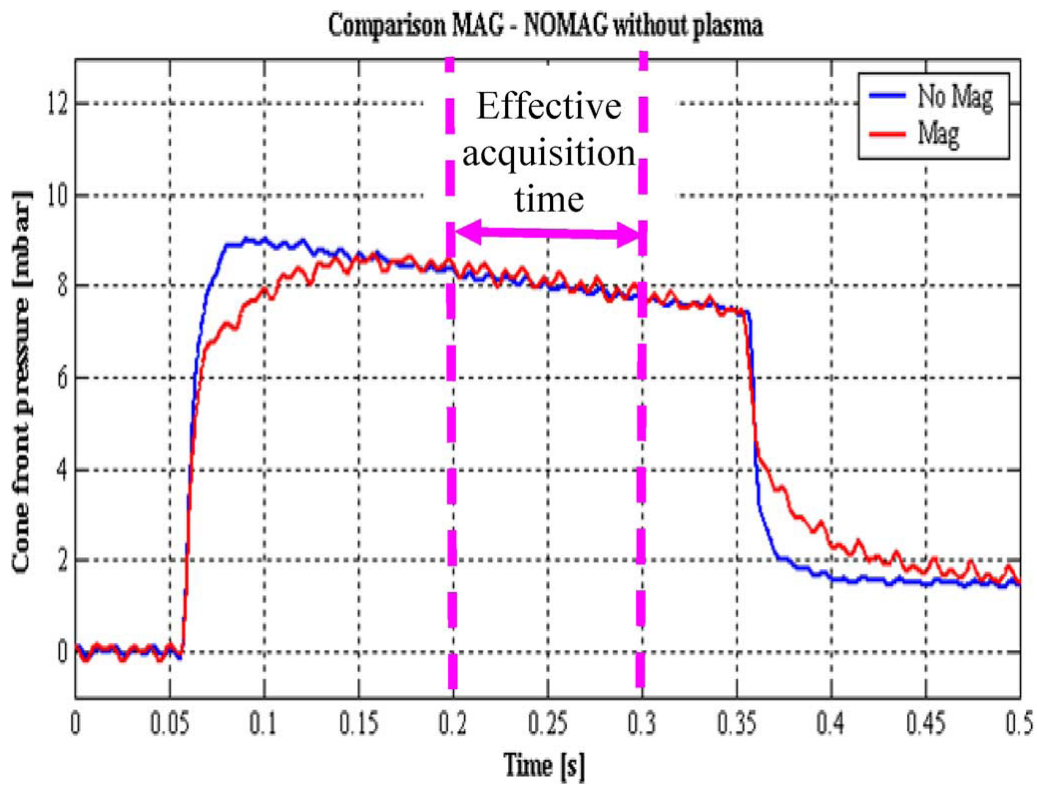


Figure 13.3.1: Pressure behaviours with magnetic and non-magnetic test bodies in cold conditions (the blue line refers to the non-magnetic case, and the red line refers to the magnetic case).

With cold flow, no plasma is formed and the MHD interaction is forbidden. The perfect superimposition of the two signals (within the effective-time interval) shows that the magnetic field has no influence in the operations of the pressure sensor.

The pressure behaviours in the magnetic and non-magnetic test bodies, and with hot flow, are shown in figure 13.3.2.

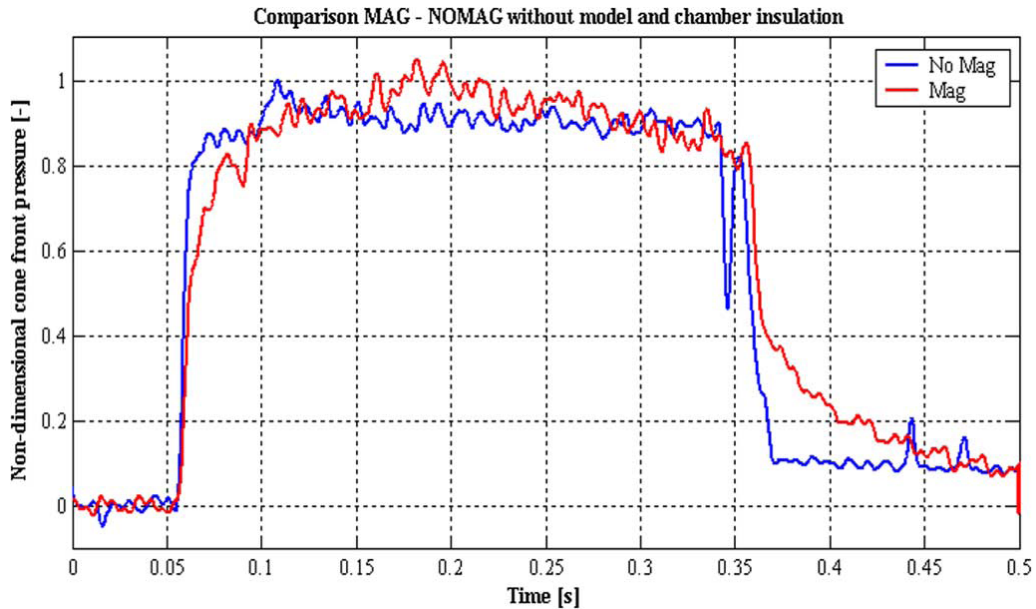


Figure 13.3.2: Pressure behaviours with magnetic and non-magnetic test bodies in an hot gas flow at condition *A*, when the vacuum tank was not electrically insulated and the Hall field was short-circuited (the blue line refers to the non-magnetic case, and the red line refers to the magnetic case).

The runs were done when the vacuum chamber wall was not electrically insulated and the Hall field was short-circuited through the conductive chamber wall.

The two signals are nearly equal, showing that the MHD interaction is spoiled by the short-circuiting of the Hall field. This is a strong indication of the importance of the Hall field in this experiment.

The results of the pressure measurements with and without MHD interaction (i.e. with and without magnetic test body) and with the vacuum chamber electrically insulated are summarized in table 13.3.1.

Here, the time averaged values over the effective-time interval of the pressure with and without magnets, the pressure increase, and the pressure coefficient with and without magnets and its increase at the three flow conditions

Conditions	<i>A</i>	<i>B</i>	<i>C</i>
Pressure non-magnetic [mbar]	8.54	8.94	10.79
Pressure with MHD [mbar]	9.71	10.01	11.57
Pressure increase [%]	13.70	11.97	7.23
Pressure coeff. non-magnetic	0.320	0.310	0.316
Pressure coeff. with MHD	0.347	0.399	0.335
Pressure coeff. increase [%]	8.57	9.35	5.85

Table 13.3.1: Time averaged of the pressure measurements for the large test body.

considered in this experiment are reported. Here, the pressure coefficient is defined as the ratio between the difference of the pressure measured in the shock layer and the free-stream pressure, and the free-stream kinetic energy per unit of volume.

The MHD interaction caused an increment of the pressure between 7% and 13%. The corresponding pressure coefficient increase lay between 5% and 9%. The pressure-coefficient increase saturated at about 9%.

In figure 13.3.3, the time behaviours of the pressure obtained during MHD-interaction runs with the magnetic test body are compared with those of the runs with the same flow conditions but with the non-magnetic cone. The red lines refer to the MHD-interaction runs, and the blue ones refer to the non-magnetic runs.

The pressure measurements in figures 13.3.3(a)-(c) are at flow conditions *A*, *B*, and *C*, respectively. The pressure behaviours of the non-magnetic runs are similar to those of the runs with a cold flow (see figure 13.3.1 at page 220). When the MHD interaction is present, fluctuations of up to 40% around the average value are observed. As fluctuations in the non-magnetic runs were not present, the fluctuations observed during the magnetic runs were caused by the MHD-interaction process and were probably due to instabilities of the MHD plasma.

At all test conditions, the MHD interaction causes an increase of the average

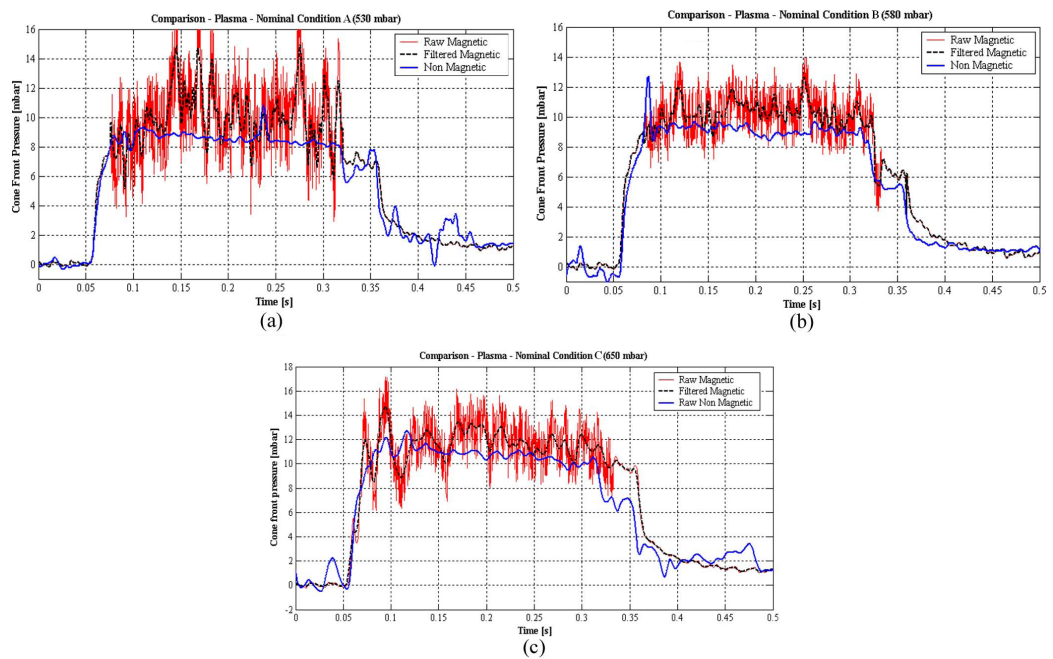


Figure 13.3.3: Pressure measurements as functions of time with and without MHD interaction at flow conditions *A* (a), *B* (b) and *C* (c) with the large test body.

pressure. The increase is larger when the stagnation pressure decreases. This effect was expected because, at a lower pressure, a larger ionization degree is present as found in the previous electrical characterization of the plasma flow (see table 12.3.2 at page 190). Hence, the short-circuited current in the Faraday direction increases, resulting in an increase of the MHD interaction.

The presence of the MHD interaction has been resulted also from imaging measurements.

In figure 13.3.4 the photos of the argon plasma flowing around the test body in condition *C* for the non-magnetic and for the MHD runs have been showed. For both photos the PCO camera had been set at an exposure time of 1[ms] and positioned perpendicular to the flow axis.

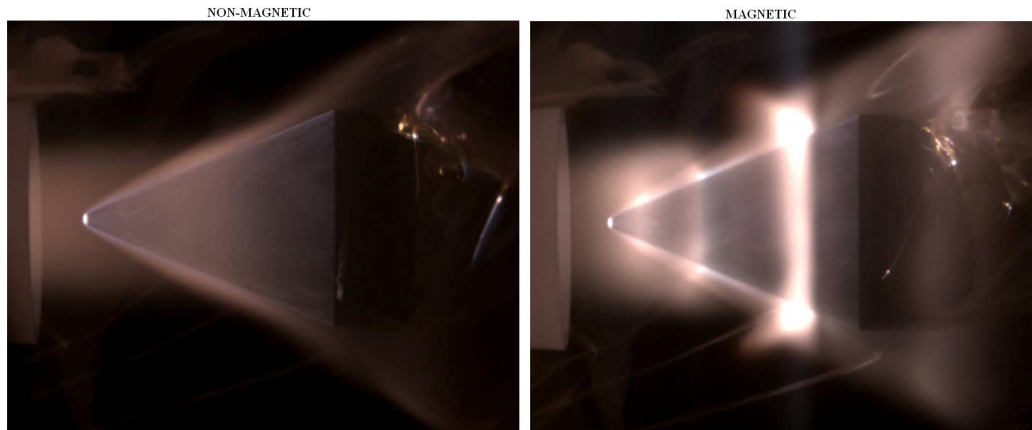


Figure 13.3.4: Flow pattern without MHD interaction (left-hand side) and with MHD interaction (right-hand side). Exposure time 1[ms].

In the left image, without magnetic field, a uniform plasma flow at the exit of the nozzle and the shock wave over the cone are visible.

The MHD interacting flow field (right-hand side) is characterized by four bright rings around the conical test body, which are concentric to it, in correspondence to the regions where the magnetic-flux-density component that is perpendicular to the flow field has a maximum, i.e. where the Faraday current component is higher.

In figure 13.3.5 a photo taken with an optical axis oblique with respect to the flow direction, and with the magnetic test body, allows to a better view of the MHD rings pattern.

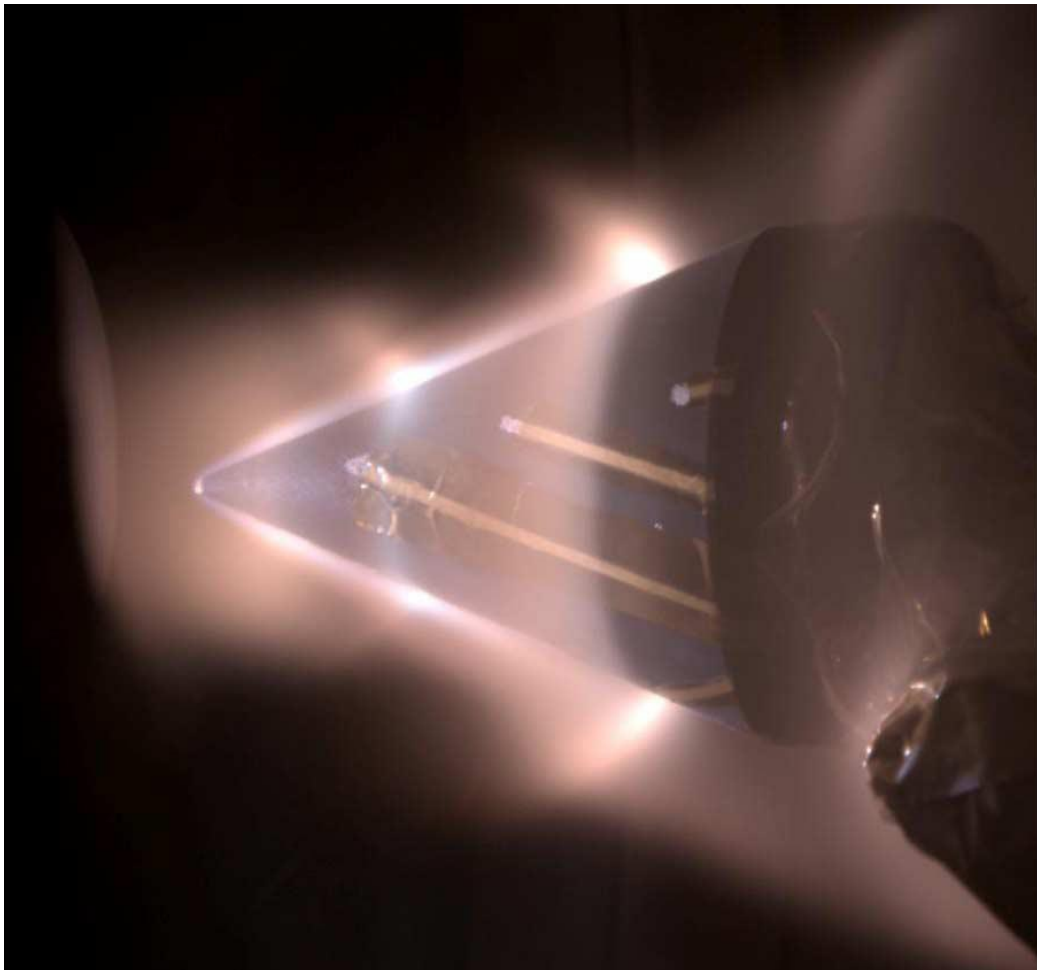


Figure 13.3.5: MHD interaction around the magnetic cone (exposure time 0.5 [ms]). The optical axis is oblique with respect to the flow direction.

Also the electrical measurements, realized by means of the electrostatic probes, showed the presence of the MHD interaction, in particular the presence of an Hall potential.

In figures 13.3.6 and 13.3.7, the time behaviours of the potential differences measured during the MHD-interaction run respectively at flow condition *A*

and C are shown. The probe closest to the cone vertex has been used as the reference one.

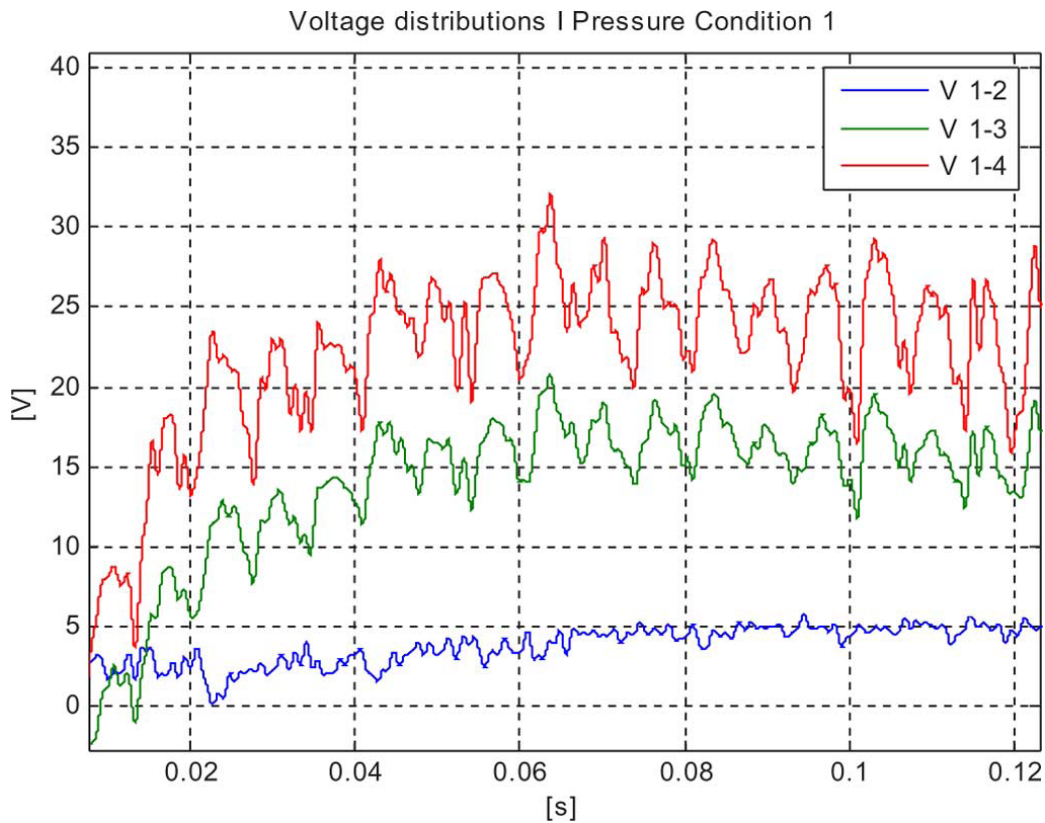


Figure 13.3.6: Hall voltage distribution along the conical surface of the test body at flow condition A .

In both figures, $V 1-2$, $V 1-3$, and $V 1-4$ refer to the potential differences between the reference probe and the second, third, and fifth one, respectively along the cone surface and starting from the cone vertex (see figure 13.2.1 at page 219). In both plots, the red line refers to $V 1-4$, the green line refers to $V 1-3$, and the blue line refers to $V 1-2$.

The measured potential differences correspond to the Hall electric field. The measured field is about $500[V/m]$.

At larger pressures, the Hall field decreases. At flow condition C , the Hall field is 20% lower than at condition A .

At both flow conditions, fluctuations of up to 30% of the potential differences

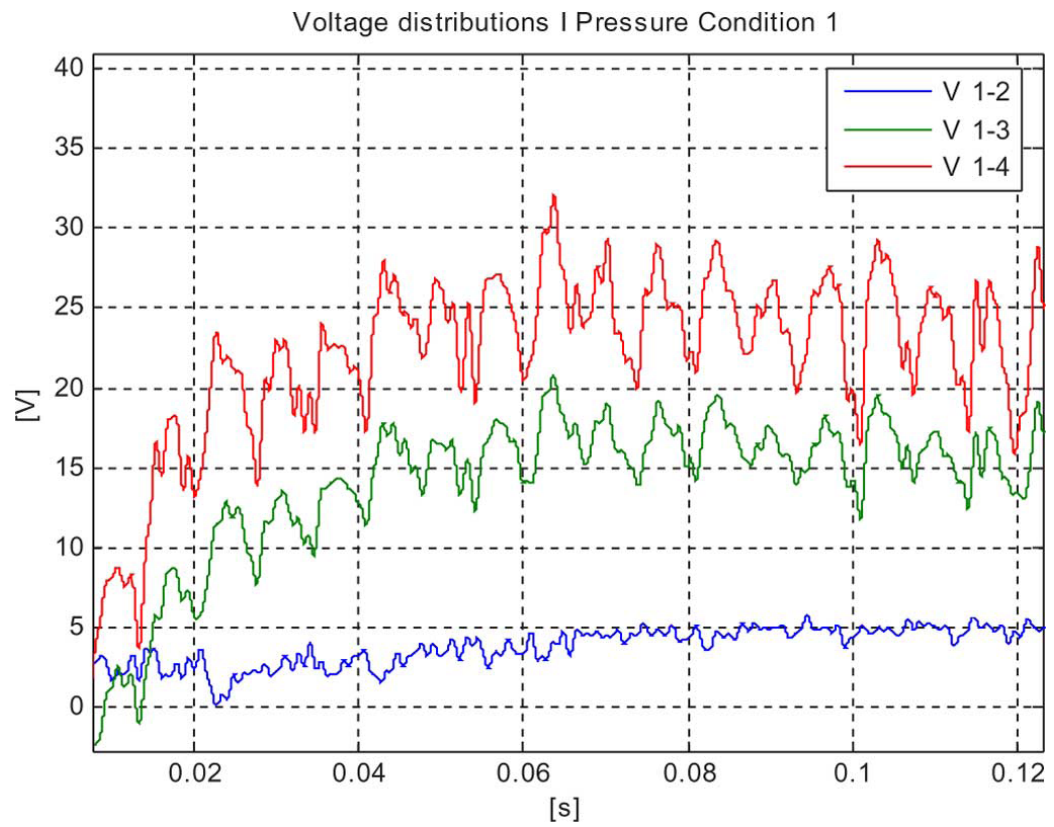


Figure 13.3.7: Hall voltage distribution along the conical surface of the test body at flow condition *C*.

are observed. These fluctuations are explainable by means of electromagnetic noise coming from the arc heater generator.

The measured values of the Hall field are reduced until 50% with respect to the fields calculated by means of the MHD time-dependent multidimensional code [108]. That behaviour could come from problems with the electrical insulation of the vacuum facility and the test body.

All the diagnostics have shown the possibility to realize an MHD interaction within a hypersonic plasma flow.

From the mapping of the flow, which has been done during the characterization runs, the region of uniform hypersonic flow at the nozzle exit lay inside a circular region with a diameter of 40[mm]. The conical shape of the utilized test body had a base cross section with a diameter of 60[mm]. In order to keep the test body completely inside the region where the flow was uniform, the smaller test body was built.

Small test body

In this small test body two pressure sensors placed in the intermagnet iron elements on the cone and cylinder lateral surfaces have been used (figure 13.3.8).

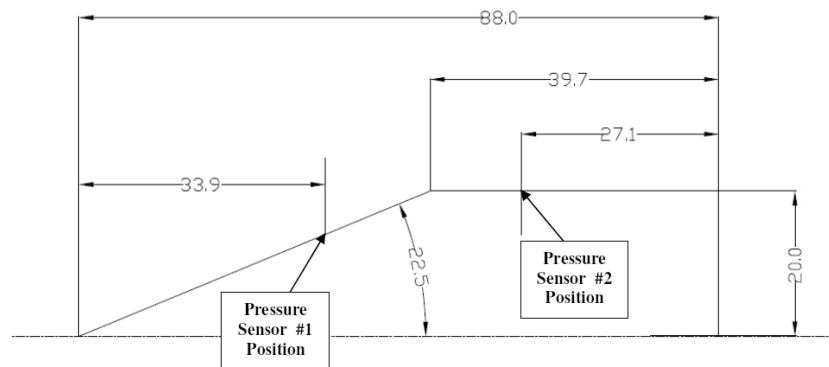


Figure 13.3.8: Geometry scheme of the small test body. The position of the two pressure sensors are visible.

In table 13.3.2 the time averaged values over the effective-time interval of the pressure, the pressure increase, and the pressure coefficient and its increase with and without magnets at the three flow conditions and for the sensor placed into the cone are reported. For all the values given in the table, the average within the effective time is the average of the measured values between 100 and 200[ms] from the flow-pulse starting time (see figure 13.3.1 at page 220).

Conditions	<i>A</i>	<i>B</i>	<i>C</i>
Pressure non-magnetic [mbar]	9.01	10.31	11.77
Pressure with MHD [mbar]	10.34	11.68	12.97
Pressure increase [%]	14.78	13.31	10.16
Pressure coeff. non-magnetic	0.344	0.343	0.343
Pressure coeff. with MHD	0.390	0.388	0.366
Pressure coeff. increase [%]	13.44	13.27	6.88

Table 13.3.2: Time averaged of the pressure measurements on the cone pressure sensor for the small test body.

An increase between 10% and nearly 15% of the pressure and an increase between 7% and 13% of pressure coefficients were observed. These confirm the results obtained in the runs with the large test body.

The measurements of the pressure sensors placed on the cylindrical surface are reported in table 13.3.3. The accuracy in this region is low due to the low values of the pressure in this location and the vicinity to the sensor minimum threshold. Nevertheless, the increases of the pressure and the pressure coefficient at conditions *A* and *B* were recorded.

In this region pressure increases in the order of 5% and pressure coefficient increases of almost 14% have been measured.

The pressure time behaviours on the cone surface are shown in figure 13.3.9(a)-(c) for flow conditions *A*, *B* and *C*, respectively. The plots were taken with and without MHD interaction (red and blue lines, respectively).

With the small test body, the intensity of the fluctuations appears to be

Conditions	<i>A</i>	<i>B</i>	<i>C</i>
Pressure non-magnetic [mbar]	1.01	1.26	1.43
Pressure with MHD [mbar]	1.06	1.34	1.43
Pressure increase [%]	5.4	6.5	≈ 0
Pressure coeff. non-magnetic	0.010	0.014	0.013
Pressure coeff. with MHD	0.012	0.017	0.013
Pressure coeff. increase [%]	10.5	17.6	≈ 0

Table 13.3.3: Time averaged of the pressure measurements on the cylinder pressure sensor for the small test body.

reduced. This is due to the better insulation used in these experiments.

In these figure is important to note another proof of the presence of the MHD interaction.

Each run covers roughly the range $0.05 \div 0.35[ms]$. Within this range the pressure is characterized by two plateau.

The first one from 0.05 to $0.32[ms]$ in which the valves are opened and the arc heater is on, so a plasma flow invests the test body.

The second plateau, characterized by a lower pressure values, in which the valves are still opened but the arc heater is off, so a cold flux interests the body.

Until the arc heater is on (first part of the run) pressure differences between magnet and non-magnet body are visible. MHD interaction is so irrefutably present.

In the final part, when the flow is cold, magnetic and non-magnetic body show the same pressure measurements.

In order to assess the quality of the pressure measurements to be used for the code validation, a dedicated detailed accuracy analysis was carried out.

The uncertainties related to each element on the measurement chain are considered. The following uncertainty sources are taken into account:

- the single-transducer performance,

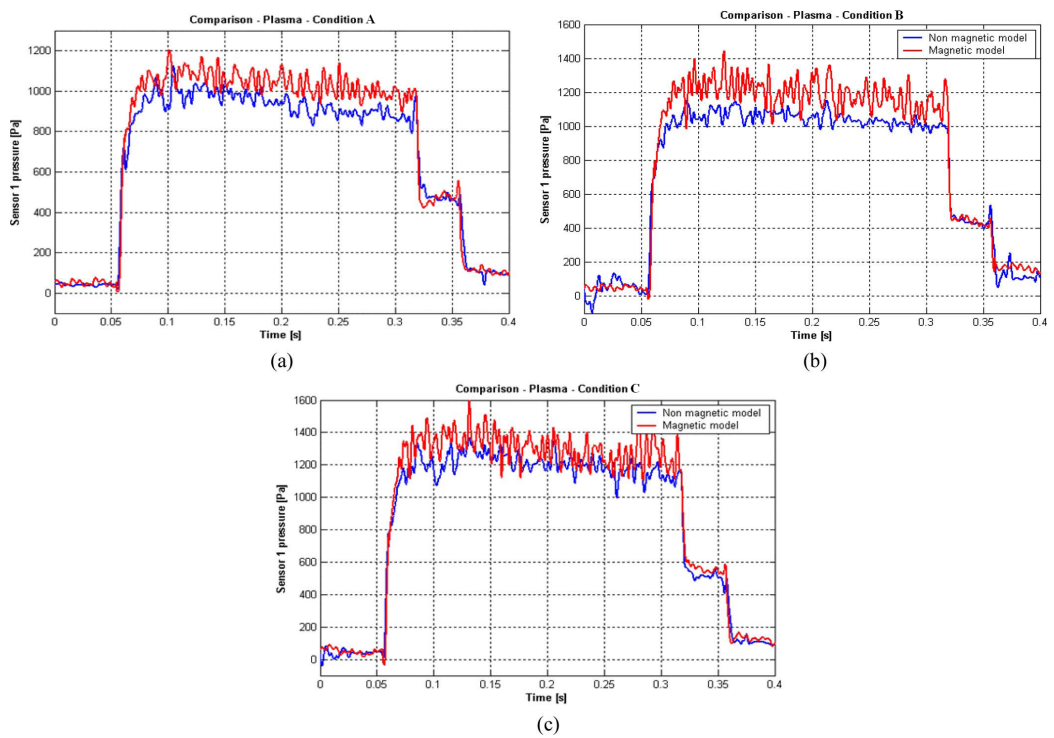


Figure 13.3.9: Pressure measurements as functions of time with and without MHD interaction at flow conditions *A* (a), *B* (b) and *C* (c) with the small test body.

- the single-amplification-channel performance,
- the single-DAQ board-channel voltage range and corresponding bit resolution,
- a conservative estimate of the noise and a minimum acceptable signal-to-noise ratio.

The results are shown in tables 13.3.4 and 13.3.5 for non-magnetic and magnetic test bodies respectively.

Conditions	<i>A</i>	<i>B</i>	<i>C</i>
Cone sensor [Pa]	901	1031	1177
Cylinder sensor [Pa]	101	126	143
Cone uncertainty [%]	0.34	0.30	0.26
Cylinder uncertainty [%]	32.78	26.39	23.22
Signal to noise cone	589.5	674.5	770.3
Signal to noise cylinder	6.1	7.6	8.6

Table 13.3.4: Accuracy analysis results for the NON-magnetic test body.

Conditions	<i>A</i>	<i>B</i>	<i>C</i>
Cone sensor [Pa]	1297	1168	1034
Cylinder sensor [Pa]	143	134	106
Cone uncertainty [%]	3.84	4.27	4.82
Cylinder uncertainty [%]	44.67	47.65	59.82
Signal to noise cone	39.0	35.2	31.11
Signal to noise cylinder	4.5	4.2	3.3

Table 13.3.5: Accuracy analysis results for the magnetic test body.

A rather good quality of the data of the sensor in the cone surface is obtained. On the other hand, for the sensor placed on the cylindrical surface,

the accuracy is extremely low ($\pm 50\%$). That is an attestation of the better measures obtained with the cone sensor.

The imaging supported the pressure measurements (figure 13.3.10). When the test body was the magnetic one, three bright rings of emitting plasma appear in the regions where the B-field intensity is maximal. This corresponds to the region above the iron sections of the magnetic test body (for a comparison see figure 13.1.8 at page 210).

At the end of the cylindrical part, where the last iron section of the test body is placed, a bright striation appears, indicating that a non-negligible MHD effect was also present in this region.



Figure 13.3.10: MHD interaction around the small magnetic test body.

In order to measure the Hall voltage in the small-test-body experiment, the electrostatic probes were realized with conductive paint placed inside the

electrical insulation shield to minimize erosion.

The Hall voltages measured during the experiments at flow conditions A , B and C , and at a stagnation pressure of $455[mbar]$ are shown in figure 13.3.11, corresponding to the blue, green, light blue, and red lines, respectively.

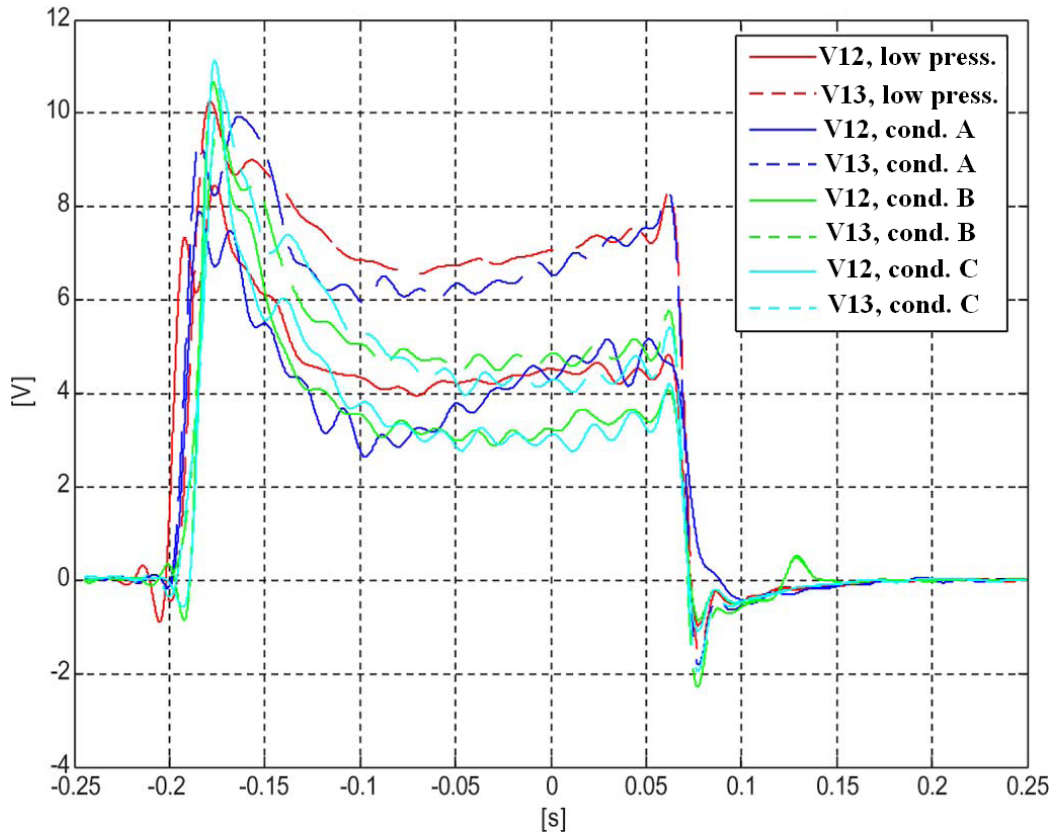


Figure 13.3.11: Hall voltages along the conical surface of the small test body at flow conditions (blue) A , (green) B , and (light blue) C and in runs with a (red) stagnation pressure of $455[mbar]$. The full and dotted lines refer to Hall potential differences measured between two probes on the cone surface at distances of 17 and $41[mm]$, respectively, along the flow.

The dotted line indicates the Hall potential differences between the cone vertex and a position at $41[mm]$ from the vertex and along the flow direction on the cone lateral surface. The full line corresponds to the Hall potential difference measured between the cone vertex and a probe at $17[mm]$ from

the vertex.

These measurements indicate the Hall fields ranging between 400 and 500[V/m] as in the case of the large test body.

The main result obtained in the experiments with the small test body is the confirmation of the results obtained with the large one. The pressure increases and the measured Hall field were in agreement.

Numerical analysis of the experimental results

The numerical model described in the Section 13.1 has been used for the realization of the magnetic configuration of the test body.

In this section a numerical investigation on the results obtained from the MHD runs have been performed.

The input data for the simulation have been carried out by the experimental characterization described in Chapter 12. These data are reported in table 13.3.6.

M_∞	p_∞	T_∞	ρ_∞	u_∞	α_∞
[—]	[Pa]	[K]	[kgm ⁻³]	[ms ⁻¹]	[—]
6.19	89.05	279.55	$1.5304 \cdot 10^{-3}$	1926.29	$3.4 \cdot 10^{-3}$

Table 13.3.6: Free stream values of the considered problem.

A sensitivity analysis has been performed assigning three different values of the electron temperature.

On the basis of the assumed values of electron temperature and ionization degree, the electric transport properties has been evaluated, utilizing the results of a model based on a two terms approximation of the Boltzmann equation, in the assumption of a maxwellian distribution of the electrons.

The quantity $n_{Ar} \times \mu_e$ as a function of electron temperature and ionization degree is reported in figure 13.3.12.

From the results reported in figure 13.3.12, the electrical conductivity and the electron mobility are evaluated in the assumption of constant electron

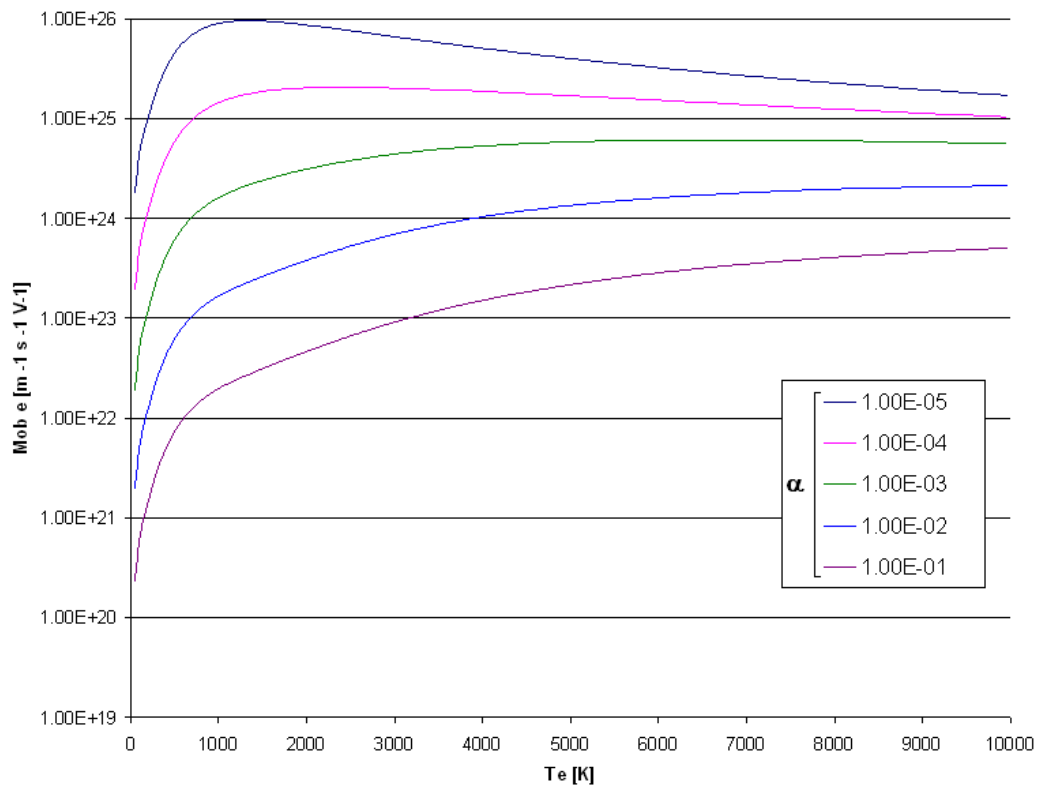


Figure 13.3.12: $n_{Ar} \times \mu_e$ as a function of electron temperature and ionization degree α .

temperature and ionization degree on the calculation domain. In the given assumption, the term $n_{Ar} \times \mu_e$ is constant on the domain.

The electrical conductivity expressed as [107]:

$$\sigma = en_e\mu_e = e\alpha(n_{Ar}\mu_e) \quad (13.3.1)$$

is also constant, whereas the electron mobility is inversely proportional to the plasma density.

Three values for the electron temperature has been chosen in order to evaluate the electric transport properties. The values of the free stream electrical conductivity and electron mobility corresponding to the condition chosen for calculation are shown in table 13.3.7.

Condition	A	B	C
T_e [eV]	0221	0.086	0.052
σ [S/m]	493	262	135
$\mu_{e,\infty}$	120	52	24

Table 13.3.7: Free stream electric transport properties

The calculations have been performed in a domain discretized by means of a 26032 points mesh.

In figure 13.3.13, the computed pressure distribution around the test body without (top) and with (bottom) MHD interaction is reported. The numerical rebuilding reproduced qualitatively the flow field (figure 13.3.13), and some of the flow patterns revealed by fast imaging appear to be correctly replicated (figure 13.3.14).

In figure 13.3.15 the Faraday component (i.e. the azimuthal component) of the current density is reported. Three bright regions characterized by high current values are visible. The same regions were visible in the fast imaging photos.

A plot of the Hall current density streamlines on the calculation domain is reported in figure 13.3.16. The effect of the boundary conditions applied

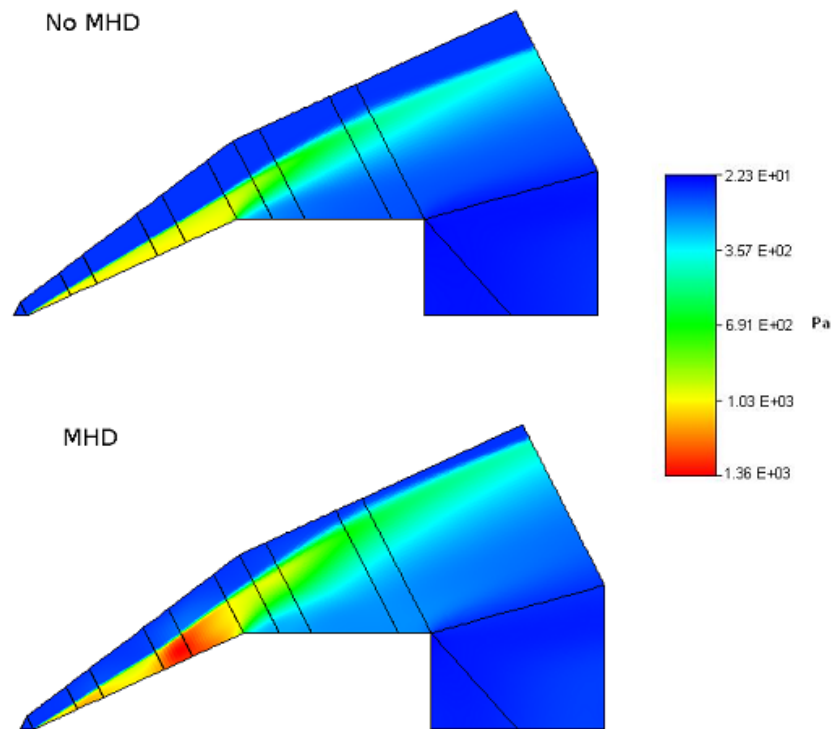


Figure 13.3.13: Computed pressure field without and with MHD interaction.

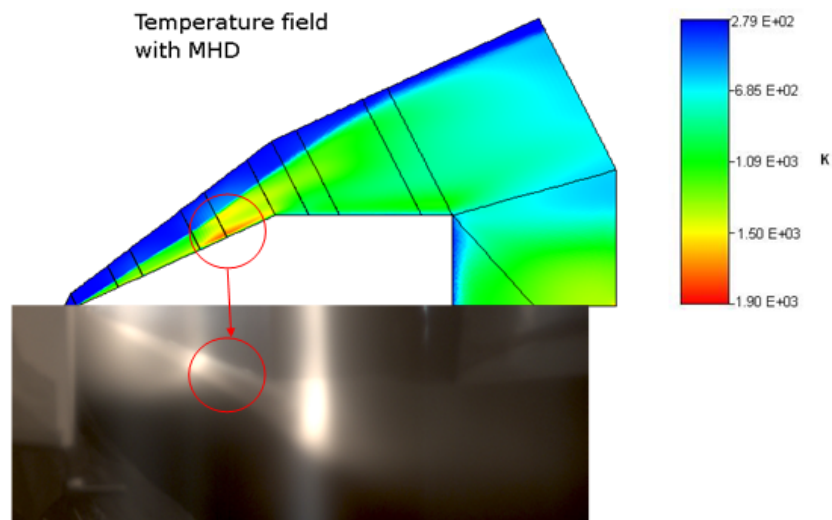


Figure 13.3.14: Comparison of flow structure details between simulation and fast imaging.

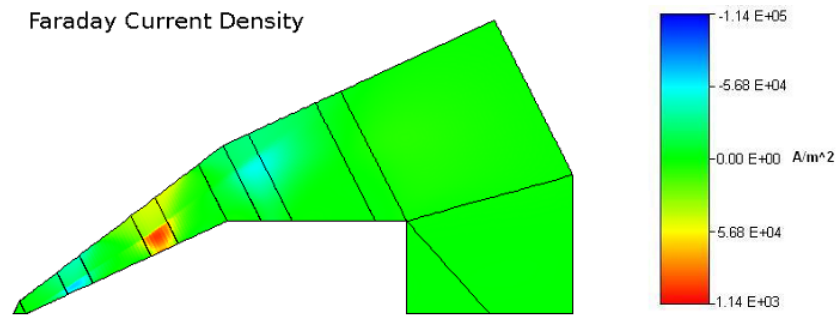


Figure 13.3.15: Simulated azimuthal current densities.

for the electrodynamics can be observed: since a null normal current density condition is assumed for all the boundary except the flow exit edges, located on the right of the domain, the current streamlines are forced to circulate on the domain.

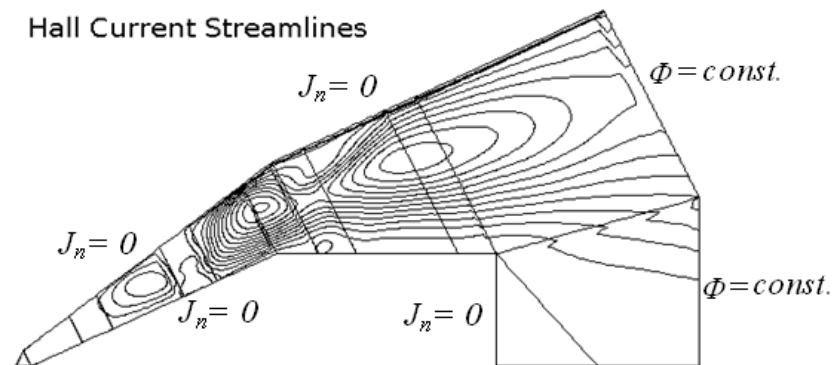


Figure 13.3.16: Simulated Hall current streamlines.

The numerical results, however, provided a higher-than-observed effect of the MHD interaction, as can be noted in the plots of pressure and voltage reported in figures 13.3.17 and 13.3.18 respectively.

This is presumably due to the lack of a model for the plasma kinetics, and to the ionization in the incoming argon jet, which actually provides the Hall current density with a wider path. A summary of the resulting computed and measured pressures considering the electric transport properties obtained for the case C is reported in table 13.3.8.

In order to investigate the effect of a wider closing path for the Hall

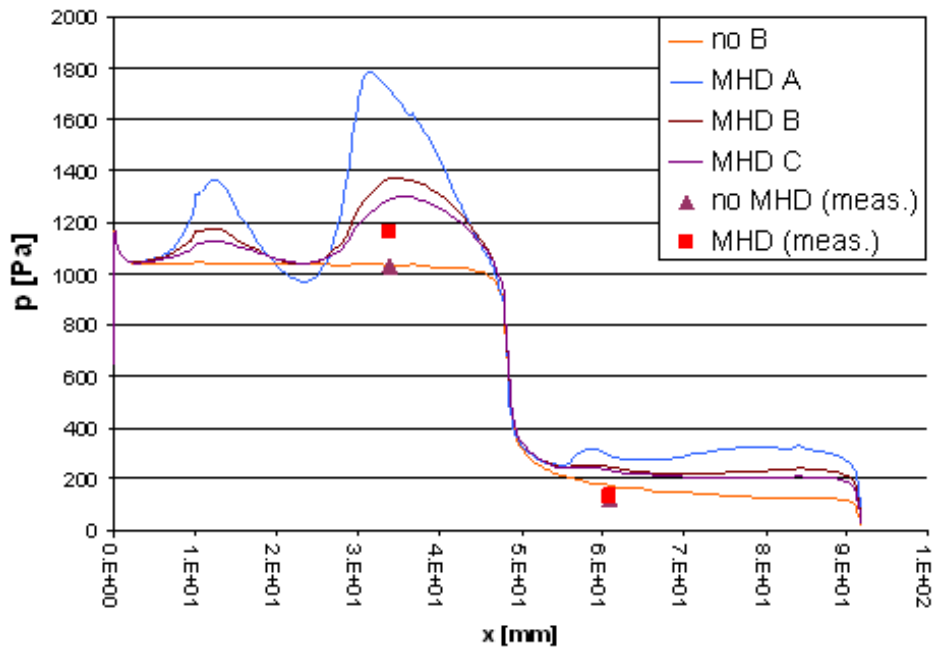


Figure 13.3.17: Pressure along the body surface for numerical and experimental results in MHD and non-MHD runs.

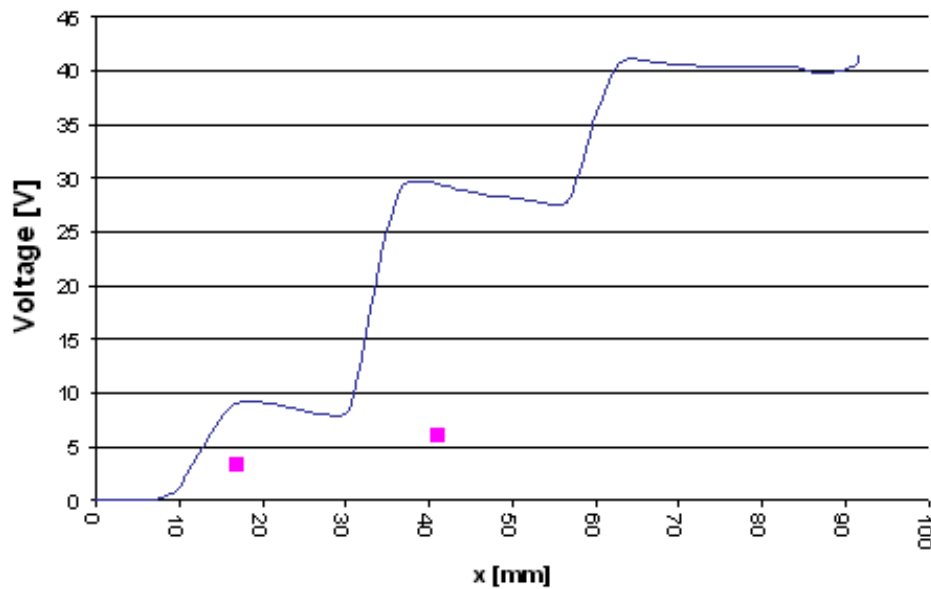


Figure 13.3.18: Voltage along the body surface for numerical and experimental results in MHD runs.

	Measured [Pa]	Calculated [Pa]	Difference [%]	Exp. uncert. [%]
Position 1 - no MHD	1031	1030	0.10	0.3
Position 1 - MHD	1168	1299	11.22	4.3
Position 2 - no MHD	125.5	168	33.86	26.4
Position 2 - MHD	133	229	71.41	47.7

Table 13.3.8: Pressure comparison between measured and numerical runs for the condition *C*.

current density on the plasma jet upstream the shock, a second calculation campaign has been carried out utilizing an extended mesh discretized by means of a 28560 points.

Results show that, as expected, the Hall current densities follow a wider path, when given the possibility (figure 13.3.19).

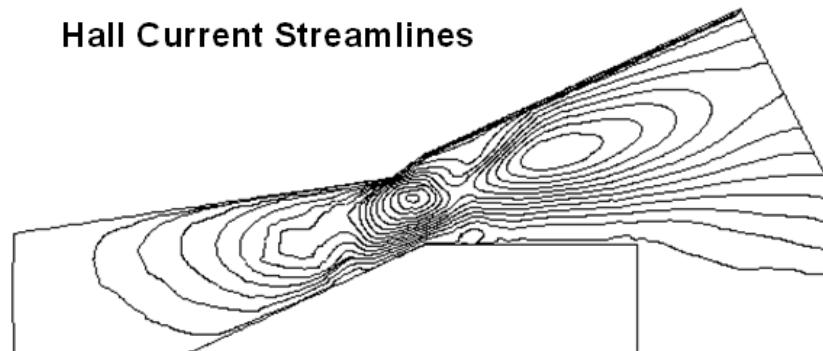


Figure 13.3.19: Hall current streamlines for the extended domain.

This results in a significant reduction both in the values of the calculated voltage and in the azimuthal current density, as can be observed in figures 13.3.20 and 13.3.21 respectively.

As introduced before, an increasing of the Hall currents generates a reduction in the azimuthal currents and in a resulting weakening of the body force acting on the plasma.

The extend domain, that enables a more realistic closing path for the Hall

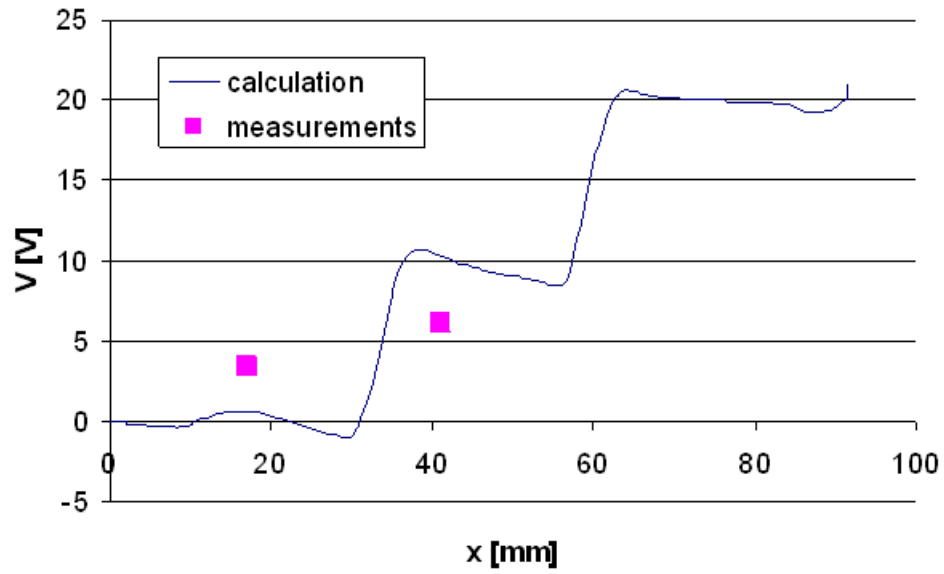


Figure 13.3.20: Voltage along the body surface for numerical and experimental results in MHD runs for the extended domain.

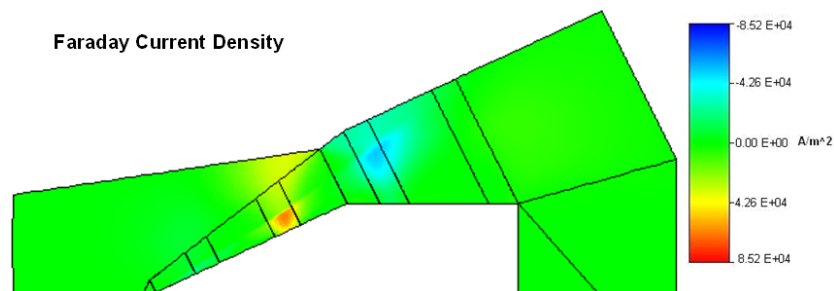


Figure 13.3.21: Simulated azimuthal current densities in the extended domain.

currents, allows to the values of the calculated pressure on the cone wall to become closer to the measured ones.

In figure 13.3.22, a very good agreement at position 1 can be observed for the set C of electric transport properties.

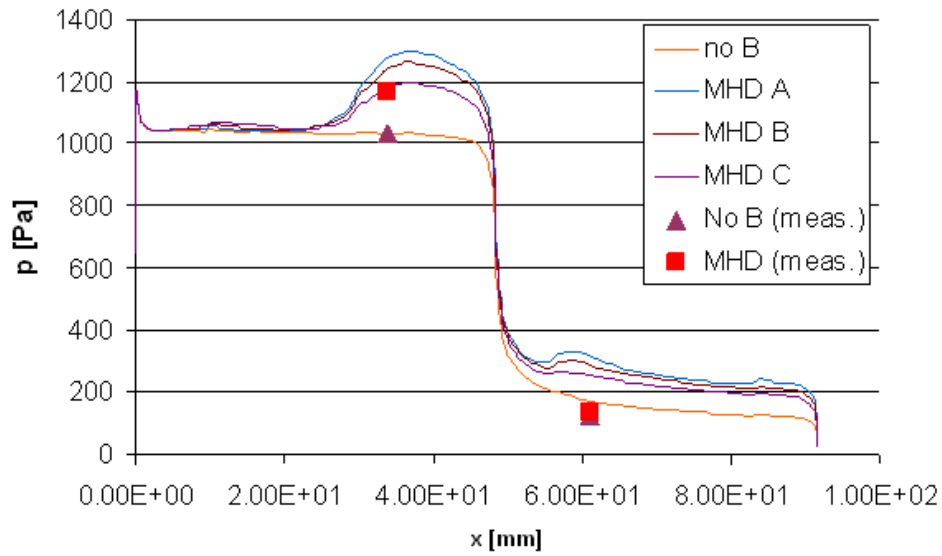


Figure 13.3.22: Pressure along the body surface for numerical and experimental results in MHD and non-MHD runs. The extended domain is now used for simulations.

Also the calculated voltage gets closer to the measures; however, a comparable agreement is not reached. This points out the need of a refinement in the modeling of the phenomenon.

A plasma kinetics model would take into account the electron behaviour and the ionization processes, providing a more realistic description of the electric transport properties of the plasma.

The pressure and the temperature distribution on the calculation domain are reported in figures 13.3.23 and 13.3.24 respectively.

A comparison between the measured and calculated values of pressure on the test body wall for the electric transport properties obtained in the case C and for the extended domain is reported in table 13.3.9.

Comparing these results with the ones achieve from the non-extended do-

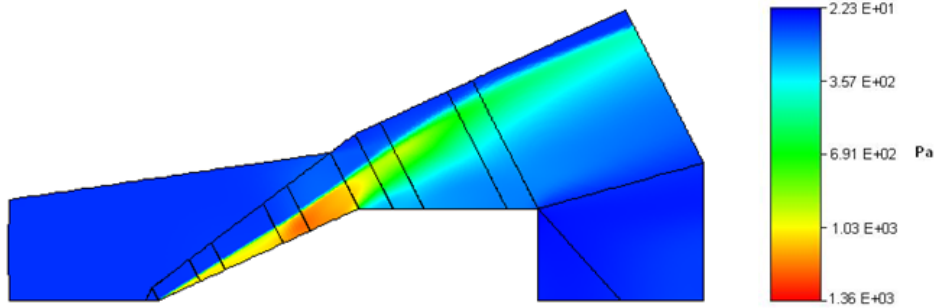


Figure 13.3.23: Computed pressure field with MHD interaction with the extended domain.

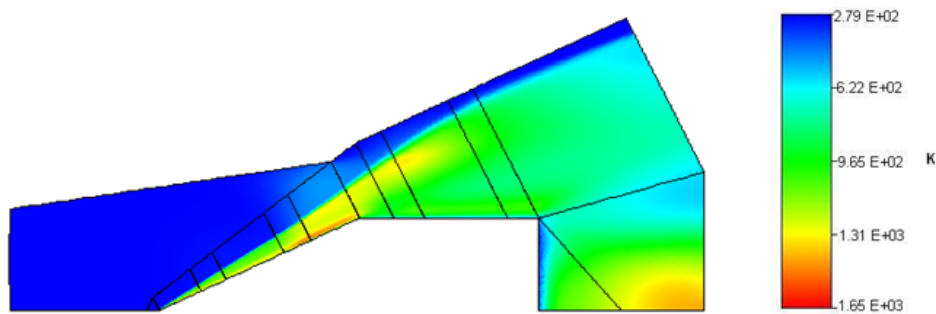


Figure 13.3.24: Computed temperature field with MHD interaction with the extended domain.

	Measured [Pa]	Calculated [Pa]	Difference [%]	Exp. uncert. [%]
Position 1 - no MHD	1031	1030	0.10	0.3
Position 1 - MHD	1168	1178	0.86	4.3
Position 2 - no MHD	125.5	168	33.86	26.4
Position 2 - MHD	133	229	71.41	47.7

Table 13.3.9: Pressure comparison between measured and numerical runs for the condition *C* (extended computational domain).

main (table 13.3.8), it is possible to note how the main difference is obtained for the MHD run for the pressure position 1. This is in agreement with the extension of the domain realized closer to the tip of the test body, where the first pressure sensor is positioned.

Chapter 14

MHD experiments conclusions

The MHD interaction in a hypersonic flow had been experimentally investigated. A conical test body had been placed at the exit of the hypersonic nozzle. An ionized argon flow at a Mach number of six had been obtained. Firstly a characterization of the plasma flow had been realized to obtain the information necessary to define the experimental conditions. Electron temperature and electron number density before the expansion in the nozzle had been estimated by means of emission spectroscopy. Moreover the electron number density of the plasma at the nozzle exit had been evaluated by means of microwave absorption measurements. These observations showed deviations from thermodynamic equilibrium and a plasma ionization degree frozen during the nozzle expansion.

Numerical simulations of the plasma flow through the nozzle reproduced the experimental conditions with fair agreement. The differences between experimental and numerical results are due to the partial local thermodynamic equilibrium with an electron temperature larger than the gas temperature in the heating chamber in front of the nozzle and to the kinetic model approximation used in the code.

In the MHD interaction experiments, two sizes of the test body were utilized. A reduction of the sizes of the body was done to keep it inside the uniformity region of the hypersonic flow at the nozzle exit. The electrical

connection scheme allowed the short-circuiting of the Faraday current inside the plasma, enhancing the effect of the MHD interaction. Pressure, imaging, and electrical observations were done.

The increases of the pressure above the conical surface were caused by the MHD interaction. The pressure increase in this experiment was between 7% and 15%.

The images around the test body showed a rather different flow field in the tests without and with MHD interaction. In the MHD tests, bright rings due to the azimuthal Faraday currents were observed.

The Hall field was measured by means of electrical probes placed along the test body lateral surface. The measured values of the Hall field were in the range between 400 and 500V/m.

Numerical simulations realized by means of a time dependent two dimensional code at low magnetic Reynolds numbers showed a good agreement with the measurements. The important role of the Hall parameter in the hypersonic MHD interaction process had been demonstrated.

The results of the experiments described in this work show the potential of the MHD technology for its utilization during the re-entry of hypersonic vehicles into the atmosphere.

Appendices

Appendix A

Plasma frequency

If we consider a uniform electron distribution with electron density of n_e , and an external one-dimensional perturbation in the x direction, a displacement $\xi(x)$ in the electron distribution along the x direction is realized. The local electron density departs from the uniform density n_e by an increment of:

$$\delta n_e = -n_e \frac{d\xi}{dx}. \quad (\text{A.0.1})$$

Assuming that the net charge density ρ is zero in the total plasma volume (electron density is equal to the ion density), the actual perturbed charge density can be expressed as:

$$\delta\rho = -e \delta n_e = n_e e \frac{d\xi}{dx} \quad (\text{A.0.2})$$

where $-e$ is the electron charge. The charge displacement creates an electric field that must be taken into account in the charge conservation by means of the Gauss' law

$$\frac{dE}{dx} = n_e e \frac{d\xi}{dx} \quad (\text{A.0.3})$$

which can be integrated giving

$$E = \frac{n_e e}{\epsilon_0} \xi \quad (\text{A.0.4})$$

within an arbitrary constant. The electric force for unit charge is expressible as

$$F = -eE = -\frac{n_e e^2}{n_e e^2}. \quad (\text{A.0.5})$$

If we neglect the viscous damping forces generated by the collision between electrons and heavy particle, thus we consider a non-collisional plasma, the newton's equation of motion become

$$m_e \ddot{\xi} + \frac{n_e e^2}{\epsilon_0} \xi = F_{EXT} \quad (\text{A.0.6})$$

where m_e is the electron mass, ϵ_0 is the dielectric constant of the vacuum, $\ddot{\xi} = \partial^2 \xi / \partial t^2$ is the electron acceleration, and F_{EXT} is the external force required to cause the perturbation. If that external force is removed, the (A.0.6) shows how the electrons start to oscillate about their equilibrium positions with a simple harmonic motion at the plasma frequency (in fact it is an angular frequency)

$$\omega_p = \left(\frac{n_e e^2}{\epsilon_0 m_e} \right)^{1/2} \quad (\text{A.0.7})$$

All this treatment is valid in the most general case, so an arbitrary spatial distribution of $\xi(x)$ can be considered. This assumption implies that a plasma oscillation does not transfer energy; that is a disturbance does not propagate beyond the region in which it exists.

Appendix B

Electromagnetic wave propagation theory

For a better comprehension about how microwaves can be usefully utilized in plasmas, it is necessary to give a better insight to their nature. Like all electromagnetic waves, microwaves can be described by electric and magnetic fields, \mathbf{E} and \mathbf{H} , which are functions of space and time. The electric and magnetic fluxes, \mathbf{D} and \mathbf{B} , in a linear and isotropic medium, at any point are related to the field intensities by (the bold notation is for vector quantities)

$$\mathbf{D} = \epsilon \mathbf{E} = \epsilon_r \epsilon_0 \mathbf{E}, \quad (\text{B.0.1})$$

$$\mathbf{B} = \mu \mathbf{H} = \mu_r \mu_0 \mathbf{H}, \quad (\text{B.0.2})$$

where ϵ_0 and μ_0 are the usual permittivity and permeability in vacuum, and ϵ_r and μ_r are the dielectric constant (also called relative permittivity) and relative permeability of the medium. With these assumptions, next equations hold.

$$\epsilon = \epsilon_r \epsilon_0, \quad (\text{B.0.3})$$

$$\mu = \mu_r \mu_0. \quad (\text{B.0.4})$$

These vector fields are all related together by Maxwell's equations:

$$\nabla \cdot \mathbf{D} = \rho, \quad (\text{B.0.5})$$

$$\nabla \cdot \mathbf{B} = 0, \quad (\text{B.0.6})$$

$$\nabla \times \mathbf{H} = \mathbf{J} + \frac{\partial \mathbf{D}}{\partial t}, \quad (\text{B.0.7})$$

$$\nabla \times \mathbf{E} = -\frac{\partial \mathbf{B}}{\partial t}. \quad (\text{B.0.8})$$

Another relation holds between \mathbf{E} and \mathbf{J} , and it is expressed by mean the Ohm's law

$$\mathbf{J} = \sigma \mathbf{E} \quad (\text{B.0.9})$$

where σ is the conductivity of the medium.

The electromagnetic proprieties of a medium can be thus specified by three independent constants ϵ_r , μ_r and σ .

The equations (B.0.7) (B.0.8), together with the constitutive relations (B.0.1) (B.0.2), may be combined to obtain a separate equation for each field under the assumption of $\mathbf{J} = 0$ in the region of interest.

For the electric field we obtain the (B.0.10):

$$\nabla \times \nabla \times \mathbf{E} = -\frac{\partial(\nabla \times \mathbf{B})}{\partial t} = -\mu \frac{\partial(\nabla \times \mathbf{H})}{\partial t} \quad (\text{B.0.10})$$

Using now the (B.0.7) and taking into account the equation (B.0.10), it is possible to obtain:

$$\nabla \times \nabla \times \mathbf{E} = \nabla(\nabla \cdot \mathbf{E}) - \nabla^2 \mathbf{E} = -\mu \epsilon \frac{\partial^2 \mathbf{E}}{\partial t^2} \quad (\text{B.0.11})$$

Since $\rho = 0$ and considering that ϵ is constant, we finally obtain

$$\nabla^2 \mathbf{E} - \mu \epsilon \frac{\partial^2 \mathbf{E}}{\partial t^2} = 0 \quad (\text{B.0.12})$$

that is a three-dimensional wave equation. In fact a wave equation is expressed by the following expression (B.0.13)

$$\nabla^2 \mathbf{u} = \frac{1}{v^2} \frac{\partial^2 \mathbf{u}}{\partial t^2} \quad (\text{B.0.13})$$

where \mathbf{u} is a solution of the equation and v is the propagation velocity of the wave.

For the (B.0.12) the propagation velocity is the light velocity $c = (\mu\epsilon)^{(1/2)}$. Starting from the same Maxwell's equations and eliminating this time the electric field, we obtain the wave relation for the Magnetic field \mathbf{H} (B.0.14)

$$\nabla^2 \mathbf{H} - \mu\epsilon \frac{\partial^2 \mathbf{H}}{\partial t^2} = 0. \quad (\text{B.0.14})$$

For an harmonic variation of the fields as $e^{j\omega t}$, the equations (B.0.12) (B.0.14) become

$$\nabla^2 \mathbf{E} - k^2 \mathbf{E} = 0 \quad (\text{B.0.15})$$

$$\nabla^2 \mathbf{H} - k^2 \mathbf{H} = 0 \quad (\text{B.0.16})$$

where $k^2 = \omega^2 \mu\epsilon$. The equations (B.0.15) (B.0.16) are referred as Helmholtz equations and are also called reduced wave equation.

The quantity k is called *wave number* and can be expressed as

$$k = \omega \sqrt{\mu\epsilon} = \frac{\omega}{v} = \frac{2\pi}{\lambda} \quad (\text{B.0.17})$$

where the wavelength λ is equal to v/f .

In the free space the wave number is normally expressed as $k_0 = \omega \sqrt{\mu_0 \epsilon_0} = 2\pi/\lambda_0$.

The general solution of equations (B.0.15) (B.0.16) can be found by separations of variables (in our study only plane waves are considered).

For the electric field (the magnetic field case follow the same path) the equation (B.0.15) is valid for each component and can be expressed as

$$\frac{\partial^2 E_i}{\partial x^2} + \frac{\partial^2 E_i}{\partial y^2} + \frac{\partial^2 E_i}{\partial z^2} + k_0^2 E_i \quad i = x, y, z. \quad (\text{B.0.18})$$

Considering now the x component (analogous considerations can be done for the other components), from equation (B.0.18) a solution by means of separation of variable in the form $E_x = f(x)g(y)h(z)$ can be determined.

Substituting this solution in the equation (B.0.18) we find

$$\frac{f''}{f} + \frac{g''}{g} + \frac{h''}{h} + k_0^2 = 0. \quad (\text{B.0.19})$$

The separation of variables determine the following relations

$$\frac{d^2 f}{dx^2} + k_x^2 f = 0 \quad \frac{d^2 g}{dy^2} + k_y^2 g = 0 \quad \frac{d^2 h}{dz^2} + k_z^2 h = 0. \quad (\text{B.0.20})$$

The only restriction for these solutions is that

$$k_x^2 + k_y^2 + k_z^2 = k_0^2. \quad (\text{B.0.21})$$

Equations (B.0.20) are a simple-harmonic differential equations with exponential solutions of the form $e^{-jk_x x}$, $e^{-jk_y y}$, $e^{-jk_z z}$. One suitable solution for E_x may be choose as

$$E_x = A e^{-jk_x x - jk_y y - jk_z z} \quad (\text{B.0.22})$$

where A is an amplitude factor.

If we consider now the more general case of a medium with finite conductivity σ , the relation (B.0.9) at page 254 holds and physically a certain amount of energy will be dissipated by Joule effect.

For this case, the wave equation presents a dumping term due to the conductivity. From Maxwell's equations and for $\mathbf{J} \neq 0$ it is possible to obtain the following relation for the electric field:

$$\nabla^2 \mathbf{E} - \mu\sigma \frac{\partial \mathbf{E}}{\partial t} - \mu\epsilon \frac{\partial^2 \mathbf{E}}{\partial t^2} = 0. \quad (\text{B.0.23})$$

An analogous equation can be expressed for the magnetic field \mathbf{H} .

$$\nabla^2 \mathbf{H} - \mu\sigma \frac{\partial \mathbf{H}}{\partial t} - \mu\epsilon \frac{\partial^2 \mathbf{H}}{\partial t^2} = 0 \quad (\text{B.0.24})$$

For the time-harmonic case with fields varying as $e^{j\omega t}$, damping effects enter in through the complex nature of ϵ and μ .

In this case the equation (B.0.7) can be expressed as

$$\nabla \times \mathbf{H} = (\sigma + j\omega\epsilon)\mathbf{E}. \quad (\text{B.0.25})$$

The form of the equation (B.0.25) makes convenient to incorporate one of the two constant σ and ϵ in the other by means of a complex notation. Generally it is customary to define a complex dielectric constant as

$$\sigma + j\omega\epsilon \rightarrow j\omega\check{\epsilon} \quad (\text{B.0.26})$$

and so

$$\check{\epsilon} \equiv \epsilon_{\Re} - j\epsilon_{\Im} = 1 - j\frac{\sigma}{\omega} \quad (\text{B.0.27})$$

where the symbol $\check{\epsilon}$ denotes a complex quantity and the subscripts \Re and \Im denote respectively the real and imaginary components.

The equation (B.0.23) can be rewritten as

$$\nabla^2 \mathbf{E} + \omega^2 \mu_0 \epsilon_0 \left(1 - j\frac{\sigma}{\omega\epsilon_0} \right) = 0. \quad (\text{B.0.28})$$

For metals, the conduction current $\sigma\mathbf{E}$ is generally much larger than the displacement current $\omega\epsilon_0\mathbf{E}$ so in equation (B.0.23) the latter term can be neglected leading to

$$\nabla^2 \mathbf{E} - \mu\sigma \frac{\partial \mathbf{E}}{\partial t} = 0. \quad (\text{B.0.29})$$

The equation (B.0.29) is a diffusion equation similar to that one which governs the flow of heat in a thermal conductor.

For the time-harmonic case we obtain

$$\nabla^2 \mathbf{E} - j\omega\mu_0\sigma\mathbf{E} = 0. \quad (\text{B.0.30})$$

The same considerations can be done for the magnetic field \mathbf{H} .

Appendix C

Schlieren refraction in geometric optic

In this appendix, the basis of the geometric theory of refraction will be explained. This theory is only an approximation to the more complex physical optics, but is sufficient for our purpose.

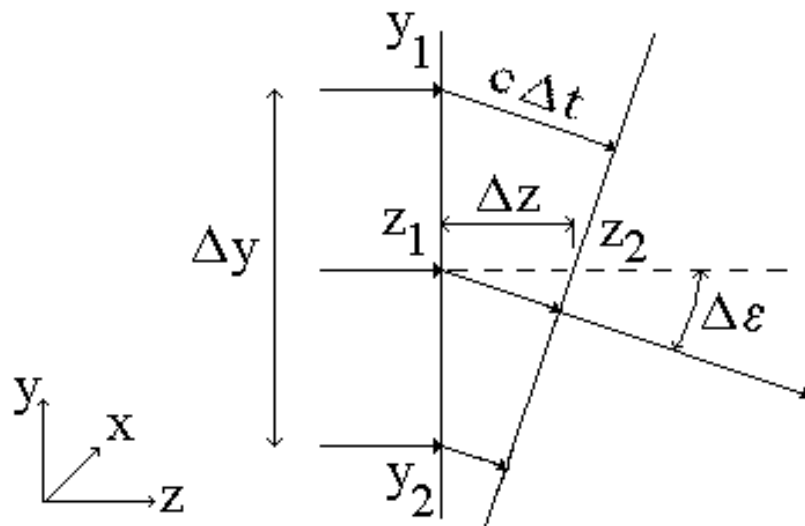


Figure C.0.1: Diagram of elemental light refraction by a refractive index gradient dn/dy

In figure C.0.1, propagating rays of light pass through a planar 2 – D Schlieren object in x and y . For simplicity we assume a negative vertical refractive index gradient $dn/dy < 0$, and no gradient in the other two directions.

The planar waveform of light is passing through z_1 directs toward z_2 .

The presence of the Schlieren object determines a refraction of the light by an angle $\Delta\epsilon$ and the wavefront propagates from z_1 to z_2 covering this differential distance Δz in a differential time Δt .

By the definition of refractive index $n = c_0/c$, the local light velocity c is equal to c_0/n (where c_0 is the light velocity in the vacuum).

The figure allows us to affirm that

$$\Delta\epsilon = \frac{(c_0/n_2 - c_0/n_1)}{\Delta y} \Delta t. \quad (\text{C.0.1})$$

The differential time Δt can be expressed as

$$\Delta t = \Delta z \frac{n}{c_0}. \quad (\text{C.0.2})$$

The union of these two equation leads to

$$\Delta\epsilon = \frac{n}{n_1 n_2} \frac{(n_1 - n_2)}{\Delta y} \Delta t. \quad (\text{C.0.3})$$

The term $n/(n_1 n_2)$ in this equation can be simplified to $1/n$ in the limit as Δy tends to zero.

Letting all the finite differences approach zero, we obtain

$$\frac{\partial\epsilon}{\partial z} = \frac{1}{n} \frac{dn}{dy}. \quad (\text{C.0.4})$$

Considering now that ϵ is a very small angle approximatively equal to dy/dz , it is possible to obtain

$$\frac{\partial^2 y}{\partial z^2} = \frac{1}{n} \frac{\partial n}{\partial y}. \quad (\text{C.0.5})$$

This equation relates the entity of the curvature of the refracted ray to the magnitude of the responsible refractive index gradient.

A similar expression can be written also for the x direction assuming a 2-D gradient field:

$$\frac{\partial^2 x}{\partial z^2} = \frac{1}{n} \frac{\partial n}{\partial x}. \quad (\text{C.0.6})$$

Bibliography

- [1] G.S. Settles. *Schlieren and shadowgraph techniques*. Springer, 1949.
- [2] H. R. Griem. *Principles of Plasma Spectroscopy*. Cambridge University Press, 2001.
- [3] L. Léger, E. Moreau, and G. Touchard. Control of low velocity airflow along a flat plate with a dc electrical discharge. *Proc. IEEE-IAS World Conf. on Industrial Applications of Electrical Energy*, 2001.
- [4] E. Moreau. Airflow control by non-thermal plasma actuators. *J. of Appl. Phys.*, 40:605–636, 2007.
- [5] D.M. Orlov. *Modeling and simulation of single dielectric barrier discharge plasma actuators*. PhD thesis, University of Notre Dame, 2006.
- [6] D. Greenblatt, B. Göksel, I. Rechenberg, C.Y. Schüle, D. Romann, and C.O. Paschereit. Dielectric barrier discharge flow control at very low flight reynolds numbers. *AIAA JOURNAL*, 46(6), 2008.
- [7] R. Van Dycken, A. Byerley H. Perez-Blanco, and T. McLaughlin. Plasma actuator for wake flow control of high camber blades during part load operation. *Proc. ASME GT2004-53227*, 2004.
- [8] C.O. Porter, J.W. Baughn, T.E. McLaughlin, C.L. Enloe, and G.I. Font. Plasma actuator force measurements. *AIAA Journal*, 45(7), 2007.

- [9] T. Corke, F. Thomas, D. Orlov, M. Iqbal, A. Kozlov, H. Othman, and D. Shatzman. ?? *DBD Plasma Actuator Workshop, USAFA*, 2006.
- [10] C.A. Borghi, M.R. Carraro, and A. Cristofolini. Magneto-hydrodynamics interaction in the shock layer of a wedge in a hypersonic flow. *IEEE Transaction on Plasma Science*, 34(5), 2006.
- [11] M.A. Heald and C.B. Wharton. *Plasma diagnostic with microwaves*. John Wiley & Sons, 1965.
- [12] G. Gardet, G. Moulard, M. Courbon, F. Rogemond, and M. Druetta. Evaluation of the rotational temperature in n_2 discharges using low-resolution spectroscopy. *Meas. Sci. Technol.*, 11:333–34, 2000.
- [13] H. R. Griem. *Plasma Spectroscopy*. McGraw Hill, 1964.
- [14] Marco A. Gigos et al. New plasma diagnosis tables of hydrogen stark broadening including ion dynamics. *J. Phys. B: At. Mol. Opt. Phys.*, 29:4795–4838, 1996.
- [15] Gad-El-Hak M 2000. *Flow Control*. Cambridge University Press, 2000.
- [16] E. Moreau. Airflow controls by non-thermal plasma actuators. *Journal Of Applied Physics*, 40:605–636, 2007.
- [17] J.R. Roth, D.M. Sherman, and S.P. Wilkinson. Boundary layer flow control with a one atmosphere uniform glow discharge surface plasma. *36th AIAA Aerospace and Exhibit Meeting*, AIAA-1998-0328, 1998.
- [18] C.A. Borghi, M.R. Carraro, and A. Cristofolini. Plasma and flow characterization in a flat panel one atmosphere uniform barrier discharge. *36th AIAA Plasmadynamic and Laser Conference*, AIAA-2005-5307, 2005.
- [19] J. Pons, E. Moreau, and G. Touchard. Electrical and aerodynamic characteristics of atmospheric pressure barrier discharges in ambient air. *Proc. ISNTPT*, pages 370–10, 2004.

-
- [20] T. Corke, D. Cavalieri, and E. Matlis. Boundary layer instability on a sharp cone at mach 3.5 with controlled input. *AIAA-2002-0350*, 2001.
- [21] D.F. Opaits, G. Neretti, A.V. Likhanskii, S. Zaidi, M. Shneider, and R.B. Miles. Experimental investigation of dbd plasma actuators driven by repetitive high voltage nanosecond pulses with dc or low-frequency sinusoidal bias. *38th AIAA Plasmadynamics and Lasers Conference*, AIAA-2007-4532, 2007.
- [22] B. Arad, Y. Gazit, and A. Ludmirsky. A sliding discharge device for producing cylindrical shock waves. *J. of Appl. Physics*, 20:360–367, 1987.
- [23] S.B. Leonov and D.A. Yarantsev. Mechanisms of flow control by near-surface electrical discharge generation. *AIAA-2005-0780*, 2005.
- [24] C.S. Kalra, M.N. Shneider, and R.B. Miles. Numerical study of shock-wave induced boundary layer separation control using plasma actuators. *46th AIAA Aerospace Science Meeting and Exhibit*, AIAA-2008-1095, 2008.
- [25] J. Huang. *Documentation and control of flow separation on a linear cascade of Pak-B blades using plasma actuators*. PhD thesis, University of Notre Dame, 2005.
- [26] D.K. Van Ness II, T.C. Corke, and S.C. Morris. Turbine tip clearance flow control using plasmas actuators. *AIAA meeting*, AIAA-2006-0021, 2006.
- [27] W. Siemens, 1857.
- [28] Overview of Dielectric Barrier Discharge.
- [29] B. Eliasson and U. Kogelschatz. *IEEE Trans. Plasma Sci.*, 19:309, 1991.

- [30] B. Eliasson, M. Hirth, , and U. Kogelschatz. *J. Phys. D: Appl. Phys.*, 20:1422, 1987.
- [31] M. Robinson. Movement of air in the electric wind of the corona discharge. *AIEE Trans*, 80:143–50, 1961.
- [32] F. Saemoto. The influence of high voltage discharge on flat plate drag at low reynolds number air flow. Master’s thesis, Iowa State University, 1992.
- [33] A. Soldati and S. Banerjee. Turbulence modification by large scale organized electrohydrodynamics flow. *Phys. Fluids*, 10:1742–56, 1998.
- [34] J.R. Roth. *Industrial Plasma Engineering*, volume 1. Bristol: Institute of Physics Publishing, 1995.
- [35] J.R. Roth. *Industrial Plasma Engineering*, volume 2. Bristol: Institute of Physics Publishing, 2001.
- [36] A. Schütze *et al.* The atmospheric-pressure plasma jet: a review and comparison to other plasma sources. *IEEE Trans. Plasma Sci.*, 26:1685–94, 1998.
- [37] A. Fridman, A. Chirokov, and A. Gutsol. Non-thermal atmospheric pressure discharges. *J. Appl. Phys.*, 38:R1–24, 2005.
- [38] L.B. Loeb. *Electrical Coronas, Their Basic Physical Mechanism*. Berkeley: University of California Press, 1965.
- [39] J.R. Roth. Electrohydrodynamically induced airflow in a one atmospheric uniform glow discharge surface plasma. *25th IEEE Int. Conf. Plasma Science*, 1998.677891, 1998.
- [40] C.A. Borghi, M.R. Carraro, A. Cristofolini, and G. Neretti. Electrohydrodynamic interaction induced by a dielectric barrier discharge. *Journal of Applied Physics*, 103-063304, 2008.

- [41] M. Forte, J. Jolibois, J. Pons, and E. Moreau. Optimization of a dielectric barrier discharge actuator by stationary and non-stationary measurements of the induced flow velocity: application to airflow control. *Exp Fluids*, 43:917–28, 2007.
- [42] A.V. Likhanskii, M.N. Shneider, S.O. Macheret, and R.B. Miles. Modeling of interaction between weakly ionized near surface plasmas and gas flow. *44th AIAA Aerospace Sciences Meeting and Exhibit*, AIAA-2006-1204, 2006.
- [43] N. Bernard, N. Balcon, and E. Moreau. Electric wind produced by a single dielectric barrier discharge actuator operating in atmospheric flight conditions - pressure outcome. *39th Plasmadynamic Conference and Laser Conference*, AIAA-2008-3792, 2008.
- [44] C.L. Enloe, T.E. McLaughlin, R.D. VanDyken, and K.D. Kachner. Plasma structure in the aerodynamic plasma actuator. *AIAA Meeting*, AIAA-2004-0844, 2004.
- [45] J.P. Boeuf and L.C. Pithford. Electrohydrodynamic force and aerodynamic flow acceleration in surface dielectric barrier discharge. *Journal of Applied Physics*, 97-103307, 2005.
- [46] J.P. Boeuf, Y. Lagmich, T. Callegari, and Pitchford. Electrohydrodynamic force and acceleration in surface discharges. *AIAA Meeting*, AIAA-2006-3374, 2006.
- [47] C.L. Enloe, T.E. McLaughlin, R.D. VanDyken, K.D. Kachner, E. Jumper, and T. Corke. Mechanisms and responses of a single-dielectric barrier plasma actuator: Plasma morphology. *AIAA 42*, pages 589–594, 2004.
- [48] G.I. Font. Boundary layer control with atmospheric plasma discharges. *40th AIAA Meeting*, AIAA-2004-2128, 2004.

- [49] M. Forte, J. Jolibois, F. Moreau, G. Touchard, and M. Cazalens. Optimization of a dielectric barrier discharge actuator by stationary and non-stationary measurements of the induced flow velocity - application to flow control. *3rd AIAA Flow Control Conference*, AIAA-2006-2863, 2006.
- [50] M.L. Post. *Plasma actuators for separation control on stationary and unstationary airfoils*. PhD thesis, University of Notre Dame, 2004.
- [51] T.C. Corke, B. Mertz, and m.P. Patel. Plasma flow control optimized airfoil. *44th AIAA Aerospace Sciences Meeting and Exhibit*, AIAA 2006-1208, 2006.
- [52] D.V Gaitonde, M.R. Visbal, and S. Roy. A coupled approach for plasma-based flow control simulations of wing sections. *44th AIAA Aerospace Sciences Meeting and Exhibit*, AIAA 2006-1205, 2006.
- [53] M.P. Patel, Z.H. Solwe, T.C. Corke, and C. He. Autonomous sensing and control of wing stall using a smart plasma slat. *44th AIAA Aerospace Sciences Meeting and Exhibit*, AIAA 2006-1207, 2006.
- [54] J.R. Roth. Aerodynamic flow acceleration using paraelectric and peristaltic electrohydrodynamic effects of a one atmosphere uniform glow discharge plasma. *PHYSICS OF PLASMAS*, 10(5), 2003.
- [55] M.L. Post and T.C. Corke. Flow control with single dielectric barrier plasma actuators. *35th AIAA Fluid Dynamics Conference and Exhibit*, AIAA 2005-4630, 2005.
- [56] M. Yadav, X. Dai, and J.R. Roth. Flow field measurements of peristaltic and combined paraelectric and peristaltic actuators using an impedance matched polyphase power supply. *The 31st IEEE International Conference*, 10.1109/PLASMA.2004.1339867, 2004.
- [57] C.A. Borghi, M.R. Carraro, A. Cristofolini, and G. Neretti. An analysis of a three phase flat panel uniform barrier discharge at atmospheric

- pressure. *37th AIAA Plasmadynamics and Lasers Conference*, AIAA-2006-3380, 2006.
- [58] A. Chelouah, E. Marode, and G. Hartmann. Measurement of rotational and vibrational temperatures in a low-pressure plasma device using the Abel transform and a spectral slit function. *Journal of Appl. Physics*, 27:770–80, 1994.
- [59] C.A. Borghi, M. R. Carraro, and A. Cristofolini. Electrical and plasma characterization of a one atmosphere uniform barrier discharge. *International Conference on Gas Discharges and their Applications*, 2004.
- [60] A. Likhanskii, M. Shneider, D. Opaitis, S. Macheret, , and R. Miles. *38th AIAA Plasmadynamics and Lasers Conference*, Paper No. AIAA-2007-4533, 2007.
- [61] Dmitry F. Opaitis, Gabriele Neretti, Alexandre V. Likhanskii, Sohail Zaidi, Mikhail N. Shneider, Richard B. Miles, and Sergey O. Macheret. Experimental investigation of dbd plasma actuators driven by repetitive high voltage nanosecond pulses with dc or low-frequency sinusoidal bias. *38th AIAA Plasmadynamics and Lasers Conference*, AIAA 2007-4532, 2007.
- [62] G.A. Mesiats, S.A. Nasibov, and V.v. Kremnev. Formirovanie nanosekundnih impulsov visokogo napriazhenia. Energia, Moscow, 1970.
- [63] Dmitry F. Opaitis, Alexandre V. Likhanskii, Gabriele Neretti, Sohail Zaidi, Mikhail N. Shneider, Richard B. Miles, and Sergey O. Macheret. Experimental investigation of dielectric barrier discharge plasma actuators driven by repetitive high-voltage nanosecond pulses with dc or low frequency sinusoidal bias. *Journal of Appl. Phys.*, 1014(043304), 2008.
- [64] S. Leonov, D. Yarantsev, and A. Kuriachy. (unpublished). 43rd AIAA Aerospace Sciences Meeting and Exhibit, 2005.

- [65] R. Sosa, E. Arnaud, and G. Artana. (unpublished). International Symposium on Electrohydrodynamics (ISEHD), 2006.
- [66] T. Jukes, K. Choi, G. Johnson, and S. Scott. (unpublished). *Third AIAA Flow Control Conference*, AIAA-2006-3693, 2006.
- [67] A. M. Konchakov, V. M. Krivtsov, S. B. Leonov, V. R. Soloviev, and D. A. Yarantsev. (unpublished). *preprint of Institute of High Temperature*, 2006.
- [68] G.I. Font, S. Jung, C.L. Enloe, T. E. McLaughlin, W. L. Morgan, and J.W. Baughn. (unpublished). *44th AIAA Aerospace Sciences Meeting and Exhibit*, AIAA-2006-167, 2006.
- [69] M. R. Visbal and D. V. Gaitonde. (unpublished). *44th AIAA Aerospace Sciences Meeting and Exhibit*, AIAA-2006-505, 2006.
- [70] M.R. Visbal, D.V. Gaitonde, and S.P. Gogineni. Direct numerical simulation of a forced transitional plane wall jet. *29th Fluid Dynamics Conference*, AIAA-1998-2643, 1998.
- [71] S. Gogineni, M. Visbal, and C. Shih. Phase-resolved piv measurements in a transitional plane wall jet: a numerical comparison. *Experiments in fluid*, 27(2), 1999.
- [72] S. Gogineni, M. Visbal, and C. Shih. (unpublished). *35th AIAA Aerospace Sciences Meeting and Exhibit, Reno*, AIAA-1997-0071, 1997.
- [73] D.A. Anderson, J.C. Tannehill, and R.H. Pletcher. *Computational Fluid Mechanics and Heat Transfer*. Hemisphere, New York, 1984.
- [74] A. Likhanskii, M. Shneider, S. Macheret, and R. Miles. Modeling of interaction between weakly ionized near-surface plasmas and gas flow. *AIAA 44th Aerospace Sciences Meeting and Exhibit*, AIAA-2006-1204, 2006.

- [75] A. Likhanskii, M. Shneider, S. Macheret, and R. Miles. Optimization of dielectric barrier discharge plasma actuators driven by repetitive nanosecond pulses. *45th AIAA Aerospace Sciences Meeting and Exhibit*, AIAA-2007-633, 2007.
- [76] J. Gregory, C. Enloe, G. Font, and T. McLaughlin. Force production mechanisms of a dielectric- barrier discharge plasma actuator. *45th AIAA Aerospace Sciences Meeting and Exhibit*, AIAA-2007-0185, 2007.
- [77] R. Van Dyken, T. McLaughlin, and C. Enloe. Parametric investigations of a single dielectric barrier plasma actuator. *42th AIAA Aerospace Sciences Meeting and Exhibit*, AIAA-2004-0846, 2004.
- [78] Yu. P. Raizer, M. N. Shneider, and N. A. Yatsenko. Radio-frequency capacitive discharges. CRC, 2006.
- [79] C.A. Borghi and M. Ishikawa. New concepts of mhd power generation, (invited paper). In *Proc. 12th Int. Conference on MHD Electrical Power Generation*, page Vol. 1, 1196.
- [80] R.K. Agarwal. Numerical simulation of compressible viscous mhd flows to study the possibility of reducing supersonic drag of blunt bodies and scramjet inlets. *AFOSR Grant*, No.F49620-99-1-0005, 1999.
- [81] J.T. Lineberry et al. Prospects for mhd flow control for hypersonics. *31st Plasmadynamics and Lasers Conference*, AIAA-2000-3057, 2000.
- [82] D.J. Moorhouse and C.F. Suchomel. Exergy methods applied to hypersonic vehicle challenge. *32sd Plasmadynamics and Lasers Conference*, AIAA-2001-30630, 2001.
- [83] E.P. Gurianov and P.T. Harsha. Ajax: new directions in hypersonic technology. *27th Plasmadynamics and Lasers Conference*, AIAA-96-4609, 1996.

- [84] V.A. Bityurin et al. Assessment of hypersonic mhd concepts. *28th Plasmadynamics and Lasers Conference*, AIAA-97-2393, 1997.
- [85] R.J. Litchford, U.B. Metha, and J.T. Lineberry. Magneto-hydrodynamic augmented hypersonic air-breathing propulsion. *Space Transportation Day*, 2000.
- [86] S. O. Macheret et al. Mhd power extraction from cold hypersonic air-flow with external ionization. *30th Plasmadynamics and Lasers Conference*, AIAA-99-4800, 1999.
- [87] D.M. Van-Wie et al. Numerical investigation of mgd interaction in non-equilibrium plasma flow in the models of supersonic intake. *3rd Workshop on Magneto-Plasma-Aerodynamics in Aerospace Applications*, 2001.
- [88] et al. S.V. Bobashev. Influence of mhd interaction on shock-wave structures in supersonic diffuser. *2nd Workshop on Magneto-Plasma-Aerodynamics in Aerospace Applications*, 2000.
- [89] W.W. Vuillermont and U. Shumlack. Multi temperature, thermal and ion fraction effects over wedge and bluff body shapes in hypervelocity flow. *ICOPS2000*, 2000.
- [90] J.T. Lineberry and V.A. Bityurin et al. Cylinder with current in hypersonic flow. *3rd Workshop on Magneto-Plasma-Aerodynamics in Aerospace Applications*, 2001.
- [91] C.A. Borghi, M.R. Carraro, and A. Cristofolini. Analysis of magnetoplasma dynamic interaction in the boundary layer of a hypersonic vehicle. *Journal of Spacecraft and Rockets*, 41(4), 2004.
- [92] J.S. Shang et al. Magneto-aerodynamic interactions in weakly ionized hypersonic flow. *40th Aerospace Sciences Meeting and Exhibit*, AIAA-2002-0349, 2002.

- [93] J.S. Shang. Recent research in magneto-aerodynamics. *Progress in Aerospace Sciences*, 37:1–20, 2001.
- [94] A.L. Kuranov et al. Modern condition of development and perspective researches of hypersonic technologies under the 'ajax' concept. *2nd Workshop on Magneto-Plasma-Aerodynamics in Aerospace Applications*, 2000.
- [95] V.A. Zeigarnik et al. Dimension optimization of mhd generators for hypersonic aircraft of 'ajax' concept. *2nd Workshop on Magneto-Plasma-Aerodynamics in Aerospace Applications*, 2000.
- [96] V.A. Bityurin et al. Studies on mhd interaction in hypervelocity ionized air flow over aero-surfaces. *34th Plasmadynamics and Lasers Conference*, AIAA-2003-1365, 2003.
- [97] V.A. Bityurin. Mhd activity in russia. *ILG-MHD International Workshop on Magneto-Hydro-Dynamics Applications: State of the Art*, 2003.
- [98] A. Passaro, L. Biagioni, and L. d'Agostino. Compressibility effects in weakly turbulent hypersonic flow fields. *4th Eur. Symp. Aerothermodynamics Space Vehicles*, ISBN: 92-9092-789-5, 2001.
- [99] K. Sutton and R. A. Graves. A general stagnation-point convective heating equation for arbitrary gas mixtures. *NASA TR R-376*, 1971.
- [100] A. Sola et. al. On the use of the line-to-continuum intensity ratio for determining the electron temperature in a high-pressure argon surface-microwave discharge. *Journal of Applied Physics*, 28:1099–110, 1995.
- [101] Marco A. Gigoso and Valentin Cardenoso. New plasma diagnosis tables of hydrogen stark broadening including ion dynamics. *Journal of Physics B: Atomic, Molecular and Optic Physics*, 29:4795–838, 1996.

- [102] G. Colonna, M. Tuttafesta, and D. Giordano. Numerical methods to solve euler equations in one-dimensional steady nozzle flow. *Computer Physics Communications*, 138:213–221, 2001.
- [103] G. Colonna, M. Tuttafesta, M. Capitelli, and D. Giordano. No formation in one dimensional nozzle air flow with state-to-state non-equilibrium vibrational kinetics. *33rd AIAA Thermophysics Conference*, AIAA 98-2951, 1998.
- [104] G. Colonna and M. Capitelli. Model of chemical, vibrational, electron kinetics in nozzle expansion. AIAA 2000-2415, 2001.
- [105] G. Colonna and M. Capitelli. The effects of electric and magnetic fields on high enthalpy plasma flows. AIAA 2003-4036, 2003.
- [106] A. Cristofolini et al. Experimental investigation on the mhd interaction around a sharp cone in an ionized argon flow. *37th AIAA Plasmadynamics and Lasers Conference*, AIAA-2006-3075, 2006.
- [107] M. Mitchner and C.H. Kruger. *Partially Ionized Gases*. Wiley-Interscience, New York, 1973.
- [108] C.A. Borghi, M.R. Carraro, and A. Cristofolini. An axi-symmetric hall configuration for mhd interaction in hypersonic flows. *36th AIAA Plasmadynamics and Lasers Conference*, AIAA-2005-4785, 2005.
- [109] Gabriele Neretti. Numerical models for the study of hall configuration in the mhd interaction for space applications. Master's thesis, University of Bologna, 2005.
- [110] A. Cristofolini. Numerical analysis of the mhd interaction around a sharp cone. Proceedings of the Thirtieth Biennial IEEE Conference on Electromagnetic Field Computation, 2008.